

**Aspects of Charged Lepton Flavor Violation in  
High-Energy Physics**

by

**Roman Marcarelli**

B.A., Cornell University, 2019

A thesis submitted to the  
Faculty of the Graduate School of the  
University of Colorado in partial fulfillment  
of the requirements for the degree of  
Doctor of Philosophy  
Department of Physics  
2025

Committee Members:

Ethan Neil, Chair

Oliver DeWolfe

Andrew Hamilton

Anna Hasenfratz

Jamie Nagle

Keith Ulmer

Marcarelli, Roman (Ph.D., Physics)

Aspects of Charged Lepton Flavor Violation in High-Energy Physics

Thesis directed by Prof. Ethan Neil

Despite its abundance in extensions to the Standard Model, charged lepton flavor violation (CLFV) has never been observed. In this dissertation, we review some potential avenues for the discovery of CLFV processes. We begin by reviewing the contributions of CLFV scalars to flavor-violating lepton decays and lepton dipole moments, emphasizing their sensitivity to parity-violation (PV) and coupling hierarchies. We then discuss a production mechanism for CLFV particles which is largely independent of PV and coupling hierarchies: on-shell production in experiments involving lepton-nucleus collisions ( $\ell^- A_Z \rightarrow \ell'^- A_Z \varphi$ ). We compare the production cross-sections for (pseudo)scalars and (axial-)vectors for a few benchmark scenarios: SLAC E137, the Electron Ion Collider (EIC), a hypothetical 1 TeV muon beam dump (MuBeD), and a hypothetical 1 TeV Muon (Synchrotron) Ion Collider (MuSIC). We examine the kinematical distributions of the final-state particles produced at these experiments, and discuss these in relation to detector geometry. We then apply these results to probe a particular class of CLFV scalar: leptophilic axion-like particles (ALPs). We compare these results to limits on the ALP-lepton couplings from Higgs-ALP decays at the LHC, assuming a substantial ALP-Higgs portal interaction. Finally, we explore the possibility of production and subsequent detection of massive gauge bosons for the anomaly-free  $U(1)_{L_i-L_j}$  symmetries at the EIC, MuBeD, and MuSIC. We also include the analysis for a dark photon and  $U(1)_{B-L}$  gauge boson, which, while not explicitly CLFV, serve as useful benchmarks for comparison.

## Dedication

*To my mother.*

## Acknowledgements

I would like to thank my great<sup>50 000 000</sup> grandmother for venturing out of the big pond. My mother for fostering my curiosity about the world from a young age, and encouraging me to pursue my passions. My father for teaching me to have a positive mental attitude toward life, and whose hard work helped put me through college. My twin sister, Gabriella, my half-sister Allison, my aunts Jill, Theresa, and Joyce, my uncles Michael and Stu, and my grandpa Bob and grandma Judy, for their company and continued support over the years.

I would never have achieved this milestone were it not for my mentors and teachers in academia. I am grateful to my advisor, Ethan Neil, for guiding my research and encouraging me to pursue new topics that piqued my interest, and whose flexibility was imperative to my success. I also thank my collaborator Hooman Davoudiasl for bringing a positive perspective to each meeting and engaging in insightful physics conversations. Finally, I thank my undergraduate professor Yuval Grossman, whose infectious commitment to teaching and physics helped guide my decision to pursue a graduate degree.

It's impossible to pursue a technical degree without a strong foundation, and for that I owe my gratitude to a handful of high school teachers. I thank my physics teacher Mr. Murray for creating the math, science, and engineering program at my high school which undoubtedly contributed to my success and the success of many others, and whose notes were *still* useful for me when studying for the physics GRE. I also thank my math teachers Ms. Bobay, Dr. Murray, Dr. Oddi and Mrs. Patsatsia who, in addition to being excellent educators inside the classroom, stayed after-school to train mathematically curious students like myself for state and national math competitions.

I thank my long-time friend and Boulder roommate Matt, for staying by my side and making graduate school during the pandemic bearable, and his dog Layla, for providing much-needed assistance with calculations from time to time. I am also grateful to the friends I met through my program in Colorado: Curtis, Kenny, and Jake for productive and interesting physics discussions, Evan, Yifan, Peter, and Sam for pushing me to my physical limits on challenging hikes and backpacking trips, Yifan and Talal for welcome lunch and coffee breaks and weekly watch-parties, and James and Evan for teaching me how to ski.

And then there are the friends who came before them: Joe, for insightful phone conversations and the occasional real-life outing. Avinash, Chau, Kenny, Kyle, and Sam, for at times engaging in helpful physics- and math-related discussions, and at other times offering a welcome means of decompression through gaming (albeit often at the expense of my sleep schedule). I also thank my friends from high school and before who contributed to my life academically and otherwise, some of whom I've kept in touch with and others whom I'd gladly reconnect with: Jeff, Jay, Aaron, Nick, Josh, Matt, Enes, Riancy, Nathan, Shreyash, Justin, and Louie.

## Contents

### **Chapter**

<b>1</b>	Introduction	<b>1</b>
<b>2</b>	Flavor-Violating Interactions in Quantum Field Theory	<b>5</b>
2.1	Introduction . . . . .	5
2.2	Flavor Violation in the SM . . . . .	7
2.3	Flavor-Violating Scalars . . . . .	10
2.3.1	Symmetry Properties of FV Scalar Interactions . . . . .	10
2.3.2	Two-Higgs-Doublet Model . . . . .	12
2.3.3	Froggatt-Nielsen Models . . . . .	14
2.4	Axion-Like Particles . . . . .	15
2.4.1	ALP Effective Field Theory . . . . .	17
2.4.2	ALP as a (Pseudo-)Scalar . . . . .	19
2.4.3	ALPs in Froggatt-Nielsen Models . . . . .	21
2.4.4	ALPs from Composite Dark Sectors . . . . .	23
2.5	New $U(1)$ Gauge Bosons . . . . .	26
<b>3</b>	Chiral Subtleties in Charged Lepton Flavor Physics	<b>29</b>
3.1	Introduction . . . . .	29
3.2	LFV Interaction . . . . .	30
3.2.1	UV Considerations . . . . .	30

3.2.2	Effective Interaction . . . . .	34
3.3	LFV Lepton Decays . . . . .	35
3.3.1	Dipole Transition Form Factors . . . . .	36
3.3.2	Approximations . . . . .	40
3.3.3	Radiative Decay . . . . .	43
3.3.4	Trilepton Decay . . . . .	44
3.3.5	Limits from LFV Decays . . . . .	46
3.4	LFV Contributions to Lepton Electric and Magnetic Dipole Moments . . . . .	49
3.4.1	Electric Dipole Moments . . . . .	50
3.4.2	Magnetic Dipole Moments . . . . .	50
3.4.3	Relevant Form Factors . . . . .	53
3.4.4	Approximations . . . . .	55
3.4.5	Electric dipole moment constraints . . . . .	56
3.4.6	Magnetic dipole moment constraints . . . . .	57
3.4.7	Explanations to electron and muon $g - 2$ anomalies . . . . .	60
<b>4</b>	<b>Particle Production from Lepton-Nucleus Collisions</b>	<b>63</b>
4.1	Introduction . . . . .	63
4.2	Feasibility of Particle Production in Lepton-Nucleus Collisions . . . . .	67
4.3	Nuclear and Atomic Form-Factors . . . . .	69
4.4	Amplitude Calculation . . . . .	70
4.4.1	Phase-Space Integration . . . . .	73
4.4.2	Features of the Production Cross-Section . . . . .	75
4.5	Weizsäcker-Williams Approximation . . . . .	80
4.5.1	$2 \rightarrow 2$ Amplitudes . . . . .	81
4.5.2	Improved Weizsäcker-Williams Approximation . . . . .	82
4.5.3	Cross-Section Comparisons . . . . .	84

4.6	Kinematical Distributions of $\varphi$	87
4.6.1	Pseudorapidity Distributions for Beam Dump vs. Collider Experiments	89
4.6.2	Boost Distributions for Beam Dump vs. Collider Experiments	92
4.7	Kinematical Distribution of Final-State Lepton	95
4.8	Case Study: Limits on LFV Scalars	96
<b>5</b>	<b>GeV-Scale LFV Axion-Like Particles in Collider Experiments</b>	<b>100</b>
5.1	Introduction	100
5.2	Higgs Decays at the LHC	102
5.2.1	Prompt ALP Decays at CMS	105
5.2.2	Displaced ALP Decays at ATLAS and MATHUSLA	108
5.2.3	Combined Limits on LFV Couplings	110
5.3	LFV ALP Production at The EIC	113
5.3.1	Detector Capabilities	114
5.3.2	Signal and Background	114
5.3.3	Combined Limits	116
5.3.4	Explanations to $(g - 2)_e$	117
5.4	LFV ALP Production at MuBeD and MuSIC	119
5.4.1	Detector Capabilities	119
5.4.2	Signal and Background	122
5.4.3	Combined Limits	124
5.4.4	Explanation to $(g - 2)_\mu$ Anomaly	126
<b>6</b>	<b>Hidden Gauge Bosons at Lepton-Ion Colliders</b>	<b>129</b>
6.1	Introduction	129
6.2	Vector Boson Decay Rates	130
6.3	Detector Geometry and Displaced Signal	133
6.4	Limits at the EIC	138

6.5	Limits at MuBeD and MuSIC . . . . .	141
6.6	Displaced Vertex Resolution Considerations . . . . .	142
<b>7</b>	<b>Concluding Remarks</b>	<b>145</b>
 <b>Bibliography</b>		 <b>151</b>
 <b>Appendix</b>		
<b>A</b>	<b>Composite ALP Matching</b>	<b>164</b>
A.1	UV Lagrangian . . . . .	164
A.2	Higgs couplings . . . . .	165
A.3	Lepton couplings . . . . .	166
A.3.1	Amplitude calculation . . . . .	167
A.3.2	Dark Pion Matching . . . . .	169
<b>B</b>	<b>Distance of Closest Approach</b>	<b>171</b>

**Tables****Table**

3.1	Current experimental constraints and future prospects on the branching fractions for the decay modes $\ell_i \rightarrow \ell_j \gamma$ and $\ell_i \rightarrow \ell_j \ell_k \bar{\ell}_l$ at the 90% confidence level. . . . .	43
3.2	A table demonstrating which LFV coupling products contribute to each LFV lepton decay. . . . .	47
6.1	The charges of the SM fermions under each of the anomaly-free abelian groups discussed in the text. . . . .	131

## Figures

### Figure

1.1	A Feynman diagram representing the LFV $\mu \rightarrow e\gamma$ decay mediated via neutrino oscillation. . . . .	3
2.1	A trapezoid which encodes the relationship between equivalent effective field theory terms. . . . .	21
3.1	Feynman diagrams which contribute to the diagonal and off-diagonal lepton dipole form-factors. . . . .	37
3.2	Feynman diagrams which contribute to the trilepton decay processes $\ell_i \rightarrow \ell_j \ell_k \bar{\ell}_l$ . . .	44
3.3	Constraints on LFV scalar and ALP couplings from LFV lepton decay limits. . . . .	48
3.4	Constraints on LFV scalar and ALP couplings from the lepton electric dipole moments. .	57
3.5	Constraints on LFV scalar and ALP couplings from the lepton magnetic moments. .	58
3.6	LFV scalar and ALP explanations to electron $g - 2$ anomalies. . . . .	60
3.7	LFV scalar and ALP explanations to muon $g - 2$ anomaly. . . . .	61
4.1	Relevant Feynman diagrams for the process $\ell A_Z \rightarrow \ell' A_Z \varphi$ via photon exchange. .	70
4.2	Production cross-sections for the process $\ell A_Z \rightarrow \ell' A_Z \varphi$ at various lepton-nucleus collision experiments. . . . .	77
4.3	Relevant $2 \rightarrow 2$ Feynman diagrams for approximating the process $\ell A_Z \rightarrow \ell' A_Z \varphi$ via the Weizsäcker-Williams approximation. . . . .	81

4.4 Comparisons between cross-sections computed exactly and via the Weizäcker-Williams and Improved Weizsäcker-Williams approximations for the process $\ell A_Z \rightarrow \ell A_Z \varphi$ at various lepton-nucleus collision experiments. . . . .	85
4.5 Comparisons between cross-sections computed exactly and via the Weizäcker-Williams and Improved Weizsäcker-Williams approximations for the process $\ell A_Z \rightarrow \tau A_Z \varphi$ at various lepton-nucleus collision experiments. . . . .	86
4.6 Pseudo-rapidity distributions of scalars produced at various lepton-nucleus collision experiments. . . . .	90
4.7 Interquartile range as a function of mass for pseudo-rapidity distributions of scalars produced at various lepton-nucleus collision experiments. . . . .	91
4.8 Boost distributions of scalars produced at various lepton-nucleus collision experiments. . . . .	93
4.9 Interquartile range as a function of mass for boost distributions of scalars produced at various lepton-nucleus collision experiments. . . . .	94
4.10 Interquartile range as a function of mass for pseudo-rapidity and boost distributions of leptons in certain scalar-production processes at lepton-nucleus collision experiments. . . . .	96
4.11 Limits on LFV scalars at various lepton-nucleus collision experiments. . . . .	98
4.12 Region in the $(m_\varphi, \theta_{\ell\tau})$ parameter space for which an LFV scalar $g - 2$ explanation is probed within $2\sigma$ at various lepton-nucleus collision experiments. . . . .	99
 5.1 ALP branching fraction assuming a democratic lepton coupling matrix. . . . .	105
5.2 Monte-Carlo estimate of efficiency of CMS search for LFV Higgs-ALP decays. . . . .	106
5.3 Limits on the effective Higgs-ALP coupling at CMS. . . . .	107
5.4 Constraints on LFV ALP models at CMS, ATLAS, and MATHUSLA in the Higgs-ALP and lepton-ALP coupling plane. . . . .	109
5.5 Constraints on LFV ALP models at CMS, ATLAS, and MATHUSLA in the ALP mass and lepton-ALP coupling plane. . . . .	112
5.6 Dita production process at lepton-ion collider experiments. . . . .	115

5.7	Projected constraints on LFV ALPs at the EIC. . . . .	116
5.8	Projected constraints on LFV ALPs at the EIC, alongside explanations for the electron $g - 2$ anomalies. . . . .	118
5.9	Region in the $m_a$ - $\Theta$ plane for which the EIC probes an LFV ALP explanation to either of the electron $g - 2$ anomalies. . . . .	118
5.10	A schematic representation of the fixed-target muon beam set up described in the text. . . . .	121
5.11	Projected constraints on LFV ALPs at the MuBeD and MuSIC. . . . .	125
5.12	Optimistic projected constraints on LFV ALPs at MuBeD. . . . .	126
5.13	Projected constraints on LFV ALPs at the MuBeD and MuSIC, alongside LFV ALP explanations to the muon $g - 2$ anomaly. . . . .	127
5.14	Region in the $m_a$ - $\Theta$ plane for which MuBeD and MuSIC probe an LFV ALP explanation to the muon $g - 2$ anomaly. . . . .	128
6.1	Branching fractions of a dark photon and anomaly-free $U(1)_X$ gauge bosons into SM final states. . . . .	132
6.2	A schematic representing the proposed ePIC detector at the EIC, along with a depiction of the distance-of-closest approach. . . . .	135
6.3	A schematic depiction of a muon beam dump experiment. . . . .	137
6.4	Projected constraints at the EIC on the kinetic mixing of a dark photon and gauge strength of anomaly-free abelian theories. . . . .	139
6.5	Projected constraints at the EIC, MuBeD, and MuSIC on the kinetic mixing of a dark photon and gauge strength of anomaly-free abelian theories. . . . .	140
6.6	A schematic representation of the difference between the transverse DCAs for a straight-line reconstructed trajectory and a circular reconstructed trajectory. . . . .	142
6.7	Limits on the dark photon kinetic mixing $\varepsilon e$ under different analyses. . . . .	144
A.1	UV matching diagram . . . . .	168

B.1 DCA Analysis Using Complex Geometry . . . . .	172
---	-----

## Chapter 1

### Introduction

In the mid-1960s, experimental physicist Raymond Davis Jr., in collaboration with theorist John Bahcall, placed a 100 000 gallon tank of dry-cleaning fluid one mile underground in a mine in South Dakota. While this may seem like a peculiar thing to do, they had a very clear goal in mind: to determine the flux of electron neutrinos produced from nuclear fusion reactions in the Sun. When a high-energy electron neutrino passes by the nucleus of a chlorine atom (which are prevalent in the dry-cleaning fluid he used), there is a small chance that the chlorine atom will absorb the neutrino and convert into an argon ion. By counting the number of argon ions accumulated over time, Davis was able to determine the number of electron neutrinos captured in their tank, and compare to the theoretical expectation calculated by Bahcall's solar model. By 1968, the first results of the experiment were published: they were capturing about one-third fewer electron neutrinos than anticipated from the leading theory at the time [1, 2]. The experiment continued until 1994, repeatedly confirming the apparent discrepancy. In that time, theorists rushed to find a potential explanation, while experimentalists rushed to confirm the result with other experiments. On the theory side, it was determined that neutrinos of the electron flavor must oscillate into neutrinos of the muon and tau flavor as they pass through the Sun and the vacuum of space. On the experimental side, the result was confirmed by the Super-Kamiokande experiment in 1998 [3] and the Sudbury Neutrino Observatory in 2001 [4]. The results are clear: although it is conserved in the Standard Model of particle physics, we know from these experiments that lepton flavor symmetry is violated in our universe.

While there is indirect evidence of physics beyond the Standard Model from astrophysical observations, no other direct-detection particle physics experiment has uncovered such a striking and persistent disagreement with the Standard Model paradigm. While the resolution – flavor oscillations of neutrinos – is straightforward, the source of this lepton flavor violation is still unknown. Many solutions have been proposed, such as heavy right-handed neutrinos and an additional Higgs boson with exotic properties [5, 6]. One of the difficulties with testing such theories is that neutrinos are electromagnetically neutral, which makes them particularly unwieldy in a lab environment. For every neutrino successfully captured in Davis’ experiment, one billion trillion neutrinos passed straight through the tank unimpeded.

Luckily for experimentalists, electromagnetically *charged* leptons also exist: the electron ( $e$ ), which is responsible for the inner-workings of all modern electronics; the muon ( $\mu$ ), which decays in two millionths of a second but has nonetheless been used to image hard-to-reach locations such as volcanic caverns and hidden rooms within the pyramids; and the tauon ( $\tau$ ), which decays in less than one trillionth of a second and, as far as we know, has no practical use (but is nonetheless of profound interest to the particle physics community!). Their charge makes these leptons much easier to study in experiments: the electromagnetic properties of the electron are the most precise measurements in all of physics, and those of the muon are not too far behind. But so far, according to both the Standard Model and modern experimental observations, the charged leptons do not appear to oscillate from one flavor to another. Nonetheless, it is possible to show that flavor violation in the neutrino sector leads directly to flavor violation in the charged lepton sector as well.

For a concrete example, consider the one-loop Feynman diagram depicting the decay of a muon to an electron and a photon  $\mu \rightarrow e\gamma$  (Fig. 1.1). The corresponding branching fraction<sup>1</sup> for this process can be estimated as [7]

$$\mathcal{B}(\mu \rightarrow e\gamma) \sim \frac{3}{32} \frac{\alpha}{\pi} \frac{(\Delta m_\nu^2)^2}{m_W^4}. \quad (1.1)$$

---

<sup>1</sup> For the uninitiated: *branching fraction* is the probability that a particle *branches*, or decays, to a specified final-state of other particles.  $\mathcal{B}(\mu \rightarrow e\gamma)$  represents the *probability* that a muon decays to an electron and a photon.

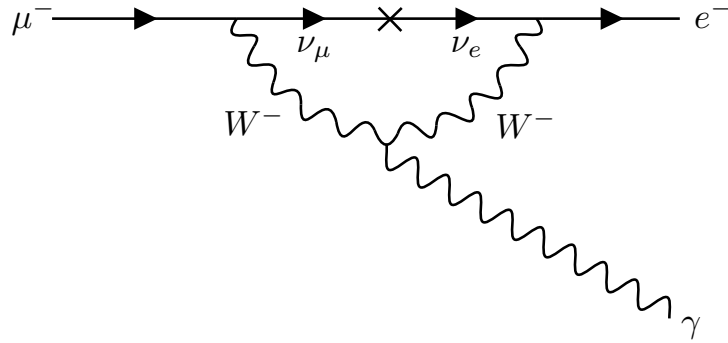


Figure 1.1: A Feynman diagram representing the LFV  $\mu \rightarrow e\gamma$  decay mediated via neutrino oscillation.

The neutrino masses  $m_{\nu_i}$  have never been measured directly and are predicted to be zero by the Standard Model. However, neutrino oscillation requires that they have non-zero mass, and observations of solar neutrinos predict a difference in the squares of the  $e$  and  $\mu$  neutrino masses of  $|m_{\nu_\mu}^2 - m_{\nu_e}^2| \approx (10 \text{ meV})^2$  [8]. This corresponds to a branching fraction of  $\mathcal{B}(\mu \rightarrow e\gamma) \approx 10^{-54}$ . Meanwhile, the leading experimental bounds on the  $\mu \rightarrow e\gamma$  decay come from the Mu to E Gamma (MEG) experiment, with a current limit on the branching fraction of  $\mathcal{B}(\mu \rightarrow e\gamma) < 4.2 \times 10^{-13}$ . Evidently, there is a large gap to fill. The upgrade to MEG, MEG II, is anticipated to improve these bounds by ten-fold by the time of its completion in 2026. If the MEG experiment continues to be upgraded with a factor-of-ten increase in sensitivity each decade, we can expect an announcement of the discovery of the  $\mu \rightarrow e\gamma$  decay mode via neutrino oscillations from the MEG XLI experiment some time in the 2400s. Let's not hold our breath.

The honest hope of particle physicists is that we will detect evidence of the  $\mu \rightarrow e\gamma$  decay mode long before then. If this occurs, it will evidently not be due to neutrino oscillations, but to some as-yet unknown process which exists beyond the Standard Model (and which may be responsible for the observed neutrino oscillations). Indeed, as we will explore in Chapter 2, it turns out to be very difficult to add new physics to the Standard Model *without* introducing charged lepton flavor violation (CLFV).

The ubiquity of CLFV in extensions of the Standard Model makes it a promising avenue

to search for new physics. After all, the charged leptons (and especially the electron) are much easier to detect and control than their neutral counterparts. But by the same token, if a CLFV signal *is* detected, the source of the flavor violation will likely remain unclear until more dedicated experiments are carried out. We have already seen this in the neutrino sector: there is a whole host of potential explanations for the existence and size of the neutrino masses, most of which can explain our observations while evading detection in other existing experiments.

In this dissertation, we will explore constraints on the existence of particles with CLFV couplings. In Chapter 2, we will review some models which exhibit this behavior, namely models with LFV scalars and axion like particles (ALPs). In Chapter 3, we will examine the constraints one can place on these models in the context of LFV charged lepton decays, such as the  $\mu \rightarrow e\gamma$  decay mode described in the Introduction. In Chapter 4, we will explore one possible production mechanism for such particles: coherent interactions between an electron or muon beam and a heavy nucleus. In Chapter 5, we will apply the results of Chapter 4 to place projected limits on the flavor-violating couplings of ALPs at various experiments involving lepton-nucleus collisions, and we will compare these to limits one can place from Higgs decays at the LHC. Finally, in Chapter 6, we will study production of dark  $U(1)$  gauge bosons at lepton-nucleus collision experiments, and resulting limits one can obtain on the gauge coupling. The code to generate the figures in this thesis can be found in the GitHub repository [github.com/rmarcarelli/thesis/](https://github.com/rmarcarelli/thesis/) [9].

## Chapter 2

### Flavor-Violating Interactions in Quantum Field Theory

#### 2.1 Introduction

If we are to discuss flavor violation, we must clarify what is meant by the *flavor* of a particle in the first place. Luckily, this does not involve licking any particles, but instead involves examining the fermion content of the Standard Model (SM). After electroweak symmetry breaking (EWSB), the SM fermions can be split into four sectors<sup>1</sup> according to their electromagnetic and color charges: there are the charged leptons, neutral leptons (or neutrinos), up-type quarks, and down-type quarks. Each of these sectors contains three fermions, any superposition of which constitutes a valid quantum state. Those superpositions which diagonalize the mass matrix of the fermions within a sector are given a flavor label, so the flavors can be defined as the names given to the mass eigenstates of the fermions within a sector. When the fermions within each sector are sorted according to their mass, they are said to be assorted according to their *generation* (so the lightest fermions within each sector belong to the *first* generation of fermions and so on).

This definition of flavor leaves some ambiguity as to the flavors of the neutrino sector, because (at least in the present form of the SM) the neutrinos are three-fold degenerate due to the lack of a neutrino mass matrix. As we will explore in more detail in Section 2.2, this allows us to define the neutrino flavors to *align* with the charged lepton flavors. This is why we typically only speak of *three* lepton flavors ( $e$ ,  $\mu$ , and  $\tau$ ), but *six* quark flavors (the up-type  $u$ ,  $c$ , and  $t$ , and the down-type

---

<sup>1</sup> Strictly speaking, these sectors are known as *super-selection sectors*, and restrict allowable quantum states to those whose kets transform identically under a gauge transformation.

*d*, *s*, and *b*). Contrary to the prediction of the SM, we know from astrophysical experiments that neutrinos do indeed have mass, as discussed in the Introduction. A more precise determination of the neutrino masses may ultimately lead to a naming convention of the neutrino mass eigenstates,<sup>2</sup> which would give a distinct set of neutrino flavors. Nevertheless, we would still be free to express the neutrino mass eigenstates in the charged lepton flavor basis, just as we can express the down-type quark mass eigenstates in the up-type quark flavor basis. The freedom to express the fermions of one sector in the flavor-basis of fermions in another sector is unique to the SM, since there is only one flavor-changing current (the  $W$ -boson interaction).

Somewhat confusingly, *flavor violation* does not directly correspond to a process which changes particles of one flavor to particles of another flavor. Rather, the term flavor-violating is reserved for interactions that contribute to flavor-changing *neutral* currents. In other words, an interaction is said to be flavor violating if it can lead to flavor transitions *within* one of the sectors of fermions described above. This can occur in one of two ways:

- (1) A charged particle exists which permits transitions *between* sectors, and multiple exchanges of this charged particle can lead to transitions *within* a sector.
- (2) A neutral particle exists which directly permits transitions from one flavor to another *within* a sector.

The  $W$ -boson interaction is of type (1), and there are no known interactions of type (2). Nevertheless, interactions of type (2) are prevalent in models of new physics, and will be the primary focus of this dissertation.

This chapter is by no means exhaustive, but serves to explore some features and examples of flavor-violation in field theories that will be studied in subsequent chapters. In Section 2.2, we will examine in detail how the flavor violation described above occurs in the quark sector of the SM but not the lepton sector. In Section 2.3, we will explore the symmetry properties of flavor-violating scalars and discuss some examples of flavor-violating scalars in models of new physics. In Section

---

<sup>2</sup> I propose the *iota*, *mote*, and *whit* neutrinos.

2.4, we will explore a special class of flavor-violating scalars: flavor-violating *axion-like particles*, which are of phenomenological interest. Finally, in Section 2.5, we will discuss dark  $U(1)$  gauge bosons, some of which exhibit lepton flavor violating couplings after spontaneous breaking of their gauge symmetry.

## 2.2 Flavor Violation in the SM

While flavor violation is present in the quark sector of the SM, it is apparently absent in the lepton sector. To understand this disparity, we can examine the differences between these sectors by expanding the SM in unitarity gauge. As a reminder, the SM gauge group is  $SU(3)_C \times SU(2)_L \times U(1)_Y$ , and unitarity gauge is defined as the gauge for which the Higgs field  $H$  (which has representation  $(1, 2)_{1/2}$  under the SM gauge group) is parametrized by  $H = e^{i\tau^a \xi_a}(0, \phi)$ , where  $\phi$  is a real scalar field,  $\xi_a$  are its angular modes, and  $\tau_a$  are the  $SU(2)_L$  generators.

We begin with the quark sector. Prior to EWSB, the quark fields are defined as a flavor triplet of Weyl fermions  $\mathbf{Q}$ ,  $\mathbf{U}_R$ , and  $\mathbf{D}_R$  with charges  $(3, 2)_{1/6}$ ,  $(3, 1)_{1/3}$ , and  $(3, 1)_{-2/3}$  under the SM gauge group. Flavor-violation in the quark sector arises from a disparity between the quark- $W$  boson interactions and the quark-Higgs interactions. By expressing the quark  $SU(2)_L$  doublet as  $\mathbf{Q} = e^{i\tau^a \xi_a}(\mathbf{U}_L, \mathbf{D}_L)$ , we can extract the  $W$ -boson interaction from the kinetic term:

$$\begin{aligned}\mathcal{L}_{Q,\text{kin.}} &= \overline{\mathbf{Q}}[i\cancel{d} - g\tau^a \cancel{W}_a - \dots] \mathbf{Q} = \dots - \frac{g}{\sqrt{2}} \overline{\mathbf{U}}_L \cancel{W}^+ \mathbf{D}_L - \frac{g}{\sqrt{2}} \overline{\mathbf{D}}_L \cancel{W}^- \mathbf{U}_L + \dots \\ &= \dots - \frac{g}{\sqrt{2}} \overline{\mathbf{U}} \cancel{W}^+ P_L \mathbf{D} + \dots + \text{H.c.}\end{aligned}\tag{2.1}$$

where we have only explicitly included the  $SU(2)$  generators in the covariant derivative, and later singled out the  $W$ -boson interactions.<sup>3</sup> In addition, there are the Higgs Yukawa interaction terms:

$$\begin{aligned}\mathcal{L}_{Q,\text{Yuk.}} &= [\overline{\mathbf{Q}} H] \mathbf{Y}^u \mathbf{U}_R + [\overline{\mathbf{Q}} \tilde{H}] \mathbf{Y}^d \mathbf{D}_R + \text{H.c.} \\ &= \phi [\overline{\mathbf{U}}_L \mathbf{Y}^u \mathbf{U}_R + \overline{\mathbf{U}}_R \mathbf{Y}^{\dagger u} \mathbf{U}_L] + \phi [\overline{\mathbf{D}}_L \mathbf{Y}^d \mathbf{D}_R + \overline{\mathbf{D}}_R \mathbf{Y}^{\dagger d} \mathbf{D}_L].\end{aligned}\tag{2.2}$$

---

<sup>3</sup> The insertion of the left-projection operator  $P_L$  ensures that only the  $W$ -boson only interacts with the left-handed component of the quarks.

In this form, while the interaction in Eq. 2.1 is diagonal in flavor space (i.e. the interaction  $\bar{\mathbf{U}}W^+P_L\mathbf{D} = \sum_i \bar{U}_i W^+ P_L D_i$  only couples up- and down-type quarks of the same index  $i$ ), the same cannot be said about the Yukawa term, due to the presence of the complex  $3 \times 3$  matrices (in flavor space)  $\mathbf{Y}^u$  and  $\mathbf{Y}^d$ . In order for quark flavor to be preserved, it must be possible to simultaneously diagonalize the Higgs interactions and the  $W$  interactions. We can try this explicitly, using singular value decomposition to write the Yukawa matrices as  $\mathbf{Y}^q = \mathbf{V}_{qL}\mathbf{y}^q\mathbf{V}_{qR}^\dagger$ , where  $\mathbf{V}_{qL}$  and  $\mathbf{V}_{qR}$  are unitary matrices and  $\mathbf{y}^q$  is diagonal and Hermitian. Then, we are free to diagonalize the Yukawa terms via the field redefinition  $\mathbf{q}_L = \mathbf{V}_{qL}^\dagger \mathbf{Q}_L$  and  $\mathbf{q}_R = \mathbf{V}_{qR}^\dagger \mathbf{Q}_R$ , and see what effect these transformations have on the  $W$ -boson interaction. While the Yukawa term

$$\begin{aligned} \mathcal{L}_{Q,\text{Yuk.}} &= \phi[\bar{\mathbf{u}}_L \mathbf{y}^u \mathbf{u}_R + \bar{\mathbf{u}}_R \mathbf{y}^u \mathbf{u}_L] + \phi[\bar{\mathbf{d}}_L \mathbf{y}^d \mathbf{d}_R + \bar{\mathbf{d}}_R \mathbf{y}^d \mathbf{d}_L] \\ &= \phi \bar{\mathbf{u}} \mathbf{y}^u \mathbf{u} + \phi \bar{\mathbf{d}} \mathbf{y}^d \mathbf{d} \end{aligned} \quad (2.3)$$

is now clearly diagonal, the  $W$ -boson interaction

$$\mathcal{L}_{Q,W} = -\frac{g}{\sqrt{2}} \bar{\mathbf{u}} W^+ P_L \mathbf{V}_{uL}^\dagger \mathbf{V}_{dL} \mathbf{d} + \text{H.c.} \quad (2.4)$$

now contains a matrix  $\mathbf{V}_{uL}^\dagger \mathbf{V}_{dL}$ . This matrix is called the *CKM Matrix* (defined  $\mathbf{V}_{\text{CKM}} \equiv \mathbf{V}_{uL}^\dagger \mathbf{V}_{dL}$ ) due to the work of Cabibbo, Kobayashi, and Maskawa [10, 11]. Notably, this matrix is an arbitrary complex matrix, and is hence generally non-diagonal, so one can expect the  $W$  boson interaction to induce mixing between the different flavors of quark. In particular, the magnitudes of the elements of the CKM matrix are given by [8]

$$|\mathbf{V}_{\text{CKM}}| \approx \begin{bmatrix} 0.974 & 0.225 & 0.004 \\ 0.225 & 0.973 & 0.042 \\ 0.009 & 0.041 & 0.999 \end{bmatrix}. \quad (2.5)$$

Interestingly, the matrix is *nearly* flavor-diagonal,<sup>4</sup> but there is a small degree of flavor-violation induced by the non-zero off diagonal components. Hence one has a choice: either the interaction with the Higgs preserves quark flavor, and the interaction with the  $W$ -boson is generically flavor-changing, or vice-versa. Given that the Higgs Yukawa interactions give rise to the fermion masses

---

<sup>4</sup> Given that  $V_{\text{CKM}}$  is *a priori* an arbitrary complex matrix, its closeness to unity is a mystery.

after EWSB and all of the standard formalism of QFT describes particles in terms of their mass eigenstates, it is convention to diagonalize these terms and leave the flavor-changing CKM matrix in the  $W$ -boson sector.

So why doesn't this happen in the lepton sector? Similar to before, the leptons are defined as a flavor triplet of Weyl fermions  $\mathbf{L}$  and  $\mathbf{E}_R$  with charges  $(1, 2)_{-1/2}$  and  $(1, 1)_{-1}$  respectively, and the doublet can be represented as  $\mathbf{L} = e^{i\tau^a \xi_a} (\mathbf{N}_L, \mathbf{E}_L)$  in unitarity gauge. The leptonic interaction with the  $W$  can be found in the kinetic term of the leptonic  $SU(2)$  doublet  $\mathbf{L}$ :

$$\begin{aligned}\mathcal{L}_{L,\text{kin.}} &= \bar{\mathbf{L}} [i\partial^\mu - g\tau^a W_a^\mu - \dots] \mathbf{L} = \dots - \frac{g}{\sqrt{2}} \bar{\mathbf{N}}_L W^+ \mathbf{E}_L - \frac{g}{\sqrt{2}} \bar{\mathbf{E}}_L W^- \mathbf{N}_L + \dots \\ &= -\frac{g}{\sqrt{2}} \bar{\mathbf{N}} W^+ P_L \mathbf{E} + \text{H.c.}\end{aligned}\quad (2.6)$$

Whereas the lepton-Higgs Yukawa interaction is given by

$$\begin{aligned}\mathcal{L}_{L,\text{Yuk.}} &= [\bar{\mathbf{L}} H] \mathbf{Y}^\ell \mathbf{E}_R + \text{H.c.} \\ &= \phi [\bar{\mathbf{E}}_L \mathbf{Y}^\ell \mathbf{E}_R + \bar{\mathbf{E}}_R \mathbf{Y}^{\dagger e} \mathbf{E}_L]\end{aligned}\quad (2.7)$$

Like before, the  $W$  interaction is diagonal and the Higgs interaction is non-diagonal, but we can diagonalize  $\mathbf{Y}^\ell$  using singular value decomposition  $\mathbf{Y}^\ell = \mathbf{V}_{\ell L} \mathbf{y}^\ell \mathbf{V}_{\ell R}^\dagger$ . Then, defining the charged lepton fields as  $\ell_{R,L} = \mathbf{V}_{\ell R,L}^\dagger \mathbf{E}_{R,L}$ , the Yukawa interaction is given by

$$\mathcal{L}_{L,\text{Yuk.}} = \phi [\bar{\ell}_L \mathbf{y}^\ell \ell_R + \bar{\ell}_R \mathbf{y}^\ell \ell_L] = \phi \bar{\ell} \mathbf{y}^\ell \ell \quad (2.8)$$

While this would seemingly introduce a non-diagonal coupling for the  $W$ -boson analogously to the quark case, the key difference is that we still have the freedom to rotate the neutrino flavors via the field redefinition  $\nu_L = \mathbf{V}_{\ell L}^\dagger \mathbf{N}_L$ , due to the absence of a neutrino Yukawa matrix  $\mathbf{Y}^\nu$ . Then, using the property  $\mathbf{V}_{\ell L}^\dagger \mathbf{V}_{\ell L} = \mathbf{1}$ , we find

$$\mathcal{L}_{L,W} = -\frac{g}{\sqrt{2}} \bar{\nu} W^+ P_L \ell + \text{H.c.} \quad (2.9)$$

Hence, the  $W$ -boson interaction still preserves lepton flavor in the SM. By the same token, we can see that the lepton flavor symmetry is hanging on by a thread. In analogy with the quark sector,

all it would take to dismantle this symmetry is the introduction of a SM singlet (under *all* the gauge groups)  $\mathbf{N}_R$ , which would act as a right-handed neutrino. This would require an additional set of rotation matrices  $\mathbf{V}_{\nu L}$  and  $\mathbf{V}_{\nu R}$  to diagonalize the Yukawa interaction,<sup>5</sup> which would in turn generate a CKM-like matrix for the lepton sector. Indeed, LFV has already been observed in the neutrino sector, as highlighted in the introduction. The CKM-like matrix is called the Pontecorvo-Maki-Nakagawa-Sakata, or PMNS, Matrix [12, 13]. Perhaps it is not surprising that one of the only pieces of evidence for physics beyond the SM (BSM) is an LFV signal.

## 2.3 Flavor-Violating Scalars

Scalar fields are the simplest fields that one can study in relativistic quantum field theories. Scalar fields are realized in the SM through the Higgs field, which is a charged, complex scalar field before EWSB, and a real scalar field after EWSB. Scalar fields are also ubiquitous in BSM theories of physics. Here we will review some of the properties of scalars with flavor-violating interactions, as well as some examples of BSM scalars.

### 2.3.1 Symmetry Properties of FV Scalar Interactions

The most generic interaction between charged<sup>6</sup> spin-1/2 Dirac fermions  $\psi_i$  and a real scalar  $\varphi$  is given by

$$\mathcal{L} = \sum_{i,j} \bar{\psi}_i (g_{ij}^S + ig_{ij}^{PS} \gamma^5) \psi_j \varphi \quad (2.10)$$

where,  $g_{ij}^S$  and  $g_{ij}^{PS}$  are complex numbers that describe the strength of the interaction. In order to ensure that the Lagrangian is real, it is required that  $g_{ij}^S = g_{ji}^{S*}$  and  $g_{ji}^{PS} = g_{ij}^{PS*}$ . In particular, this means that the on-diagonal (flavor-preserving) couplings must be real. When only the left (right) coupling in Eq. 2.10 is present, the  $\phi$  is referred to as a (pseudo)scalar. This can be understood by

---

<sup>5</sup> More generally, the right-handed neutrino could have a Majorana term, and the total mass matrix (Majorana + Dirac) would have to be diagonalized, leading to flavor violation in both the Higgs and  $W$ -boson interactions.

<sup>6</sup> If they were uncharged, one could also have the terms  $\phi \bar{\psi}_i^c \Gamma_{ij} \psi_j$ . Alternatively, if  $\varphi$  is complex and charged under the same symmetry as the  $\psi_i$ , then this term can occur.

examining the parity transformation of the interaction. Parity acts on the interaction term as

$$\begin{aligned} P^{-1}\mathcal{L}P &= \sum_{i,j} P^{-1}\bar{\psi}_i(g_{ij}^S + ig_{ij}^{PS}\gamma^5)\psi_j P P^{-1}\varphi P \\ &= \sum_{i,j} \bar{\psi}_i(g_{ij}^S - ig_{ij}^{PS}\gamma^5)\psi_j P^{-1}\varphi P. \end{aligned} \quad (2.11)$$

Note that for a general coupling, one cannot consistently assign a parity charge for  $\varphi$  that leaves the interaction term invariant under a parity transformation. However, if  $g_{ij}^{PS} = 0$ , then one can choose  $P^{-1}\varphi P = +\varphi$ , and if  $g_{ij}^S = 0$ , then one can choose  $P^{-1}\varphi P = -\varphi$ . Hence, if only the left coupling is present,  $\varphi$  transforms as a scalar under parity, and if only the right-coupling is present,  $\varphi$  transforms as a pseudoscalar under parity. If we instead apply charge-conjugation, we have

$$\begin{aligned} C^{-1}\mathcal{L}C &= \sum_{i,j} C^{-1}\bar{\psi}_i(g_{ij}^S + ig_{ij}^{PS}\gamma^5)\psi_j C C^{-1}\varphi C \\ &= \sum_{i,j} \bar{\psi}_j(g_{ij}^S + ig_{ij}^{PS}\gamma^5)\psi_i C^{-1}\varphi C \\ &= \sum_{i,j} \bar{\psi}_i(g_{ij}^{S*} + ig_{ij}^{PS*}\gamma^5)\psi_j \varphi. \end{aligned} \quad (2.12)$$

Here, we cannot assign a C-charge to  $\varphi$  as it is a real scalar. We see that charge-conjugation-symmetry is obeyed precisely when the couplings are strictly real. Combining both yields the CP transformation

$$CP^{-1}\mathcal{L}CP = \sum_{i,j} \bar{\psi}_i(g_{ij}^{S*} - ig_{ij}^{PS*}\gamma^5)\psi_j CP^{-1}\varphi CP. \quad (2.13)$$

It follows that for flavor-preserving ( $j = i$ ) couplings,  $\varphi$  can be designated CP-even if  $g_{ij}^{S*} = g_{ij}^S$  and  $g_{ij}^{PS*} = -g_{ij}^{PS}$ , and CP-odd if  $g_{ij}^{S*} = -g_{ij}^S$  and  $g_{ij}^{PS*} = g_{ij}^{PS}$ . More generally, if there is still freedom to absorb phases into the fermion fields, then the term can be made CP-conserving as long as  $\arg(g_{ij}^S) = \arg(ig_{ij}^{PS})$ .

It is sometimes convenient to parametrize the interaction in terms of angles and phases. In particular, we define  $g_{ij} = \sqrt{|g_{ij}^S|^2 + |g_{ij}^{PS}|^2}$ ,  $\theta_{ij} = \arctan(|g_{ij}^{PS}/g_{ij}^S|)$ , and  $\phi_{ij}^{(P)S} = \arg(g_{ij}^{(P)S})$ . We also define  $\delta_{ij} = \phi_{ij}^{PS} - \phi_{ij}^S$  so that we can highlight the difference in phases between the two terms.

Then the interaction is of the form

$$\mathcal{L} = \sum_{ij} g_{ij} e^{i\phi_{ij}^S} \bar{\psi}_i (\cos \theta_{ij} + ie^{i\delta_{ij}} \sin \theta_{ij} \gamma^5) \psi_j \varphi. \quad (2.14)$$

Without loss of generality, we can take  $\theta_{ij} \in [0, \pi/2]$ . Then, the reality condition becomes  $g_{ij} = g_{ji}$ ,  $\theta_{ij} = \theta_{ji}$ ,  $\phi_{ij}^{(P)S} + \phi_{ji}^{(P)S} = 0$ , and  $\delta_{ij} + \delta_{ji} = 0$ . The on-diagonal phases satisfy  $\phi_{ii}^{(P)S} = \delta_{ii} = 0$ , as expected. Such a parametrization is useful when calculating Feynman diagrams, where one can use trigonometric identities to simplify expressions. In this notation, we see that  $\theta_{ij}$  directly controls the degree of parity-violation (PV),  $\phi_{ij}^S$  and  $\phi_{ij}^{PS}$  controls the degree of C-violation, and  $\delta_{ij} = \phi_{ij}^{PS} - \phi_{ij}^S$  controls the degree of CP-violation (CPV).

The situation for a complex scalar is (ironically) simpler, in the sense that the couplings, angles and phases are now free to be chosen independently, as there is no reality condition to satisfy. The trade-off is that an interaction with an outgoing  $\varphi$  is the complex-conjugate of an interaction with an ingoing  $\varphi$ . One phenomenologically interesting case is when the angles and phases are chosen such that the complex scalar interacts chirally with the fermions; that is,  $\theta_{ij} = \pi/4$  and  $\delta_{ij} = \pm\pi/2$ . This situation is often well-motivated due to the chiral nature of the SM fields. Indeed, this is the case for the Higgs interaction with fermions before EWSB occurs.

It should be noted that the complex scalar can be written as two real scalars  $\varphi = \varphi_r + i\varphi_i$ . Written in this form, the reality condition implies that the  $\varphi_r$  plays the role of a scalar and the  $\varphi_i$  plays the role of a pseudoscalar, at least for the on-diagonal couplings. However as we have seen, even these real fields can have non-diagonal interactions for which there is no consistent choice of parity.

### 2.3.2 Two-Higgs-Doublet Model

What if there were a second Higgs? This is the question that the two-Higgs doublet model (2HDM) aims to answer. The question is far from arbitrary, as a second Higgs doublet is required in supersymmetric extensions of the SM [14, 15], appears in the spectrum of many grand-unified theories [16–18], and also can appear in models that provide a neutrino mass mechanism [16–18] or

a candidate for dark matter [19–21]. Here we will divorce the second Higgs doublet from any particular new model of physics, and instead consider the broad ramifications one can expect from its inclusion. For a review of 2HDMs, we refer to Refs. [22–24].

We call the two Higgs doublets  $\Phi_1$  and  $\Phi_2$ . Unless one imposes additional symmetries, each of them has the same interactions with the fermions as the SM Higgs field. These are

$$\begin{aligned} \mathcal{L}_{\text{Yuk.}} = & [\bar{\mathbf{L}}\Phi_1] \mathbf{Y}_1^\ell \mathbf{E}_R + [\bar{\mathbf{Q}}\Phi_1] \mathbf{Y}_1^u \mathbf{U}_R + [\bar{\mathbf{Q}}\tilde{\Phi}_1] \mathbf{Y}_1^d \mathbf{D}_R \\ & + [\bar{\mathbf{L}}\Phi_2] \mathbf{Y}_2^\ell \mathbf{E}_R + [\bar{\mathbf{Q}}\Phi_2] \mathbf{Y}_2^u \mathbf{U}_R + [\bar{\mathbf{Q}}\tilde{\Phi}_2] \mathbf{Y}_2^d \mathbf{D}_R + \text{H.c.} \end{aligned} \quad (2.15)$$

Referring to Section 2.2, we can already see how such a model will lead to flavor violation in the lepton sector and additional flavor violation in the quark sector: After spontaneous breaking of the electroweak symmetry, the mass matrices will be obtained from singular value decomposition of the matrix  $\mathbf{M}^f = v_1 \mathbf{Y}_1^f + v_2 \mathbf{Y}_2^f$ , where  $v_1$  and  $v_2$  are the vacuum expectation values (VEVs) of  $\Phi_1$  and  $\Phi_2$ . Unlike in the SM, diagonalization of  $\mathbf{M}^f$  will generically not diagonalize either of the Higgs interactions, so one can expect each scalar in the theory to have flavor-violating couplings. Flavor-violating interactions with the SM Higgs have yet to be observed, which places limits on the strength of the Yukawa couplings and size of the second Higgs VEV. It should also be noted that an additional Higgs doublet introduces not one, but *five* new real scalar fields after EWSB.<sup>7</sup> After diagonalization of the fermion mass matrices, each of these will have flavor-violating couplings unless a symmetry is explicitly imposed to prevent them. In Type I Type II, lepton-specific (or Type X), and flipped (or Type Y) 2HDMs, a discrete  $\mathbb{Z}_2$  symmetry is imposed that restricts each Higgs doublet to interact with different fermion sectors, which has the effect of forbidding tree-level flavor-changing neutral currents [22–26]. However, the most general incarnation of the 2HDM has flavor-violating scalars whose mass and couplings are constrained by experiments [27, 28].

---

<sup>7</sup> This is because each Higgs doublet has two complex (four real) degrees of freedom, and only three degrees of freedom are “eaten” by the gauge fields corresponding to the broken generators of the electroweak symmetry.

### 2.3.3 Froggatt-Nielsen Models

One of the biggest outstanding problems in particle physics is the fermion hierarchy problem: why is there such a large separation of scales between the observed masses of each generation of fermions? Ignoring the neutrinos (whose internal hierarchy is unknown and which may very well get their low masses through a different mechanism than the other fermions), the other sectors have hierarchies of  $m_\tau/m_e \approx 3.5 \times 10^3$ ,  $m_b/m_d \approx 900$ , and  $m_t/m_u \approx 8 \times 10^4$  between their first and third generations. While such hierarchies can be obtained by simply asserting that the Higgs Yukawa matrices are hierarchical, this explanation is unsatisfactory for most particle physicists.

Froggatt-Nielsen models attempt to solve this problem by introducing a global horizontal symmetry group  $U(1)_H$  along with a generation-dependent charge structure for the SM fermions [29]. Generically, the left- and right-handed fermion fields of each generation have different  $U(1)_H$  charges, so  $Q_H[F_i] = q_i^F$  and  $Q_H[F_{Ri}] \equiv q_i^{F_R}$ . This has the effect of forbidding the usual SM Yukawa terms

$$\mathcal{L}_{\text{Yuk}} = \sum_{i,j} \left[ Y_{ij}^\ell \bar{L}_i H E_{Rj} + Y_{ij}^u \bar{Q}_i H U_{Rj} + Y_{ij}^d \bar{Q}_i \tilde{H} D_{Rj} \right] + \text{H.c.} \quad (2.16)$$

as these terms have  $U(1)_H$  charge  $q_i^{F_R} - q_j^F \neq 0$ . These terms are restored by introduction of a complex scalar field  $\Phi$ , the flavon, with  $U(1)_H$  charge 1. Then, the charge  $q_i^{F_R} - q_j^F$  can be canceled by powers of the flavon,  $\Phi^{q_i^F - q_j^{F_R}}$ . The lowest-order effective field theory (EFT) term is then

$$\mathcal{L}_{\text{FN}} = \sum_{i,j} \left[ X_{ij}^\ell \left( \frac{\Phi}{M} \right)^{n_{ij}^\ell} \bar{L}_i H E_{Rj} + X_{ij}^u \left( \frac{\Phi}{M} \right)^{n_{ij}^u} \bar{Q}_i H U_{Rj} + X_{ij}^d \left( \frac{\Phi}{M} \right)^{n_{ij}^d} \bar{Q}_i \tilde{H} D_{Rj} \right] + \text{H.c.} \quad (2.17)$$

where  $n_{ij}^f \equiv q_i^F - q_j^{F_R}$  and  $X_{ij}^f$  are  $\mathcal{O}(1)$  couplings. If the flavon acquires a VEV  $v_\Phi \ll M$ , this will naturally generate a hierarchy in the Yukawa couplings  $Y_{ij}^f = X_{ij}^f (v_\Phi/M)^{n_{ij}^f} \sim X_{ij}^f \epsilon^{n_{ij}^f}$ . The hierarchy of the fermion masses in the SM can be recovered by choosing appropriate values for  $q_i^F$  and  $q_i^{F_R}$ . To get a sense of the charges required to reproduce the SM fermion mass spectrum, we refer to Ref. [30], which scans over valid Froggatt-Nielsen solutions to the fermion hierarchy problem with  $|q_i^{F_R}|, |q_i^F| < 7$  (or  $|q_i^{F_R}|, |q_i^F| < 9$  with the inclusion of three Dirac right-handed neutrinos).

In addition to the effective coupling between the flavon and the SM, the flavon has a potential, given by

$$V(\Phi) = \mu_\Phi^2 |\Phi|^2 + \frac{1}{2} \lambda_\Phi |\Phi|^4. \quad (2.18)$$

The global  $U(1)_H$  symmetry is spontaneously broken when the flavon acquires a VEV  $v_\Phi \neq 0$ . This form of the potential motivates a decomposition of the flavon  $\Phi$  in terms of its radial and angular components,  $\Phi = (v_\Phi + \rho)e^{ia/v_\Phi} \sim v_\Phi + \rho + ia$ . The leading order interaction of these fields with the SM fermion fields (after EWSB but *before* diagonalization of the mass matrices) is given by

$$\mathcal{L}_{\text{FN,int.}} = \sum_{i,j} v_H Y_{ij}^f n_{ij}^f \frac{\rho + ia}{v_\Phi} \bar{F}_{Li} F_{Rj}. \quad (2.19)$$

Notably, the presence of  $n_{ij}^f$  prevents simultaneous diagonalization of this interaction term with the Yukawa matrices  $Y_{ij}^f$ . Hence, we see that the Froggatt-Nielsen scalars generically appear with flavor-violating interactions. The degree to which these interactions are constrained by existing searches for flavor-violation is explored in Ref. [30].

While the  $\rho$  attains its mass from the potential (2.18) after  $U(1)_H$  symmetry-breaking, the  $a$  is a Goldstone boson of the  $U(1)_H$  symmetry. However, the chiral nature of the  $U(1)_H$  charges results in a chiral anomaly, so the  $U(1)_H$  is approximate and the  $a$  acquires a small mass. This property of the  $a$  makes it an example of an *axion-like particle*, which are the subject of Section 2.4. We will briefly return to the  $a$ , which is sometimes called the *axiflavor* [31] or *flaxion* [32], in Section 2.4.3.

## 2.4 Axion-Like Particles

An axion-like particle (ALP) is a pseudo<sup>8</sup>-Nambu-Goldstone boson (pNGB) that results from the spontaneous breaking of an approximate global symmetry. They are ubiquitous in extensions beyond the SM, as global symmetries are often imposed directly (as we have seen with Froggatt-Nielsen models), or arise accidentally from imposing gauge symmetries (as is the case with the

---

<sup>8</sup> *Pseudo* here refers to the fact that it is not a *true* Nambu-Goldstone boson, as it has a small mass by virtue of explicit symmetry breaking.

lepton family, lepton number, and baryon number symmetries in the SM). For a review of ALPs in various contexts, see Refs. [33, 34].

The namesake of the ALP is a hypothetical particle called the axion, which was devised by Peccei and Quinn in the 1960s as a possible solution to the Strong CP problem [35, 36]. In short, the Strong CP problem is the observation that the CP-odd gluon-gluon interaction

$$\mathcal{L}_\theta = \frac{\theta}{32\pi^2} \text{Tr}\{G^{\mu\nu}\tilde{G}_{\mu\nu}\} \quad (2.20)$$

is apparently absent from the SM, despite respecting all of the SM symmetries. Measurements of the neutron electric dipole moment indicate that  $|\theta| < 10^{-13}$ , whereas naturalness would predict  $\theta = \mathcal{O}(1)$ ,<sup>9</sup> so physicists expect that there must be some mechanism at play to prevent this interaction. The axion is the pNGB of an anomalous  $U(1)$  symmetry, whose VEV aligns with  $\theta$  to dynamically force the term (2.20) to zero. While the original axion model proposed by Peccei and Quinn has been ruled out, generalizations such as the DFSZ axion [37, 38] and KSVZ axion [39, 40] still have a large parameter space untouched by modern experiments, and double as a promising candidate for dark matter [41].

While the ALP is named after a particle that has yet to be observed, we need not look beyond the SM to find an example: the pions. In particular, the QCD Lagrangian for the two lightest quarks ( $u$  and  $d$ ) exhibits a global  $SU(2)_L \times SU(2)_R$  chiral flavor symmetry in the limit of vanishing quark masses. This symmetry is explicitly broken by the quark Yukawa couplings and, to a much lesser extent, the electroweak interactions. Since the quark Yukawa couplings are small relative to the QCD confinement scale, this can be understood as an *approximate* global symmetry. At low temperatures, the QCD vacuum develops a chiral condensate that spontaneously breaks the chiral symmetry down to an  $SU(2)_V$  isospin flavor symmetry, giving rise to three pseudo-Goldstone bosons. These are the pions  $\pi^\pm$  and  $\pi^0$ , which acquire a small mass due to the explicit symmetry breaking, in accordance with Goldstone's theorem.<sup>10</sup> This introduces the possibility that ALPs

---

<sup>9</sup> The problem is subtly worse. Since CP-violation exists in the CKM-matrix of the SM, (2.20) receives loop-level corrections. To reproduce our observations, the *bare*  $\theta$  must not be zero, but instead must conspire to exactly cancel out with quantum corrections from the quark sector at our energy scale. This is a fine-tuned scenario and hence an unsatisfactory solution for many physicists.

<sup>10</sup> This same analysis can be extended to include the strange quark, so that a global  $SU(3)_L \times SU(3)_R$  chiral flavor

can arise as pions from composite dark sectors. We will explore an example of this possibility in Section 2.4.4.

Perhaps the most exciting feature of ALPs for a phenomenologist is that they are, by definition, much lighter than the energy-scale of the new physics from which they come. Coupled with the fact that generic ALP interactions mix both quark and lepton flavor, ALPs provide a tantalizing target for physics experiments. We will explore limits on ALPs from existing searches for LFV in Chapter 3, and for a broader set of existing and upcoming collider experiments in Chapter 5.

#### 2.4.1 ALP Effective Field Theory

Here, we provide a brief overview of the low-energy EFT of the ALP. More detailed analyses of its structure and renormalization properties can be found in Refs. [43–46]. From their definition as pNGBs of some approximate global symmetry, all that is important for the EFT is that the ALP interactions obey a continuous shift symmetry  $a \rightarrow a + \text{const.}$  (characteristic of Nambu-Goldstone bosons) which is explicitly broken either by a term in the Lagrangian or by anomalous quantum effects. The symmetry can be imposed directly with terms of the form  $\partial_\mu a \mathcal{O}$  and  $e^{ia/f} \mathcal{O}$ , where  $\mathcal{O}$  is any SM gauge-invariant operator. However, the latter term subtly breaks the symmetry due to a chiral anomaly, so it is preferable to rotate the SM fields in such a way that remove these operators in favor of equivalent operators which demonstrate the symmetry-breaking more explicitly. In particular, performing the rotation not only modifies the coefficients of the  $\partial_\mu a \mathcal{O}$  terms, but also introduces linear couplings to the gauge fields  $a \tilde{F} F$ . While these terms are sufficient to break the ALP’s shift symmetry into a discrete symmetry, the shift symmetry may be broken explicitly by other means; this can be accounted for phenomenologically by allowing the ALP to have a mass  $m_a$  (along with higher-order potential terms). All told, we have the low-energy effective Lagrangian

---

symmetry breaks to an  $SU(3)_V$  isospin symmetry. In this case, there are eight Goldstone modes, associated with the eight mesons in Gell-Mann’s “eightfold way” [42]. The remaining mesons, the eta ( $\eta$ ) and the kaons ( $K^\pm, K^0$ ), are heavier than the pions, because the strange quark breaks the approximate chiral symmetry much more than the up or down quarks ( $m_s/(m_u + m_d) \approx 14$ ).

[43, 46]

$$\begin{aligned}\mathcal{L}_{\text{ALP}} = & \frac{1}{2}(\partial_\mu a)^2 - \frac{1}{2}m_a^2 a^2 - \frac{1}{\Lambda}\partial_\mu a \sum_{f,i,j} \bar{f}_i \gamma^\mu [V_{ij}^f - A_{ij}^f \gamma_5] f_j + e^2 C_{\gamma\gamma} \frac{a}{\Lambda} F_{\mu\nu} \tilde{F}^{\mu\nu} + \dots \\ & + \frac{1}{4}\lambda_a \frac{m_a^2}{\Lambda^2} a^4 + C_{ah} \frac{(\partial_\mu a)^2}{\Lambda^2} v h + C'_{ah} \frac{m_a^2 a^2}{\Lambda^2} v h + \dots\end{aligned}\quad (2.21)$$

where the dots on the first line include other  $\mathcal{O}(\Lambda^{-1})$  interactions with gauge fields, and the dots on the second line include  $\mathcal{O}(\Lambda^{-2})$  terms.<sup>11</sup> The Higgs couplings on the second line warrant extra discussion. The first obeys the shift symmetry and is thus generically allowed in the ALP effective theory. The second is explicitly symmetry violating, but can occur in some UV-completions for which the source of explicit symmetry breaking is an interaction with the Higgs (such as the model studied in Section 2.4.4). Phenomenological constraints on these couplings in the context of LFV ALPs are presented in Chapter 5.

While the derivative coupling of the ALP to fermions emphasizes the shift symmetry, it is possible to integrate the fermion interaction term by parts and use the equations of motion to obtain a standard scalar interaction for the ALP,

$$\frac{1}{\Lambda}\partial_\mu a \sum_{f,i,j} \bar{f}_i \gamma^\mu [V_{ij}^f - A_{ij}^f \gamma_5] f_j \longrightarrow -ia \sum_{f,i,j} \bar{f}_i \gamma^\mu \left[ \frac{m_i - m_j}{\Lambda} V_{ij}^f + \frac{m_i + m_j}{\Lambda} A_{ij}^f \gamma_5 \right] f_j. \quad (2.22)$$

Written in this form, we see a hallmark feature of ALPs: they couple to fermions with a strength proportional to the mass of the fermions. This entails that (as long as the couplings  $A_{ij}$  and  $V_{ij}$  themselves are not hierarchical) ALPs will couple primarily to the third generation of fermions.

However, one cannot rewrite the fermion interaction as in Eq. 2.22 without inducing a modification to the gauge boson couplings, due to the chiral anomaly. For example, when the Lagrangian is rewritten in this form, the photon coupling becomes

$$\tilde{C}_{\gamma\gamma} = C_{\gamma\gamma} + \sum_{f \in \{\ell, u, d\}} \sum_{i=1}^3 \frac{N_c^f Q_f^2}{8\pi^2} A_{ii}^f, \quad (2.23)$$

---

<sup>11</sup> While these operators are not six-dimensional, the Higgs interactions are derived from six-dimensional operators prior to EWSB, and the quartic term in the ALP potential is anticipated to be suppressed by  $(m_a/\Lambda)^2$  due to the approximate symmetry.

and there are analogous formulae for the other gauge boson couplings [46]. An effective photon coupling is often cited as the full one-loop contribution to the coupling, given by

$$C_{\gamma\gamma}^{\text{eff.}} = C_{\gamma\gamma} + \sum_{f \in \{\ell, u, d\}} \sum_{i=1}^3 \frac{N_c^f Q_f^2}{8\pi^2} A_{ii}^f B_1(4m_{f_i}^2/m_a^2) \quad (2.24)$$

where

$$B_1(\tau) = 1 - \tau f(\tau)^2, \quad f(\tau) = \begin{cases} \arcsin \frac{1}{\sqrt{\tau}} & \tau \geq 1, \\ \frac{\pi}{2} + \frac{i}{2} \log \frac{1+\sqrt{1-\tau}}{1-\sqrt{1-\tau}} & \tau < 1. \end{cases} \quad (2.25)$$

However, we note that this formula is only strictly valid when the momenta are on shell, i.e. for the decay process  $a \rightarrow \gamma\gamma$ . When the  $a\gamma\gamma$  vertex appears inside a diagram, one must compute the full two-loop contribution to the diagram. Nevertheless, Eq. 2.23 captures a useful qualitative feature of the vertex which survives the general off-shell treatment: light fermions contribute  $N_c^f Q_f^2/8\pi^2 A_{ii}^f$  to the photon vertex whereas heavy fermions decouple. For a more rigorous two-loop treatment of  $C_{\gamma\gamma}^{\text{eff.}}$ , we refer to Refs. [47, 48].

#### 2.4.2 ALP as a (Pseudo-)Scalar

As seen in the previous section, ALPs can be treated as scalars by integrating by parts and using the equations of motion, at the expense of modifying the ALP-gauge boson coupling. Let us consider the interaction between an ALP  $a$  and a set of fermions  $\psi_i$ :

$$\mathcal{L} = \sum_{ij} \frac{\partial_\mu a}{\Lambda} \bar{\psi}_i \gamma^\mu (g_{ij}^V + g_{ij}^A \gamma_5) \psi_j. \quad (2.26)$$

To ensure the Lagrangian is real, we have  $g_{ij}^V = g_{ji}^{V*}$ , and  $g_{ij}^A = g_{ji}^{A*}$ .

After integrating by parts and applying the equations of motion,

$$\mathcal{L} = \sum_{ij} a \bar{\psi}_i \left[ -i \frac{m_i - m_j}{\Lambda} g_{ij}^V - i \frac{m_i + m_j}{\Lambda} g_{ij}^A \gamma_5 \right] \psi_j. \quad (2.27)$$

This can be matched directly onto the real scalar interaction term Eq. 2.10, so that

$$g_{ij}^S = -i \frac{m_i - m_j}{\Lambda} g_{ij}^V, \quad g_{ij}^{PS} = -\frac{m_i + m_j}{\Lambda} g_{ij}^A. \quad (2.28)$$

In particular,  $g_{ij}^S = g_{ji}^{S*}$  and  $g_{ij}^{PS} = g_{ji}^{PS*}$ , as expected. This means that in principle, amplitudes calculated involving fermions and scalars can be easily recast to involve ALPs instead, or vice-versa.

As before, we can define a magnitude  $C_{ij} = \sqrt{|g_{ij}^A|^2 + |g_{ij}^V|^2}$ , angles  $\Theta_{ij} = \arctan(|g_{ij}^V/g_{ij}^A|)$ , and phases  $\Phi_{ij}^{A,V} = \arg(g_{ij}^{A,V})$ , with  $\Delta_{ij} = \Phi_{ij}^A - \Phi_{ij}^V$ . The resulting interaction Lagrangian is

$$\mathcal{L} = \sum_{ij} \frac{\partial_\mu a}{\Lambda} C_{ij} e^{i\Phi_{ij}^V} \bar{\psi}_i \gamma^\mu (e^{i\Delta_{ij}} \sin \Theta_{ij} + \cos \Theta_{ij} \gamma_5) \psi_j. \quad (2.29)$$

It is then possible to directly recast the ALP parameters to the scalar parameters and vice-versa.

For the magnitude and angles, we have

$$\frac{C_{ij}}{\Lambda} = \frac{g_{ij}}{|m_i^2 - m_j^2|} \sqrt{m_i^2 + m_j^2 + 2m_i m_j \cos 2\theta_{ij}} \quad \tan \Theta_{ij} = \frac{m_i + m_j}{|m_i - m_j|} \cot \theta_{ij} \quad (2.30)$$

$$g_{ij} = \frac{C_{ij}}{\Lambda} \sqrt{m_i^2 + m_j^2 + 2m_i m_j \cos 2\Theta_{ij}} \quad \tan \theta_{ij} = \frac{m_i + m_j}{|m_i - m_j|} \cot \Theta_{ij}. \quad (2.31)$$

The phases require careful thought due to the sign of the  $m_j - m_i$  term. In particular, if  $\theta_{ij}$  is taken to be positive, then we must have  $i\text{sgn}(m_j - m_i)e^{i\Phi_{ij}^A} = e^{i\phi_{ij}^S}$  and  $ie^{i\Phi_{ij}^V} = ie^{i\phi_{ij}^{PS}}$ , which can be easily solved for the resulting phases. This can be avoided if  $\theta_{ij}$  is allowed to run negative.

The term in the square-root invites the definition of a mass parameter

$$m_{ij}(\gamma) = \sqrt{m_i^2 + m_j^2 + 2m_i m_j \cos 2\gamma} \quad (2.32)$$

which often appears in Feynman amplitudes. When transferring from scalar notation to ALP notation, we can then use

$$m_{ij}(\theta_{ij})m_{ij}(\Theta_{ij}) = |m_i^2 - m_j^2|. \quad (2.33)$$

Curiously, these equations appear to represent a geometric relationship between the parameters of the two equivalent EFT terms. In particular, the first and second column of Eqs. (2.30)-(2.31) look similar to the Law of Cosines and Law of Tangents, respectively. This relationship is represented graphically with the trapezoid in Fig. 2.1. We then recognize Eq. 2.33 as the equation for the relationship between an isosceles trapezoid's diagonal and its side-lengths.

It's unclear whether this geometric relationship is superficial or if there is a deeper interpretation. In the special case that the scalar couplings are pure real, one can always write the

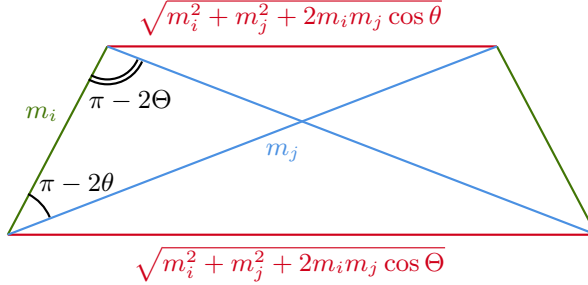


Figure 2.1: A trapezoid which encodes the relationship between the equivalent EFT terms. The indices on the angles are suppressed.

current in the interaction as  $g\bar{\psi}_i e^{i\gamma_5 \theta_{ij}} \psi_j$  and define  $\psi'_i = e^{i\gamma_5 \theta_{ij}/2} \psi_i$ . This field redefinition leaves the kinetic term invariant, but introduces a complex mass for the  $\psi'_i$ , namely  $\mu_i = m_i e^{i\theta_{ij}/2}$ . Then,  $m_{ij}(\theta) = |\mu_i + \mu_j|$ , so it seems plausible that one can re-frame this as a statement about complex masses. However, this is difficult to generalize for arbitrary complex couplings. We also note that this is not necessarily a geometric relationship between scalars and ALPs, but between equivalent effective theory terms. It would be interesting to explore whether other effective field theory terms obey similar geometric relationships, but this is beyond the scope of this dissertation. If nothing else, this observation makes it convenient to convert between scalar and ALP formulae, as long as one is careful to include any additional contributions that may arise from gauge-boson triangle diagrams. As such, we will employ it numerous times in subsequent chapters.

#### 2.4.3 ALPs in Froggatt-Nielsen Models

We encountered an ALP in the context of Froggatt-Nielsen models at the end of Section 2.3.3: the axiflavoron. The degree of symmetry-breaking associated with the chiral anomaly is typically quite small, so the axiflavoron is usually assumed to be very light relative to the scale  $M$ . However, Ref. [49] points out that axiflavons can generically be much heavier in a broader class of Froggatt-Nielsen models which demote the  $U(1)_H$  flavor symmetry to a discrete  $\mathbb{Z}_N \subset U(1)_H$  symmetry. With this

modification, the Froggatt-Nielsen Lagrangian has the form

$$\mathcal{L}_{\text{FN}} = \left[ X_{ij}^f \left( \frac{\Phi}{M} \right)^{n_{ij}^f} + X'_{ij}^f \left( \frac{\Phi^*}{M} \right)^{N-n_{ij}^f} \right] \bar{F} H F_R \quad (2.34)$$

and the potential takes the form

$$V_{\mathbb{Z}_N}(\Phi) = V_{\text{FN}}(\Phi) - \frac{1}{4} \lambda_N \left[ \left( \frac{\Phi}{M} \right)^N + \left( \frac{\Phi^*}{M} \right)^N \right] M^4. \quad (2.35)$$

In this case, one might not expect the theory to yield ALPs, as Goldstone's theorem does not apply to discrete symmetries. However, the  $\mathbb{Z}_N$ -symmetric terms in Eqs. 2.34-2.35 can be viewed as a soft breaking of the  $U(1)_H$  symmetry for  $N > 4$ , due to suppression by the heavy mass scale  $M$ . Hence, ALPs are a generic feature of these models, and can once again be understood as the angular component of the flavon  $\Phi = (v_\Phi + \rho)e^{ia/v_\Phi}$ . If one is no longer concerned with this ALP as a solution to the Strong-CP problem, then it can be quite heavy. Its mass is no longer set by the chiral anomaly, but by the explicit  $U(1)_H$  symmetry-breaking terms.

As we have already seen in Section 2.3.3, the axiflavor generically has flavor-violating couplings. Non-trivial hierarchies and chiral behavior can emerge from these couplings depending on the details of the charge assignments. It is interesting to examine the interactions for the  $N = 8$  wheel model [49]. To write the axiflavor-fermion interaction, we note that either the term with a power of  $n_{ij}^f$  or  $n'_{ij}^f \equiv N - n_{ij}^f$  will dominate, depending on which is smaller. Then, we have

$$\mathcal{L}_a \approx \sum_{f,i,j} v_H Y_{ij}^f e^{in_{ij}^{(f)} a/v_\Phi} \bar{F}_{Li} F_{Rj} + \text{H.c.} \quad (2.36)$$

which we note includes the (un-diagonalized) mass term as the zeroth order expansion in  $a/v_\Phi$ .<sup>12</sup>

In this model, the charges are given by  $Q[Q_1] = -Q[E_3] = -Q[U_1] = 2$ ,  $Q[Q_2] = -Q[E_2] = -Q[U_2] = 1$ ,  $Q[d_i] = -2$  and  $Q[L_i] = 4$ , with all other charges zero. Then, the exponents  $n_{ij}^f$  are

$$n_{ij}^\ell = \begin{pmatrix} 4 & 5 & 6 \\ 4 & 5 & 6 \\ 4 & 5 & 6 \end{pmatrix}, \quad n_{ij}^d = \begin{pmatrix} 4 & 4 & 4 \\ 3 & 3 & 3 \\ 2 & 2 & 2 \end{pmatrix}, \quad n_{ij}^u = \begin{pmatrix} 4 & 3 & 2 \\ 3 & 2 & 1 \\ 2 & 1 & 0 \end{pmatrix}. \quad (2.37)$$

---

<sup>12</sup> If  $n_{ij}^f = n'_{ij}^f = N/2$ , then  $Y_{ij}^f \equiv X_{ij}^f + X'_{ij}^f$ , so the interaction can always be written in this form to lowest order in  $v_\Phi/M$ .

and  $n_{ij}^{\prime f} = N - n_{ij}^f$ . Notably,  $n_{ij}^{(\prime)d} \equiv n_i^{(\prime)d}$  and  $n_{ij}^{(\prime)\ell} \equiv n_j^{(\prime)\ell}$  only vary along one of these indices, so the axiflavor interaction can be entirely rotated into one of the Weyl fields. Focusing explicitly on the leptons, we can simultaneously diagonalize the Yukawa matrix and remove the axiflavor interaction from the mass term via the field redefinition  $\ell_{Ri} = \sum_j (V_R^\dagger)_{ij} e^{in_j^{(\prime)\ell} a/v_\Phi} E_{Rj}$  and  $\ell_{Li} = \sum_j (V_L^\dagger)_{ij} E_{Lj}$ . This leads to an axiflavor derivative coupling of the form

$$\begin{aligned}\mathcal{L}_a &= \frac{\partial_\mu a}{v_\Phi} \sum_{ijk} \bar{\ell}_{Ri} \left[ (V_R^\dagger)_{ik} n_k^{(\prime)\ell} (V_R)_{kj} \right] \gamma^\mu \ell_{Rj} \\ &\equiv \frac{\partial_\mu a}{v_\Phi} \bar{\ell} \left( \mathbf{V}_R^\dagger \mathbf{n}^{(\prime)\ell} \mathbf{V}_R \right) \gamma^\mu P_R \ell.\end{aligned}\quad (2.38)$$

Written in this form, we see that the axiflavor has a purely chiral coupling to the right-handed leptons. It is easy to verify that a similar set of field redefinitions will yield a derivative coupling solely to the left-handed down-type quarks, while the dependence on both  $i$  and  $j$  of  $n_{ij}^u$  will generically lead to an axiflavor derivative coupling to both the left-handed and right-handed up-type quark currents. This detour serves to highlight an important point which we will return to in Chapter 3: the chiral nature of the SM fermions can often lead to new physics with chiral interactions, which can drastically affect the limits one can place on such theories.

#### 2.4.4 ALPs from Composite Dark Sectors

The SM offers an excellent description of the matter we interact with on a day-to-day basis. However, according to indirect astrophysical observations, 85% of the matter content in the Universe is unaccounted for. Given its inability to be directly observed, this matter has been dubbed *dark matter*. It is appealing to imagine that while this matter is dark with respect to the SM forces, it has its own rich gauge structure. One possibility is that dark matter is governed by strongly-coupled dynamics, much like QCD, and that the inert nature of dark matter is due to confinement of the charged fermions into neutral composite states. We refer to Ref. [50] for a review of such models.

In the SM, the pions are the pNGBs of a spontaneously broken approximate chiral flavor symmetry of the up and down (and sometimes strange) quarks in QCD. If confinement occurs in

some sector of physics beyond the SM as described above, it is possible that the resulting spectrum may include light ALPs of a similar nature. As a concrete example, we turn to the model from Ref. [51], which presents a mechanism for neutrino mass generation and a solution to the dark matter problem by introducing a strongly-coupled  $SU(3)_D$  dark sector with three massless triplet fermions  $\psi_i$ , the *dark quarks*. The  $SU(3)_D$  is taken to confine at an energy scale  $\mu_D = 1$  TeV. In addition to the strongly-coupled gauge group, a discrete  $\mathbb{Z}_2$  symmetry is imposed under which  $Q(\psi_3) = -1$ , which will ultimately provide a stable candidate for dark matter.

Here, we focus on the ALPs that appear in the low-energy spectrum of the theory. These are the *dark pions*, the pNGBs associated with the spontaneous breaking of a chiral symmetry  $SU(3)_L \times SU(3)_R \rightarrow SU(3)_V$ . This structure is more-or-less identical to chiral symmetry breaking in QCD, so the story is the same. The dark quarks have a non-zero effective Higgs coupling, which induces a mass  $m_i \sim 60$  MeV after EWSB. This Higgs coupling explicitly breaks the chiral symmetry, yielding a small mass for the dark pions relative to the confinement scale. There are eight broken generators associated with the symmetry breaking, so the dark pions appear in an octet:

$$K_D^0 \sim \bar{\psi}_1 \psi_3 \quad K'_D \sim \bar{\psi}_2 \psi_3$$

$$\begin{aligned} \pi'_D &\sim \bar{\psi}_1 \psi_2 & \pi_D &\sim \frac{1}{\sqrt{2}} (\bar{\psi}_1 \psi_1 - \bar{\psi}_2 \psi_2) \\ \eta_D &\sim \frac{1}{\sqrt{6}} (\bar{\psi}_1 \psi_1 + \bar{\psi}_2 \psi_2 - 2\bar{\psi}_3 \psi_3) & \bar{\pi}'_D &\sim \bar{\psi}_2 \psi_1 \end{aligned} \quad (2.39)$$

$$\bar{K}'_D \sim \bar{\psi}_3 \psi_2 \quad \bar{K}_D^0 \sim \bar{\psi}_3 \psi_1$$

The mass splitting between the quarks is assumed to be small, so each dark pion mass is given by the Gell-Mann–Oakes–Renner relation [52]

$$M_\Pi^2 \sim 2b\mu_D \hat{m} \quad (2.40)$$

with  $b \sim 2.5$  and  $\hat{m}$  the average of the dark quark masses. For the benchmark parameters in the

model, this yields  $M_\Pi \sim 10$  GeV. The *dark kaons*,  $K_D$  and  $K'_D$ , are odd under the  $\mathbb{Z}_2$ -symmetry, while the rest of the dark pions are even. The lightest of these is taken to be the  $K_D$ . By virtue of the  $\mathbb{Z}_2$ -symmetry, the  $K_D$  is stable on cosmological time scales, and is thus a prime candidate for dark matter.

While the dark kaons are symmetry-protected from decays to SM final states, the same cannot be said about the other dark pions. The allowed decay modes of these dark pions are set by the nature of the UV theory that gives rise to the effective SM couplings, potentially providing a production and detection mechanism for these ALPs at modern experiments. Ref. [51] provides a UV realization of the model (which we present in Appendix A). The UV interactions which reproduce the desired behavior of the theory (namely a neutrino mass mechanism and a stable dark matter candidate) lead to an effective leptonic interaction for the  $\mathbb{Z}_2$ -even ( $\Pi_x \in \{\pi_D, \pi'_D, \bar{\pi}'_D, \eta_D\}$ ) dark pions:

$$\mathcal{L}_{\Pi\ell\ell} = \sum_{a,b,x} \frac{C_{ab}^x}{\Lambda} \partial_\mu \Pi_x \bar{\ell}_a \gamma^\mu P_L \ell_b. \quad (2.41)$$

Much like the axiflavor in the  $N = 8$  wheel model, we see that the ALPs predicted by this mode have a purely chiral interaction with the charged leptons. In addition, there are no interactions to the other SM fermions to first order in perturbation theory. We will discuss chiral, leptonically coupled scalars and ALPs in more detail in Chapter 3.

The matching coefficient  $C_{ab}^x/\Lambda$  is computed in Appendix A; the final result warrants further discussion. It is given by

$$\frac{C_{ab}^x}{\Lambda} = \frac{i\lambda'_a \lambda'^*_b}{32\pi^2 M_S} \sum_{i,j} i \left[ g_{aS}^{ij} g_{bPS}^{ij*} - g_{aPS}^{ij} g_{bS}^{ij*} \right] \frac{F_{\Pi_x}}{M_S} \lambda_{ij}^x, \quad (2.42)$$

where  $\lambda'_a$ ,  $g_{aS}^{ij}$ ,  $g_{bPS}^{ij}$  and  $M_S$  are parameters of the UV model,  $F_{\Pi_x}$  is the decay constant of the dark pion  $\Pi_x$ , and  $\lambda_{ij}^x$  are the Gell-Mann matrices. For the benchmark parameters provided in Ref. [51], we find a value of  $C_{ab}^x/\Lambda \sim 10^{-7}$  TeV $^{-1}$ . This coupling is too small to be probed at current experiments, but depending on the ALP-Higgs coupling, may be accessible at future searches for long-lived decay products of the Higgs, such as MATHUSLA at CERN [53]. In particular, the

effective dark pion-Higgs interaction is anticipated to have the form

$$\mathcal{L}_{\Pi H} = \xi \Pi^2 H^\dagger H = \frac{1}{\sqrt{2}} \xi \Pi^2 v_H h + \dots \quad (2.43)$$

where  $\xi \sim M_\Pi^2/v_H^2 \sim 10^{-3}$ . Matching to the ALP EFT (2.21), we find a relatively large Higgs coupling of  $C'_{ah}/\Lambda^2 \sim 16 \text{ TeV}^{-2}$ . The prospect of probing leptophilic ALPs with substantial Higgs couplings will be discussed in more detail in Chapter 5.

Finally, we note that if  $g_{aS}$  and  $g_{bPS}$  are purely real, the on-diagonal couplings  $C_{aa}/\Lambda$  completely vanish. This can be achieved in the UV model by imposing C-symmetry on the interactions. Although this choice is arbitrary, it is certainly interesting to consider the possibility that details of a UV model prevent on-diagonal couplings in a manner which is symmetry-protected. As we will explore in Chapter 3, some of the leading constraints on lepton-flavor-violating couplings require non-zero diagonal couplings as well, so particles with purely flavor-violating couplings can potentially avoid detection.

## 2.5 New $U(1)$ Gauge Bosons

At the end of last section, we explored a scenario in which the dark sector is governed by a strongly-coupled gauge theory. There is, of course, a much simpler case to consider: a dark abelian symmetry  $U(1)_X$ , under which none of the SM gauge fields are charged. Curiously, if one abides by the totalitarian principle,<sup>13</sup> such a field automatically has a gauge-invariant interaction with the SM photon,  $\mathcal{L} \supset F^{\mu\nu} F'_{\mu\nu}$ . Then, the  $U(1)$ -sector of the Standard-Model has the form

$$\mathcal{L} = -\frac{1}{4} F^{\mu\nu} F_{\mu\nu} - \frac{1}{4} F'^{\mu\nu} F'_{\mu\nu} - \epsilon F^{\mu\nu} F'_{\mu\nu} - e J_\mu^{\text{EM}} A^\mu - g_X J_\mu^X A'^\mu \quad (2.44)$$

where  $\epsilon$  is known as the *kinetic mixing*. The kinetic term can then be diagonalized via the field redefinition

$$\begin{pmatrix} A' \\ A \end{pmatrix} = \begin{pmatrix} \frac{1}{\sqrt{1-\epsilon^2}} & 0 \\ -\frac{\epsilon}{\sqrt{1-\epsilon^2}} & 1 \end{pmatrix} \begin{pmatrix} \cos \theta & -\sin \theta \\ \sin \theta & \cos \theta \end{pmatrix} \begin{pmatrix} \hat{A}' \\ \hat{A} \end{pmatrix} \quad (2.45)$$

---

<sup>13</sup> “Everything not forbidden is compulsory.” [54]

where a hat ( $\hat{\cdot}$ ) represent the diagonalized eigenstates of the theory. If both  $A$  and  $A'$  are massless, any value of  $\theta$  provides a valid diagonalization of the kinetic term. However, if the  $U(1)_X$  symmetry is spontaneously broken, one must have  $\theta = 0$ , so we will assume this is the case for the rest of this discussion. Then, the Lagrangian in terms of the diagonalized fields (to lowest order in  $\epsilon$ ) is given by

$$\mathcal{L} = -\frac{1}{4}\hat{F}^{\mu\nu}\hat{F}_{\mu\nu} - \frac{1}{4}\hat{F}'^{\mu\nu}\hat{F}'_{\mu\nu} - \frac{1}{2}m_{A'}^2\hat{A}'_\mu\hat{A}'^\mu - eJ_\mu^{\text{EM}}\hat{A}^\mu + \epsilon eJ_\mu^{\text{EM}}\hat{A}'^\mu - g_X J_\mu^X\hat{A}'^\mu. \quad (2.46)$$

We see that the  $\hat{A}'$  couples to the ordinary electromagnetic current, but suppressed by a factor  $\epsilon$ . This property earns the  $\hat{A}'$  the title of *dark photon*, and its coupling to the electromagnetic current is known as *millicharge*.

If the  $U(1)_X$  symmetry is entirely in a dark sector, then this alone doesn't induce any flavor-violation. However, there is also the possibility that the the SM fermions themselves are charged under the  $U(1)_X$ . In this case, one can expect experimental sensitivity to the strength of the gauge coupling  $g_X$  as well as the kinetic mixing  $\epsilon$ , although the kinetic mixing can be avoided by embedding the  $U(1)_X$  in some larger non-abelian group [55]. Without charging additional fermions under the  $U(1)_X$  and the SM gauge groups, there are only three possibilities for which the symmetry is anomaly-free: these are the gauged lepton family symmetries  $U(1)_{L_i-L_j}$  [56–58]. While these may appear contrived at first glance,<sup>14</sup> they introduce a somewhat satisfying hierarchical structure between generations; for example,  $U(1)_{L_\tau-L_e}$  has  $Q(\{e, \mu, \tau\}) = \{-1, 0, 1\}$ . The  $U(1)_{L_\mu-L_\tau}$  theory is of particular phenomenological interest because it can reproduce the structure of the PMNS matrix and can also provide an explanation to the muon  $g - 2$  anomaly [59–61].

The gauge boson in these theories is often accompanied with a scalar or spectrum of scalars that are charged under the  $U(1)_{L_i-L_j}$  symmetry, and which may be responsible for spontaneously breaking the symmetry. These scalars have the peculiar property that (at least prior to diagonalization of the mass matrices) they couple only to off-diagonal lepton currents. For example, the  $-1$  ( $L_\mu - L_\tau$ )-charged Higgs-doublet  $\phi$  in Ref. [60] primarily couples to  $e\mu$  and  $e\tau$ . More generally, any

---

<sup>14</sup> At least they did to me when I first encountered them.

Higgs-like doublet with charge  $\pm 2$  under  $U(1)_{L_i-L_j}$  couples to at most one off-diagonal lepton current. Such particles can yield substantial contributions to the lepton dipole moments while evading constraints from other experiments. We will discuss this possibility in more detail in Chapter 3.

If one appends three right-handed neutrinos  $N_{Ri}$  to the SM, then  $U(1)_{B-L}$  (baryon minus lepton number) is also anomaly-free and can be gauged. The addition of a  $U(1)_{B-L}$  gauge symmetry is appealing because it obeys the apparent flavor structure of the SM (which sequesters the fermions into sectors of triplets that have identical charges under the gauge group), and appends only one additional sector and (in its simplest case) one additional scalar. Depending on the scalar content of the theory,  $U(1)_{B-L}$  models can lead to Dirac or Majorana neutrino masses without introducing substantial flavor-violation in the charged lepton sector [62–64]. However, certain incarnations of the gauge symmetry, including supersymmetric extensions [65, 66], can lead to CLFV which is potentially detectable in the near future.

Limits on the anomaly-free hidden gauge bosons in upcoming and potential future lepton-nucleus collision experiments will be discussed in Chapter 6.

## Chapter 3

### Chiral Subtleties in Charged Lepton Flavor Physics

#### 3.1 Introduction

As we have discussed in the Introduction and Chapters 2, lepton flavor violation (LFV) is a hallmark of many extensions to the SM, and is hence a promising avenue to search for new physics. This chapter will explore spin-zero particles with generically flavor-violating and CP-violating interactions to the SM charged leptons. For simplicity, we assume that these particles are *leptophilic*, so they couple only to the lepton sector of the SM. It is not too difficult to provide charge assignments in the UV that forbid direct interaction with quarks. As examples, we refer to lepton-specific 2HDM models [67], gauged  $U(1)_{L_i-L_j}$  extensions to the SM [56–58, 60], and the composite dark matter model in Ref. [51] which is reviewed in Section 2.4.4. That said, most of our results are independent of this choice, with the exception being the induced photonic coupling one finds when treating an LFV ALP interaction with the (pseudo)-scalar current (which would have a contribution from quarks in more generic models).

We have already seen in Chapter 2 that chirally coupled particles can appear naturally as low-energy modes of some extensions to the SM. We have also encountered two scenarios where ALPs appear in the low energy theory with purely chiral interactions with the leptons. The appearance of particles with chiral interactions is not too surprising given that the Standard-Model fermion fields themselves are Weyl fermions prior to EWSB, with the Dirac structure only emerging after imposing unitary gauge and diagonalizing the SM quadratic terms. While mixing sometimes spoils the pure chiral nature of the interactions (as is the case when the  $W_3$  mixes with the  $B$  to make the

$Z$  boson), this is not guaranteed to happen (as is the case with the  $(W_1 \pm iW_2)/\sqrt{2} = W_{\pm}$  bosons), so we believe the chiral scenario should be examined more closely.

In this chapter, we will consider the leading constraints on the LFV couplings of scalars and ALPs, exploring the role of PV and CPV in the process. In Section 3.2, we will examine how a chiral interaction (and more exotic PV and CPV interactions) may arise from interactions involving the SM gauge fields prior to EWSB. In Section 3.3, we will consider the limits one can obtain from LFV decay modes of the  $\mu$  and  $\tau$  leptons, comparing “pure” (parity-conserving) interactions to chiral interactions for both scalars and ALPs. Finally, in Section 3.4, we consider the contribution of LFV scalars and ALPs to the lepton electric and magnetic dipole moments. The electric dipole moments receive no contribution from pure or chiral interactions because these interactions preserve CP, so in this case we consider limits on the degree of CP violation in the coupling. For the magnetic dipole moments, we explore LFV scalar and ALP explanations for the electron and muon  $g - 2$  anomalies, and also place limits on the couplings in the event that these anomalies are resolved. Throughout this chapter, we will refer to the boson as the  $\varphi$  and its mass as  $m_\varphi$  unless we are specializing to an ALP-specific scenario, for which we will refer to it as the  $a$  with mass  $m_a$ .

## 3.2 LFV Interaction

### 3.2.1 UV Considerations

In this section, we will review some scenarios in which LFV scalars can arise naturally from some UV model. We will focus on two concrete examples: an additional Higgs doublet, and an ALP coupled to the lepton sector.

#### 1. Higgs Doublet

We begin by examining the interaction between a second Higgs doublet  $\Phi$  and the leptons. For simplicity, we will assume that the SM Higgs-lepton interaction is already diagonalized, so that we

are operating with the SM lepton eigenstates.<sup>1</sup> Then, the  $\Phi$ -lepton interaction is given by

$$\mathcal{L}_{\text{int}} = \sum_{i,j} \left[ y_{ij} \bar{L}_i \Phi \ell_{jR} + y_{ji}^* \bar{\ell}_{iR} \Phi^\dagger L_j \right] \quad (3.1)$$

In the following, we will only focus on interactions with the charged leptons, so we will isolate the charge-neutral component of the Higgs doublet,  $\Phi^0$ :

$$\mathcal{L}_{\text{int}} = \sum_{i,j} \left[ y_{ij} \Phi^0 \bar{\ell}_i P_R \ell_j + y_{ji}^* \Phi^{0\dagger} \bar{\ell}_i P_L \ell_j \right] + \dots \quad (3.2)$$

Due to the nature of the  $SU(2)$  symmetry, the  $\Phi^0$  coupling is chiral: a  $\Phi^0$  can only decay to an  $\ell_L^- \ell_R^+$ , not an  $\ell_R^- \ell_L^+$ . Since  $\Phi^0$  is a complex scalar, it can be split into real and imaginary parts,  $\Phi^0 \equiv s + ia$ . Depending on the potential between the  $\Phi$  and other scalars, the  $s$  and  $a$  may acquire a significant mass splitting after diagonalizing the quadratic interaction, so it is instructive to treat each of them as separate fields and see whether any notion of “chirality” persists. Doing so, we find the following interaction term:

$$\mathcal{L}_{\text{int}} = \sum_{i,j} \left\{ s \bar{\ell}_i [y_{ij} P_R + y_{ji}^* P_L] \ell_j + ia \bar{\ell}_i [y_{ij} P_R - y_{ji}^* P_L] \ell_j \right\} \quad (3.3)$$

It is worth examining these interactions using the magnitude, angle, and phase formalism described in Section 2.3.1. Then, the magnitude, angles and phases for the scalar  $s$  are given by

$$g_{ij}^s = \sqrt{\frac{|y_{ij}|^2 + |y_{ji}|^2}{2}} \quad (3.4)$$

$$-ie^{i\delta_{ij}^s} \tan \theta_{ij}^s = \frac{y_{ij} - y_{ji}^*}{y_{ij} + y_{ji}^*}, \quad (3.5)$$

and the magnitudes, angles and phases for the pseudoscalar  $a$  are given by

$$g_{ij}^a = \sqrt{\frac{|y_{ij}|^2 + |y_{ji}|^2}{2}} \quad (3.6)$$

$$-ie^{i\delta_{ij}^a} \tan \theta_{ij}^a = \frac{y_{ij} + y_{ji}^*}{y_{ij} - y_{ji}^*}. \quad (3.7)$$

The parameters for the  $s$  and  $a$  are related:  $g_{ij}^a = g_{ij}^s$ ,  $\delta_{ij}^a = -\delta_{ij}^s$ , and  $\theta_{ij}^a = \pi/2 - \theta_{ij}^s$ . Note that the  $s$  is a “pure” scalar and  $a$  a “pure” pseudoscalar only when  $y_{ij} = y_{ji}^*$  (i.e., when the Yukawa

---

<sup>1</sup> If the  $\Phi$  acquires a VEV, these are not the true eigenstates of the low-energy theory.

matrix  $\mathbf{y}$  is Hermitian), but there is no reason to expect this in general. The only reason the SM Higgs Yukawa matrices are Hermitian and diagonal is because we redefined the fields to diagonalize the mass matrix and make it so; any additional Higgs doublet interactions do not have this luxury, and even the SM Higgs interaction in principle does not have this luxury if there are other Higgs doublets which acquire a VEV. Something interesting happens when  $y_{ij} \neq 0$  but  $y_{ji} = 0$  (which can occur in interactions with explicit flavor symmetries, such as Froggatt-Nielsen models<sup>2</sup> [29, 49] and gauged  $U(1)_{L_i - L_j}$  models with charged Higgs doublets [60]). Then,  $\theta_{ij}^{s,a} = -\theta_{ji}^{s,a} = \pi/4$ , and  $\delta_{ij}^{s,a} = \delta_{ji}^{s,a} = \pm\pi/2$ , so the  $s$  and  $a$  fields are also chiral. More generally, it is easy to convince oneself that the fraction on the right can be any complex number, so the angles and phases can take on any value depending on the complex texture of the Yukawa couplings. Near-chiral interactions may arise if there is only an approximate flavor symmetry for which  $|y_{ji}| \ll |y_{ij}|$ . One can expect more complicated behavior in the event that the real and imaginary parts are not eigenstates of the low-energy theory, but that is beyond the scope of this discussion.

One important difference between complex chiral scalars and real chiral scalars is the flavor-diagonal couplings. In particular, one cannot have  $y_{ii}^* = 0$  but  $y_{ii} \neq 0$ , so there can be no “chiral coupling” of scalars to the flavor-conserving scalar current. The same is not true for a complex scalar. One might object that a complex scalar is just two real scalars, so how can one have a chiral coupling and not the other? The key is that if the  $s$  and  $a$  have the same mass, they have the same propagator, so for  $i = j$  their contributions to Feynman diagrams can cancel exactly to give the effect of a chiral coupling to the flavor-conserving scalar currents.

## 2. Leptophilic Axion-Like Particle

If an ALP comes from some approximate global symmetry in a UV model, it will not couple directly to the SM fermion eigenstates, but the SM gauge fields. In full generality, the ALP will couple

---

<sup>2</sup> In this case, the Higgs Yukawas have this property *prior* to diagonalization of the mass matrix, but one could imagine a similar effect with a second Higgs doublet coupled to the Froggatt-Nielsen scalar.

with different coefficients to the left-handed lepton doublets and right-handed lepton singlets:

$$\mathcal{L}_{\text{int}} = \frac{\partial_\mu a}{\Lambda} \sum_{i,j} [C_{ij}^L \bar{L}_i \gamma^\mu L_j + C_{ij}^R \bar{\ell}_{Ri} \gamma^\mu \ell_{Rj}] \quad (3.8)$$

To ensure Hermiticity of the Lagrangian, we must have  $C_{ij}^L = C_{ji}^{L*}$  and  $C_{ij}^R = C_{ji}^{R*}$  because  $a$  is real. Of course, it is possible to express this interaction in terms of the lepton eigenstates of the SM. Focusing only on the charged leptons,<sup>3</sup> we have

$$\mathcal{L} = \frac{\partial_\mu a}{\Lambda} \sum_{i,j} \bar{\ell}_i \gamma^\mu [C_{ij}^L P_L + C_{ij}^R P_R] \ell_j \quad (3.9)$$

In this case, if one of  $C_{ij}^R$  or  $C_{ij}^L$  is zero, then the ALP has a chiral coupling to the charged leptons. We have encountered this in Chapter 2 both for the axiflavor with certain Froggatt-Nielsen textures, and for the composite ALP model. Rewriting the left-right projection operators as  $P_{R(L)} = \frac{1}{2}(1 \pm \gamma^5)$ , we see that the vector and axial-vector coupling strengths are  $A_{ii} = C_{ij}^R - C_{ij}^L$  and  $V_{ii} = C_{ij}^R + C_{ij}^L$ . We can use the notation from Section 2.4.2 to decompose the couplings into magnitudes, angles, and phases:

$$C_{ij} = \sqrt{\frac{|C_{ij}^L|^2 + |C_{ij}^R|^2}{2}} \quad (3.10)$$

$$e^{i\Delta_{ij}} \tan \Theta_{ij} = \frac{C_{ij}^R + C_{ij}^L}{C_{ij}^R - C_{ij}^L}. \quad (3.11)$$

Hermiticity requires  $\Delta_{ji} = -\Delta_{ij}$  and  $\Theta_{ji} = -\Theta_{ij}$ . The ALP couples to the axial-vector current only when  $C_{ij}^L = -C_{ij}^R$ , which is an arbitrary choice that would only apply to very specific UV models. In the event that  $C_{ij}^R = C_{ij}^L$ ,  $\Theta_{ij} = \pi/2$  and the ALP will couple directly to the vector current. This scenario has interesting implications, because the absence of an axial vector current in the interaction effectively removes the on-diagonal interaction. This is easier to see when the ALP interaction is rewritten to be scalar-like; substituting  $\Theta_{ii} = 0$  into the effective scalar coupling in Eq. 2.31 reveals  $g_{ii} = \frac{C_{ii}}{\Lambda} \sqrt{m_i^2 + m_i^2 + 2m_i m_i \cos \pi} = 0$ . As we will see, an ALP with this property would evade many of the existing constraints from LFV lepton decay modes, because most of the diagrams that contribute in these channels involve one on-diagonal coupling and one off-diagonal coupling.

---

<sup>3</sup> The ALP interaction can be completely rotated away in the neutrino sector provided they are massless.

More generally, we point out that while the ALP can couple to both the flavor-changing vector and axial-vector currents, any non-zero coupling to the flavor-conserving vector current is illusory. Once again using Eq. 2.31, we have that the scalar form of the on-diagonal coupling is given by  $g_{ii} = \frac{C_{ii}}{\Lambda} \sqrt{m_i^2 + m_i^2 + 2m_i m_i \cos 2\Theta_{ii}} = \frac{m_i C_{ii}}{\Lambda} (2 \cos \Theta_{ii}) = \frac{2m_i A_{ii}}{\Lambda}$ . Hence, only the axial-vector component of the on-diagonal interaction contributes to physical observables. This happens because the chirally-symmetric field redefinition  $\ell_i \rightarrow e^{iV_{ii}a/\Lambda} \ell_i$  induces an ALP derivative coupling which cancels the on-diagonal vector component of Eq. 3.9 ( $\bar{\ell}_i i \not{\partial} \ell_i \rightarrow \bar{\ell}_i i \not{\partial} \ell_i - V_{ii} \frac{\partial_\mu a}{\Lambda} \bar{\ell}_i \gamma^\mu \ell_i$ ) without inducing an ALP coupling in the lepton mass term ( $m_i \bar{\ell}_i \ell_i \rightarrow m_i \bar{\ell}_i \ell_i$ ).

### 3.2.2 Effective Interaction

To encompass the examples above, we generically consider two possibilities. We have a scalar (real or complex) with LFV interaction

$$\mathcal{L}_{\varphi \ell \ell} = \varphi \sum_i \bar{\ell}_i (g_{ij}^S + ig_{ij}^{PS} \gamma_5) \ell_j + \text{H.c.} \quad (3.12)$$

and an ALP with LFV interaction

$$\mathcal{L}_{a \ell \ell} = \frac{\partial_\mu a}{\Lambda} \sum_{i,j} \bar{\ell}_i (V_{ij} - A_{ij} \gamma_5) \ell_j + \text{H.c.} \quad (3.13)$$

One can drop the +H.c. in (3.12) for a real scalar as long as one imposes  $g_{ji}^{*(P)S} = g_{ij}^{(P)S}$ , and similarly, one can drop +H.c. in (3.13) if one imposes  $V_{ji}^* = V_{ij}$  and  $A_{ji}^* = A_{ij}$ . As discussed in Section 2.4.2, it is possible to rewrite the ALP interaction to have the same form as Eq. 3.12:

$$\mathcal{L}_{a \ell \ell} = -ia \sum_{i,j} \bar{\ell}_i \gamma^\mu \left[ \frac{m_i - m_j}{\Lambda} V_{ij} + \frac{m_i + m_j}{\Lambda} A_{ij} \gamma_5 \right] \ell_j. \quad (3.14)$$

It follows that if one calculates diagrams involving LFV processes with the scalar interaction in Eq. 3.12, they can be recast into LFV ALP diagrams via the substitutions  $g_{ij}^S = -i(m_i - m_j)V_{ij}/\Lambda$  and  $g_{ij}^{PS} = -i(m_i + m_j)A_{ij}/\Lambda$ . However, there is a catch: due to the chiral anomaly, the field redefinition required to rewrite the ALP interaction term as a scalar-like interaction induces an ALP-photon interaction. In particular, this will induce a Lagrangian term

$$\mathcal{L}_{a \gamma \gamma} = 4\pi \alpha C'_{\gamma \gamma} \tilde{F}^{\mu\nu} F_{\mu\nu} \quad (3.15)$$

where  $C'_{\gamma\gamma} = C_{\gamma\gamma} + \sum_\ell [A_{\ell\ell}/8\pi^2]^4$ <sup>4</sup> (although for our purposes,  $C_{\gamma\gamma} = 0$ ). Hence, even if the photon coupling is zero in the low-energy EFT for the ALP, it is non-zero when one rewrites the ALP interaction in scalar form. Of course, it is not *impossible* for the ALP to have zero tree-level photon coupling when its leptonic interaction is written in the form of Eq. 3.12 but this would require fine-tuning in the tree-level photon coupling of the ALP, e.g.,  $C_{\gamma\gamma} = -\sum_\ell [C_{\ell\ell}/8\pi^2]$ .

Going forward, we find it useful to decompose the couplings into magnitudes, angles and phases, as done in Sections 2.3.1 and 2.4.2. For the scalar, this entails  $g_{ij}^S = g_{ij}e^{i\phi_{ij}} \cos \theta_{ij}$ ,  $g_{ij}^{PS} = g_{ij}e^{i[\phi_{ij}+\delta_{ij}]} \sin \theta_{ij}$ , while for the ALP,  $V_{ij} = C_{ij}e^{i\Phi_{ij}} \sin \Theta_{ij}$ ,  $A_{ij} = C_{ij}e^{i[\Phi_{ij}+\Delta_{ij}]} \cos \Theta_{ij}$ . The relationship between the magnitudes, angles and phases for the scalar and the ALP is given by Eqs. (2.30)-(2.31). In this form, a ‘pure’ scalar is given by  $\theta_{ij} = 0$ , while a ‘pure’ pseudoscalar is given by  $\theta_{ij} = \pi/2$ . We can also identify chirally-coupled particles with the assignment  $\theta_{ij} = \pi/4$  and  $\delta_{ij} = \pm\pi/2$  (or  $\Theta_{ij} = \pi/4$  and  $\Delta_{ij} = 0, \pi$  in the case of an ALP); in this scenario, the couplings are proportional to the left or right projection operators  $P_{L,R} = (1 \pm \gamma_5)/2$ . While limits are often cast on particles in the pure scalar or pure pseudoscalar scenario, the UV discussion above gives motivation to consider the chiral scenario as well. We will compare results for pure scalars and pseudoscalars to the chiral scenario to understand the role that PV can play in determining leptonic observables.

### 3.3 LFV Lepton Decays

Most of the leading constraints on CLFV physics come from limits on the branching fractions to LFV final-states of the charged leptons [68, 69]. For light scalars  $\varphi$  with LFV couplings, these are very strong limits due to the ability for  $\mu$  and  $\tau$  leptons to decay directly via  $\ell_i \rightarrow \ell_j \varphi$ , which can give contributions to both  $\ell_i \rightarrow \ell_j + \text{invis.}$  and  $\ell_i \rightarrow \ell_j \ell_k \bar{\ell}_l$  depending on the available decay modes and lifetime of the  $\varphi$ . There is also the process  $\ell_i \rightarrow \ell_j \gamma$ , but this is loop-suppressed so is

---

<sup>4</sup> This term is often given additional dependence on the ALP and fermion masses by examining the fermionic one-loop contribution to the  $a \rightarrow \gamma\gamma$  decay, but this result assumes the ALP and photons are on shell. The full two-loop calculation is performed approximately in Ref. [47] and exactly in Ref. [48], which finds that there are negligible differences between the one-loop and two-loop results for heavy ALPs.

subdominant for light  $\varphi$ . For more work on light LFV scalars and ALPs, see Refs. [31, 70].

In this chapter our focus is on heavy (GeV-scale) scalars and ALPs, for which the story is slightly different. The  $\ell_i \rightarrow \ell_j \phi$  becomes kinematically forbidden, so that  $\ell_i \rightarrow \ell_j + \text{invis.}$  is no longer available, and the tri-lepton decay  $\ell_i \rightarrow \ell_j \ell_k \bar{\ell}_l$  occurs via an off-shell  $\varphi$ . Unlike before, the trilepton signal is now similar in scale to the loop-induced radiative decay  $\ell_i \rightarrow \ell_j \gamma$ , so both processes must be considered. In principle, each of these decay modes can receive contributions from the  $\ell_i \rightarrow \ell_j$  transition dipole form factors, because (for  $l = k$ , at least) one can have  $\ell_i \rightarrow \ell_j \gamma^* (\gamma^* \rightarrow \ell_k \bar{\ell}_l)$ . Hence, we will derive formulae for these form-factors before placing limits on the LFV scalar and ALP models.

### 3.3.1 Dipole Transition Form Factors

We begin by solving for the transition dipole form-factors for the  $\ell_i \rightarrow \ell_j$  flavor-changing neutral current. These form-factors have been computed in the past [46, 70, 71], but we will emphasize the role that PV can play on the size of the form-factors by expressing the form-factors explicitly in terms of the magnitudes, angles, and phases described in Section 3.2.2. In particular, we will find that in many cases, the form-factors can be suppressed by multiple orders of magnitude for chirally-coupled particles as compared to pure scalars or pure pseudoscalars and ALPs, which has clear implications for the limits one can place on new physics.

The most general gauge-invariant decomposition of the  $\ell_i \rightarrow \ell_j$  flavor-changing current into dimensionless form-factors is [72]

$$\bar{u}_j(q_2) \Gamma_\mu^{ij} u_i(q_1) = e \bar{u}_j(q_2) \left[ \left( q_\mu + \frac{q^2}{m_i - m_j} \gamma_\mu \right) F_1^{ij}(q^2) + \frac{i\sigma^{\mu\nu}}{m_i + m_j} q_\nu F_2^{ij}(q^2) + \frac{\sigma^{\mu\nu}}{m_i - m_j} q_\nu \gamma^5 F_3^{ij}(q^2) + \left( q_\mu - \frac{q^2}{m_i + m_j} \gamma_\mu \right) \gamma^5 F_4^{ij}(q^2) \right] u_i(q_1) \quad (3.16)$$

where  $\sigma^{\mu\nu} = \frac{i}{2} [\gamma^\mu, \gamma^\nu]$ . Here,  $F_1(q^2)$  is the charge transition form factor,  $F_2(q^2)$  and  $F_3(q^2)$  are magnetic and electric dipole transition form-factors, and  $F_4(q^2)$  is the anapole transition form-factor. For our purposes, we are only concerned with the dipole transition form-factors evaluated at  $q^2 = 0$ . Higher  $q^2$ -dependence and the other form-factors become important when the  $\ell_i \rightarrow \ell_j$

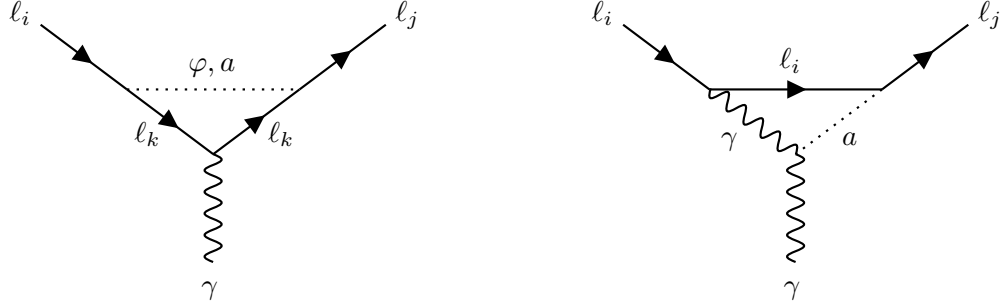


Figure 3.1: Feynman diagrams which contribute to the form-factors relevant to the process  $\ell_i \rightarrow \ell_j \gamma$ , as well as to the lepton dipole moments for  $i = j$ , for particles with the interaction terms in Eqs. 3.12 and 3.13. For leptophilic particles, the right-most diagram only applies to an ALP, which has an induced coupling to photons when rewriting the leptonic interaction to be scalar-like.

transition occurs in loops with an off-shell photon. The only place where this may affect our results is in the loop-induced contribution to  $\ell_i \rightarrow \ell_j \ell_k \bar{\ell}_k$  mediated by an off-shell photon. However, in this instance, the bounds from  $\ell_i \rightarrow \ell_j \gamma$  are dominant anyway.

We compute the dipole transition form-factors generated by the interactions in Eqs. 3.12 and 3.14 by evaluating the left-most Feynman diagram in Fig. 3.1. Using PackageX in Mathematica [73], we find that the exact one-loop form factors at  $q^2 = 0$  can be written in the form

$$F_2^{ijk}(0) = \frac{g_{ik}g_{jk}e^{i\Delta\phi}}{32\pi^2} \left[ f(\mu_i, \mu_j, \mu_k) \cos \theta_{ik} \cos \theta_{jk} + e^{i\Delta\delta} f(-\mu_i, -\mu_j, \mu_k) \sin \theta_{ik} \sin \theta_{jk} \right] \quad (3.17)$$

and

$$F_3^{ijk}(0) = \frac{g_{ik}g_{jk}e^{i\Delta\phi}}{32\pi^2} \left[ f(-\mu_i, \mu_j, \mu_k) e^{-i\delta_{jk}} \cos \theta_{ik} \sin \theta_{jk} - f(\mu_i, -\mu_j, \mu_k) e^{i\delta_{ik}} \sin \theta_{ik} \cos \theta_{jk} \right] \quad (3.18)$$

where  $\mu_i = m_i/m_\varphi$ .<sup>5</sup> The function  $f$  is given by

$$\begin{aligned} f(x, y, z) = & \frac{(2z+y)x^2 - (2x+y)(z^2 + 2xz - 1)}{(x^2 - y^2)x^3} \sqrt{(1-x^2+z^2)^2 - 4z^2} \operatorname{arccosh} \left( \frac{1-x^2+z^2}{2z} \right) \\ & - \frac{(2z+x)y^2 - (2y+x)(z^2 + 2yz - 1)}{(x^2 - y^2)y^3} \sqrt{(1-y^2+z^2)^2 - 4z^2} \operatorname{arccosh} \left( \frac{1-y^2+z^2}{2z} \right) \\ & - \frac{[(x+y)(1-z^2) - xyz]^2 - 3x^2y^2z^2}{x^3y^3} \log z - \frac{1+xy-z^2}{xy} \\ & - \lim_{\varepsilon \rightarrow 0} \int_0^1 \int_0^{1-s} \frac{2(x+y+z)z ds dt}{x^2 - (x^2 - y^2)st + (1 - y^2 - z^2)t + y^2t^2 + i\varepsilon}, \end{aligned} \quad (3.19)$$

where we are using  $\operatorname{arccosh} u = \log(u + \sqrt{u^2 - 1})$  with the principle branch on the logarithm.<sup>6</sup>

The integral in the last line is a special case of the scalar  $C_0$  function obtained through Passarino-Veltman reduction [74, 75]. It can be evaluated in terms of dilogarithms, but one must be careful to choose the branch that corresponds to the  $+i\varepsilon$  prescription. Note that for pure scalar or pure pseudoscalar couplings,  $F_3^{ijk}(0)$  is zero, and only one of the terms involving  $f(\pm\mu_i, \pm\mu_j, \mu_k)$  in  $F_2^{ijk}(0)$  remains. The pure (pseudo)-scalar scenario is often the focus of works which aim to limit LFV couplings, but as we have seen, the chiral asymmetry of the SM gauge groups can naturally lead to chiral couplings instead.

To explore the chiral scenario, we will consider the special case  $\delta_{ik} = \delta_{jk} = \pm\pi/2$ , so that the interactions involving the scalar and pseudoscalar currents of each fermion pair have the same phase.<sup>7</sup> This choice encompasses the pure chiral scenario (for which the interaction is proportional to  $1 \pm \gamma^5$ ) but allows for arbitrary PV angles  $\theta_{ik}$  and  $\theta_{jk}$ . In this scenario, it is convenient to define the functions

$$f_{\pm}(\mu_i, \mu_j, \mu_k) = \frac{1}{2} [f(\mu_i, \mu_j, \mu_k) \pm f(-\mu_i, -\mu_j, \mu_k)]. \quad (3.20)$$

Then, using the reverse cosine and sine product identities, the form-factors can be expressed as

$$F_2^{ijk}(0) = \frac{g_{ik}g_{jk}e^{i\Delta\phi}}{32\pi^2} (f_-(\mu_i, \mu_j, \mu_k) \cos(\theta_{ik} + \theta_{jk}) + f_+(\mu_i, \mu_j, \mu_k) \cos(\theta_{ik} - \theta_{jk})) \quad (3.21)$$

<sup>5</sup> In the case of a complex scalar,  $g_{ij} \neq g_{ji}$  in general, so there is an analogous contribution mediated by the antiparticle which involves the couplings  $g_{ki}$  and  $g_{kj}$  (and associated phases) as long as they are non-zero.

<sup>6</sup> In Mathematica and NumPy,  $\operatorname{arccosh} u = \log(u + \sqrt{u - 1}\sqrt{u + 1})$ , which leads to an overall sign difference in the real part for  $u < -1$ . Care must be taken to ensure the proper branch, which is determined by the  $\varepsilon$ -prescription of the Feynman propagator.

<sup>7</sup> This is one step away from the CP-preserving scenario, which also requires  $\phi_{ik} = \phi_{jk} = 0$ .

and

$$F_3^{ijk}(0) = \pm \frac{ig_{ik}g_{jk}e^{i\Delta\phi}}{32\pi^2} (f_+(\mu_i, -\mu_j, \mu_k) \sin(\theta_{ik} + \theta_{jk}) - f_-(\mu_i, -\mu_j, \mu_k) \sin(\theta_{ik} - \theta_{jk})). \quad (3.22)$$

At this point, it is customary to expand in the lepton mass hierarchy  $m_e \ll m_\mu \ll m_\tau$ . For certain processes, this hierarchy can manifest itself within the functions  $f_\pm$  such that  $|f_+| \gg |f_-|$  or  $|f_+| \ll |f_-|$ , in which case the smaller of the two terms is often neglected. However, this becomes invalid if  $\cos(\theta_{ik} \pm \theta_{jk})$  or  $\sin(\theta_{ik} \pm \theta_{jk})$  is also small. Such is the case for a scalar with chiral coupling to the leptons, for which  $\theta_{ik} = \theta_{jk} = \pm\pi/4$  and hence  $\cos(\theta_{ik} + \theta_{jk}) = \sin(\theta_{ik} - \theta_{jk}) = 0$ .

The form factors are then given by

$$F_2^{ijk}(0) = \frac{g_{ik}g_{jk}e^{i\Delta\phi}}{32\pi^2} f_+(\mu_i, \mu_j, \mu_k), \quad (3.23)$$

$$F_3^{ijk}(0) = \pm \frac{ig_{ik}g_{jk}e^{i\Delta\phi}}{32\pi^2} f_+(\mu_i, -\mu_j, \mu_k). \quad (3.24)$$

Hence, even if  $|f_+| \ll |f_-|$ , it would be invalid to neglect the terms involving  $f_+$ , as the terms involving  $f_-$  are exactly zero in the chiral case. We will find that this is the case for quite a few of the chiral scalar contributions to the form-factors.

A similar effect can also occur for the ALP, with some important differences. After rewriting the interaction into the form of Eq. 3.14, the difference in lepton masses forces  $\theta_{ii} = \pi/2$ . Also, for  $i \neq j$ ,  $\theta_{ij}$  isn't exactly  $\pi/4$ , but, assuming  $m_i > m_j$ , has  $\mathcal{O}(m_j/m_i)$  corrections. Rather than treating these cases separately, we can use the relation Eq. 2.31 with  $\Theta_{ij} = \pi/4$  and  $\Delta_{ij} = \pm\pi/2$  to find

$$F_2^{ijk}(0) = \pm \frac{C_{ik}C_{jk}e^{i\Delta\phi}}{32\pi^2} \left[ \frac{(m_i + m_j)m_k}{\Lambda^2} f_-(\mu_i, \mu_j, \mu_k) - \frac{m_i m_j + m_k^2}{\Lambda^2} f_+(\mu_i, \mu_j, \mu_k) \right] \quad (3.25)$$

and

$$F_3^{ijk}(0) = \pm \frac{C_{ik}C_{jk}e^{i\Delta\phi}}{32\pi^2} \left[ \frac{(m_i - m_j)m_k}{\Lambda^2} f_-(\mu_i, -\mu_j, \mu_k) - \frac{m_i m_j - m_k^2}{\Lambda^2} f_+(\mu_i, -\mu_j, \mu_k) \right]. \quad (3.26)$$

In this case, most of the  $\ell_i \rightarrow \ell_j$  dipole form factors are insensitive to the difference between pure and chiral couplings. However, there are still significant differences between the chiral and pure

pseudoscalar scenarios for the  $\mu \xrightarrow{\tau} e\gamma$  decay mode, which (all couplings equal) happens to produce the strongest limits of all the decay modes.

Finally, we must address the additional photonic coupling in the case of the ALP. This can generate the diagram on the right of Fig. 3.1. Rather than provide an exact expression, we use an expression which is valid for  $m_i \gg m_j$  [71]

$$F_2^{ij\gamma}(0) = -\frac{\alpha A_{ij} \sum_\ell A_{\ell\ell}}{16\pi^3} \frac{m_i^2}{\Lambda^2} \left[ 2 \log \frac{\Lambda^2}{m_i^2} + 2 + (x_i - 1) \log(x_i - 1) - \frac{x_i^2}{x_i - 1} \log x_i \right] \quad (3.27)$$

$$F_3^{ij\gamma}(0) = -\frac{i\alpha V_{ij} \sum_\ell A_{\ell\ell}}{16\pi^3} \frac{m_i^2}{\Lambda^2} \left[ 2 \log \frac{\Lambda^2}{m_i^2} + 2 + (x_i - 1) \log(x_i - 1) - \frac{x_i^2}{x_i - 1} \log x_i \right]. \quad (3.28)$$

Neglecting interference with diagrams involving the other form-factors, we will find that the  $\ell_i \rightarrow \ell_j \gamma$  and  $\ell_i \rightarrow \ell_j \ell_k \bar{\ell}_l$  decay rate mediated by the fermion-loop-induced photonic coupling are proportional to  $|A_{ij}|^2 + |V_{ij}|^2 = C_{ij}^2$ , and are hence independent of PV in the interaction.

### 3.3.2 Approximations

Here we will cite approximate formulae for  $f_\pm$  for the relevant hierarchies of  $m_i$ ,  $m_j$ , and  $m_k$ . These formulae appear to match the exact results within 10% over almost all ranges of parameters, with especially good agreement for  $m_a > m_i$ . For easy comparison with other results in the literature, we rewrite the functions in terms of  $x_i = m_\varphi^2/m_i^2 = 1/\mu_i^2$ . Not only are these formulae useful for examining the effect of chiral interactions, but they are also useful for avoiding floating-point errors when numerically evaluating Eq. 3.19.

(1)  $i = k > j$

This regime is relevant for  $\mu \rightarrow e\gamma$  with an internal  $\mu$ , and  $\tau \rightarrow e\gamma$  and  $\tau \rightarrow \mu\gamma$  with an

internal  $\tau$ . In the limit  $m_i \gg m_j$ ,

$$\begin{aligned}
f_+(\mu_i, \mu_j, \mu_k) &= 2x_i - 3 - (x_i - 3)x_i \log x_i + 2(x_i - 1)\sqrt{x_i(x_i - 4)} \log \left( \frac{x_i + \sqrt{x_i(x_i - 4)}}{2\sqrt{x_i}} \right) \\
&\quad - \log^2 \left( \frac{x_i + \sqrt{x_i(x_i - 4)}}{2x_i} \right) - 2\text{Li}_2(1 - x_i) \\
&\quad - 2\text{Li}_2 \left( \frac{x_i - \sqrt{x_i(x_i - 4)}}{2x_i} \right) + 2\text{Li}_2 \left( \frac{2 - x_i - \sqrt{x_i(x_i - 4)}}{2} \right), \\
f_-(\mu_i, \mu_j, \mu_k) &= -2 + \frac{(x_i - 3)x_i}{x_i - 1} \log x_i - 2\sqrt{x_i(x_i - 4)} \log \left( \frac{x_i + \sqrt{x_i(x_i - 4)}}{2\sqrt{x_i}} \right) \\
&\quad - \log^2 \left( \frac{x_i + \sqrt{x_i(x_i - 4)}}{2x_i} \right) - 2\text{Li}_2(1 - x_i) \\
&\quad - 2\text{Li}_2 \left( \frac{x_i - \sqrt{x_i(x_i - 4)}}{2x_i} \right) + 2\text{Li}_2 \left( \frac{2 - x_i - \sqrt{x_i(x_i - 4)}}{2} \right). \tag{3.29}
\end{aligned}$$

The terms involving the dilogarithms are identical for both  $f_+$  and  $f_-$ , and hence cancel for the pure pseudoscalar amplitude (for which the surviving part of the form factor is  $f(-\mu_i, -\mu_j, \mu_k) = f_+(\mu_i, \mu_j, \mu_k) - f_-(\mu_i, \mu_j, \mu_k)$ ). In this case, any significant differences between the pure scalar scenario and chiral scenario are due solely to differences in the functional form of  $f_+$  and  $f_-$ , as there is no explicit lepton mass ratio appearing in either of the functions. Nevertheless, the final results in Fig. 3.3 show that the difference in functional forms is enough to induce a substantial difference between the pure-scalar and chiral couplings.

(2)  $i > j, k$

This regime is relevant for  $\tau \rightarrow \mu\gamma$  and  $\tau \rightarrow e\gamma$ , with an internal  $\mu$  or  $e$ . In the limit  $m_\tau \gg m_\mu, m_e$ , we have

$$\begin{aligned}
f_+(\mu_i, \mu_j, \mu_k) &= -1 + 2x_i + 2(x_i - 1)x_i \log \left( \frac{x_i - 1}{x_i} \right) \\
f_-(\mu_i, \mu_j, \mu_k) &= \frac{2\mu_k}{\mu_i} \left[ \left( 1 - x_i - \log \left( \frac{(x_i - 1)x_k}{x_i} \right) \right) \log \left( \frac{x_i - 1}{x_i} \right) - \text{Li}_2 \left( \frac{1}{x_i} \right) - 1 \right]. \tag{3.30}
\end{aligned}$$

The second term is often neglected compared to the first in the  $m_k/m_i$  expansion, but we note that this is not valid in the case of  $\tau \xrightarrow{\mu} \ell\gamma$ . In particular, even though  $\mu_\tau/\mu_\mu =$

$m_\mu/m_\tau \approx 0.06$ ,  $|f_-| > |f_+|$  for almost all  $x_\tau > 1$ . Hence, similar to case (1), differences in the functional forms of  $f_\pm$  are enough to induce differences in the pure-scalar and chiral cases for  $\tau \rightarrow \mu\gamma$ , which is apparent in the second and third panels of Fig. 3.3. (Although not particularly relevant for the masses we consider, we note that for  $x_i < 1$ , one should choose the branch  $\log(x) = -i\pi + \log(-x)$ .)

(3)  $k > i, j$

This regime is relevant for  $\mu \rightarrow e\gamma$  with an internal  $\tau$ . In the limit  $m_\tau \gg m_\mu, m_e$ , we have

$$\begin{aligned} f_+(\mu_i, \mu_j, \mu_k) &= \left(\frac{\mu_i + \mu_j}{\mu_k}\right)^2 \left[ \frac{2x_k^2 + 5x_k - 1}{6(x_k - 1)^3} - \frac{x_k^2}{(x_k - 1)^4} \log x_k \right], \\ f_-(\mu_i, \mu_j, \mu_k) &= \frac{\mu_i + \mu_j}{\mu_k} \left[ -\frac{3x_k - 1}{(x_k - 1)^2} + \frac{2x_k^2}{(x_k - 1)^3} \log x_k \right]. \end{aligned} \quad (3.31)$$

Typically, only the functional form in  $f_-$  is cited, because  $(m_\mu + m_e)/m_\tau \ll 1$ . Unlike in case (2) for  $\tau \rightarrow \mu\gamma$ , this approximation is valid, and  $|f_+| \ll |f_-|$  for large  $m_\varphi$ . As discussed before, only  $f_+$  contributes for chiral interactions, so the contribution of a chiral scalar to  $\mu \xrightarrow{\tau} e\gamma$  is massively suppressed compared to the contribution of a pure scalar, as seen in the first panel of Fig. 3.3. This is also apparent (though to a lesser extent) for ALPs, as seen in Fig. 3.3.

The approximate functional forms for cases (1)-(3) are in agreement with those found in Refs. [46, 70, 71], but include additional terms that may be relevant depending on the PV nature of the interaction. Apart from these results for lepton mass hierarchies, we can also derive a general result when  $m_\varphi$  is large ( $\mu_i, \mu_j, \mu_k \ll 1$ ). Then, the form-factor function takes on the simplified form

$$f(\mu_i, \mu_j, \mu_k) = (\mu_i + \mu_j) \left( \frac{\mu_i + \mu_j}{3} - 3\mu_k - 4\mu_k \log \mu_k \right). \quad (3.32)$$

So in particular,  $f_+(\mu_i, \mu_j, \mu_k) \approx (\mu_i + \mu_j)^2$  and  $f_-(\mu_i, \mu_j, \mu_k) \approx -(\mu_i + \mu_j)(3\mu_k + 4\mu_k \log \mu_k)$ . This formula is only accurate when  $m_\varphi$  is very large, so is only relevant at the right-most end of the plots in Fig. 3.3.

Process	Constraints		Projections	
	Experiment	$\mathcal{B}$ limit (90% CL)	Experiment	$\mathcal{B}$ limit (90% CL)
$\mu \rightarrow e\gamma$	MEG, MEG II	$< 3.1 \times 10^{-13}$ [77]	MEG II	$\lesssim 6 \times 10^{-14}$ [78]
$\tau \rightarrow e\gamma$	BaBar	$< 3.3 \times 10^{-8}$ [79]	Belle II	$\lesssim 9 \times 10^{-9}$ [80]
$\tau \rightarrow \mu\gamma$	Belle	$< 4.2 \times 10^{-8}$ [81]	Belle II	$\lesssim 7 \times 10^{-9}$ [80]
$\mu \rightarrow ee\bar{e}$	SINDRUM	$< 1.0 \times 10^{-12}$ [82]	Mu3e	$\lesssim 2 \times 10^{-15}$ [83]
$\tau \rightarrow ee\bar{e}$	Belle	$< 2.7 \times 10^{-8}$ [84]	Belle II	$\lesssim 5 \times 10^{-10}$ [80]
$\tau \rightarrow ee\bar{\mu}$	Belle	$< 1.5 \times 10^{-8}$ [84]	Belle II	$\lesssim 3 \times 10^{-10}$ [80]
$\tau \rightarrow e\mu\bar{e}$	Belle	$< 1.8 \times 10^{-8}$ [84]	Belle II	$\lesssim 3 \times 10^{-10}$ [80]
$\tau \rightarrow \mu\mu\bar{\mu}$	Belle	$< 2.1 \times 10^{-8}$ [84]	Belle II	$\lesssim 4 \times 10^{-10}$ [80]
$\tau \rightarrow \mu e\bar{\mu}$	Belle	$< 2.7 \times 10^{-8}$ [84]	Belle II	$\lesssim 5 \times 10^{-10}$ [80]
$\tau \rightarrow \mu\mu\bar{e}$	Belle	$< 1.7 \times 10^{-8}$ [84]	Belle II	$\lesssim 3 \times 10^{-10}$ [80]

Table 3.1: Current experimental constraints and future prospects on the branching fractions for the decay modes  $\ell_i \rightarrow \ell_j \gamma$  and  $\ell_i \rightarrow \ell_j \ell_k \ell_l$  at the 90% confidence level.

### 3.3.3 Radiative Decay

Now, we are ready to place limits from LFV lepton decays, beginning with the radiative decay  $\ell_i \rightarrow \ell_j \gamma$ . The spin-averaged decay rate for  $\ell_i \rightarrow \ell_j \gamma$  is given by

$$\Gamma(\ell_i \rightarrow \ell_j \gamma) = \frac{\alpha_{\text{em}}}{2} \left( \frac{(m_i - m_j)^2}{m_i} \left| F_2^{ij}(0) \right|^2 + \frac{(m_i + m_j)^2}{m_i} \left| F_3^{ij}(0) \right|^2 \right). \quad (3.33)$$

These decay modes have been searched for extensively in particle physics experiments, as observation of such an event would be smoking-gun evidence of new physics. The Mu E Gamma (MEG) experiment, which ran from 2009 to 2013, constrained the branching fraction for  $\mu \rightarrow e\gamma$  by  $\mathcal{B}(\mu \rightarrow e\gamma) < 4.2 \times 10^{-13}$  at the 90% confidence level [76]. More recently, the first results from the upgrade, MEG II, have improved these results to  $\mathcal{B}(\mu \rightarrow e\gamma) < 3.1 \times 10^{-13}$  [77]. By the end of its run in 2026, MEG II expects to improve the sensitivity to  $\lesssim 6 \times 10^{-14}$  [78]. There have also been less stringent limits placed on the  $\tau \rightarrow \ell\gamma$  decays by the BaBar experiment at SLAC and the Belle experiment at KEK-B. The BaBar experiment achieved an upper limit on the  $\tau \rightarrow \ell\gamma$  branching fraction of  $\mathcal{B}(\tau \rightarrow e\gamma) < 3.3 \times 10^{-8}$  and  $\mathcal{B}(\tau \rightarrow \mu\gamma) < 4.4 \times 10^{-8}$  at the 90% confidence level [79]. More recently, the Belle experiment has reported upper limits at the 90% confidence level of  $\mathcal{B}(\tau \rightarrow e\gamma) < 5.6 \times 10^{-8}$  and  $\mathcal{B}(\tau \rightarrow \mu\gamma) < 4.2 \times 10^{-8}$  [81], slightly improving the  $\tau \rightarrow \mu\gamma$  result from BaBar. These results are expected to be superceded by Belle II, which aims to achieve

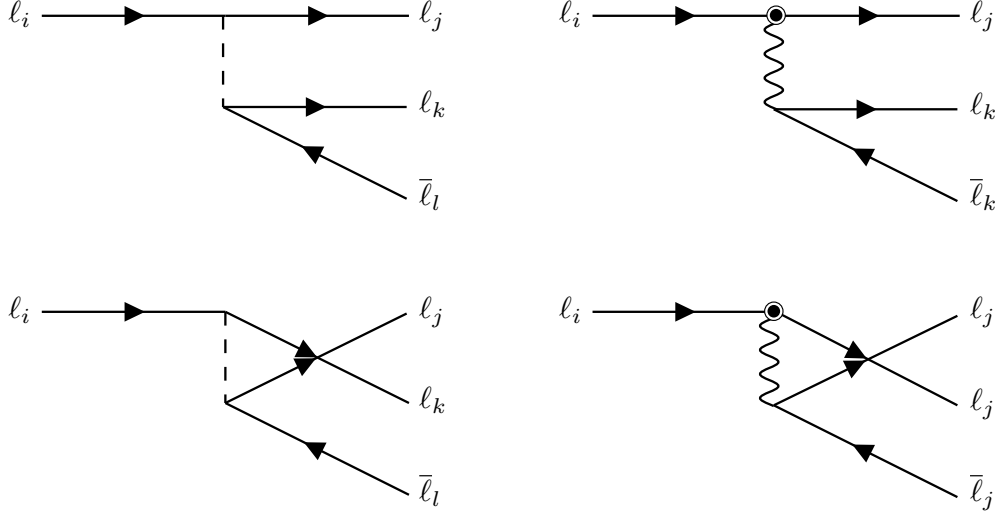


Figure 3.2: Feynman diagrams which contribute to the trilepton decay processes  $\ell_i \rightarrow \ell_j \ell_k \bar{\ell}_l$ . For light  $\varphi$ , the left-most diagrams dominate, whereas for heavy  $\varphi$  the left and right can be comparable in size.

a sensitivity of  $\mathcal{B}(\tau \rightarrow e\gamma) \lesssim 9 \times 10^{-9}$  and  $\mathcal{B}(\tau \rightarrow \mu\gamma) \lesssim 7 \times 10^{-9}$  by the year 2030 [85]. A summary of these radiative decay limits is shown in Table 3.3.3.

### 3.3.4 Trilepton Decay

Now, we turn to the trilepton decay modes  $\ell_i \rightarrow \ell_j \ell_k \bar{\ell}_l$ , depicted in Fig. 3.2. There are two main subprocesses: mediation via an off-shell  $\varphi$  ( $\ell_i \rightarrow \ell_j \varphi^* (\varphi^* \rightarrow \ell_k \bar{\ell}_k)$ ) and (for  $l = k$ ) via the transition lepton dipole moment and an off-shell photon ( $\ell_i \rightarrow \ell_j \gamma^* (\gamma^* \rightarrow \ell_k \bar{\ell}_k)$ ). We will not concern ourselves with interference between these diagrams. Rather than computing the dipole transition contribution directly, we estimate

$$\Gamma(\ell_i \rightarrow \ell_j \ell_k \bar{\ell}_k) \approx \frac{\alpha}{3\pi} \left( \log \frac{m_i^2}{m_k^2} - 3 + \frac{\delta_{jk}}{4} \right) \Gamma(\ell_i \rightarrow \ell_j \gamma) \quad (3.34)$$

in line with Refs. [71, 86] (ignoring contributions from the anapole form-factors). While this term is typically subdominant for scalars, it can be dominant depending on the relative strengths of the couplings. For ALPs, it is typically dominant when  $\ell_k = e$ , because the analogous contribution from an off-shell ALP involves an  $ee$  coupling which is suppressed to  $m_e^2/\Lambda^2$ . Given that the coefficient is suppressed by  $\alpha/3\pi$ , we expect that when this diagram is the main contribution to the trilepton

decay rate, the corresponding limits from  $\ell_i \rightarrow \ell_j \gamma$  are stronger.

Defining  $s_{ij} \equiv (p_i - p_j)^2 = 4p_k^2$  and  $s_{ik} \equiv (p_i - p_k)^2 = (p_j + p_k)^2$ , we find that the  $\ell_i \rightarrow \ell_j \ell_k \bar{\ell}_l$  amplitude is given by

$$\begin{aligned} \overline{|\mathcal{M}|^2} &= 2g_{ij}^2 g_{kl}^2 \frac{[m_{ij}^2(\theta_{ij}) - s_{ij}][s_{ij} - m_{kl}^2(\theta_{kl})]}{(m_\varphi^2 - s_{ij}^2)^2} \\ &\quad + 2g_{ik}^2 g_{jl}^2 \frac{[m_{ij}^2(\theta_{ik}) - s_{ik}][s_{ik} - m_{jl}^2(\theta_{jl})]}{(m_\varphi^2 - s_{ik}^2)^2} \\ &\quad + 4g_{ij}g_{kl}g_{ik}g_{jl} \frac{s_{ij}s_{ik}}{(m_\varphi^2 - s_{ij})(m_\varphi^2 - s_{ik})} \mathcal{S}_{ijkl} \end{aligned} \quad (3.35)$$

where  $m_{ij}^2(\theta) = m_i^2 + m_j^2 + 2m_i m_j \cos 2\theta_{ij}$  and we have defined

$$\begin{aligned} \mathcal{S}_{ijkl} &= \frac{1}{2} \text{Re}\{e^{i\Phi} U(\theta_{ij}, \delta_{ij}) \overline{U}(\theta_{jk}, \delta_{jk}) U^*(\theta_{ik}, \delta_{ik}) \overline{U}^*(\theta_{kl}, \delta_{kl}) \\ &\quad + e^{i\Phi} \overline{U}(\theta_{ij}, \delta_{ij}) U(\theta_{jk}, \delta_{jk}) \overline{U}^*(\theta_{ik}, \delta_{ik}) U^*(\theta_{kl}, \delta_{kl})\} \end{aligned} \quad (3.36)$$

with  $\Phi = \phi_{ij} - \phi_{ik} + \phi_{jl} - \phi_{kl}$  and

$$U(\theta, \delta) \equiv \cos \theta + ie^{i\delta} \sin \theta, \quad \overline{U}(\theta, \delta) \equiv \cos \theta - ie^{i\delta} \sin \theta. \quad (3.37)$$

We can see immediately that the size of the interference term is strongly dependent on both the PV and CPV nature of the  $\varphi$  couplings. In the event that all  $\theta_{ij} \equiv \theta$  and  $\delta_{ij} \equiv \delta$ , we have  $|\mathcal{M}|_{\text{int}}^2 \propto 1 - \sin^2 2\theta \sin^2 \delta$ . In particular, for chirally coupled particles ( $\theta = \pi/4$ ,  $\delta = \pi/2$ ), the interference term goes to zero. This is in contrast to the diagonal terms, which are only affected by the PV angle at  $\mathcal{O}(m_j/m_i)$  or  $\mathcal{O}(m_k/m_i)$ .

Ignoring the width of the  $\varphi$  and using  $m_j, m_k, m_l \ll m_i$ , we find that the decay rate is given by

$$\begin{aligned} \Gamma(\ell_i \rightarrow \ell_j \ell_k \bar{\ell}_l) &= \frac{1}{\sigma_{jk}} \frac{1}{32\pi^2} \int ds_{ij} ds_{ik} \Theta(s_{ik} - (m_k - m_l)^2) \Theta((m_i + m_j)^2 - s_{ik}) |\mathcal{M}|^2 \\ &\approx \frac{1}{\sigma_{jk}} \frac{m_i}{512\pi^3} [(g_{ij}^2 g_{kl}^2 + g_{ik}^2 g_{jl}^2) h_1(x_i) + 2g_{ij}g_{jl}g_{ik}g_{kl} \mathcal{S}_{ijkl} h_2(x_i)] \end{aligned} \quad (3.38)$$

where  $x_i = m_\varphi^2/m_i^2$ ,  $\sigma_{jk} = 1 + \delta_{jk}$  is a symmetry factor, and

$$h_1(x) = -5 + 6x - 2(1 - 4x + 3x^2) \log \frac{x}{x-1} \quad (3.39)$$

$$h_2(x) = 2 - 8x - \frac{2\pi^2}{3}x^2 + 8(x-1)x \log \frac{x}{x-1} + 4x^2 \log^2 \frac{x}{2x-1} + 8x^2 \text{Li}_2 \left( \frac{x}{2x-1} \right). \quad (3.40)$$

These functions are in agreement with those found in Ref. [71] for ALP-mediated processes. In particular,  $h_1(x) \approx h_2(x) \approx 1/12x^2$  for large  $x$ , so (assuming  $\mathcal{S}_{ijkl} = 1$ )

$$\Gamma(\ell_i \rightarrow \ell_j \ell_k \bar{\ell}_l) \approx \frac{1}{\sigma_{jk}} \frac{m_i^5}{6144\pi^3 m_\varphi^4} (g_{ij}g_{kl} + g_{ik}g_{jl})^2. \quad (3.41)$$

This is in agreement with Ref. [87], which studies such decays mediated by LFV neutral scalars. This expression is valid when the  $\varphi$  is heavy and its width can be ignored. For  $m_\varphi < m_i$ , the width becomes important. In this case, one can use the narrow width approximation

$$\Gamma(\ell_i \rightarrow \ell_j \ell_k \bar{\ell}_l) = \Gamma(\ell_i \rightarrow \ell_j \varphi) \mathcal{B}(\varphi \rightarrow \ell_k \bar{\ell}_l) + \Gamma(\ell_i \ell_k \varphi) \mathcal{B}(\varphi \rightarrow \ell_j \bar{\ell}_l) \quad (3.42)$$

with

$$\Gamma(\ell_i \rightarrow \ell_j \varphi) = g_{ij}^2 \frac{m_i}{16\pi} \left(1 - \frac{m_\varphi^2}{m_i^2}\right)^2 \quad (3.43)$$

and

$$\Gamma(\varphi \rightarrow \ell_i \bar{\ell}_j) = g_{ij}^2 \frac{m_\varphi}{8\pi} \left(1 - \frac{m_{ij}^2(\theta_{ij})}{m_\varphi^2}\right) \sqrt{\left(1 - \frac{(m_i + m_j)^2}{m_\varphi^2}\right) \left(1 - \frac{(m_i - m_j)^2}{m_\varphi^2}\right)}. \quad (3.44)$$

Like the radiative decays in the previous section, the branching fractions for these trilepton decay modes are highly constrained by modern particle physics experiments. The leading limit on  $\mu \rightarrow ee\bar{e}$  has remained the same since 1988, when the SINDRUM experiment found it to be  $\mathcal{B}(\mu \rightarrow ee\bar{e}) < 1.0 \times 10^{-12}$  at the 90% confidence level [82]. All of the leading limits on  $\mathcal{B}(\tau \rightarrow 3\ell)$  come from the Belle experiment, ranging from  $1.7 \times 10^{-8}$  to  $2.7 \times 10^{-8}$  at the 90% confidence level [84]. The Belle II experiment is expected to improve these bounds to between  $3 \times 10^{-10}$  and  $5 \times 10^{-10}$  by 2030. A summary of all the trilepton branching limits and projections is shown in Table 3.3.3.

### 3.3.5 Limits from LFV Decays

Now we present limits on the scalar and ALP interactions from Section 3.2.2. Each of these processes requires two distinct couplings to occur, so we place limits on the coupling products  $\sqrt{g_{ij}g_{kl}}$  and  $\sqrt{C_{ij}C_{kl}}/\Lambda$  under the assumption that all couplings which don't enter the product are zero. A summary of the relevant coupling products for each LFV decay mode is shown in Table 3.2.

Process	$g_{ee}g_{e\mu}$	$g_{\mu\mu}g_{e\mu}$	$g_{\tau\tau}g_{e\mu}$	$g_{e\tau}g_{\mu\tau}$	$g_{ee}g_{e\tau}$	$g_{\mu\mu}g_{e\tau}$	$g_{\tau\tau}g_{e\tau}$	$g_{e\mu}g_{\mu\tau}$	$g_{ee}g_{\mu\tau}$	$g_{\mu\mu}g_{\mu\tau}$	$g_{\tau\tau}g_{\mu\tau}$	$g_{e\mu}g_{\tau}$
$\mu \rightarrow e\gamma$	✓	✓	!	✓	✗	✗	✗	✗	✗	✗	✗	✗
$\mu \rightarrow ee\bar{e}$	✓	✓	!	✓	✗	✗	✗	✗	✗	✗	✗	✗
$\tau \rightarrow e\gamma$	✗	✗	✗	✗	✓	!	✓	✓	✗	✗	✗	✗
$\tau \rightarrow ee\bar{e}$	✗	✗	✗	✗	✓	!	✓	✓	✗	✗	✗	✗
$\tau \rightarrow e\mu\bar{\mu}$	✗	✗	✗	✗	✓	✓	✓	✓	✗	✗	✗	✗
$\tau \rightarrow \mu\gamma$	✗	✗	✗	✗	✗	✗	✗	✗	!	✓	✓	✓
$\tau \rightarrow \mu e\bar{e}$	✗	✗	✗	✗	✗	✗	✗	✗	✓	✓	✓	✓
$\tau \rightarrow \mu\mu\bar{\mu}$	✗	✗	✗	✗	✗	✗	✗	✗	!	✓	✓	✓
$\tau \rightarrow ee\bar{\mu}$	✗	✗	✗	✗	✗	✗	✗	✗	✗	✗	✗	✓
$\tau \rightarrow \mu\mu\bar{e}$	✗	✗	✗	✗	✗	✗	✗	✓	✗	✗	✗	✗

Table 3.2: A table demonstrating which coupling products contribute to each process. A green check-mark (✓) indicates the product  $g_{ijkl}$  contributes to the process, whereas a red X-mark (✗) indicates it does not. Orange exclamation marks (!) indicate that the process is only sensitive to leptophilic ALPs (per the induced photon coupling), not leptophilic scalars. Light green checkmarks (✓) and light orange exclamation marks (!) for the trilepton decay modes  $\ell_i \rightarrow \ell_j \ell_k \bar{\ell}_k$  indicate that the process only occurs due to the corresponding dipole transition  $\ell_i \rightarrow \ell_j \gamma$ , and so the branching for these processes through these couplings is suppressed compared to the  $\ell_i \rightarrow \ell_j \gamma$  process.

While generic scalar and ALP models will typically have more than two non-zero couplings, limits of this form illustrate which couplings are the most sensitive to each processes, and limits on models with more complicated hierarchies can in-principle be derived from these limits.

We begin with limits on pure scalars (solid lines) and chiral scalars (dashed lines) in the top of Fig. 3.3. Darker shades represent limits from the radiative decay modes, whereas lighter shades represent limits from the trilepton decay modes. We find that while the trilepton decay limits are largely unaffected by the presence of chiral couplings, the radiative decay limits on chiral scalars are substantially suppressed compared to the limits on pure scalars. The effect is most drastic for the  $\mu \xrightarrow{\tau} e\gamma$  decay mode, for which  $\sqrt{g_{\mu\tau}g_{e\tau}}$  is reduced by an order of magnitude for the chiral scalar. This corresponds to a factor of  $10^4$  in the decay rate.

The corresponding limits for LFV ALPs are shown in the bottom of Fig. 3.3. For those limits on the product  $\sqrt{C_{ii}C_{ij}}/\Lambda$ , the photonic contribution is also included. As opposed to the

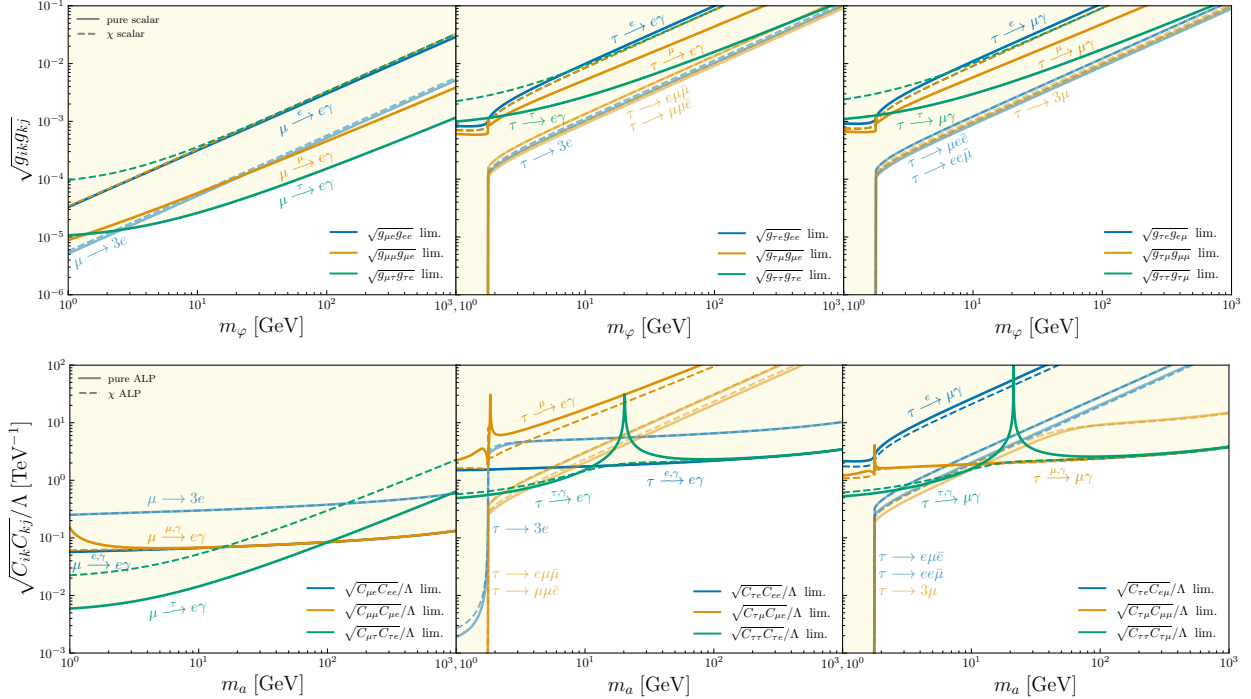


Figure 3.3: (Top) Limits (90% CL) on the relevant LFV and LFC scalar couplings for the LFV decays  $\ell_i \rightarrow \ell_j \gamma$  and  $\ell_i \rightarrow \ell_j \ell_k \bar{\ell}_l$ , assuming the interaction Lagrangian in Eq. 3.12. (Bottom) The same limits on the corresponding LFV and LFC ALP couplings in the interaction Lagrangian in Eq. 3.13, with  $\Lambda = 10$  TeV (apart from the photonic contribution to the diagonal ALP vertex, the limits are unaffected by changes in  $\Lambda$ ). The limits for pure (parity-conserving) particles are represented as solid lines, whereas the limits for chiral particles are dashed lines.

complex scalar, most of the contributions to the ALP decay modes are largely independent of the chiral nature of the ALP, with the only exception being the  $\mu \xrightarrow{\tau} e\gamma$  decay mode. That said, this is by far (all couplings equal) the most dominant contribution to the  $\mu \rightarrow e\gamma$  decay rate, due in part to the mass-dependence of the ALP coupling. Hence, this effect can be important in limits on LFV ALPs from the  $\mu \rightarrow e\gamma$  decay. While the effect is not as drastic, we still see a factor of  $\sim 4$  difference in the limits in Fig. 3.3, corresponding to a factor of  $\sim 250$  in the  $\mu \rightarrow e\gamma$  decay rate.

Before ending this section, we reiterate that each of the limits presented in Fig. 3.3 is on a product of two couplings. As a result, it is impossible to pin down constraints on any single flavor-violating (or flavor-conserving) coupling without fixing another. One can make some progress by appealing to naturalness or the minimal flavor-violating hypothesis [88] in order to relate the size

of the couplings, but this is not a fully general treatment. In particular, it is possible to construct symmetry-protected LFV interactions that completely evade the bounds in Figs. 3.3. For a concrete example, consider a  $U(1)_{L_i-L_j}$  extension to the SM, along with a complex scalar field  $\varphi$  of  $L_i - L_j$  charge +2. This particle has a singular non-zero coupling to the leptons,  $g_{ij}$ , and hence is not constrained at all by Fig. 3.3.<sup>8</sup> Such a particle exists in the scalar spectrum in Ref. [89] for  $U(1)_{L_\mu-L_\tau}$ . One can also consider particles with charge +1 under the  $U(1)_{L_i-L_j}$ , which have only two off-diagonal couplings and no diagonal-couplings, such as the  $\phi$  in Ref. [60]. Something similar can also happen for an ALP which only couples to the lepton vector current instead of the axial-vector current (i.e.  $C_L = C_R$  in Eq. 3.9); then, the on-diagonal couplings are zero, which removes most of the constraints in Fig. 3.3.

This leads us naturally into the next section: while singular couplings cannot be directly probed with the radiative and trilepton decay modes, they *can* be individually probed with the leptonic dipole moments (at least up to fine-tuned deconstructive interference between diagrams). For generic CP-violating couplings, the most stringent constraints come from the electron electric dipole moment. However, the contribution to the electric dipole moment from the models we consider vanish in the pure (pseudo)-scalar and chiral scenarios. These models can be probed complementarily by the lepton magnetic dipole moments, and can even be used to explain the electron and muon  $g - 2$  anomalies.

### 3.4 LFV Contributions to Lepton Electric and Magnetic Dipole Moments

The lepton electric and magnetic dipole moments are perhaps the most heavily scrutinized observables in modern particle physics. Whereas observables involving hadrons are rife with systematic error due to the non-perturbative nature of the strong interaction, leptons provide a clean environment which allows for very precise determination of their properties.

---

<sup>8</sup> This is partly due to the fact that the  $\varphi$  preserves the flavor symmetry by carrying its own  $e - \tau$  charge. In the event that the  $U(1)_{L_e-L_\tau}$  symmetry is spontaneously broken, the resulting physical scalars of the theory will couple predominantly to  $e\tau$ , with only minor couplings to the other lepton currents.

### 3.4.1 Electric Dipole Moments

While the electric dipole moment (EDM) of the electron has never been measured directly, it is constrained to a very high degree. The most stringent limit on the electron EDM comes from the University of Colorado, with  $|d_e| < 4.1 \times 10^{-30} \text{ e cm}$  at the 90% confidence level [90]. This is still some five orders of magnitude above the SM prediction of  $|d_e| \approx 10^{-35} \text{ e cm}$  [91],<sup>9</sup> but can nonetheless provide strong bounds on new CP-violating physics in the charged lepton sector [93, 94]. The muon and tau EDMs have also been indirectly constrained from their loop-level contributions to heavy atom EDMs, with  $|d_\mu| < 1.9 \times 10^{-20} \text{ e cm}$  and  $|d_\tau| < 1.6 \times 10^{-18} \text{ e cm}$  [95]. The corresponding SM predictions of  $|d_\mu| = 10^{-42} \text{ e cm}$  [95] and  $|d_\tau| \approx 3 \times 10^{-37} \text{ e cm}$  [96], far below the current experimental reach. While these constraints can also be used to limit CP-violating new physics, the resulting bounds are not very strong, so we will focus mainly on the electron EDM.

### 3.4.2 Magnetic Dipole Moments

The magnetic dipole moment (MDM) of the leptons (and in particular, the electron) have a special place in the history of quantum field theory. The MDM of a particle with charge  $q$ , mass  $m$ , and spin  $S$  can generically be parametrized by  $\mu = g \frac{q}{4m} S$ , with non-relativistic quantum theory predicting  $g = 2$  exactly for spin-1/2 particles. However, higher order corrections are expected from relativistic effects, which can be encoded in the *anomalous* magnetic moment, defined as the deviation of the  $g$ -factor from 2,  $a \equiv (g - 2)/2$ . In the 1940s, Tomonaga, Schwinger and Feynman independently used their theories of perturbative quantum electrodynamics at the time to calculate the electron anomalous magnetic moment  $a_e$  to lowest order in the fine structure constant, each finding  $a_e \approx \alpha/2\pi$  [97–99]. This was the first quantitative prediction of quantum electrodynamics, and it won Feynman, Schwinger, and Tomonaga the Nobel Prize in 1965 [100].

Now, the electron anomalous magnetic moment is the most precisely calculated and measured

---

<sup>9</sup> Technically, the experimental bound in Ref. [90] and the corresponding SM prediction [91] is of the quantity  $d_e^{\text{equiv}} = d_e^{\text{free}} + rC_S$ , where  $d_e^{\text{free}} \sim 6 \times 10^{-40} \text{ e cm}$  is the EDM of a free electron[92],  $C_S$  is the coefficient of an effective semileptonic electron-nucleon coupling, and  $r$  is a constant which depends on the molecule used to compute the electric dipole moment, with  $r \approx 1.5 \times 10^{-20} \text{ e cm}$  for a thorium monoxide molecule.

observable in physics. The theoretical prediction is so precise that its value is currently dependent on whether one uses the experimental value for the fine structure constant measured from Cesium (Cs) [101] or Rubidium (Rb) [102] atomic recoils, which deviate from each other at only one part per billion. If one uses the value of  $\alpha(\text{Cs})$ , the theoretical prediction is [101]

$$a_e^{\text{th.}}(\text{Cs}) = 1159652181.61(23) \times 10^{-12}, \quad (3.45)$$

whereas for  $\alpha(\text{Rb})$ , [102]

$$a_e^{\text{th.}}(\text{Rb}) = 1159652180.252(95) \times 10^{-12}. \quad (3.46)$$

Intriguingly, each of these is in modest disagreement with the current leading experimental value, in opposing directions. The leading experimental determination for  $a_e$  is [103]

$$a_e^{\text{exp.}} = 1159652180.59(13) \times 10^{-12} \quad (3.47)$$

corresponding to the anomalies

$$\Delta a_e(\text{Cs}) = (-101 \pm 27) \times 10^{-14}, \quad \Delta a_e(\text{Rb}) = (34 \pm 16) \times 10^{-14}. \quad (3.48)$$

In particular, there is a  $-3.7\sigma$  anomaly in  $\Delta a_e(\text{Cs})$  and a milder  $+2.1\sigma$  anomaly in  $\Delta a_e(\text{Rb})$ .

While the muon anomalous magnetic moment is not measured as precisely as that of the electron, it has been the subject of immense scrutiny since the E821 Experiment at Brookhaven National Lab reported a  $2.6\sigma$  deviation between their measurement of  $a_\mu$  and the SM value at the time [104]. This discrepancy has stood the test of time, through the completed analysis of E821 [105] and the continuation of the experiment at Fermilab. As of 2021, the data analysis from Run 1 of the Fermilab  $g - 2$  experiment confirmed the Brookhaven result, finding a combined value of [106]

$$a_\mu^{\text{exp.}} = 1165920.61(41) \times 10^{-9} \quad (3.49)$$

Concurrently, the Muon  $g - 2$  Theory Initiative has reported an SM value of [107]

$$a_\mu^{\text{th.}} = 1165918.10(43) \times 10^{-9}. \quad (3.50)$$

thus confirming the anomaly with

$$\Delta a_\mu = 2.51(60) \times 10^{-9}, \quad (3.51)$$

corresponding to a  $4.2\sigma$  deviation.

The apparent anomalies in the muon and (to a lesser extent) electron anomalous magnetic moments are exciting indications of potential contributions from physics beyond the SM. However, it is important to temper our expectations. The disagreements for the electron  $g - 2$  anomaly are mild, and may disappear with more experimental data. While the muon anomaly is less likely to be a statistical fluke (1 in  $10^5$ ), there is increasing evidence to suggest that the experimental result agrees with lattice calculations of the hadronic-vacuum-polarization (HVP) contribution to the muon  $g - 2$  [108–111], indicating that the disagreement may lie within the data-driven approach used to determine the HVP. Recently, data analysis for Runs 2 and 3 of the Fermilab  $g - 2$  experiment was completed, confirming the experimental result with slightly more precision [112], but they defer direct comparison with theory until the HVP discrepancy is resolved. Time will tell whether the tension between these experiments and the theoretical results remain; if they disappear, the electric and magnetic dipole moments can still be used to place constraints on new physics.

The lepton EDMs and MDMs are sensitive to any new physics involving leptons, the LFV scalars and ALPs in this chapter being no exception. These observables receive independent contributions from each non-zero coupling  $g_{\ell\ell'}$ , and hence can be used to probe individual couplings in isolation. To examine this effect, we begin by computing the contribution of LFV scalars and ALPs to the relevant dipole form-factors.

### 3.4.3 Relevant Form Factors

The most general gauge-invariant decomposition of the electromagnetic ( $\ell_i \rightarrow \ell_i$  flavor-conserving) current into real, dimensionless form-factors is [72]

$$\bar{u}_i(q_2)\Gamma_\mu^i u_i(q_1) = e\bar{u}_i(q_2) \left[ F_1^i(q^2)\gamma^\mu + \frac{i\sigma^{\mu\nu}}{2m_i}q_\nu F_2^i(q^2) + \frac{\sigma^{\mu\nu}}{2m_i}q_\nu\gamma_5 F_3^i(q^2) \right. \\ \left. + \frac{1}{2m_i} \left( q^\mu - \frac{q^2}{2m_i}\gamma^\mu \right) \gamma_5 F_4^i(q^2) \right] u_i(q_1). \quad (3.52)$$

Here,  $F_1^i(q^2)$  is the electromagnetic charge,  $F_2^i(q^2)$  is related to the magnetic dipole moment (MDM) form-factor,  $F_3^i(q^2)$  is the electric dipole moment (EDM) form-factor, and  $F_4^i(q^2)$  is the anapole form-factor. In particular, we have the freedom to define  $F_1^i(0) = 1$  so that the electromagnetic charge is  $e$ . The benefit of decomposing the electromagnetic current in this form is that each of the form-factors  $F^i$  is real-valued.<sup>10</sup> The MDM form-factor is related to the MDM via

$$\mu_i \equiv g_i \frac{e}{4m_i} = \frac{e}{2m_i} (1 + F_2^i(0)). \quad (3.53)$$

The anomalous magnetic moment is then defined as  $a_i \equiv (g_i - 2)/2 = F_2^i(0)$ . The EDM form-factor is related to the EDM via

$$d_i = -\frac{e}{2m_i} F_3^i(0). \quad (3.54)$$

With this in mind, we can compute the dipole moment form-factors for an LFV scalar and ALP with interactions governed by Eqs. 3.12 and 3.13. This amounts to calculating the amplitude for the Feynman diagram on the left of Fig. 3.1. Using a similar decomposition as in Eqs. 3.20, we find using PackageX in Mathematica [73] that the contribution to the dipole form factors are given by

$$F_2^{ij}(0) = \frac{g_{ij}^2}{32\pi^2} [g_+(\mu_i, \mu_j) + g_-(\mu_i, \mu_j) \cos 2\theta_{ij}] \quad (3.55)$$

and

$$F_3^{ij}(0) = -\frac{g_{ij}^2}{32\pi^2} g_-(\mu_i, \mu_j) \sin 2\theta_{ij} \cos \delta_{ij}. \quad (3.56)$$

---

<sup>10</sup> For  $m_\varphi + m_j < m_i$ , the form-factors have an imaginary part which reflects the fact that the particle  $m_\varphi$  and the internal fermion  $\ell_j$  can go on-mass-shell. These imaginary parts do not contribute to the dipole moments, but instead encode the probability that the parent lepton may decay via  $\ell_i \rightarrow \ell_j \varphi$ .

The functions  $g_{\pm}$  are given by

$$g_+(x, y) = \frac{2y}{x^2} \left[ 1 + \frac{1+x^2-y^2}{x^2} \log y + \frac{(1+x^2-y^2)^2 - 2x^2}{\sqrt{(1+x^2-y^2)^2 - 4x^2}} \operatorname{arccosh} \left( \frac{1-x^2+y^2}{2y} \right) \right] \quad (3.57)$$

and

$$\begin{aligned} g_-(x, y) = & -\frac{1}{x^3} \left[ 2 + x^2 - 2y^2 + \frac{2(1-y^2)^2 - 2x^2y^2}{x^2} \log y \right. \\ & \left. - \frac{2[x^4 - (1-y^2)((1+x^2-y^2)^2 - 3x^2)]}{\sqrt{(1+x^2-y^2)^2 - 4x^2}} \operatorname{arccosh} \left( \frac{1-x^2+y^2}{2y} \right) \right]. \end{aligned} \quad (3.58)$$

These can be computed directly from the transition dipole form-factors in Eqs. 3.17-3.18 by performing the limit  $m_j \rightarrow m_i$  and replacing  $m_k$  with  $m_j$ . In particular, we can identify

$$g_+(x, y) = \lim_{z \rightarrow x} f_+(x, z, y) \quad (3.59)$$

$$g_-(x, y) = \lim_{z \rightarrow x} f_-(x, z, y). \quad (3.60)$$

While this identification is clear for the functional form of  $F_2^{ij}(0)$ , it is less apparent why  $F_3^{ij}(0)$  should depend on only  $g_-(x, y)$ . Based on the form of Eq. 3.18, one would expect the functions  $g'_+$  and  $g'_-$  to appear in  $F_3^{ij}$ , where

$$g'_+(x, y) = \lim_{z \rightarrow x} \frac{x+z}{x-z} f_+(x, -z, y) \quad (3.61)$$

$$g'_-(x, y) = \lim_{z \rightarrow x} \frac{x+z}{x-z} f_-(x, -z, y). \quad (3.62)$$

Explicit evaluation of the limits reveals  $g'_+(x, y) = 0$  and  $g'_-(x, y) = g_-(x, y)$ , confirming Eq. 3.56.

Similar to the transition dipole form-factors, one can expect substantial differences between the contributions of chiral and pure scalars to  $F_2^{ij}(0)$  when  $|g_+(\mu_i, \mu_j)| \ll |g_-(\mu_i, \mu_j)|$ , and at least marginal differences when  $|g_+(\mu_i, \mu_j)| \sim |g_-(\mu_i, \mu_j)|$ . The EDM form-factor  $F_3^{ij}(0)$ , on the other hand, is zero for pure and chiral scalars and ALPs, and more generally whenever  $\delta_{ij} = \pi/2$  (regardless of  $\theta_{ij}$ ).

When considering ALPs, we can use Eqs. 2.30 to re-express the form-factors in terms of the

ALP parameters. We have

$$\begin{aligned} F_2^{ij}(0) &= \frac{C_{ij}^2}{32\pi^2\Lambda^2} \left[ (m_i^2 + m_j^2 + 2m_i m_j \cos 2\Theta_{ij}) g_+(\mu_i, \mu_j) \right. \\ &\quad \left. - (2m_i m_j + (m_i^2 + m_j^2) \cos 2\Theta_{ij}) g_-(\mu_i, \mu_j) \right] \end{aligned} \quad (3.63)$$

$$F_3^{ij}(0) = \frac{C_{ij}^2}{32\pi^2\Lambda^2} (m_i^2 - m_j^2) g_-(\mu_i, \mu_j) \sin 2\Theta_{ij} \sin \Delta_{ij}. \quad (3.64)$$

There is an additional contribution to the magnetic dipole form-factor in the case of an ALP from the chiral anomaly. This contribution is [71]

$$F_2^{i\gamma}(0) = -\frac{\alpha A_{ii} \sum_\ell A_{\ell\ell}}{2\pi^3} \frac{m_i^2}{\Lambda^2} \left[ \log \frac{\Lambda^2}{m_i^2} - 1 - \frac{x_i^2}{6} \log x_i + \frac{x_i}{3} + \frac{x_i+2}{3} \sqrt{x_i^2 - 4x_i} \operatorname{arccosh} \frac{\sqrt{x_i}}{2} \right]. \quad (3.65)$$

There is no additional contribution to the electric dipole form-factor.

### 3.4.4 Approximations

Like in the flavor-changing current case, we can examine various limits of the form-factor functions  $g_\pm$ . We will examine each of the cases  $m_i \ll m_j$ ,  $m_i = m_j$ , and  $m_i \gg m_j$ .

(1)  $i = j$

This scenario is relevant for all the lepton dipole moments, given that the LFV particle has a flavor-conserving interaction. Unlike the  $i = k > j$  case in the previous section, these results are exact, as there is no lepton mass ratio to expand around.

$$\begin{aligned} g_+(\mu_i, \mu_j) &= 2 - 4x_i + 2x_i(x_i - 2) \log x_i - 4(x_i^2 - 4x_i + 2) \sqrt{\frac{x_i}{x_i - 4}} \log \left( \frac{x_i + \sqrt{x_i(x_i - 4)}}{2\sqrt{x_i}} \right) \\ g_-(\mu_i, \mu_j) &= 4 - 2x_i \log x_i + 4(x_i - 2) \sqrt{\frac{x_i}{x_i - 4}} \log \left( \frac{x_i + \sqrt{x_i(x_i - 4)}}{2\sqrt{x_i}} \right) \end{aligned} \quad (3.66)$$

For ALPs, it is necessarily the case that  $\theta_{ii} = \pi/2$ , so only the function  $g_-(\mu_i, \mu_j)$  contributes. Hence, there should not be any difference between a pure ALP or chiral ALP. However, there can be significant differences between the pure and chiral scalar contributions to the  $i = j$  MDM form-factor.

(2)  $i < j$

This scenario is relevant for the electron dipole moments with an internal  $\mu$  or  $\tau$ , and the muon dipole moments with an internal  $\tau$ . We have

$$\begin{aligned} g_+(\mu_i, \mu_j) &= \frac{2\mu_i^2}{\mu_j^2} \left[ \frac{2x_j^2 + 5x_j - 1}{3(x_j - 1)^3} - \frac{2x_j^2}{(x_j - 1)^4} \log x_j \right] \\ g_-(\mu_i, \mu_j) &= \frac{2\mu_i}{\mu_j} \left[ \frac{1 - 3x_j}{(x_j - 1)^2} + \frac{2x_j^2}{(x_j - 1)^3} \log x_j \right]. \end{aligned} \quad (3.67)$$

Since  $\mu_i \ll \mu_j$ , the term involving  $g_+$  is often neglected, but this can not be done for particles with a chiral interaction. Hence, we can expect significant differences between the contribution from pure and chiral scalars *and* ALPs.

(3)  $i > j$

This scenario is relevant for the muon dipole moment contributions with an internal  $e$ , and the tau dipole moments with an internal  $\mu$  or  $e$ . We have

$$\begin{aligned} g_+(\mu_i, \mu_j) &= -2 - 4x_i + 4x_i^2 \log \frac{x_i}{x_i - 1} \\ g_-(\mu_i, \mu_j) &= \frac{4\mu_j}{\mu_i} \left[ 1 - \frac{x_i^2 + 1}{x_i - 1} \log \left( \frac{x_i}{x_i - 1} \right) + \frac{1}{x_i - 1} \log x_j \right]. \end{aligned} \quad (3.68)$$

Since  $\mu_j \ll \mu_i$ , the second term is typically neglected. As opposed to case (2), this is a valid approximation for all PV angles  $\theta_{ij}$ , so we shouldn't expect any major differences between the pure and chiral scenarios.

### 3.4.5 Electric dipole moment constraints

Limits on LFV scalars from the electron EDM constraint are shown in Fig. 3.4. Notably, these bounds far exceed the bounds obtained in Fig. 3.3, and are able to constrain a singular coupling  $g_{e\ell}$  rather than a product. However, they are only present when there is a significant amount of CP violation in the interaction (when  $\sin 2\theta_{e\ell} \cos \delta_{e\ell} \sim \mathcal{O}(1)$ ), and hence do not apply to pure *or* chirally-coupled particles. Similar bounds can be found for the  $\mu$  and  $\tau$  EDMs, but these are much less constrained by experiment, so the bounds are not competitive.

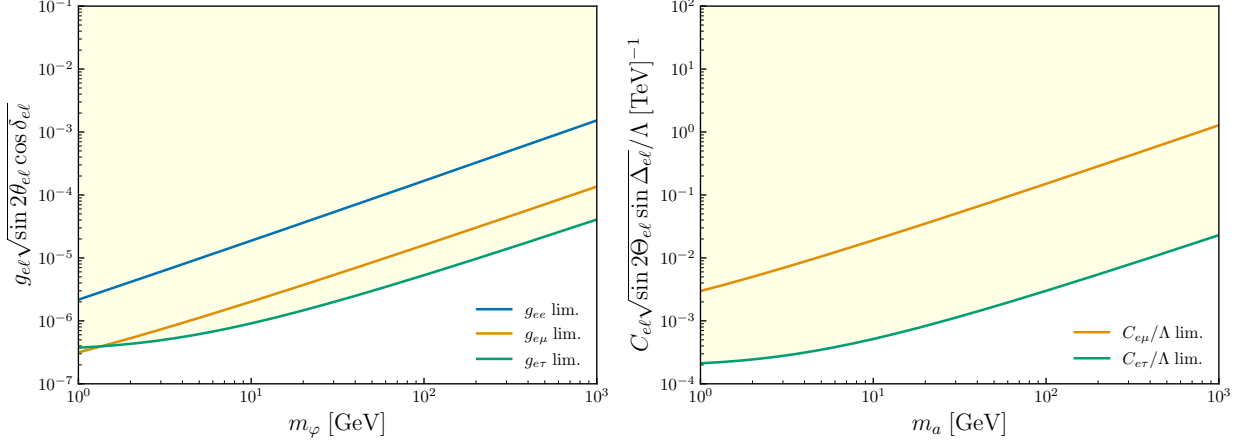


Figure 3.4: Limits on leptonic couplings for scalar (left) and ALP (right) from experimental constraints on the electron EDM. For the ALP, only the off-diagonal couplings are probed. For both pure and chiral particles, the bounds derived from the electron EDM vanish.

### 3.4.6 Magnetic dipole moment constraints

For decades, the muon  $g - 2$  anomaly has captured the minds of particle physicists as a tantalizing hint at new physics, and more recently, the ( $\alpha$ -dependent) electron  $g - 2$  anomalies have also garnered considerable interest. However, recent studies indicate that the muon  $g - 2$  experiment may agree more closely with the theoretical result when using a lattice determination of the HVP [108–111], and the electron anomalies could very well be statistical flukes. In this section we will consider the less exciting scenario that these anomalies are resolved, or at the very least, that the new physics under consideration does not contribute to  $a_e$  or  $a_\mu$  at experimental levels. We will defer potential explanations of the  $e$  and  $\mu$  anomalies, in the event that they persist, to next section.

To produce the limits, we assume an upper limit on the new physics contribution to the anomalous magnetic moment is  $|\Delta a_\ell| < 2\sigma_\ell^{\text{exp}}$ , where  $\sigma_\ell^{\text{exp}}$  is the error in the experimental determination of  $a_\ell$ . For the electron  $g - 2$ , we take the experimental error to be  $\sigma_e^{\text{exp.}} = 13 \times 10^{-14}$  [103]. For the muon  $g - 2$ , we use the combined experimental error from the Brookhaven results and Run 1 of the Fermilab results,  $\sigma_\mu^{\text{exp.}} = 40 \times 10^{-11}$  [106]. We compute limits on a single coupling  $g_{e\ell}$  (from  $\Delta a_e$ ) or  $g_{\mu\ell}$  (from  $\Delta a_\mu$ ) under the assumption that all other couplings are zero. We compute

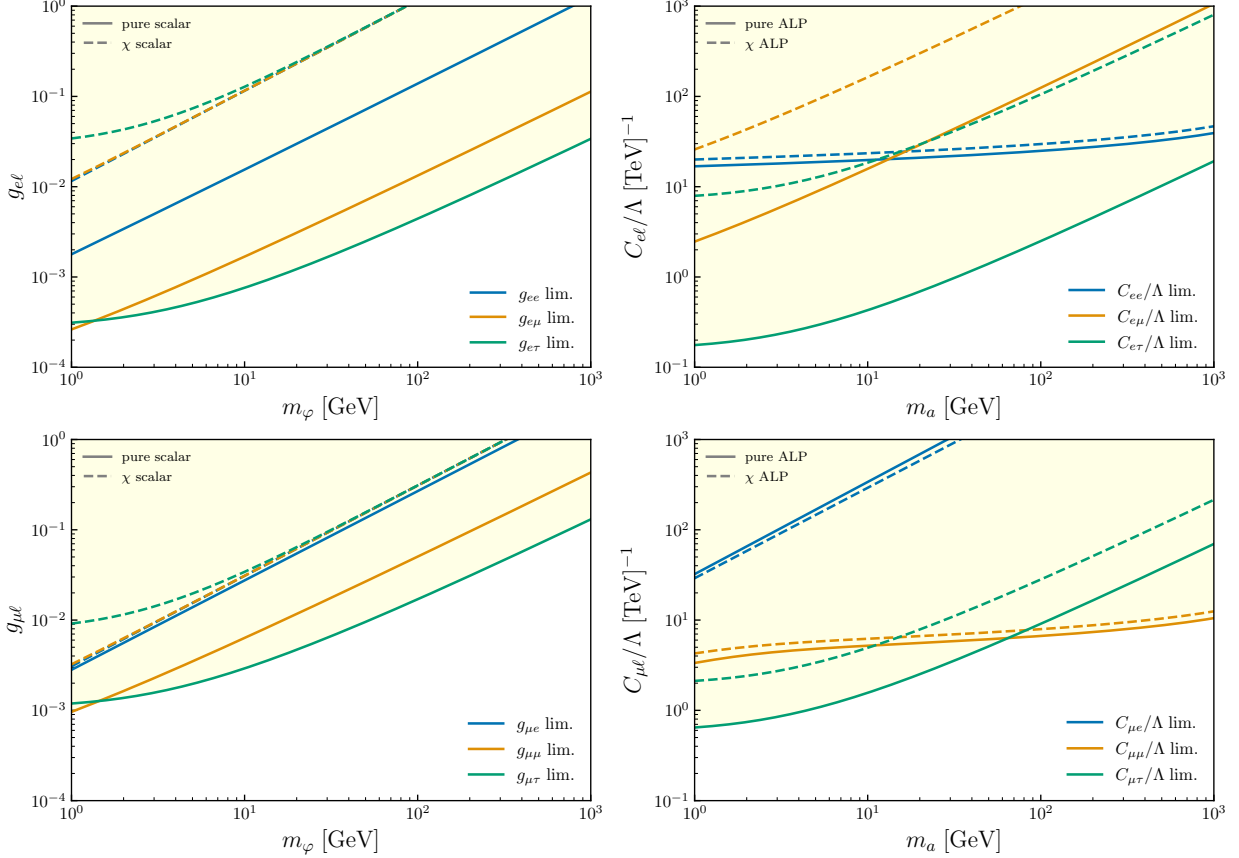


Figure 3.5: Limits on scalar (left) and ALP ( $\Lambda = 10$  TeV, right) contributions to the anomalous magnetic moment of the electron (top) and muon (bottom), assuming the contributions lie within two standard deviations of the current experimental results. Pure scalars and ALPs are represented as solid lines, and chiral scalars and ALPs are represented as dashed lines. The limits are generated assuming  $g_{\ell\ell'}$  is the only coupling present.

contributions from both scalars and ALPs, and compare the pure and chiral scenarios. The results are shown in Fig. 3.5, with pure scalar and ALP limits represented with solid lines and chiral scalar and ALP limits represented with dashed lines.

Once again, we see a pronounced decrease in the contributions to the dipole moments for chiral scalars when compared to pure scalars. The largest of these differences is in the contribution of the scalars to  $\Delta a_{e\tau}$ , with a two order of magnitude suppression in the bound for  $g_{e\tau}$ . There are also substantial differences between chiral and pure scalars for the  $g_{\mu\tau}$  bound, and the  $g_{e\mu}$  bound from  $\Delta a_e$  (but not  $\Delta a_\mu$ ), which is in line with the notion that for the  $i < j$  scenario (case (2)),

there is an anticipated  $m_i/m_j$  suppression in the form-factor for chiral particles.

We also see that more of the ALP channels are sensitive to a difference between pure and chiral couplings than for the LFV lepton decay limits obtained in Fig. 3.3 (for which only the  $\mu \xrightarrow{\tau} e\gamma$  mode was affected). In particular, the  $\Delta a_{e\tau}$  channel is the most affected, with the bound on  $C_{e\tau}$  decreasing by a factor of  $\sim 50$  for chiral ALPs. The bounds on  $C_{e\mu}$  from  $a_e$  and  $C_{\mu\tau}$  are also suppressed for chiral ALPs, albeit to a lesser degree. The on-diagonal contributions  $\Delta a_{\ell\ell}$  are unaffected, which is in line with our expectation for ALPs, since (as mentioned previously) any ALP coupling to the vector current is illusory.

These bounds are considerably weaker than those obtained through radiative decays in Fig. 3.3, but they allow us to isolate a single coupling (ignoring interference with other diagrams of a similar magnitude). They also indicate that the interactions of chiral particles are often less constrained than their parity-conserving counterparts, especially for LFV couplings. Concretely, we can consider the limit on  $g_{\tau e}$  in Fig. 3.5 in conjunction with the limit on  $\sqrt{g_{\tau e} g_{ee}}$  from Fig. 3.3 for  $m_\varphi = 10$  GeV. For pure scalars,  $g_{\tau e} \lesssim 10^{-3}$  from Fig. 3.5 and  $\sqrt{g_{ee} g_{\tau e}} \lesssim 10^{-3}$  from Fig. 3.3, so we can parametrize the combined constraints as  $g_{\tau e} \lesssim 10^{-3}\epsilon$  and  $g_{ee} \lesssim 10^{-3}/\epsilon$  with  $\epsilon < 1$ . In contrast, the limits for chiral scalars entail  $g_{\tau e} \lesssim 10^{-1}\epsilon$  and  $g_{ee} \lesssim 10^{-5}/\epsilon$  for  $\epsilon < 1$ , allowing for a considerably larger off-diagonal chiral coupling  $g_{\tau e}$ . While this scenario may seem exotic, a VEV-less Higgs doublet  $\varphi$  with charge +2 under  $U(1)_{L_e - L_\tau}$  would have this property; such a particle is very unconstrained in spite of its strongly LFV coupling. More generally, any particle with a single off-diagonal coupling  $g_{ij}\varphi\bar{\ell}_i[\cos\theta_{ij} + \gamma_5 \sin\theta_{ij}]\ell_j$  is perturbatively protected by a  $\mathbb{Z}_4$  symmetry with, e.g.,  $Q(\varphi) = -1$ ,  $Q(\ell_i) = i$  and  $Q(\ell_j) = -i$ . Such particles, if perverse, represent a region of the LFV scalar parameter space that is largely unconstrained by current experiments, especially when the interaction is chiral. In the next section, we will consider such particles in the context of the electron and muon  $g - 2$  anomalies.

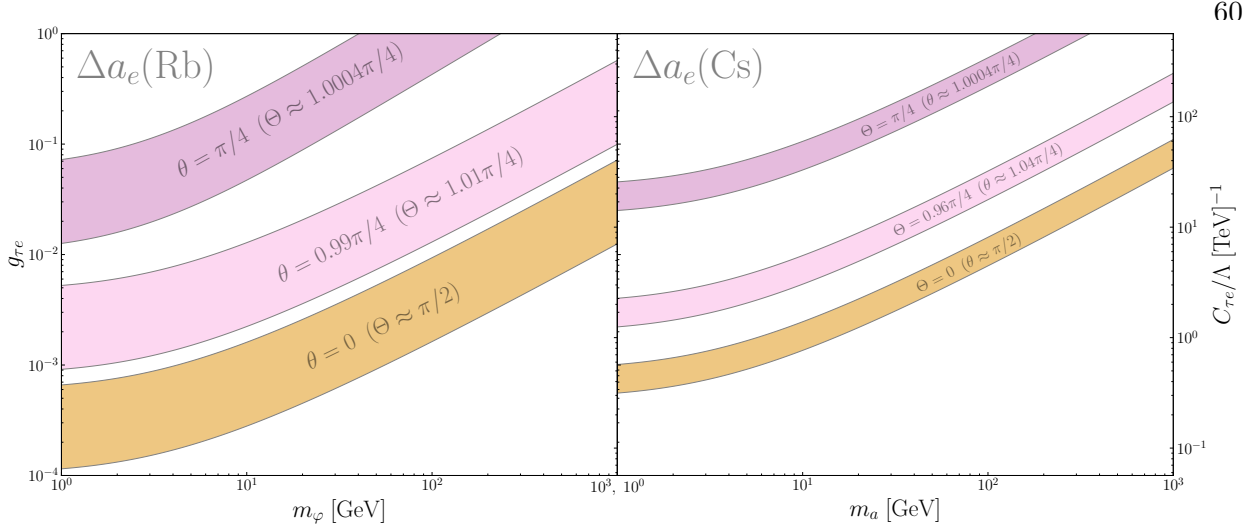


Figure 3.6: Viable explanations for both the Cesium and Rubidium electron  $g - 2$  anomalies at  $2\sigma$  for a scalar (ALP) with flavor off-diagonal coupling  $g_{\tau e}$  ( $C_{\tau e}$ ) and PV angles  $\theta$  ( $\Theta$ ). We note that chiral ( $\theta, \Theta = \pi/4$ ) solutions require much larger couplings, but this effect is very sensitive to even slight deviations in the angle.

### 3.4.7 Explanations to electron and muon $g - 2$ anomalies

Here, we indulge in the possibility that the electron and muon  $g - 2$  anomalies are genuine, and new physics is needed to explain them. We focus on particles with a single non-zero leptonic coupling,  $g_{\ell\tau}$ , with  $\ell = e (\mu)$  for the electron (muon) anomaly. We will also assume that  $\phi_{\tau\ell}, \Phi_{\tau\ell} = 0$  and  $\delta_{\tau\ell}, \Delta_{\tau\ell} = \pi/2$ , so as to evade the EDM constraints. Then, the interactions we consider are

$$\mathcal{L}_\varphi = g_{\tau\ell}\varphi\bar{\tau}(\cos\theta + \gamma_5\sin\theta)\ell + \text{H.c.}, \quad \mathcal{L}_a = C_{\tau\ell}\frac{\partial_\mu a}{\Lambda}\bar{\tau}(\sin\Theta + \gamma_5\cos\Theta)\ell + \text{H.c.} \quad (3.69)$$

Given that  $m_\tau \gg m_\ell$ , we ignore the  $\theta/\Theta$ -dependence in the conversion between the ALP and scalar couplings, so the ALP has an effective scalar coupling  $g_{\tau\ell}^a \approx C_{\tau\ell}m_\tau/\Lambda$ . In this limit, the PV angles are related via

$$\Theta \approx \frac{m_\tau + m_\ell}{m_\tau - m_\ell} \left( \frac{\pi}{2} - \theta \right) \approx \left( 1 + \frac{2m_\ell}{m_\tau} \right) \left( \frac{\pi}{2} - \theta \right). \quad (3.70)$$

To explore the full role of the PV angle, we consider explanations to each of the anomalies for three different PV angles: chiral ( $\theta$  or  $\Theta = \pi/4$ ), parity-conserving ( $\theta$  or  $\Theta = 0$ ), and a representative angle in between. We begin with explanations for the electron  $g - 2$  anomalies using  $\alpha(\text{Rb})$  and

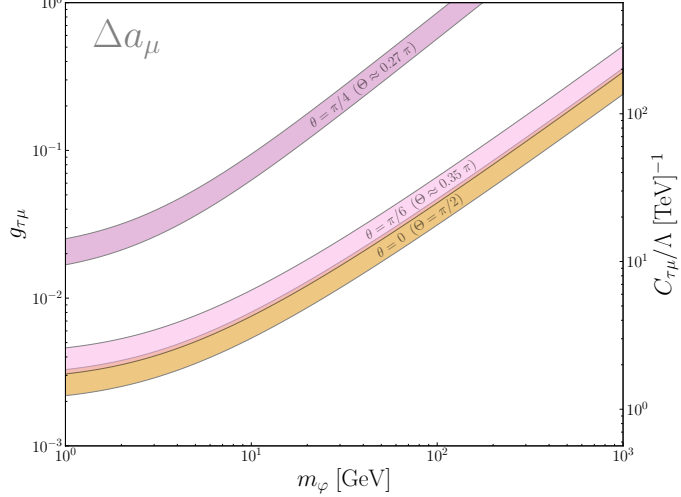


Figure 3.7: Viable explanations for the muon  $g - 2$  anomaly at  $2\sigma$ , for a scalar (ALP) with flavor off-diagonal coupling  $g_{\tau\mu}$  ( $C_{\tau\mu}$ ) and PV angles  $\theta$  ( $\Theta$ ). Like the scalar case, the chiral solutions require much larger couplings, but this effect is very sensitive to deviations in the PV angle.

$\alpha(\text{Cs})$  in Fig. 3.6, noting that  $\Delta a_e(\text{Rb}) > 0$  while  $\Delta a_e(\text{Cs}) < 0$ . While we explore a variety of PV angles, it is well known that pure scalars contribute a *positive* contribution to the lepton dipole moments, whereas pure pseudoscalars contribute an *negative* contribution.<sup>11</sup> To emphasize this point, we primarily consider a scalar explanation to the *positive* Rubidium anomaly for the pure and chiral scenarios  $\theta = 0$  and  $\theta = \pi/4$ , as well as a near-chiral angle  $\theta = 0.99\pi/4$ , with the corresponding ALP PV angles  $\Theta$  shown in parentheses. Similarly, we consider an ALP explanation to the *negative* Cesium anomaly, for pure and chiral scenarios  $\Theta = 0$  and  $\Theta = \pi/4$ , as well as a near-chiral angle  $\Theta = 0.96\pi/4$ , with the corresponding scalar angles  $\theta$  shown in parentheses. It is interesting to note just how delicate the chiral suppression is: for even a 1% deviation in the PV angle, the  $g_\tau$  required to explain the anomalies approaches the parity-conserving explanation. Hence, if one is interested in this chiral effect, any higher-order non-chiral contributions must be suppressed by at least the ratio  $m_e/m_\tau$ .

We repeat this analysis for explanations to the muon  $g - 2$  anomaly in Fig. 3.7. Since

<sup>11</sup> This is technically only valid for on-diagonal contributions and contributions with a heavier internal lepton. For contributions with a lighter internal lepton, both scalars and pseudoscalars (and anything in between) have a positive contribution.

$\Delta a_\mu > 0$ , we primarily consider scalar explanations to the anomaly for the chiral scenarios  $\theta = 0$  and  $\theta = \pi/4$ , as well as an intermediate angle  $\theta = \pi/3$ , with the corresponding ALP angles shown in parentheses. Once again, we see that the chiral suppression of the contribution to  $a_\mu$  requires a much larger coupling, but this effect is very sensitive to deviations from  $\theta = \pi/4$ .

For each of the anomalies, the couplings required for an explanation are quite large, especially for chirally-coupled particles. However, we note that these couplings in isolation are entirely unconstrained by modern experiments. In Chapter 4, we will explore the degree to which this range of couplings can be probed at lepton-ion colliders and beam-dump experiments for scalars, and in Chapter 5 we will repeat this analysis for ALPs.

## Chapter 4

### Particle Production from Lepton-Nucleus Collisions

#### 4.1 Introduction

Ever since Ernest Rutherford discovered the atomic nucleus by shining a beam of  $\alpha$ -particles onto a gold foil in the early twentieth century [113], fixed target experiments have enjoyed a rich history of probing interatomic structure. With  $\alpha$ -particles used again by Rutherford in 1919 to discover the proton [114] and by James Chadwick in 1932 to discover the neutron [115], a concrete theory of the atom was formed. The elements of the Periodic Table were forever stripped of their status as fundamental particles, replaced by the protons, neutrons, and electrons that comprise them.

This was not the end of the story. Showers of particles rained down from the heavens which did not fit neatly into this reductive description of the elements, and scattering experiments in the 1950s and ‘60s began producing these particles in experiments. Many of these particles were neatly described by Gell-Mann’s Eightfold Way and quark model, which proposed that hadrons were built from more fundamental constituents. However, confirming the existence of such substructure in nucleons would require a beam of particles much smaller than the  $\alpha$ , which itself is a helium nucleus composed of two protons and two neutrons. Indeed, the first direct evidence for nucleon substructure came from the SLAC-MIT experiments of the late 1960s, which aimed high-energy electrons (notably *much* smaller than the  $\alpha$ ) at fixed hydrogen and deuterium targets [116, 117]. The resulting scattering distribution was consistent with the existence of three point-like constituents within the nucleons, providing the first direct evidence for quarks and lending strong support to

the quark model.

While fixed targets were originally used to probe the internal structure of nuclei and nucleons, SLAC repurposed some of their experimental infrastructure in the early 1980s to conduct searches for neutral particles produced in collisions between the beam and the target. At that time, theoretical interest had grown around the possible existence of light, long-lived particles, such as dark photons, right-handed neutrinos, and axions, whose weak coupling prevented direct-detection at other experiments. If one of the electrons in their fixed target experiments skirted by the nucleus of an atom in the target, it would still experience a coherent electromagnetic interaction with the nuclear Coulomb field, potentially receiving enough energy to go off-shell and produce one of these particles. The first experiment to search for such states was SLAC E137 [118], and while the experiment concluded with null results, it inspired a new generation of *beam-dump* experiments<sup>1</sup> like it. These include the electron beam-dump experiments E141 [119], E774 [120], and NA64 [121], the proton beam dump experiments CHARM [122], E613 [123], and NuCal [124], and the ongoing muon beam dump experiment NA64 $\mu$  [125].

None of these experiments has detected a new neutral particle, but they have refined the allowed parameter space of couplings and masses for these particles. Current bounds imply that if these particles exist, they are either *very* weakly interacting (with couplings  $g \lesssim 10^{-8}$ ) or *not* very light (with masses  $m \gtrsim 1$  GeV), and perhaps a combination of both (for more detailed bounds, see e.g. [46, 126]). Weaker couplings can be probed by increasing the luminosity of the beam dump or increasing the distance from the target to the detector, allowing long-lived particles to decay after passing through the shielding. Improving the mass reach is a different story, as it requires a substantial increase in the energy of the colliding beam. While this will be achieved at the Search for Hidden Particle (SHiP) with a 400 GeV proton beam [127, 128], it is very difficult to accelerate electrons to hundreds of GeV or TeV of energy, in part due to their small mass. In particular,

---

<sup>1</sup> Conceptually, fixed target and beam dump experiments have similar collision set-ups, but the terms are used to distinguish the manner and scope of detection. Fixed target experiments typically have detectors much closer to the collision point, with the goal of capturing the incident beam particles to determine their deflection and hence the properties of the constituents within the target material. Beam dump experiments, on the other hand, typically have a detector far from the interaction point, with the goal of removing any SM background while allowing long-lived, neutral particles to propagate through empty space before decaying in or near the detector region.

circular beams are typically required to accelerate particles to high energies, but the energy loss for a circular beam of particles with energy  $E$  and mass  $m$  goes as  $P \propto (E/m)^4$ .

A similar energy limitation was encountered in the deep-inelastic scattering experiments described before. After the discovery of the quark, nuclear substructure experiments focused on determining the parton distribution functions (PDFs)  $f_i(x, Q^2)$ , which characterize the probability that parton  $i$  has momentum fraction  $x$  when probed at a scale  $Q^2$ . The behavior of the PDFs at lower  $x$  and higher  $Q^2$  is crucial for accurate QCD predictions, but each of these requires high beam energy. A clear solution to this problem is to accelerate the “fixed target” as well, by colliding an electron beam with a similarly relativistic beam of nucleons or nuclei. The most notable experiment with this approach was the Hadron-Electron Ring Accelerator (HERA) experiment at DESY between 1992 and 2007, which collided 28 GeV electrons with 920 GeV protons, thereby probing the PDFs down to  $x \sim 10^{-5}$  and up to  $Q^2 \sim 10^5$  GeV $^2$  [129]. More recently, the Electron-Ion Collider (EIC) is being constructed at Brookhaven National Lab (BNL) and is expected to begin operating by the early 2030s [130]. The EIC will collide 18 GeV electrons with protons and heavy ions at up to 110 GeV/nucleon. While the available energy is not as high at HERA, the luminosity is expected to be much larger, and the addition of heavy ion beams will allow for precise determination of PDFs for heavy nuclei down to  $x \sim 10^{-4}$  and up to  $Q^2 \sim 10^4$  GeV $^2$  with high statistics. In particular, the electron in the frame of a heavy ion at the EIC will have 4 TeV of energy, so the resulting cross-section has equivalent kinematics to a 4 TeV electron beam dump experiment.

It is therefore worthwhile to investigate whether the EIC, and other lepton-nucleus collider experiments such as the Electron Ion Collider in China (EicC) [131], would be able to probe the existence of neutral particles with heavier masses than the beam dump experiments before them. While these experiments lose out on luminosity relative to their predecessors (due to the lower density of the ion beam bunches as opposed to the high density target), their higher available energy may be advantageous for probing heavier neutral particles.

Of course, increasing collision energy is not limited to electron beams. Muons offer an attrac-

tive alternative, given that they lose much less energy than electrons from synchrotron radiation by a factor of  $(m_e/m_\mu)^4 = 10^{-10}$ . This fact has helped to fuel interest in the possibility of a multi-TeV muon collider in the future [132–134]. As part of the research and development for such a collider, multi-TeV muon beam dumps will likely be produced, which could be incorporated into a high-energy muon beam dump experiment. In particular, Refs. [135, 136] have shown that muon beam dumps can probe muon-coupled neutral particles at mass scales well beyond those accessible to current or planned electron and proton experiments, extending the sensitivity well into the multi-GeV regime. A more ambitious possibility is the construction of a *muon-ion collider*. Such a facility could be realized as an upgrade to the EIC, or as an entirely new experiment built at a separate site. While the technical feasibility of a muon-ion collider is under investigation, there is evidence to suggest that it would be far-superior to a fixed-target experiment for nuclear physics applications [137, 138], and it would excel at some BSM applications as well [139].

In this chapter, we will focus on characterizing the production mode  $\ell A_Z \rightarrow \ell' A_Z \varphi$  at experiments which involve lepton-nucleus collisions, where  $A_Z$  is a heavy ion and  $\varphi$  is a neutral particle which can couple to the (pseudo)-scalar or (axial)-vector lepton currents. These results will be applied more directly to LFV ALPs in Chapter 5, and hidden vector bosons in Chapter 6. For concreteness, we will apply our results to some of the existing, planned, and hypothetical detectors described above:

- (1) E137: E137 was a beam-dump experiment at SLAC which deposited a 20 GeV electron beam into a block of Aluminum ( $^{26}_{13}\text{Al}$ ). While it did not make any new discoveries, its null results allow us to place limits on light, long-lived particles to this day.
- (2) EIC: The EIC is an upcoming experiment at BNL which will collide electrons with energies up to 18 GeV and heavy ions with energies up to 110 GeV per nucleon. While a variety of heavy ions will be used and the experiment will also operate in proton mode, here we will focus on the EIC in gold ( $^{197}_{79}\text{Au}$ ) mode assuming an energy of 110 GeV/nucleon.
- (3) MuBeD: “MuBeD” is our name for a hypothetical future (Mu)on (Be)am (D)ump exper-

iment. We assume the muon beam has energy 1 TeV and is incident on a block of lead ( $^{204}_{82}\text{Pb}$ ). Given that we mainly discuss production cross-sections in this chapter, we defer specific assumptions about the surrounding detector apparatus to later chapters.

- (4) MuSIC: The Muon (Synchrotron) Ion Collider is our name for a hypothetical upgrade to the EIC which replaces the electron beam with a 1 TeV muon beam. While the feasibility of such an upgrade is questionable, it provides a useful benchmark for comparison of lepton beam-dump experiments and lepton-ion colliders. For simplicity, we take the ion beam to be a 110 GeV beam of Gold ( $^{197}_{79}\text{Au}$ ) ions, in line with our benchmark EIC scenario.

In Section 4.2, we discuss some conceptual aspects of the production process. In Section 4.3, we review our simplified model of atoms and their nuclei. In Section 4.4,, we provide analytic expressions for the amplitudes and crosss-section, and compare the production cross-sections at each experiment. In Section 4.5, we compare the exact results to the Weizsäcker-Williams approximation and Improved Weizsäcker-Williams approximation. In Sections 4.6 and 4.7, we discuss the kinematic distributions of the final-state particles in the collision. Finally, in Section 4.8, we apply the results of the chapter to examine limits on a scalar with an  $e\tau$  or  $\mu\tau$  flavor-violating interaction.

## 4.2 Feasibility of Particle Production in Lepton-Nucleus Collisions

We will begin by discussing the kinematics of ultra-peripheral particle production in lepton-nucleus collisions. We are interested in the scenario in which the ion or nucleus acts as a source of photons for the incoming lepton. After a high-energy collision with one of these photons, a particle  $\varphi$  is produced, potentially converting the lepton  $\ell$  into a different lepton  $\ell'$ . Before moving to more technical results, it is worth considering just how massive the boson  $\varphi$  can be. To do so, it is convenient to examine the collision in the rest-frame of the initial-state nucleus. Suppose in this frame, the lepton has energy  $E$  and momentum  $\mathbf{p}$ , so that its four-momentum is

$$p^\mu = (E, 0, 0, |\mathbf{p}|) \tag{4.1}$$

with  $E^2 = |\mathbf{p}|^2 + m_\ell^2$ . Let  $q^\mu = P_f^\mu - P_i^\mu$  be the four-momentum exchanged from the ion to the lepton, where  $P_i^\mu$  and  $P_f^\mu$  represent the initial and final-state four-momenta of the ion. The produced particle can be its heaviest when the smallest possible amount of momentum is imparted to the ion, so we assume the ion recoils along the beam axis. If this recoil momentum is  $Q$ , then

$$P_i^\mu = (M, 0, 0, 0), \quad P_f^\mu = (\sqrt{M^2 + Q^2}, 0, 0, Q). \quad (4.2)$$

As long as the recoil momentum of the nucleus is small relative to its mass, we have

$$q^\mu \approx \left( \frac{Q^2}{2M}, 0, 0, -Q \right). \quad (4.3)$$

Finally, let the combined four-momentum of the final-state lepton  $\ell'$  and boson  $\varphi$  be  $p_{\varphi\ell'}^\mu$ . Then, conservation of four-momentum implies

$$p^\mu - q^\mu = p_{\varphi\ell'}^\mu \quad (4.4)$$

As a consequence of the Cauchy-Schwartz inequality,  $p_{\varphi\ell'}^2 \geq (m_\varphi + m_{\ell'})^2$ . Also, under the assumption that  $E, |\mathbf{p}_\ell| \gg m_\ell$ , we have  $(p - q)^2 \approx 2Q|\mathbf{p}|$ . We can use this to place a limit on the mass  $m_\varphi$  of the boson:

$$(p - q)^2 \approx 2Q|\mathbf{p}| = p_{\varphi\ell'}^2 \geq (m_\varphi + m_{\ell'})^2 \quad (4.5)$$

$$\implies m_\varphi + m_{\ell'} \leq \sqrt{2Q|\mathbf{p}|}. \quad (4.6)$$

Therefore, the mass of the produced boson is limited by  $m_\varphi + m_{\ell'} \leq \sqrt{2Q|\mathbf{p}|}$ , where  $Q$  is the transfer-momentum of the exchanged photon and  $|\mathbf{p}|$  is the initial-state lepton momentum in the rest frame of the initial-state ion.

If one limits the analysis to coherent interaction of the lepton with the nucleus, this limits the photon transfer momentum to  $Q \lesssim 1/r_A \sim 100 \text{ MeV}^2$ <sup>2</sup> where  $r_A$  is the radius of the ion. For the benchmark experiments considered in the introduction, this corresponds to  $m_\varphi \lesssim 2 \text{ GeV}$  at E137,  $m_\varphi \lesssim 30 \text{ GeV}$  at the EIC,  $m_\varphi \lesssim 15 \text{ GeV}$  at MuBeD, and  $m_\varphi \lesssim 60 \text{ GeV}$  at MuSIC. Alternatively,

---

<sup>2</sup> Technically, the coherent nuclear form-factor is still non-zero at higher values of  $Q$ , but it is very small, so the cross-section of producing heavier particles coherently is severely suppressed.

if one is willing to sacrifice coherence and interact electromagnetically with the protons within the nucleus, it is possible to push  $Q$  to  $1/r_p \sim 1 \text{ GeV}$ , where  $r_p$  is the proton radius. In this case,  $m_\varphi \lesssim 6 \text{ GeV}$  at E137,  $m_\varphi \lesssim 90 \text{ GeV}$  at the EIC,  $m_\varphi \lesssim 45 \text{ GeV}$  at MuBeD, and  $m_\varphi \lesssim 200 \text{ GeV}$  at MuSIC. In principle, it is possible to push beyond this and consider deep inelastic scattering within the nucleons, but the cross-sections for this process will be severely suppressed.

### 4.3 Nuclear and Atomic Form-Factors

In order to compute the cross-section for peripheral production of a boson, we must know how the lepton interacts electromagnetically with the nucleus. This is encoded with the electromagnetic nuclear and atomic form-factors. In general, the electromagnetic form-factor of the nucleus receives a coherent contribution from the nucleus as a whole and an incoherent contribution from the individual protons and neutrons within the nucleus.<sup>3</sup> For the coherent nuclear form-factor, we use an approximation of the Fourier transform of the Woods-Saxon distribution [140], given by

$$G_{\text{coh}}^{\text{nuc}}(t) = \frac{9Z^2}{(R_A \sqrt{t})^6} \left[ \left( \sin(R_A \sqrt{t}) - R_A \sqrt{t} \cos(R_A \sqrt{t}) \right) \frac{1}{1 + a_0^2 t} \right]^2 \quad (4.7)$$

where  $a_0 = 0.79 \text{ fm}$  and  $R_A = (1.2 \text{ fm})A^{1/3}$ . Note that for small  $t$ , this agrees with the form of the coherent nuclear form-factor used in Refs. [141, 142], but falls off more quickly at larger  $t$  ( $\sim 1/t^5$  instead of  $\sim 1/t^2$ ). For the incoherent nuclear form factor, we use the dipole approximation for the electromagnetic form-factors of the nucleons within the nucleus [141, 142],

$$G_{\text{incoh}}^{\text{nuc}}(t) = \frac{1}{(1 + t/t_0)^4 (1 + t/4m_p^2)} [Z(1 + (\mu_p^2/4m_p^2)t) + (A - Z)(\mu_n^2/4m_p^2)t] \quad (4.8)$$

The dipole approximation becomes less accurate at higher momentum transfer [143], so to be safe, we impose a cut-off on the form-factors at  $t = 1 \text{ GeV}$ .

In the case that the nucleus is inside of an atom (as opposed to being a stripped ion), one must also parametrize shielding from the electron shells. This is accomplished with the atomic form-factors. Following Refs. [141, 142], we take the coherent and incoherent atomic form-factors

---

<sup>3</sup> There is also the possibility of deep-inelastic scattering with the quarks within the nucleons, but we do not consider that here.

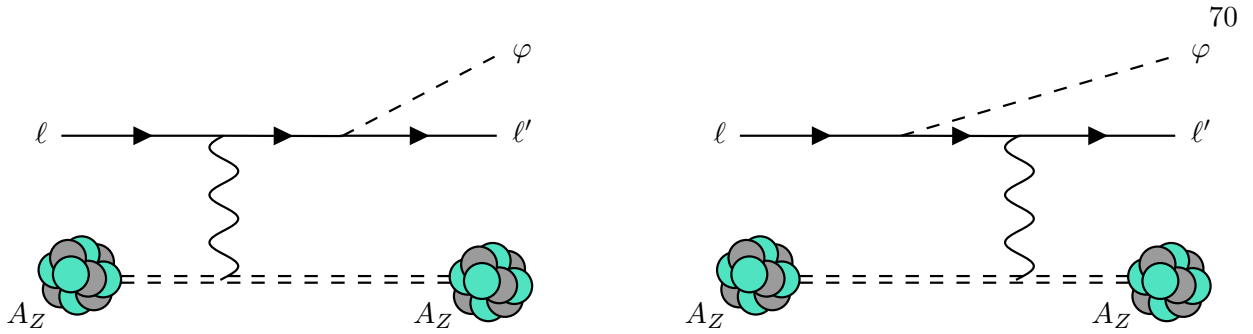


Figure 4.1: Relevant Feynman diagrams for the process  $\ell A_Z \rightarrow \ell' A_Z \varphi$  via photon exchange.

to be

$$G_{\text{coh}}^{\text{atom}}(t) = \left[ \frac{a^2 t}{1 + a^2 t} \right]^2, \quad G_{\text{incoh}}^{\text{atom}}(t) = \left[ \frac{a'^2 t}{1 + a'^2 t} \right]^2 \quad (4.9)$$

with  $a = 111Z^{-1/3}/m_e$  and  $a' = 571.4Z^{-2/3}/m_e$ .

Throughout this chapter and subsequent chapters, we will only focus on *coherent* production of particles at the EIC and MuSIC, as this will allow us to avoid potentially high background from breakup of the nucleus. For the beam-dump experiments, on the other hand, we will consider the full coherent and incoherent nuclear and atomic form-factors.

#### 4.4 Amplitude Calculation

Now we will compute the amplitude for peripheral particle production in lepton-nucleus collisions. This process is often treated with the Weizsäcker-Williams approximation, but this can potentially over-estimate the differential cross-section in some regions of the parameter space. Hence, we opt to evaluate the tree-level diagram exactly; we will compare the exact results to the Weizsäcker-Williams approximation in Section 4.5. A similar analysis was performed in Refs. [144, 145], but we treat the situation more generally, allowing for CLFV interactions and arbitrary PV. While we restrict our analysis to CLFV processes, we note that the initial and final-state charged leptons can be replaced with any fermion in this analysis without any qualitative differences.

The diagrams relevant for this process are shown in Fig. 4.1. We take  $p^\mu = (E, \mathbf{p})$  to be four-momentum of the initial state lepton,  $P_i^\mu$  and  $P_f^\mu$  to be the four-momenta of the initial and

final-state nucleus,  $p'^\mu = (E', \mathbf{p}')$  to be the four-momentum of the final-state  $\ell'$ , and  $k^\mu = (E_k, \mathbf{k})$  to be the four-momentum of the final-state  $\varphi$ . It is additionally useful to define the transfer momentum  $q^\mu = P_f^\mu - P_i^\mu$  and the sum  $P^\mu = P_f^\mu + P_i^\mu$ , along with the Mandelstam variables

$$s = (p' + k)^2 - m_\ell^2 = 2p' \cdot k + m_\varphi^2 + m_{\ell'}^2 - m_\ell^2 \quad (4.10)$$

$$u = (p - k)^2 - m_{\ell'}^2 = -2p \cdot k + m_\varphi^2 + m_\ell^2 - m_{\ell'}^2 \quad (4.11)$$

$$t_2 = (p' - p)^2 = -2p' \cdot p + m_\ell^2 + m_{\ell'}^2 \quad (4.12)$$

$$t = -q^2. \quad (4.13)$$

The lepton-photon vertex is the standard QED vertex. The photon-ion vertex is parametrized by a form-factor  $F(q^2)$ , so that

$$V_{A_Z\gamma}^\mu = ieF(q^2)P^\mu \quad (4.14)$$

where the details of the form-factor were discussed in Section 4.3. For stripped ions,  $F(q^2 \rightarrow 0) = Z$ , where  $Ze$  is the charge of the nucleus. In this low- $q^2$  regime, the incoming lepton views the nucleus as a whole as a coherent source of photons. For nuclei that are within atoms in materials (such as in fixed-target or beam-dump experiments)  $F(q^2 \rightarrow 0) = 0$ , as the charge of the nuclei is shielded by the electron shell at large distances. However, there is still a coherent regime  $1/r_{A_Z}^2 > q^2 > Z^2/r_{\text{Bohr}}^2$  for which  $F(q^2) \approx Z$ . The only other vertex is the  $\varphi\text{-}\ell\text{-}\ell'$  vertex. We consider scalars with interaction vertex

$$V_{\varphi\ell\ell'} = ig e^{i\phi} (\cos \theta + \gamma_5 e^{i\delta} \sin \theta) \quad (4.15)$$

and vectors with interaction vertex

$$V_{\varphi\ell\ell'}^\mu = ig e^{i\phi} \gamma^\mu (\cos \theta + \gamma_5 e^{i\delta} \sin \theta). \quad (4.16)$$

Following the discussions in Chapters 2 and 3, we note that the scalar interaction in Eq. 4.18 can easily be recast to apply to ALPs. The amplitude for the process in Feynman gauge is then given by

$$i\mathcal{M} = [F(q^2)P^\mu] \frac{ig e^2}{q^2} e^{i\phi} [\bar{u}(p')\Gamma_\mu(p, p', k)u(p)] \quad (4.17)$$

with

$$\Gamma_\mu^S = \gamma_\mu \frac{1}{\not{p} - \not{k} - m_{\ell'}} (\cos \theta + \gamma_5 e^{i\delta} \sin \theta) + (\cos \theta + \gamma_5 e^{i\delta} \sin \theta) \frac{1}{\not{p}' + \not{k} - m_\ell} \gamma_\mu \quad (4.18)$$

for scalars and

$$\Gamma_\mu^V = \epsilon^\alpha(k) \left[ \gamma_\mu \frac{1}{\not{p} - \not{k} - m_{\ell'}} \gamma_\alpha (\cos \theta + \gamma_5 e^{i\delta} \sin \theta) + \gamma_\alpha (\cos \theta + \gamma_5 e^{i\delta} \sin \theta) \frac{1}{\not{p}' + \not{k} - m_\ell} \gamma_\mu \right] \quad (4.19)$$

for vectors. We are now equipped to compute the differential cross-section for producing a scalar and vector via lepton-nucleus collisions. The spin-averaged squared amplitude is given by

$$\overline{|\mathcal{M}|^2} = g^2 e^4 \frac{F(q^2)^2}{q^2} \overline{|\mathcal{A}|^2} \quad (4.20)$$

where in general, the amplitude can be decomposed as  $\overline{|\mathcal{A}|^2} = \overline{|\mathcal{A}_0|^2} + \overline{|\mathcal{A}_{PV}|^2} \sin^2 \theta$ . The label “PV” refers to the fact that the angle  $\theta$ , absent the other couplings, controls the degree of PV in the interaction. At tree-level, the phases  $\phi$  and  $\delta$  drop out of the calculation. The amplitudes for the scalar scenario are given by

$$\begin{aligned} \overline{|\mathcal{A}_{S,0}|^2} &= \frac{(s+u)^2}{su} P^2 - 4 \frac{t}{su} (P \cdot k)^2 \\ &\quad + \frac{(s+u)^2}{s^2 u^2} (m_\varphi^2 - (m_\ell + m_{\ell'})^2) \left[ P^2 t - 4 \left( \frac{u P \cdot p + s P \cdot p'}{s+u} \right)^2 \right] \\ \overline{|\mathcal{A}_{S,PV}|^2} &= 4m_\ell m_{\ell'} \frac{(s+u)^2}{s^2 u^2} \left[ P^2 t - 4 \left( \frac{u P \cdot p + s P \cdot p'}{s+u} \right)^2 \right]. \end{aligned} \quad (4.21)$$

And for the vector scenario (using  $\Delta m_{\ell\ell'}^2 = (m_{\ell'} - m_\ell)^2$ ),

$$\begin{aligned} \overline{|\mathcal{A}_{V,0}|^2} &= \left[ \frac{(s+u)^2}{su} \left( 2 + \frac{\Delta m_{\ell\ell'}^2}{m_\varphi^2} \right) - 4 \right] P^2 - 4 \frac{t}{su} \frac{\Delta m_{\ell\ell'}^2}{m_\varphi^2} (P \cdot k)^2 \\ &\quad - 8 \frac{t}{su} \left[ (P \cdot p)^2 + (P \cdot p')^2 + \frac{t_2 + m_\varphi^2 - 2\Delta m_{\ell\ell'}^2}{2} P^2 \right] \\ &\quad + \frac{(s+u)^2}{s^2 u^2} \left( 1 - \frac{\Delta m_{\ell\ell'}^2}{m_\varphi^2} \right) (2m_\varphi^2 + (m_\ell + m_{\ell'})^2) \left[ P^2 t - 4 \left( \frac{u P \cdot p + s P \cdot p'}{s+u} \right)^2 \right] \\ \overline{|\mathcal{A}_{V,PV}|^2} &= \frac{4m_\ell m_{\ell'}}{m_\varphi^2} \left[ \frac{(s+u)^2}{su} P^2 - 4 \frac{t}{su} (P \cdot k)^2 + 8m_\varphi^2 \frac{t}{su} P^2 \right. \\ &\quad \left. - 3m_\varphi^2 \frac{(s+u)^2}{s^2 u^2} \left[ P^2 t - 4 \left( \frac{u P \cdot p + s P \cdot p'}{s+u} \right)^2 \right] \right]. \end{aligned} \quad (4.22)$$

These results are in agreement with Refs. [144, 145] for the special case  $\ell' = \ell$  and  $\theta = 0, \pi/2$ .<sup>4</sup>

Here, we note that the PV contributions to each amplitude are suppressed both for  $m_\ell \neq m_{\ell'}$  (due to the lepton mass hierarchy) and  $m_\ell, m_{\ell'} \ll m_\varphi$ . However, PV effects can become significant for  $m_\varphi \ll m_\ell = m_{\ell'}$ , especially for light on-diagonal vectors, for which the PV contributions are proportional to  $4m_\ell^2/m_\varphi^2$ . This effect could be utilized to provide more stringent constraints on PV vectors compared to their PC counterparts.

#### 4.4.1 Phase-Space Integration

We perform the cross-section integration in the rest-frame of the ion. The differential cross-section is given by

$$d\sigma = \frac{1}{(2E)(2M)|\mathbf{v}|} |\mathcal{M}|^2 (2\pi)^4 \delta^{(4)}(p' + k - p - q) \frac{d^3 p'}{(2\pi)^3 2E'} \frac{d^3 P_f}{(2\pi)^3 2E_f} \frac{d^3 k}{(2\pi)^3 2E_k} \quad (4.23)$$

where  $\mathbf{v}$  is the velocity of the incoming electron, so  $|\mathbf{v}| = |\mathbf{p}|/E$ . Using this and simplifying the denominators yields

$$d\sigma = \frac{1}{1024\pi^5 |\mathbf{p}| M E' E_f E_k} |\mathcal{M}|^2 \delta^{(4)}(p' + k - p - q) d^3 \mathbf{p}' d^3 \mathbf{P}_f d^3 \mathbf{k}. \quad (4.24)$$

It is then possible to split the four-momentum-conserving  $\delta$ -function into energy-conserving and momentum-conserving  $\delta$  functions, then integrate over  $p'$  to remove the momentum-conserving  $\delta$ -function. Also trading  $P_f$  with  $q = P_f - P_i$ , we have

$$d\sigma = \frac{1}{1024\pi^5 |\mathbf{p}| M E' E_f E_k} |\mathcal{M}|^2 \delta(E' + E_k - E - q_0) d^3 \mathbf{q} d^3 \mathbf{k}. \quad (4.25)$$

At this point, it is useful to define  $\mathbf{V} = \mathbf{p} - \mathbf{k}$  with  $V = |\mathbf{V}|$ , and then decompose  $\mathbf{q} = (Q, \theta_q, \phi_q)$  in spherical coordinates with  $z$ -axis pointed along  $\mathbf{V}$ . Then, one can show

$$\delta(E' + E_k - E - q_0) = \frac{E'}{QV} \delta(\cos \theta_q - \cos \theta_q^0) \quad (4.26)$$

where

$$\cos \theta_q^0 = \frac{u - \left(1 + \frac{E - E_k}{M}\right)t}{2QV}. \quad (4.27)$$

---

<sup>4</sup> The apparent sign disagreements with these references are due to a difference in metric convention.

As a result, the integral over  $\cos \theta_q$  can be performed, collapsing the  $\delta$ -function. Decomposing  $\mathbf{k} = (|\mathbf{k}|, \cos \theta_k, \phi_k)$  in spherical coordinates with  $z$ -axis along the beam axis, the integrand is independent of  $\phi_k$ , so this can be integrated over as well. The resulting differential cross-section is

$$d\sigma = \frac{1}{1024\pi^5 |\mathbf{p}| M E_f E_k Q V} |\mathcal{M}|^2 \Theta(1 - \cos^2 \theta_q^0) Q^2 dQ d\phi_q |\mathbf{k}|^2 d|\mathbf{k}| d(\cos \theta_k). \quad (4.28)$$

Now, we can replace the integral over  $Q$  with an integral over the Mandelstam variable  $t$  via the substitution  $dQ = E_f dt / (2MQ)$ , and we can replace the integral over  $|\mathbf{k}|$  with an integral over the energy of the  $\varphi$  particle  $E_k$ . This gives us the energy-angle differential cross-section

$$\frac{d\sigma}{dE_k d\theta_k} = \frac{\sin \theta_k}{64\pi^3} \frac{|\mathbf{k}|}{|\mathbf{p}| V} \int_{t_-}^{t_+} dt \left( \frac{1}{8M^2} \int_0^{2\pi} \frac{d\phi_q}{2\pi} |\mathcal{M}|^2 \right). \quad (4.29)$$

Here,  $t_{\pm}$  are the solutions to  $\cos^2 \theta_q^0 = 1$ . They are given by

$$t_+ = \frac{M \left[ (E - E_k + M)u + 2MV^2 + V \sqrt{4M^2V^2 + [4M(E - E_k + M) + u]u} \right]}{(E - E_k + M)^2 - V^2} \quad (4.30)$$

$$t_- = \frac{Mu^2}{(E - E_k + M)u + 2MV^2 + V \sqrt{4M^2V^2 + [4M(E - E_k + M) + u]u}}. \quad (4.31)$$

Rather than rationalizing the denominator in  $t_-$ , we find it convenient to keep the present form for numerical evaluation, as this avoids large cancellations which result in floating-point errors. Alternatively, one can integrate over a wider range of  $t$  and keep the Heaviside function  $\Theta(1 - \cos^2 \theta_q^0)$  in the integrand.

As it turns out, the angular integral in Eq. 4.29 is exactly solvable for the amplitudes in Eqs. 4.21 and 4.22. All of the dependence on  $\phi_q$  enters through the dot-product

$$\mathbf{q} \cdot \mathbf{p} = \frac{Q|\mathbf{p}|}{V} \left[ |\mathbf{p}| \cos \theta_q^0 - |\mathbf{k}| (\cos \theta_q^0 \cos \theta_k - \sin \theta_q^0 \sin \theta_k \cos \phi_q) \right], \quad (4.32)$$

which in turn appears in  $s$ . In particular, the necessary substitutions in terms of the integration

variables are

$$s = - \left( 1 + \frac{E}{M} \right) t + 2(\mathbf{q} \cdot \mathbf{p}) \quad (4.33)$$

$$u = (E - E_k)^2 - V^2 - m_f^2 \quad (4.34)$$

$$t_2 = m_\varphi^2 - s - u - t \quad (4.35)$$

$$P^2 = 4M^2 + t \quad (4.36)$$

$$P \cdot p = 2ME - \frac{1}{2}(s + t) \quad (4.37)$$

$$P \cdot k = 4ME_k - \frac{1}{2}(s + u) \quad (4.38)$$

$$P \cdot p' = 2M(E - E_k) + \frac{1}{2}(u - t). \quad (4.39)$$

Examining the amplitudes, we see that  $\phi_q$  appears only as  $\cos \phi_q$ , which only appears in the denominator within powers of  $s$  up to  $s^2$ . Then, each term can be written as

$$\mathcal{F}_k(\{\mathcal{Q}_i\}, s) = \frac{\mathcal{Q}_0 + \mathcal{Q}_1 s + \mathcal{Q}_2 s^2}{s^k} \quad (4.40)$$

with  $k = 0$  or  $1$ . The integral over these terms is straightforward using methods from complex analysis. Hence, the  $E_k$ - $\theta_k$  differential cross-section can be computed with a single integral over the photon transfer  $t$ .

#### 4.4.2 Features of the Production Cross-Section

In this section, we present results for the total production cross-section  $\sigma(\ell A_Z \rightarrow \ell' A_Z \varphi)$ . We choose a hard maximum cut-off on the transfer momentum of  $t_+ = 1/r_p = 1$  GeV. Beyond this point, there is still a contribution to the cross-section from deep-inelastic scattering off the quarks inside the nucleons, but the cross-section would be far too small to measure in the contexts we are considering. Given the generality of the discussion above, there are many parameters to consider; namely the details of the experiment (beam energy, nucleus species, and initial-state lepton) and the details of the interaction (vector or scalar-like interaction current, degree of PV in the coupling, and final-state lepton). We explore the effect of all of these parameters in Fig. 4.2, which plots

the production cross-section of the particle  $\varphi$  as a function of its mass  $m_\varphi$ . In particular, the top panels represent production of the  $\varphi$  at experiments involving an electron beam (E137 and EIC), while the bottom panels represent production of the  $\varphi$  at hypothetical experiments involving a muon beam (MuBeD and MuSIC, described in the introduction). The panels on the left represent production of a (pseudo)scalar  $\varphi$ , whereas the panels on the right represent production of an (axial) vector  $\varphi$ . To account for all PV couplings, we note that the cross-section can always be written as  $\sigma(\theta) = \sigma_0 + \sigma_{PV} \sin^2 \theta$ , where  $\theta$  is an angle characterizing the degree of PV in the coupling. Hence, we shade between  $\sigma(0)$  and  $\sigma(\pi/2)$ , although this is only noticeable in some of the plots in the lower panel. Finally, within each panel, the cross-section for production of a  $\varphi$  and an  $e$  (solid),  $\mu$  (dashed) and  $\tau$  (dotted) is shown. We note that while these plots represent the *production* cross-section of the particle  $\varphi$  at each of these experiments, the actual signal cross-section is often much smaller, due in part to signal selection but mostly to detector efficiency and geometry. We will explore this in the context of the  $\varphi$ 's lab-frame kinematic distributions in Section 4.6.

We begin by examining the light  $m_\varphi$  regime in Fig. 4.2. For light masses, the difference between lepton beam-dumps and lepton-ion collisions is largely insubstantial. In the electron case, we see that the cross-sections are larger for the EIC than E137, but this is mostly due to the difference in the charge of the nucleus involved with the collision (aluminum with  $Z = 13$  for E137 and gold with  $Z = 79$  for the EIC), as well as the additional available energy at the EIC in the rest frame of the gold ion. The comparison between lepton beam-dumps and lepton ion-collisions is more straightforward for the hypothetical muon collision experiments we consider, which have the same lepton beam energy ( $E = 1$  TeV) and nucleus charge (lead with  $Z = 82$ ). In this case, we see in the bottom of Fig. 4.2 that there is only a minor increase in the production cross-section for light  $m_\varphi$  at MuSIC compared to at MuBeD. Coupled with the fact that beam-dump experiments will most definitely have a higher luminosity and favorable detector geometry for forward-produced particles, it appears that they are preferable over lepton-ion colliders for probing the existence of light particles.

While one may take this to be a statement about the inefficacy of lepton-ion colliders for

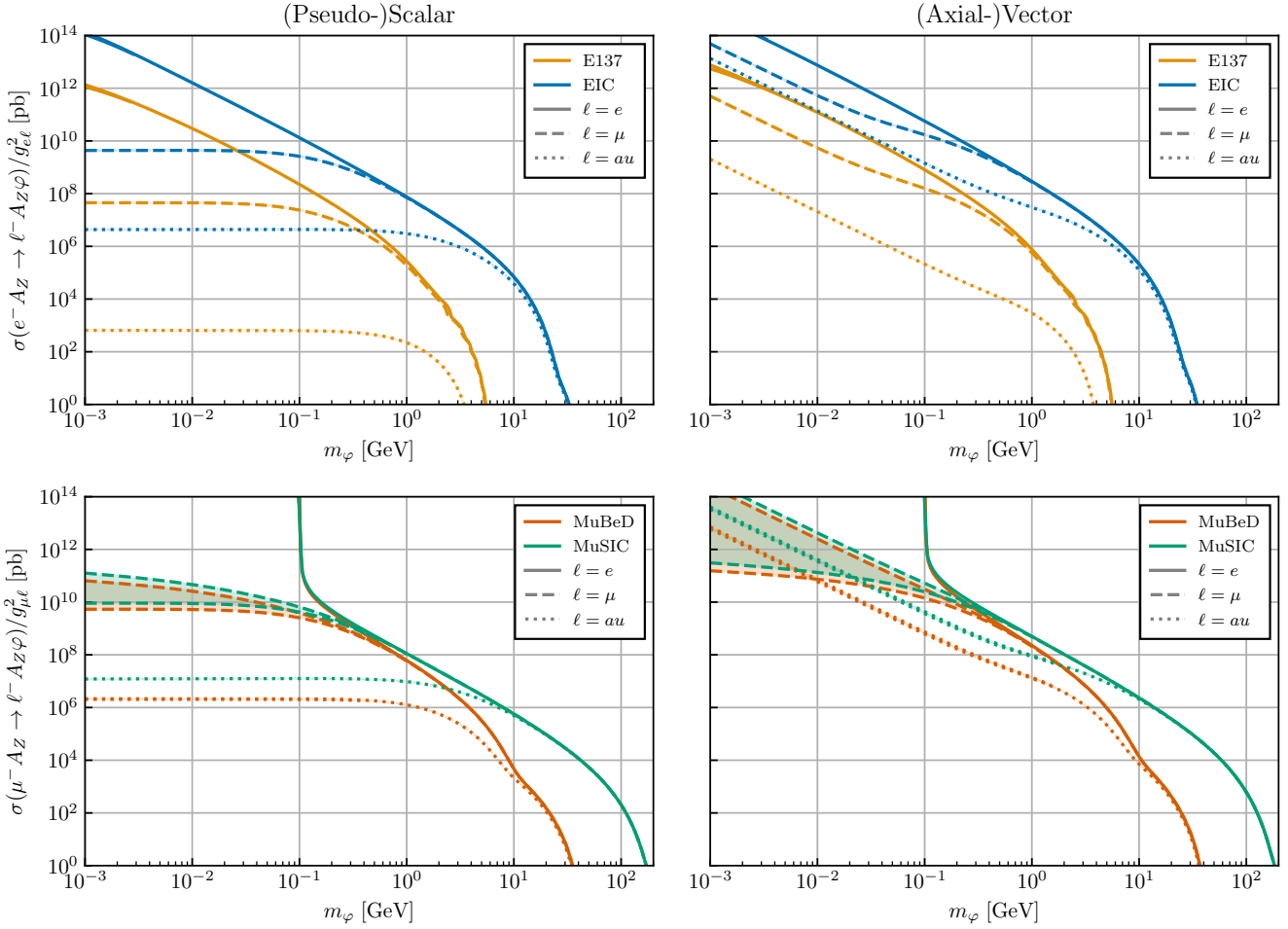


Figure 4.2: *Production* cross-sections for the processes ( $\ell A_Z \rightarrow \ell' A_Z \varphi$  for  $\ell' = e, \mu, \tau$ ), particle-types (scalar (left) and vector (right)), and lepton collision experiments (E137, EIC (top) and MuBeD, MuSIC (bottom)) discussed in the text. To account for PV couplings, we note that the production cross-section can always be written as  $\sigma(\theta) = \sigma_0 + \sin^2(\theta)\sigma_{PV}$ , so we shade the area between  $\sigma(0)$  and  $\sigma(\pi/2)$ . PV effects only appear important for flavor-conserving production modes at the muon-nucleus colliders (dashed, bottom) when  $m_\varphi < m_\mu$ , although we expect that there is also a substantial difference at electron-nucleus colliders when  $m_\varphi < m_e$ .

probing lighter-mass particles, it can be understood as a more general statement about the diminishing returns of higher-energy beams. To understand this, we note that in the rest-frame of the ion, the electron beam at the EIC will have an energy  $E \approx 4$  TeV, as opposed to E137's energy of  $E = 20$  GeV, and the muon beam at MuSIC would have a whopping  $E \approx 20$  TeV of energy as opposed to MuBeD's  $E = 1$  TeV of energy. Despite these large differences in energy, there is not much of an increase in the production cross-section.

Whereas lepton-ion collisions may not have much to offer in terms of probing lighter-mass particles, they have a much larger mass reach than their beam-dump counterparts. This is unsurprising given the additional available energy in the collisions, and highlights the main advantage of lepton-ion colliders, at least as far as peripheral particle production is concerned. In particular, with the hard cut-off of  $t_+ = 1$  GeV, the maximum producible particle via this process at the EIC and MuSIC are  $m_\varphi = 95$  GeV and 200 GeV respectively, as opposed to  $m_\varphi = 6$  GeV and 44 GeV at E137 and MuBeD respectively.

Apart from the discrepancies between lepton beam dumps and lepton-ion colliders, we can also glean some insight into how PV in the interaction affect the cross-section. As anticipated in the end of Section 4.4, PV effects are only significant for  $m_\varphi < m_\ell = m_{\ell'}$ . Given that the lower-bound on the plots is  $m_\varphi = 1$  MeV  $> m_e$ , these effects are only noticeable in the bottom plots. PV effects are especially dramatic in the vector scenario, for which there is a factor of  $\sim 10^2$  increase in the cross-section for axial-vectors as opposed to pure vectors at  $m_\varphi = 10$  MeV.

In context of the results from Chapter 3, the PV-independence of the cross-sections for large  $m_\varphi$  is notable. In particular, it was found in Section 3.3.5 that limits on scalar LFV couplings  $g_{\ell\ell'}$  can be substantially weaker for chiral scalars than pure scalars. In contrast, limits placed on the LFV couplings at lepton-nucleus collision experiments are largely immune to the PV details of the interaction, especially for large  $m_\varphi$ . At the same time, lepton-nucleus colliders with polarization-control such as the EIC will still have the ability to distinguish between PC and PV interactions in the event that such a particle is found. To see this, we note that the interaction between a scalar  $\varphi$ ,  $\ell$ , and  $\ell'$  can be rewritten

$$\mathcal{L}_{\varphi\ell\ell'} = g_{\ell\ell'} e^{i\phi} \left[ (\cos \theta - ie^{i\delta} \sin \theta) \varphi \bar{\ell}' P_L \ell + (\cos \theta + ie^{i\delta} \sin \theta) \varphi \bar{\ell}' P_R \ell \right] + \text{H.c.} \quad (4.41)$$

The left- and right-polarized cross-sections can be found by isolating each of these terms. Using  $\sigma(\theta) = \sigma_0 + \sigma_{PV} \sin^2 \theta$  to represent the unpolarized cross-section, we see that we can set  $\theta = \pi/4$  ( $-\pi/4$ ) to isolate  $\sigma_R$  ( $\sigma_L$ ), provided we modify the coupling to account for the  $\cos \theta \pm ie^{i\delta} \sin \theta$

prefactors. We find

$$\sigma_{L,R} = \frac{1}{2}(1 \pm \sin \delta \sin 2\theta)\sigma(\mp\pi/4). \quad (4.42)$$

Using  $\sigma(\pm\pi/4) \approx \sigma_0$  (since the PV effects are subdominant in the heavy  $\varphi$  regime), we find a left-right asymmetry

$$\left| \frac{\sigma_L - \sigma_R}{\sigma_L + \sigma_R} \right| = |\sin \delta \sin 2\theta|. \quad (4.43)$$

More realistically, the polarization control will be limited such that only some proportion  $p$  of all the leptons are appropriately polarized (for example, the EIC is expected to have 70% polarization control [130], corresponding to  $p = (1 + 0.7)/2 = 0.85$ ). Then, the cross-sections in either polarization mode are given by  $\bar{\sigma}_L \approx p\sigma_L + (1-p)\sigma_R$  and  $\bar{\sigma}_R \approx (1-p)\sigma_L + p\sigma_R$ . In that case, the observed left-right asymmetry will be

$$\left| \frac{\bar{\sigma}_L - \bar{\sigma}_R}{\bar{\sigma}_L + \bar{\sigma}_R} \right| = (2p - 1) |\sin \delta \sin 2\theta|. \quad (4.44)$$

Hence, given enough statistics, one can use polarization control to determine the nature of the leptonic interaction of the  $\varphi$ . This, however, requires not only a non-zero PV-angle  $\theta$  but also a non-zero CP-angle  $\delta$  (although CP is still conserved when  $\delta = \pi/2$ ). Then, the left-right asymmetry could be used to extract the PV angle  $\theta$  directly. A similar analysis can likely be performed at lepton-lepton colliders with polarization control as well, but lepton-ion colliders have an advantage in that they can probe higher masses due to the high energy of the relativistic ions.

It is also important to recognize that the production cross-section for  $\ell A_Z \rightarrow \ell' A_Z \phi$  depends only on the coupling  $g_{\ell\ell'}$ . In contrast, the most stringent constraints on LFV couplings for heavy  $m_\varphi$  from Chapter 3 come from the LFV decay modes  $\ell_i \rightarrow \ell_j \gamma$  and  $\ell_i \rightarrow \ell_j \ell_k \bar{\ell}_l$ , which only limit products of the couplings (i.e.  $g_{ee} g_{e\mu}$  or  $g_{e\tau} g_{\mu\tau}$ , see Fig. 3.3). While individual LFV couplings can be isolated from their contributions to the lepton dipole moments, contributions to the EDMs require CP-violation to exist, and the electron and muon  $g - 2$  have disagreements in their theoretically determined and experimentally measured values. Even if one takes the experimental results at face-value and assumes that any outstanding theoretical discrepancies will be resolved, these limits

are weaker than those set by LFV lepton decay modes, and comparable to limits that could be placed at the EIC or a future MuBeD or MuSIC experiment.

#### 4.5 Weizsäcker-Williams Approximation

To derive the results above, we have used the exact form of the Feynman amplitude, but it is customary to instead consider the  $2 \rightarrow 2$  scattering process  $\ell\gamma^* \rightarrow \ell'\varphi$ , where  $\gamma^*$  is an off-shell photon with the minimum momentum transfer required for the process to be kinematically allowed. Then, the resulting cross-section is multiplied by an effective photon flux to account for the electromagnetic field of the atomic nucleus. This is known as the Weizsäcker-Williams approximation [146, 147]. According to Refs. [141, 142], the approximation is valid so long as the energy of the incoming lepton beam is much larger than the  $m_\ell$  and  $m_\varphi$ .

The validity of the Weizsäcker-Williams approximation has been assessed in the past for beam-dump E137 for production of scalars in Ref. [144], and for pseudo-scalars, vectors, and axial-vectors in Ref. [145]. The Weizsäcker-Williams approximation for production of a vector is also assessed in the context of a muon beam dump in Ref [148]. We complement these analyses by considering production of such particles at lepton-ion colliders in comparison to lepton beam-dump experiments, and also extend the interactions to include arbitrary PV and LFV couplings. As far as we can tell, this is the first test of the validity of the approximation for LFV interactions, although there is no reason to suspect it should be any more or less accurate than the LFC case.

For this process, the Weizsäcker-Williams approximation corresponds to the substitution [141]

$$\frac{1}{8M^2} \int \frac{d\phi_q}{2\pi} |\mathcal{M}^{2 \rightarrow 3}|^2 \rightarrow \frac{t - t_-}{2t_-} \frac{F(t)^2}{t^2} |\mathcal{M}^{2 \rightarrow 2}|_{t=t_-}^2. \quad (4.45)$$

where  $|\mathcal{M}^{2 \rightarrow 2}|_{t=t_{\min}}^2$  is the amplitude for the  $2 \rightarrow 2$  scattering process  $\ell^-\gamma^* \rightarrow \ell'^-\varphi$  evaluated at photon transfer momentum  $t = t_-$ .

Looking at Eq. 4.29 for the differential cross-section, we see that the differential cross-section in the Weizsäcker-Williams approximation is given by

$$\left( \frac{d\sigma}{dE_k d\theta_k} \right)_{WW} = \frac{1}{32\pi^3} \frac{|\mathbf{k}| \sin \theta_k}{|\mathbf{p}| V} |\mathcal{M}^{2 \rightarrow 2}|_{t=t_-}^2 \int_{t_-}^{t_+} \frac{t - t_-}{2t_-} \frac{F(t)^2}{t^2}. \quad (4.46)$$



Figure 4.3: Relevant  $2 \rightarrow 2$  Feynman diagrams for approximating the process  $\ell A_Z \rightarrow \ell' A_Z \varphi$  via the Weizsäcker-Williams approximation.

From here, we can define the effective photon flux from the nucleus

$$\chi = \int dt \frac{t - t_-}{t^2} F(t)^2 \quad (4.47)$$

so that the differential cross-section is given by

$$\left( \frac{d\sigma}{dE_k d\theta_k} \right)_{WW} = \frac{1}{64\pi^3} \alpha^2 \frac{|\mathbf{k}| \sin \theta_k}{|\mathbf{p}| V} \frac{\chi}{t_-} |\mathcal{M}^{2 \rightarrow 2}|^2|_{t=t_-}. \quad (4.48)$$

To employ this approximation, we must compute the  $2 \rightarrow 2$  scattering amplitudes. This is done in the next section.

#### 4.5.1      $2 \rightarrow 2$ Amplitudes

We compute the  $2 \rightarrow 2$  amplitudes from the diagrams in Fig. 4.3, with the implicit understanding that the photon is off-shell with  $q^2 = -t_-$ . The amplitudes are given by

$$i\mathcal{M}^{2 \rightarrow 2} = \epsilon^{\star\mu}(q) i g e^2 e^{i\phi} [\bar{u}(p') \Gamma_\mu(p, p', k) u(p)] \quad (4.49)$$

where the Dirac-vertices  $\Gamma$  for (pseudo)-scalars and (axial)-vectors are the same as those in Eqs. 4.18-4.19. Averaging over the square of the amplitude yields

$$\overline{|\mathcal{M}^{2 \rightarrow 2}|^2} = g^2 e^4 \overline{|\mathcal{A}^{2 \rightarrow 2}|^2}. \quad (4.50)$$

Similarly to the  $2 \rightarrow 3$  process, the amplitude can be decomposed into a PC and PV piece,  $|\mathcal{A}^{2 \rightarrow 2}|^2 = |\mathcal{A}_0^{2 \rightarrow 2}|^2 + \sin^2 \theta |\mathcal{A}_{PV}^{2 \rightarrow 2}|^2$ . For scalars,  $|\mathcal{A}^{2 \rightarrow 2}|^2$  is given by

$$\begin{aligned}\overline{|\mathcal{A}_{S,0}^{2 \rightarrow 2}|^2} &= -\frac{(s+u)^2}{su} + 2(m_\varphi^2 - (m_\ell + m_{\ell'})^2) \frac{s+u}{su} \left(1 + \frac{m_\ell^2}{s} + \frac{m_{\ell'}^2}{u} - \frac{m_\varphi^2}{s+u}\right), \\ \overline{|\mathcal{A}_{S,\text{PV}}^{2 \rightarrow 2}|^2} &= 8m_\ell m_{\ell'} \frac{s+u}{su} \left(1 + \frac{m_\ell^2}{s} + \frac{m_{\ell'}^2}{u} - \frac{m_\varphi^2}{s+u}\right).\end{aligned}\quad (4.51)$$

Whereas for vectors,

$$\begin{aligned}\overline{|\mathcal{A}_{V,0}^{2 \rightarrow 2}|^2} &= -\frac{(s+u)^2}{su} \left(2 + \frac{\Delta m_{\ell\ell'}^2}{m_\varphi^2}\right) + 4 \\ &\quad + 2 \left(1 - \frac{\Delta m_{\ell\ell'}^2}{m_\varphi^2}\right) (2m_\varphi^2 + (m_\ell + m_{\ell'})^2) \frac{s+u}{su} \left(1 + \frac{m_\ell^2}{s} + \frac{m_{\ell'}^2}{u} - \frac{m_\varphi^2}{s+u}\right), \\ \overline{|\mathcal{A}_{V,\text{PV}}^{2 \rightarrow 2}|^2} &= -\frac{4m_\ell m_{\ell'}}{m_\varphi^2} \left[\frac{(s+u)^2}{su} + 3m_\varphi^2 \frac{s+u}{su} \left(1 + \frac{m_\ell^2}{s} + \frac{m_{\ell'}^2}{u} - \frac{m_\varphi^2}{s+u}\right)\right].\end{aligned}\quad (4.52)$$

To evaluate at  $t = t_-$ , we note that the only dependence on  $t$  is in  $s$  (Eq. 4.33). At  $t = t_-$ ,

$\cos \theta_k^0 = \pm 1$ , so

$$s|_{t=t_-} = -\left(1 + \frac{E}{M}\right)t_- \pm \frac{2Q_-}{V}|\mathbf{p}|[|\mathbf{p}| - |\mathbf{k}| \cos \theta_k]. \quad (4.53)$$

Numerically, we find that  $\cos \theta_q^0|_{t=t_-}$  is usually  $-1$ , which is what one would expect if the lepton and photon collided head-on.

#### 4.5.2 Improved Weizsäcker-Williams Approximation

In the *Improved*<sup>5</sup> Weizsäcker-Williams approximation (as defined in Ref. [141]), the effective photon flux  $\chi$  is additionally simplified to be independent of  $E_k$  and  $\theta_k$ . To accomplish this, we take  $t_- = [(m_\ell + m_\varphi)^2 - m_{\ell'}^2]/2E$  and  $t_+ = 4ME^2/(2E + M)$  in the bounds of integration. Other references take  $t_+ = m_\ell^2 + m_\varphi^2$  which is likely sufficient to capture most of the dependence of the form-factor, but we note Eqs. 4.30-4.31 implies  $t_+ t_- = M^2 u^2 / [(E - E_k + M)^2 - V^2]$ , which in the appropriate limit gives our value of  $t_+$  above as an absolute upper-bound on  $t$ . Given the behavior of  $F(t)^2/t^2$  for large  $t$ , we expect the difference between these  $t_+$  to be inconsequential.

---

<sup>5</sup> It is so-called not due to an increase in accuracy of the approximation, but to a decrease in computational complexity.

While we stop at this point in our analysis when computing the differential cross-sections in the Improved Weizsäcker-Williams approximation, there are additional approximations one can make to perform the angular integral, resulting in an approximation for  $d\sigma/dE_k$ . In particular, if  $m_\ell/E, m_{\ell'}/E, m_\varphi/E, \theta_k \ll 1$  and  $t \sim t_-$ , then one can approximate

$$s \approx -\frac{u}{1-x} \quad (4.54)$$

$$u \approx (1-x)m_\ell^2 - m_{\ell'}^2 - (1-1/x)m_\varphi^2 - x\theta_k^2 E^2 \quad (4.55)$$

$$t_- \approx \frac{u^2}{4(1-x)^2 E^2} \quad (4.56)$$

inside the  $2 \rightarrow 2$  amplitudes in Eqs. 4.51 and 4.52. With everything expressed in terms of  $u$ , the integral over  $\theta_k$  can be replaced with an integral over  $u$  with  $du \approx -2x\theta_k E^2 d\theta_k \approx -2xE^2 \sin \theta_k d\theta_k$ . Then we have

$$\begin{aligned} \left( \frac{d\sigma}{dE_k} \right)_{IWW} &= \frac{g^2}{8\pi} \alpha^2 \chi \int_{\theta_{\min}}^{\theta_{\max}} d\theta_k \sin \theta_k \frac{|\mathbf{k}|}{|\mathbf{p}|V} \frac{1}{t_-} |\mathcal{A}^{2 \rightarrow 2}|_{t=t_-}^2 \\ &= \frac{g^2}{4\pi\alpha^2} \chi \frac{|\mathbf{k}|}{E^2} \frac{1-x}{x} \int_{u_{\min}}^{u_{\max}} \frac{du}{u^2} |\mathcal{A}^{2 \rightarrow 2}|_{t=t_-}^2. \end{aligned} \quad (4.57)$$

Finally, assuming that  $\theta_k$  becomes large enough that  $\theta_k E^2 \gg m_\ell^2, m_{\ell'}^2, m_\varphi^2$ , we can take  $u_{\min} = -\infty$ , and keep  $u_{\max} = (1-x)m_\ell^2 + (1-1/x)m_\varphi^2 - m_{\ell'}^2 - x\theta_{\min}^2 E^2$ . While for beam-dump or fixed-target experiments,  $\theta_{\min}$  is often zero,  $\theta_{\min}$  is set by the detector geometry for lepton-ion colliders.

For completion, we evaluate the integral over  $du$  in Eq. 4.57 for the terms that appear in  $|\mathcal{A}^{2 \rightarrow 2}|_{t=t_-}^2$  for both scalars and vectors. In particular, we have

$$\int_{-\infty}^{u_{\max}} \frac{du}{u^2} \left[ -\frac{(s+u)^2}{su} \right] \approx -\frac{x^2}{1-x} \frac{1}{u_{\max}} \quad (4.58)$$

$$\int_{-\infty}^{u_{\max}} \frac{du}{u^2} \frac{s+u}{su} \left[ 1 + \frac{m_\ell^2}{s} + \frac{m_{\ell'}^2}{u} - \frac{m_\varphi^2}{s+u} \right] \approx -\frac{x(u_{\max} - 2x\theta_{\min}^2 E^2)}{6u_{\max}^3} \quad (4.59)$$

It is straightforward to combine these results with Eqs. 4.51 and 4.52 to find approximate expressions for  $d\sigma/dE_k$ . We do not compare these formulae to the exact cross-sections  $d\sigma/dE_k$ , as we are more interested in the lab-frame differential cross-sections. For analysis of these approximate differential cross-sections in the context of beam-dump experiments, we again refer to Refs. [144, 145, 148].

### 4.5.3 Cross-Section Comparisons

To test the validity of the WW and IWW approximations, we can plot the exact and approximate cross-sections (along with the relative error) for a variety of processes and colliders. For simplicity, we focus on two cases: the diagonal process  $\ell A_Z \rightarrow \ell A_Z \varphi$ , and the off-diagonal process  $\ell A_Z \rightarrow \tau A_Z \varphi$ . In either case, we allow the interaction to be scalar-like or vector-like with arbitrary parity violation. The results for each process are shown in Fig. 4.4 and Fig. 4.5, respectively.

First, we focus on the diagonal process shown in Fig. 4.4. These are most directly comparable to the results from Refs. [144, 145, 148], although those references compare the differential cross-section  $d\sigma/dx$  w.r.t.  $x = E_k/E$ . For the diagonal case, we find excellent agreement between the WW approximation and exact result for almost all range of masses, with better agreement for higher lepton beam energy. In particular, there are  $\mathcal{O}(1)$  deviations for E137 at small masses, but otherwise the EIC approximation agrees with the exact result to within 10% at small masses and within 1% at large masses. The agreement for the muon beam experiments is even better, with an agreement of within 1% or less across the total range of masses considered. We also find very good agreement with the IWW approximation, with only  $O(1)$  deviations at large masses. In particular, the agreement we find between the IWW and exact methods is better than is found in Refs. [144, 145], even for E137. This is likely due to the fact that while we assume  $t_{\pm}$  are independent of  $E_k$  and  $\theta_k$  in the bounds of the  $t$  integral to simplify the photon flux, we do not employ the additional approximation for the angular integral described in Section 4.5.2.

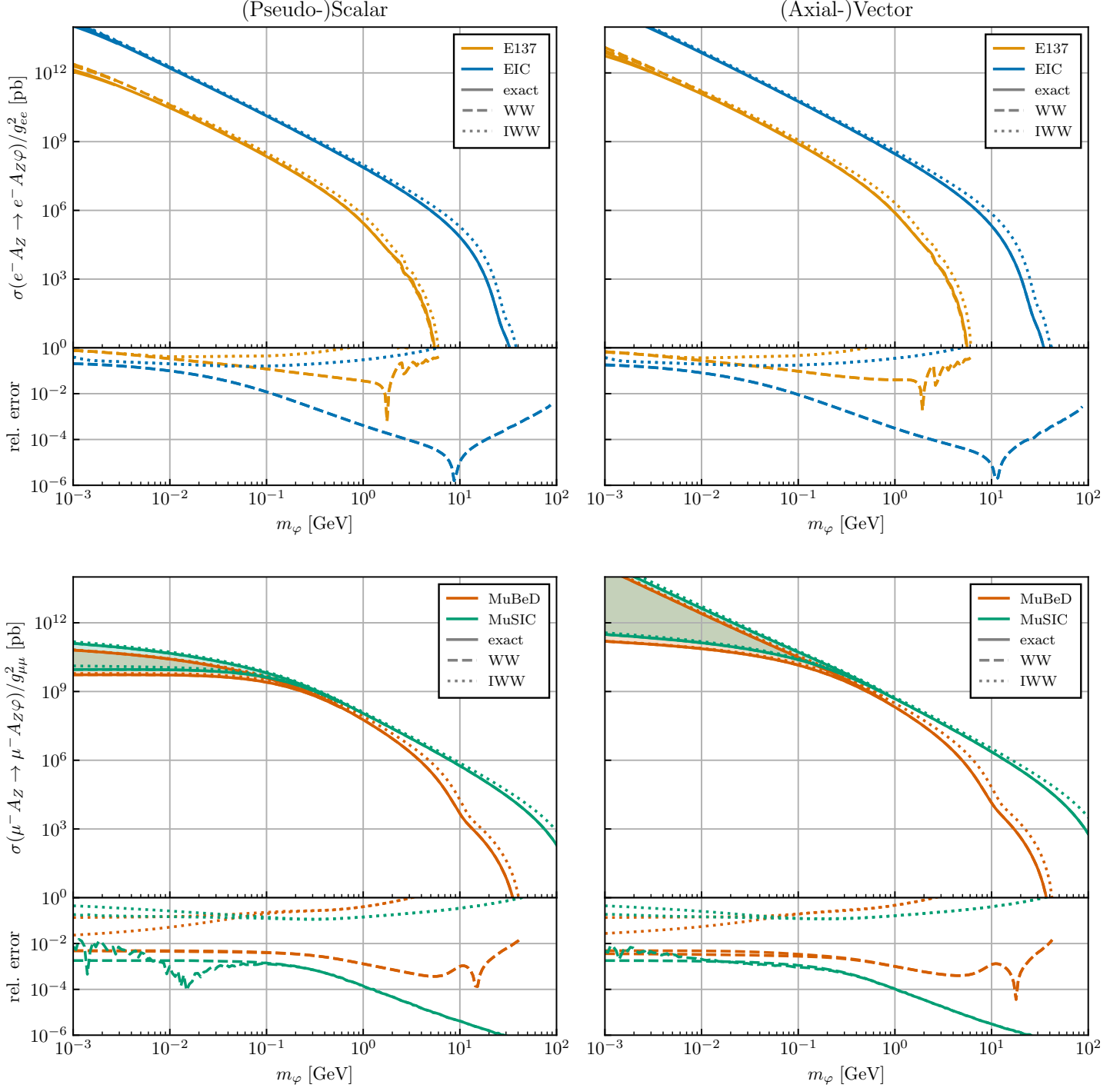


Figure 4.4: Comparisons between exact (solid) and approximate (“WW,” dashed and “IWW,” dotted) cross-sections, along with relative errors (bottom of each plot), for some lepton-nucleus collisions. The plots on the top compare the approximate and exact cross-sections for the electron-nucleus collisions at E137 and the EIC, whereas the plots on the bottom compare the approximate and exact cross-sections for the muon-nucleus collisions at the hypothetical 1 TeV MuBeD and MuSIC (defined in the text). The plots on the left compare the results for (pseudo)-scalars, while the plots on the right compare the results for (axial)-vectors.

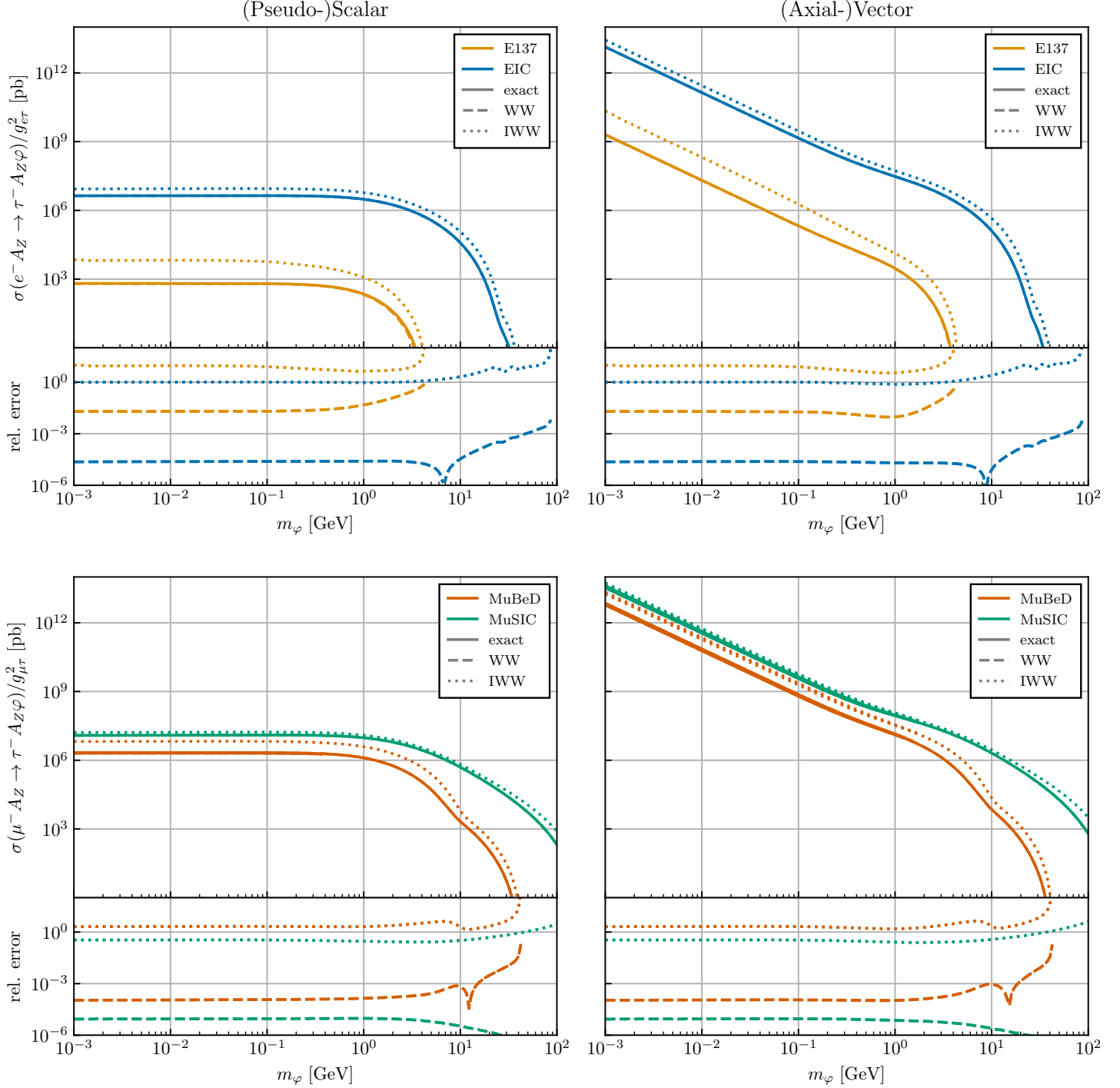


Figure 4.5: Comparisons between exact (solid) and approximate (“WW,” dashed and “IWW,” dotted) cross-sections, along with relative errors (bottom of each plot), for some lepton-nucleus collisions. The plots on the top compare the approximate and exact cross-sections for the electron-nucleus collisions at E137 and the EIC, whereas the plots on the bottom compare the approximate and exact cross-sections for the muon-nucleus collisions at the hypothetical 1 TeV MuBeD and MuSIC (defined in the text). The plots on the left compare the results for (pseudo)-scalars, while the plots on the right compare the results for (axial)-vectors.

Given that the analyses in the literature focus on the diagonal case, it is worth considering whether the WW approximations still apply for LFV particle production. In Fig. 4.5, we consider the LFV  $\ell$ - $\tau$ -conversion process  $\ell^- A_Z \rightarrow \ell'^- A_Z \varphi$  for  $\varphi$ . Once again, we find excellent agreement between the WW approximation and the exact result, especially at higher lepton beam energies. In particular, the WW approximation is accurate to within 1% for E137, 0.01% for the EIC and MuBeD, and 0.001% for MuSIC. The IWW also fares well for the EIC and MuSIC, with a disagreement of at most a factor of 2 for most masses. However, it performs slightly worse for the beam dump experiments E137 and MuBeD, disagreeing by a factor of few (although no more than 10) over the masses considered.

#### 4.6 Kinematical Distributions of $\varphi$

In the preceding sections, we have examined the total production cross-section for various lepton beam-dump experiments and lepton-ion colliders. However, the signal cross-section is often much smaller, as the particle must decay to visible and identifiable products within or near a detector. Hence, particles that are extremely boosted can evade detection by decaying far from the experimental apparatus, and (particularly for the lepton-ion collision case) particles that are produced too far forward or backward may escape along the beam axis. Hence, in order to better compare lepton-beam dump and lepton-ion collider scenarios, it is important to examine the kinematic distributions of the final-state particles as well.

It is straightforward to derive the kinematic distributions of  $\varphi$  from the differential cross-section 4.29. In particular, the energy-angle distribution for the final-state particle  $\varphi$  in the nucleus frame is given by

$$\rho_{E,\theta}(E_\varphi, \theta_\varphi) = \frac{1}{\sigma} \frac{\partial \sigma}{\partial E_\varphi \partial \theta_\varphi}(E_\varphi, \theta_\varphi). \quad (4.60)$$

This is all well and good in beam-dump and fixed-target experiments, for which the frame of the nucleus is the same as the frame of the lab, but surely must fail for an ion moving close to the speed of light relative to the lab. Indeed, labeling those variables in the ion rest frame ‘ion’ and

those in the lab frame ‘lab’, one has to perform a coordinate transformation

$$\frac{1}{\sigma} \frac{\partial \sigma}{\partial E^{\text{lab}} \partial \theta^{\text{lab}}} = \frac{1}{\sigma} \frac{\partial(E^{\text{ion}}, \theta^{\text{ion}})}{\partial(E^{\text{lab}}, \theta^{\text{lab}})} \frac{\partial \sigma}{\partial E^{\text{ion}} \partial \theta^{\text{ion}}}. \quad (4.61)$$

Surprisingly, it turns out that

$$\frac{\partial(E^{\text{ion}}, \theta^{\text{ion}})}{\partial(E^{\text{lab}}, \theta^{\text{lab}})} = 1. \quad (4.62)$$

This can be verified through explicit computation using Eqs. 4.65-4.66 below, but can also be understood by examining the Lorentz-invariant measure  $\delta(p^2 - m^2)d^4p$ . We can expand the four-momentum  $p^2 = E^2 - |\mathbf{p}|^2$  and the integration measure  $d^4p = |\mathbf{p}|^2 \sin \theta dE d|\mathbf{p}| d\theta d\phi$ , where  $\theta$  is the momentum angle with-respect-to the beam axis and  $\phi$  is the transverse angle. With this in mind, we have

$$\begin{aligned} \delta(E^2 - |\mathbf{p}|^2 - m^2) |\mathbf{p}|^2 \sin \theta dE d|\mathbf{p}| d\theta d\phi &= \frac{\delta(|\mathbf{p}| - \sqrt{E^2 - m^2})}{2|\mathbf{p}|} |\mathbf{p}|^2 \sin \theta dE d|\mathbf{p}| d\theta d\phi \\ &= \frac{1}{2} \sqrt{E^2 - m^2} \sin \theta dE d\theta d\phi \\ &= \frac{1}{2} [|\mathbf{p}_\perp| d\phi] [dE d\theta]. \end{aligned} \quad (4.63)$$

In the last line, we have identified  $\sqrt{E^2 - m^2} \sin \theta \equiv |\mathbf{p}_\perp|$  and split the measure into two terms. The first term,  $|\mathbf{p}_\perp| d\phi$ , is invariant under boosts along the beam-axis because  $\mathbf{p}'_\perp = \mathbf{p}_\perp$  and  $\phi' = \phi$  under these transformations. The left-hand-side is manifestly Lorentz-invariant, and so is also invariant under boosts along the beam-axis. Hence, it must be the case that the remaining measure,  $dE d\theta$ , is also invariant under boosts along the beam-axis.<sup>6</sup> With this useful fact, the  $E$ - $\theta$  kinematic distribution in the lab frame is indeed given by

$$\rho(E_\varphi^{\text{lab}}, \theta_\varphi^{\text{lab}}) = \frac{1}{\sigma} \frac{\partial \sigma}{\partial E_\varphi^{\text{ion}} \partial \theta_\varphi^{\text{ion}}} (E_\varphi^{\text{ion}}, \theta_\varphi^{\text{ion}}) \quad (4.64)$$

without an associated Jacobian factor. While this is not a massive conceptual shift, it does simplify numerical evaluation of the distributions substantially. One simply needs the expressions for  $E^{\text{ion}}$

---

<sup>6</sup> While we have proven this for a Lorentz-invariant measure, we note that the same derivation applies to the Galilean-invariant measure with  $\delta(E^2 - |\mathbf{p}|^2 - m^2) \rightarrow \delta(E - |\mathbf{p}|^2/2m)$ .

and  $\theta^{\text{ion}}$  in terms of  $E^{\text{lab}}$  and  $\theta^{\text{lab}}$ . These are

$$E_\varphi^{\text{ion}} = \gamma_{\text{ion}} \left( E_\varphi^{\text{lab}} + v_{\text{ion}} |\mathbf{k}_\varphi^{\text{lab}}| \cos \theta_\varphi^{\text{lab}} \right) \quad (4.65)$$

$$\tan \theta_\varphi^{\text{ion}} = \frac{\sin \theta_\varphi^{\text{lab}}}{\gamma_{\text{ion}} (\cos \theta_\varphi^{\text{lab}} + v_{\text{ion}}/v_\varphi^{\text{lab}})}. \quad (4.66)$$

where  $v_{\text{ion}}$  is the speed of the ion in the lab frame and  $\gamma_{\text{ion}} = 1/\sqrt{1-v_{\text{ion}}^2}$  its boost. In lab settings, it is often preferable to speak in terms of the boost  $\gamma_\varphi^{\text{lab}} = E_\varphi^{\text{lab}}/m_\varphi$  and the pseudorapidity  $\eta_\varphi^{\text{lab}} = -\log \tan(\theta_\varphi^{\text{lab}}/2)$ . The former is useful for considering the decay lengths of particles in the lab, and the latter is convenient when describing a detector's ability to identify signals on either side of the interaction vertex. In particular, in collider experiments, particles with large  $|\eta|$  may escape along the beam-pipe.

#### 4.6.1 Pseudorapidity Distributions for Beam Dump vs. Collider Experiments

The pseudorapidity distribution for the particle  $\varphi$  can be obtained from Eq. 4.60 by integrating over  $dE$  and multiplying by the Jacobian  $|d\theta/d\eta|$ :

$$\begin{aligned} \rho_\eta(\eta) &= \int dE \rho_{E,\theta}(E, \theta(\eta)) \left| \frac{d\theta}{d\eta} \right| \\ &= \int dE \rho_{E,\theta}(E, 2 \arctan e^{-\eta}) \operatorname{sech} \eta. \end{aligned} \quad (4.67)$$

Equipped with this result, we can compare the distributions at different experiments. To begin, we examine the distributions for the diagonal interaction  $\ell A_Z \rightarrow \ell A_Z \varphi$  with a PC scalar. To get a sense of the distributions over a large range of masses, we fill in the envelope of all distributions between a minimum and maximum  $m_\varphi$ , and then plot the endpoints in solid. For the electron beam experiments, we plot over the range  $m_\varphi = 1$  MeV to  $m_\varphi = 5$  GeV, whereas for the muon beam experiments we plot over the range  $m_\varphi = 1$  MeV to  $m_\varphi = 40$  GeV. The results are shown in Fig. 4.6. For low masses, it appears that there is little difference between the distributions at the lepton-ion colliders and their beam-dump counterparts, but deviations become significant at higher masses.

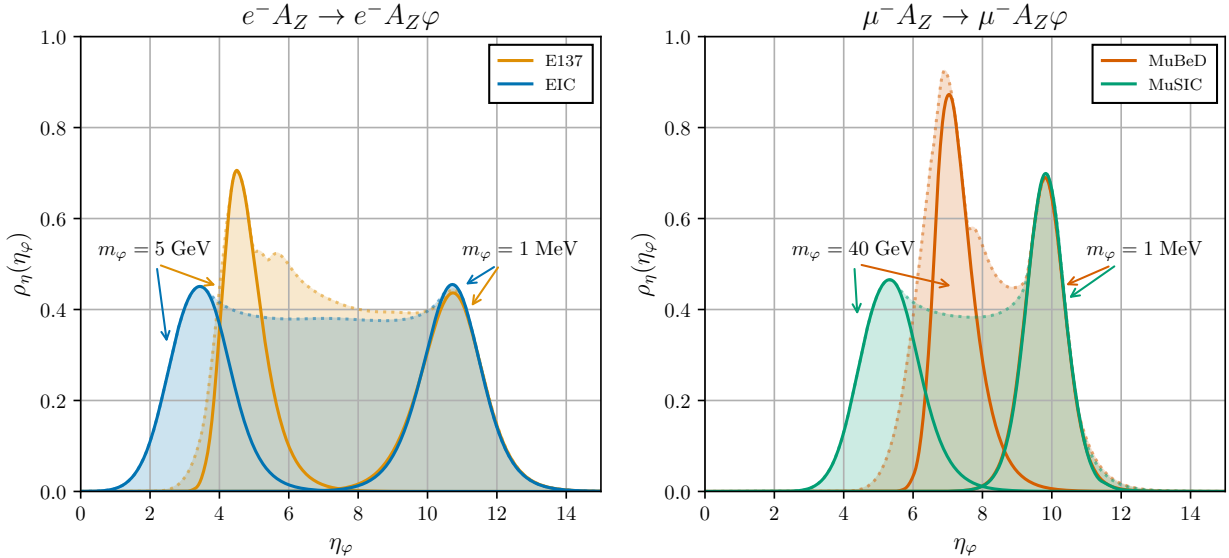


Figure 4.6: A plot illustrating the range of pseudorapidity distributions at E137, the EIC, MuBeD and MuSIC. For the electron beam experiments, the distributions are swept from  $m_\varphi = 1 \text{ MeV}$  to  $m_\varphi = 5 \text{ GeV}$ , whereas for the muon beam experiments, the distributions are swept from  $m_\varphi = 1 \text{ MeV}$  to  $m_\varphi = 40 \text{ GeV}$ . The envelope of all such distributions is plotted with a dashed line and shaded in, with the nedpoint distributions plotted in solid.

It is important to put these distributions into the context of the detector apparatus at each experiment. Beam-dump experiments typically have detectors along the beam axis far past the target, so they should in principle have no difficulty capturing forward-produced (high  $\eta$ ) particles. The EIC and MuSIC, however, are collider experiments, so particles with high pseudorapidity can escape down the beam-pipe undetected, unless a dedicated forward or backward detector apparatus is constructed. In particular, the pseudo-rapidity range on the electron-side of the EIC is expected to be  $|\eta| < 3.5$  [130]. Based on the left panel of Fig. 4.6, we see that for  $m_\varphi \lesssim 5 \text{ GeV}$ , most particles will have a an average pseudo-rapidity  $|\bar{\eta}| > 4$ , and hence only a small fraction of such particles will have the potential to be detected at the EIC. In Chapter 6, we will explore the possibility of capturing such forward-produced particles with the addition of a “far backward” detector, with a tracking module at  $z \approx 6 \text{ m}$  from the interaction point (similar to the planned B0 spectrometer on the ion side of ePIC detector [149]). In the right panel of Fig. 4.6, we see that the average pseudorapidity at MuSIC is even higher, with  $|\bar{\eta}| \gtrsim 6$  for  $m_\varphi < 40 \text{ GeV}$ . Although

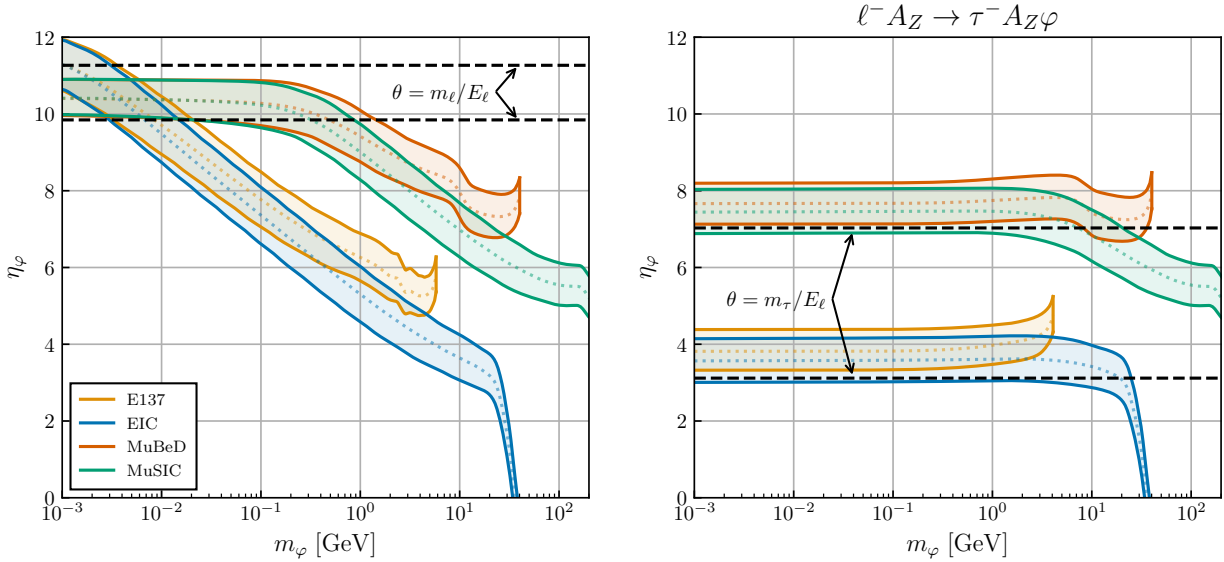


Figure 4.7: Interquartile range of  $\eta$  as a function of mass for on-diagonal production of a  $\varphi$  (left) and production of a  $\varphi$  via  $\tau$ -conversion (right). The dashed lines represent the opening angle in the limit of small mass, which is roughly  $\theta \approx m_\ell/E_\ell$ , or  $\eta \approx \log(2E_\ell/m_\ell)$ .

no concrete pseudo-rapidity requirement has currently been proposed for MuSIC, higher pseudo-rapidity resolution would require detectors far down the beam-pipe. Hence, one can expect that for light masses, the EIC and MuSIC will be out-performed by the corresponding beam-dumps E137 and MuBeD, while these lepton-ion colliders will have the advantage in the heavy-mass regime.

To better visualize the pseudo-rapidity distributions at these experiments, we can plot the interquartile range of the pseudo-rapidity  $\eta$  as a function of masses. This is shown for both the diagonal case, as well as the  $\tau$ -conversion case  $\ell A_Z \rightarrow \tau A_Z \varphi$ , in Fig. 4.7. For these experiments, it appears the angle of the  $\varphi$  asymptotes near  $\theta = m_\ell/E_\ell$ , where  $m_\ell$  is the mass of the final-state lepton and  $E_\ell$  is the energy of the initial-state lepton in the lab frame. For the EIC, we see that in the diagonal production case, only heavy particles fall within the  $|\eta| < 3.5$  pseudo-rapidity requirement, while for the off-diagonal  $\tau$  conversion case, a substantial portion of all particles fall within the  $|\eta| < 3.5$  case. For MuSIC, on the other hand, almost all particles in both cases lie far beyond the EIC's pseudorapidity requirement. We expect that higher pseudo-rapidities are a generic feature of such a collider due to the much larger inertia of the incident muons, so in the

event such a detector is created, additional instrumentation will be included to cover a range of pseudorapidities at least up to  $|\eta| < 6$ .

As discussed previously, higher pseudo-rapidities are not a problem at beam dump experiments, so these experiments should in principle be able to detect the decay products of all particles  $\varphi$  produced in this fashion. The only caveat is that these particles (especially the lighter ones) are often produced with a very high boost, so it is possible depending on their coupling that they decay far beyond the confines of the experiment.

While we have only plotted the PC scalar case here, we do not expect the qualitative features for other particle types to differ, as the particle type does not strongly impact the kinematics of the process. The same can not be said about changing the final-state lepton, as the kinematics of  $\varphi$  and the final-state lepton is directly dependent on their relative mass and energy. The processes we have omitted from discussion ( $e^- A_Z \rightarrow \mu^- A_Z \varphi$  and  $\mu^- \rightarrow e^- A_Z \varphi$ ) are already very constrained from limits on  $\mu \rightarrow e\gamma$  and (for light  $\varphi$ )  $\mu \rightarrow e + \text{inv.}$ , and are therefore unlikely to have any signal potential at these experiments.

#### 4.6.2 Boost Distributions for Beam Dump vs. Collider Experiments

Similar to before, the boost distribution for the particle  $\varphi$  can be obtained from Eq. 4.60 by integrating over  $d\theta$  and multiplying by the Jacobian  $|dE/d\gamma|$ :

$$\begin{aligned} \rho_\gamma(\gamma) &= \int d\theta \rho_{E,\theta}(E(\gamma), \theta) \left| \frac{dE}{d\gamma} \right| \\ &= \int d\theta \rho_{E,\theta}(\gamma m_\varphi, \theta) m_\varphi. \end{aligned} \quad (4.68)$$

With this, we plot the boost distributions over a range of masses for the process  $\ell^- A_Z \rightarrow \ell^- A_Z \varphi$  in Fig. 4.8.

We see that not only are light particles produced with very high pseudo-rapidity, but can also have immense boosts as well. In particular, most 1 MeV particles are produced with upwards of  $10^4$  boost, indicating that they will easily escape the detector apparatus before decaying. While the boosts become  $\mathcal{O}(1)$  at E137 and the EIC for GeV-scale ALPs, they are still  $\mathcal{O}(10)$  at MuBeD and

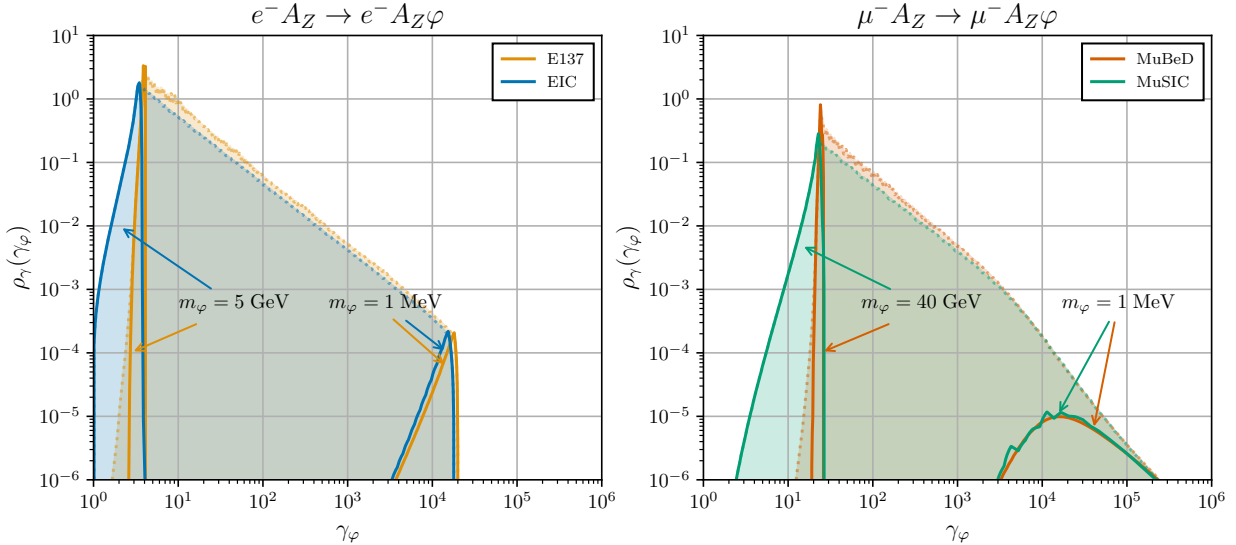


Figure 4.8: A plot illustrating the range of boost distributions at E137 and the EIC (left) and MuBeD and MuSIC (right). For the electron beam experiments, the distributions are swept from  $m_\varphi = 1 \text{ MeV}$  to  $m_\varphi = 5 \text{ GeV}$ , whereas for the muon beam experiments, the distributions are swept from  $m_\varphi = 1 \text{ MeV}$  to  $m_\varphi = 40 \text{ GeV}$ . The envelope of all such distributions is plotted with a dashed line and shaded in, with the nedpoint distributions plotted in solid.

MuSIC even up to  $m_\varphi = 40 \text{ GeV}$ . Notably, despite the additional available energy at the lepton-ion colliders compared to their beam-dump counterparts, the boost distributions (and hence, the energy imparted to the  $\varphi$  in the interaction) are almost identical.

Once again, it is instructive to examine the interquartile range of the boost distributions; we do so in Fig. 4.9 for diagonal production of a  $\varphi$  (left) and production of a  $\varphi$  via  $\tau$ -conversion (right). Here, we see that the boost distributions are very narrow, so almost all particles are produced with the same boost, which is quite significant for most masses. It is also clear that for almost the entire range of masses, the boost is near the maximum  $\gamma_{\max} \approx E_\ell/m_\varphi$ .<sup>7</sup>

One hallmark of particles produced with such a high boost is displaced decay signals. This will be investigated in more detail in Chapter 6, but here we can do some back-of-the-envelope calculations. In particular, if the decay rate of the  $\varphi$  is taken to be  $\Gamma \approx g^2 m_\varphi / 8\pi$ , this corresponds to a decay length of  $\gamma c/\Gamma \approx 8\pi E_\ell / g^2 m_\varphi^2$ . Typically, displaced decay searches are characterized

<sup>7</sup> Technically, this is not the true maximum, because some energy can be taken from the nucleus as well. However, it is a good approximation for the maximum until  $\varphi$  is heavy.

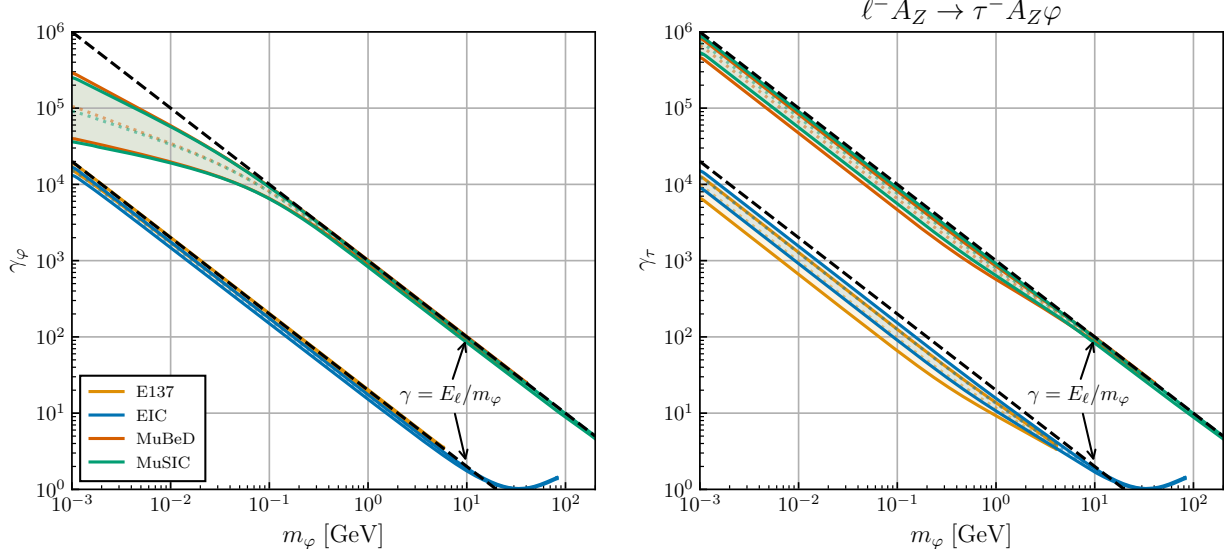


Figure 4.9: Interquartile range of  $\gamma$  as a function of mass for on-diagonal production of a  $\varphi$  (left) and production of a  $\varphi$  via  $\tau$ -conversion. The black dashed lines represent the curve  $\gamma = E_\ell/m_\varphi$  for each of the colliders, which is a rough upper-bound which is only exceeded for large  $m_\varphi$ , when the  $\varphi$  must “borrow” a significant amount of energy from the nucleus in order to be produced.

by a minimum and maximum resolvable displacement,  $d_{\min}$  and  $d_{\max}$ . Here,  $d_{\min}$  is set either by the geometry of the detector apparatus or the tracking resolution of the detectors, and  $d_{\max}$  is set roughly by the overall size of the detector apparatus. Very roughly, given  $d_{\min}$  and  $d_{\max}$ , we can expect that (so long as the production cross-section is sufficiently large) these experiments will be able to probe mass-coupling products in the range  $\sqrt{8\pi E_\ell/d_{\max}} \lesssim gm_\varphi \lesssim \sqrt{8\pi E_\ell/d_{\min}}$ . At the EIC, choosing  $d_{\min} = 1$  mm and  $d_{\max} = 1$  m, this corresponds to  $3 \times 10^{-7}$  GeV  $\lesssim gm_\varphi \lesssim 10^{-5}$  GeV. The parameters of MuBeD are much less certain, but choosing the  $E = 1.5$  TeV scenario from Refs. [135, 136] (which has  $d_{\min} \approx 10$  m and  $d_{\max} \approx 100$  m), we have  $2 \times 10^{-7}$  GeV  $\lesssim gm_\varphi \lesssim 7 \times 10^{-7}$  GeV. These rough estimates line up well with the more detailed analysis performed in Chapter 6, although the range of accessible parameters is considerably wider, due to the non-zero probability that particles with  $c\tau < d_{\min}$  or  $c\tau > d_{\max}$  still decay within the detector.

## 4.7 Kinematical Distribution of Final-State Lepton

Here, we briefly comment on the kinematical distribution of the final-state lepton. In order to obtain this distribution in full generality, one must perform the cross-section integration over  $E'$  and  $\theta'$  rather than  $E_k$  and  $\theta_k$ . This can be computed by multiplying Eq. 4.29 *within* the  $t$ -integral by the Jacobian determinant

$$\left| \frac{\partial(E_k, \theta_k)}{\partial(E', \theta')} \right| = \frac{|\mathbf{p}'|' \sin \theta'}{|\mathbf{k}| \cos \theta_k} = \frac{\sqrt{(E - E_k + \frac{t}{2M})^2 - m_f^2 - (E_k^2 - m_\varphi^2) \sin^2 \theta_k}}{\sqrt{E_k^2 - m_\varphi^2} \cos \theta_k} \quad (4.69)$$

which will convert  $\frac{d\sigma}{dE_k d\theta_k}$  to  $\frac{d\sigma}{dE' d\theta'}$ . Given the reliability of the WW-approximation, one can obtain an approximation for the distribution by substituting  $t = t_{\min} \approx \frac{[(m+m_f)^2 - m_i^2]^2}{4E_i^2}$  into Eq. 4.69. For a rough approximation, one can also perform the limit  $\theta_k, m_\varphi/E, m_f/E, \sqrt{t}/E \ll 1$ , for which  $|\partial(E_k, \theta_k)/\partial(E', \theta')| \approx E/E_k - 1$ .

Using these formulae, it is possible to examine distributions for the final-state lepton akin to those distributions of the final-state  $\varphi$  studied in the previous sections. In Fig. 4.10, we plot the interquartile range for the  $\eta$  and  $\gamma$  distributions of the final-state lepton at each of the experiments considered in this chapter. Once again, we consider the scenario where  $\varphi$  is a scalar, and assess the distributions for the flavor-diagonal production process  $\ell^- A_Z \rightarrow \ell^- A_Z \varphi$  as well as the flavor-violating  $\tau$ -conversion process  $\ell^- A_Z \rightarrow \tau^- A_Z \varphi$ . The pseudo-rapidity distributions for the final-state  $\ell'$  look similar to those of the  $\varphi$ , which is reasonable given that these must satisfy (up to nuclear recoil)  $|\mathbf{p}_\varphi| \sin \theta_\varphi = |\mathbf{p}_{\ell'}| \sin \theta_{\ell'}$ . Notably, the boost distributions are much less dependent on  $m_\varphi$ , which is also understandable. In particular, when the  $\ell'$  is the heavier of the two, one expects  $\gamma_{\ell'} \approx E_\ell/m_{\ell'}$ , which is a constant at these experiments. Dependence on  $m_\varphi$  only enters when most of the available energy from  $E_\ell$  goes to the  $\varphi$ , so that  $\gamma_{\ell'} \ll E_\ell/m_{\ell'}$ . Even so, we see only mild dependence of  $\gamma_\ell$  on  $m_\varphi$  in the diagonal production case for  $m_\ell < m_\varphi$ .

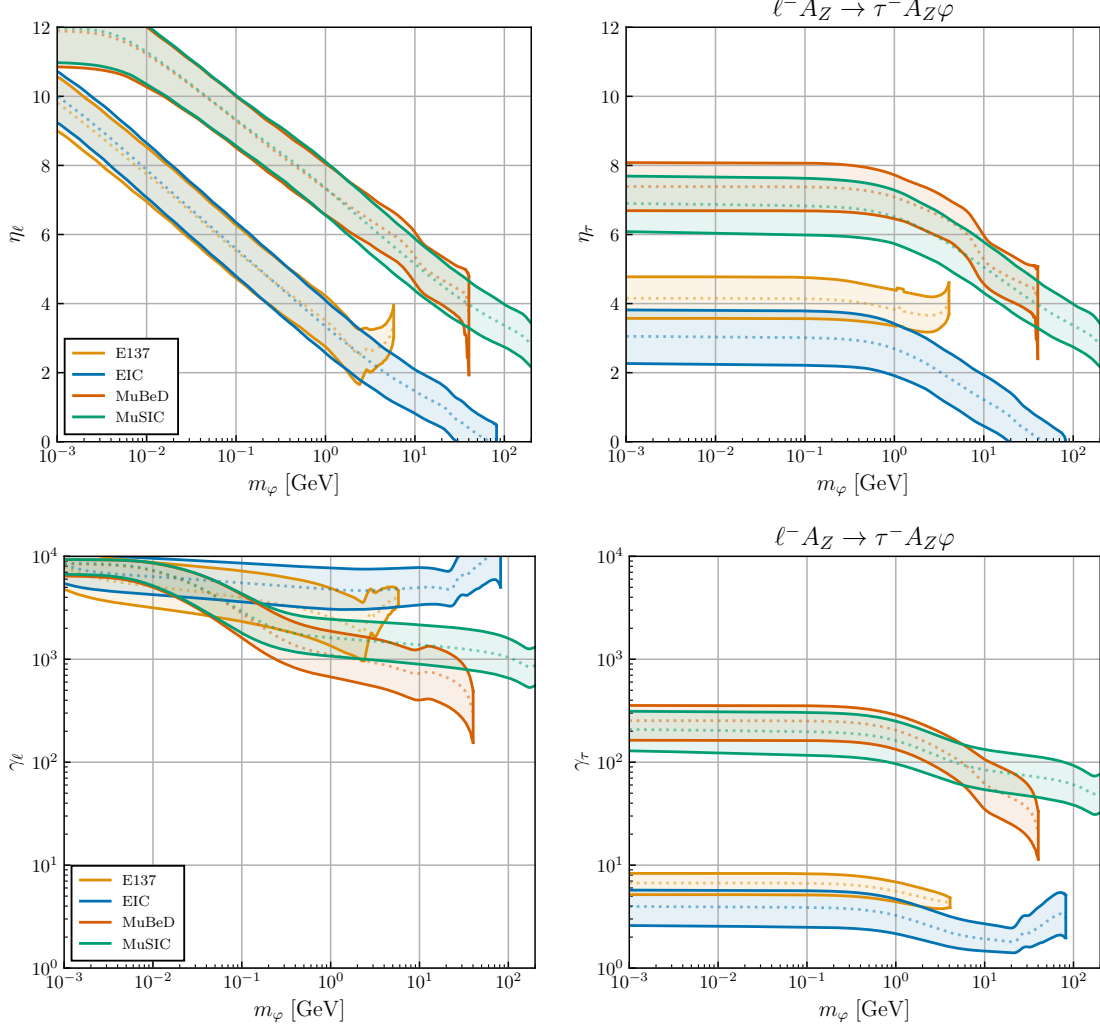


Figure 4.10: The interquartile range as a function of mass  $m_\varphi$  for the pseudo-rapidity of the final-state lepton (top) and the boost of the final-state lepton (bottom), for both flavor-diagonal (left) and  $\tau$ -conversion (right) processes.

#### 4.8 Case Study: Limits on LFV Scalars

To close out the chapter, we will apply the results of this section to present limits on LFV scalars for the EIC, MuBeD, and MuSIC. This is a natural extension to our previous work on LFV ALPs [139, 150, 151] through the conversion formula Eq. 2.31. We assume the same signal and background analysis, which we describe in more detail in Chapter 5 for LFV ALPs but summarize

here. We consider production of an LFV scalar  $\varphi$  with mass  $m_\varphi$  and  $\ell\text{-}\tau$  interaction

$$\mathcal{L}_{\text{int.}} = g_{\ell\tau} \varphi \bar{\tau} (\cos \theta_{\ell\tau} + \sin \theta_{\ell\tau} \gamma^5) \ell + \text{H.c.} \quad (4.70)$$

where  $\ell = e$  for the EIC and  $\ell = \mu$  for MuBeD and MuSIC. For simplicity, we assume all other couplings are zero, although our results are only dependent on this choice through the branching-fraction of the  $\varphi$  to  $e^+\tau^-$ . The main effect that this has is opening up the available parameter space to be probed, since models with multiple non-zero couplings are much more constrained by LFV lepton decays (see Chapter 3). We consider production and subsequent decay of a  $\varphi$  through the process  $\ell^- A_Z \rightarrow \tau^- A_Z \varphi (\varphi \rightarrow \tau^- \ell^+)$ , which has a very distinctive LFV final-state.

We begin by describing the lepton-ion collider analysis. Due to the difficulty of multi- $\tau$  identification, we only require identification of one  $\tau^-$  in the final-state, along with an  $\ell^+$ , and we veto on identification of an  $\ell^-$  to reinforce the LFV nature of the final-state. Such a signal can still be mimicked at the EIC or MuSIC through ditau production  $\ell^- A_Z \rightarrow \ell^- A_Z \tau^+ \tau^-$  if the final-state  $\ell^-$  escapes down the beam-pipe, evading the  $\ell^-$  veto. Then, the leptonic decay  $\tau^+ \rightarrow \ell^+ \bar{\nu}_\tau \nu_\ell$  could allow for identification of a  $\tau^-$  and  $\ell^+$  in the final-state. The complete background analysis for this process at these detectors is provided in Section 5.3.2 for LFV ALPs. In this section, we take  $\epsilon_\tau = 1\%$  at the EIC and MuSIC. The only specific detector geometry we will consider is the pseudo-rapidity range. For the EIC, we take  $|\eta| < 3.5$ , whereas for MuSIC, we take  $|\eta| < 6$ . The latter choice is in line with the anticipated pseudo-rapidity reach of the B0 spectrometer at the EIC [149]. Given the additional beam energy and larger mass of the initial-state muon, we believe this is a reasonable detector requirement to ensure the final-state muon is able to be IDed.

For the muon fixed-target experiment MuBeD, we consider a set-up where the 1 TeV muon beam is incident on a 2 cm block of lead, instrumented on either end by veto and tracking layers, and accompanied on the far end by a spectrometer. We assume a modest number of muons on target,  $N_\mu = 10^{16}$ , which should be achievable in at most a few days of operation. For the signal, we require identification of the  $\mu^+$  and both final state  $\tau^-$ . We expect that the experiment can be instrumented such that all 3-prong-decaying  $\tau^-$  which have a decay length greater than 2 cm

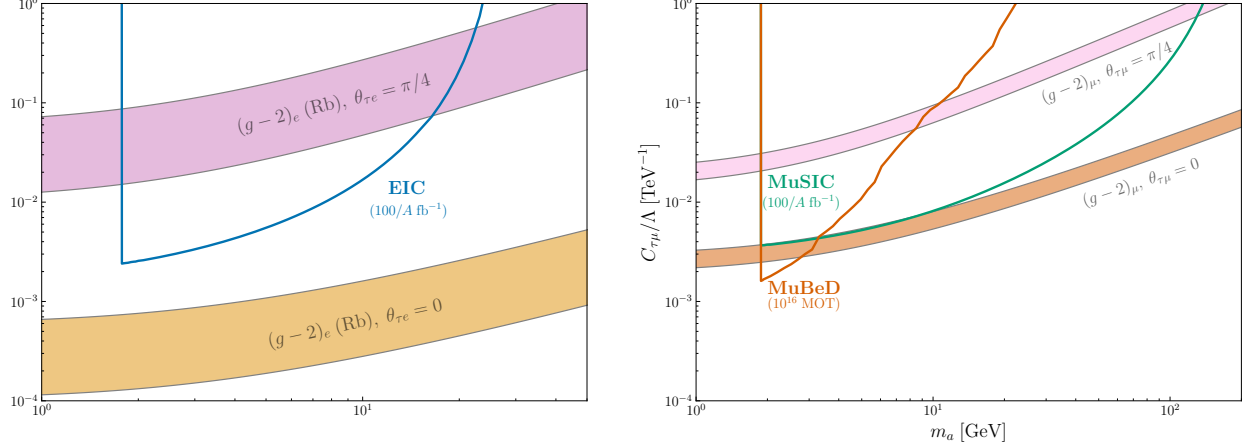


Figure 4.11: (Left) limits on the  $g_{\tau e}$  coupling at the EIC (assuming a  $\tau$ -identification efficiency of  $\epsilon_\tau = 1\%$ ), alongside pure and chiral scalar explanations to the electron  $g - 2$  anomaly using  $\alpha(\text{Rb})$ . (Right) limits on the  $g_{\tau \mu}$  coupling at MuSIC (assuming a  $\tau$ -identification efficiency of  $\epsilon_\tau = 1\%$ ) and MuBeD (according to the analysis in the text), alongside pure and chiral scalar explanations to the muon  $g - 2$  anomaly.

can be identified. Given the boost of the final-state  $\tau^-$  at such an experiment (see Fig. 4.10), this corresponds to a significant fraction of all  $\tau^-$  produced in the interaction. Provided the charge of the leptons can be resolved, the identification of a  $\mu^+\tau^-\tau^-$  final-state is a clear LFV signal with no SM background.

We plot the results of the analyses in Fig. 4.11. Interestingly, the parameter-space probed is very close to the LFV explanations to the electron and muon  $g - 2$  anomalies reviewed in Section 3.4.7. To emphasize this point, we plot pure and chiral explanations to these anomalies alongside the limits. It appears that the EIC is able to probe chiral and near-chiral explanations of the electron  $g - 2$  anomaly (at least using  $\alpha(\text{Rb})$ ), and MuBeD and MuSIC both explore nearly the entire parameter space of such explanations for GeV-scale  $\varphi$ . To get a better sense of the sensitivity of each experiment to these explanations, we plot the region of accessible solutions to the anomalies in the  $(m_\varphi, \theta_{\tau\ell})$  plane in Fig. 4.12.

In the event that the electron and muon anomalies are resolved, the “explanations” in Fig. 4.11 correspond roughly to constraints that one obtains from the magnetic dipole moment measurements, as shown in Fig. 3.5. Then, we see that these experiments provide competitive and sometimes

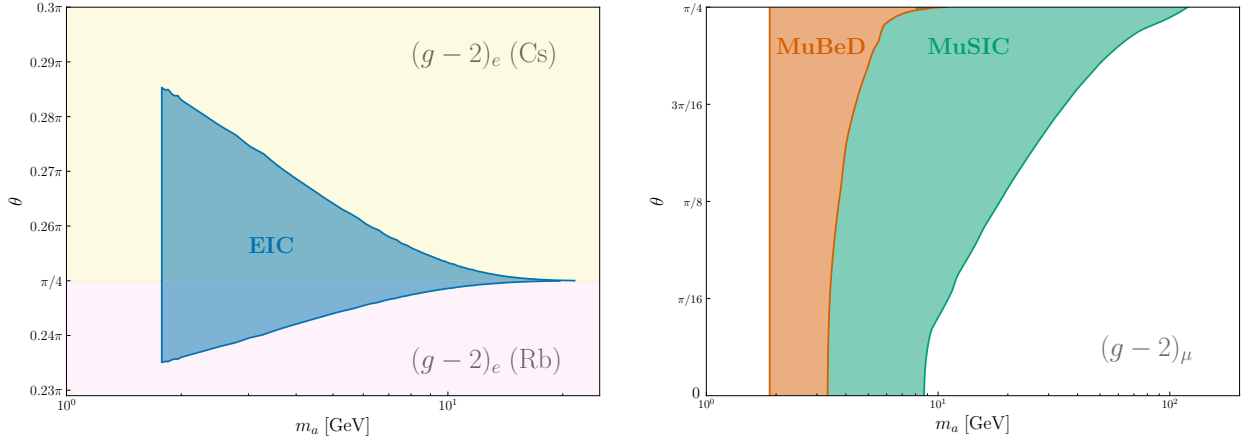


Figure 4.12: Region in the  $(m_\varphi, \theta_{\ell\tau})$  parameter space for which a  $g - 2$  explanation is probed within  $2\sigma$  at each of the colliders. In particular, the EIC is sensitive to explanations for *both* the Cesium and Rubidium electron  $g - 2$  anomalies depending on whether the angle  $\theta_{e\tau}$  is above or below  $\pi/4$ . However, explanations to the muon  $g - 2$  anomaly require  $\theta_{\mu\tau} < \pi/4$ . The EIC is sensitive to chiral and near-chiral explanations of the electron  $g - 2$  anomalies, whereas both MuSIC and MuBeD probe nearly all explanations of the muon  $g - 2$  anomaly for GeV-scale  $\varphi$ .

superior constraints, depending on the PV nature of the scalar interaction. Notably, while the limits from these experiments are nearly independent of the degree of PV angle for heavy  $\varphi$ , the limits from the magnetic dipole moment weaken considerably. However, it should be noted that such limits are superseded by limits from LFV lepton decays provided that additional couplings are non-zero, as is evident in Fig. 3.3. Hence, while these experiments provide limits on the flavor-violating  $g_{\ell\tau}$  coupling which are model-dependent up to the branching of the  $\varphi$ , the resulting limits are less sensitive than those obtained for models with generic non-zero couplings.

## Chapter 5

### GeV-Scale LFV Axion-Like Particles in Collider Experiments

*This chapter is based on work done in Refs. [150–153].*

#### 5.1 Introduction

One of the biggest potential challenges for discovery in modern-day particle physics is the vast disparity of scales between our current highest energy experiments ( $\mathcal{O}(10^4 \text{ GeV})$ ), and the Planck scale ( $10^{18} \text{ GeV}$ ). In principle, new physics can lie anywhere between these two scales, possibly far beyond the reach of our experimental capabilities. A naive estimate for the scale that generates neutrino mass yields  $\Lambda \sim 10^{15} \text{ GeV}$ , which is intriguingly close to the expected scale of grand unification [154]. If new physics doesn't appear until this scale (or even many orders of magnitude below it), how can we ever hope to make progress in the field?

Axion-like particles (ALPs) offer a promising way out of this conundrum. As described in Section 2.4, ALPs are the pseudo-Nambu-Goldstone bosons of spontaneously broken approximate global symmetries. By virtue of this definition, they are light relative to the physics scale from whence they came. While the discovery of an ALP wouldn't give us a complete description of the underlying physics, analyzing its couplings to the SM particles would help us determine the symmetry-breaking scale, potentially guiding design for future particle-physics experiments.

ALPs are often thought of as very light, but they can generically be quite heavy if their associated global symmetry is spontaneously broken at a large scale or if the explicit breaking of said symmetry is substantial. In Chapter 2, we encountered a few scenarios in which the low-energy

effective theory contained ALPs with multi-GeV masses, namely ALPs from  $\mathbb{Z}_N$  Froggatt-Nielsen models [49] and dark pions from composite dark matter models [51]. The prospect of new particles at this scale which couple to the SM is exciting, as they are in a “Goldilocks zone” for modern experiments: not so heavy that they can’t be produced in GeV or TeV-scale collisions, but not so light that they decay far beyond the confines of the experimental apparatus. In addition to lying within an accessible mass range, the ALPs in these models also exhibit LFV couplings to the ALP, offering an enticing avenue for their discovery. While we have only focused on a few scenarios in which LFV ALPs arise, we note that any UV theory that couples to the lepton sector of the SM will contain LFV unless it is explicitly protected.

We have already explored limits on LFV couplings to the ALPs in Chapter 2. Notably, the limits become much weaker for  $m_a > m_\tau$ , since the heavily constrained decay mode  $\tau \rightarrow \ell_i \ell_j \bar{\ell}_k$  can no longer proceed via an on-shell ALP. In this regime, Fig. 3.3 indicates that a scale of  $\Lambda \sim 10$  TeV is still very much in reach as the source of such particles. One important caveat from these limits is that they are limits on the products of two couplings. In the reasonable scenario that the on-diagonal couplings are larger than the off-diagonal couplings, one could even expect unconstrained LFV physics at  $\Lambda \sim 1$  TeV. While the leptonic decay modes involve products of the couplings, individual couplings (flavor-conserving and flavor-violating) can be probed by measurements of the lepton dipole moments. If one takes these as constraints, we have also found  $\Lambda \sim 1$  TeV.

Given their direct coupling to leptons, one might expect strong limits for such ALPs to come from electron-positron colliders such as LEP and CESR via the production-process  $e^+e^- \rightarrow a\gamma$  or the  $s$ -channel  $e^+e^- \rightarrow a^* \rightarrow \ell^+\ell^-$ . However, due to the mass-dependence of ALP-fermion couplings, the cross-section of this process would be suppressed by  $m_e^2/\Lambda^2 \sim 10^{-13}$  for  $\Lambda = 1$  TeV. Hence, we are forced to look elsewhere for signatures of such particles.

In the event that the LFV ALP couples to the Higgs (as is the case for the composite ALP from Ref. [51]), one promising avenue for discovery is through decays of the form  $h \rightarrow aa \rightarrow \ell^+\ell^-\ell^+\ell^-$  for  $\ell \neq \ell'$ , as this is a very distinct LFV final-state. LFV decays of the Higgs boson of this form were studied previously in Ref. [155], but in that work the intermediate particles were taken to

be scalar rather than ALPs. With ALPs, the parameter space of constraints will be somewhat different. In particular, since the ALP decay widths are proportional to the mass-squared of the final-state particles, decays of the form  $h \rightarrow aa \rightarrow \tau^\pm \tau^\pm \ell^\mp \ell'^\mp$  will be dominant.

An alternative approach which does not rely on a Higgs coupling is production from coherent electromagnetic interactions between leptons and heavy nuclei ( $\ell^- A_Z \rightarrow \ell^- A_Z a$ ), such as those studied in Chapter 4. While most existing electron and muon beam dumps have energies too small to produce GeV-scale ALPs at any appreciable rate, this may change with research and development into a multi-TeV muon collider [132–134]. In addition, the Electron Ion Collider (EIC) will be the equivalent of a multi-TeV electron beam dump in the rest frame of the heavy nuclei,<sup>1</sup> so peripheral production of GeV-scale particles will be possible. Looking forward, the case has been made for a future Muon (Synchrotron)-Ion Collider (MuSIC) due to its potential to probe nuclear substructure [137, 138] and new physics beyond the SM [153]. The benefit of these approaches is that, up to the branching of the final-state ALP, they are independent from the other couplings in the model. Hence, they provide an absolute constraint on the coupling  $C_{\tau\ell}/\Lambda$ .

In this Chapter, we will explore constraints on GeV-scale LFV ALPs in various collider settings. In Section 5.2, we find limits on such particles at the LHC in the presence of a Higgs portal interaction for the ALP. In Section 5.3, we examine limits on the  $e\tau$  coupling of the ALP from the upcoming EIC, and explore a region of the parameter space for which the interaction can explain either of the electron  $g - 2$  anomalies. In Section 5.4, we repeat this analysis for a muon beam dump experiment (MuBeD) along with the hypothetical MuSIC experiment, exploring a region of the  $\mu\tau$  coupling parameter space that is of interest for the muon  $g - 2$  anomaly.

## 5.2 Higgs Decays at the LHC

We begin by studying LFV ALPs with a significant Higgs-portal interaction, under the assumption that the ALP is leptophilic. Then, the relevant terms from the EFT Lagrangian 2.21 are

---

<sup>1</sup> With a sacrifice in luminosity.

[43, 45]

$$\mathcal{L} = \frac{1}{2}(\partial_\mu a)^2 - \frac{1}{2}m_a^2 a^2 + \mathcal{L}_\ell + \mathcal{L}_h \quad (5.1)$$

where the ALP-lepton interaction is given by

$$\mathcal{L}_\ell = \frac{\partial_\mu a}{\Lambda} \sum_{\ell, \ell'} \bar{\ell} \gamma^\mu [A_{\ell\ell'} - \gamma_5 V_{\ell\ell'}] \ell' + \text{H.c.} \quad (5.2)$$

and the ALP-Higgs interaction is

$$\mathcal{L}_h = \frac{C_{ah}}{\Lambda} v (\partial_\mu a)^2 h + \frac{C'_{ah}}{\Lambda^2} v m_a^2 a^2 h. \quad (5.3)$$

The presence and size of each coupling  $C_{ah}$  and  $C'_{ah}$  is dependent on the nature of the UV theory that gives rise to the ALP. Given the interaction term (5.3), the decay rate for  $h \rightarrow aa$  is given by

$$\Gamma(h \rightarrow aa) = \frac{1}{32\pi} \frac{v^2 m_h^3}{\Lambda^4} \sqrt{1 - \frac{4m_a^2}{m_h^2}} \left( C_{ah} - 2(C_{ah} - C'_{ah}) \frac{m_a^2}{m_h^2} \right)^2. \quad (5.4)$$

At this point, it is useful to parametrize the Higgs decay rate in terms of an effective ALP-Higgs coupling:

$$\Gamma(h \rightarrow aa) = \frac{1}{32\pi} \frac{v^2 m_h^2}{\Lambda^4} \left( 1 - \frac{2m_a^2}{m_h^2} \right)^2 \sqrt{1 - \frac{4m_a^2}{m_h^2} \bar{C}_{ah}^2} \quad (5.5)$$

where

$$\bar{C}_{ah} \equiv C_{ah} + C'_{ah} \frac{2m_a^2}{m_h^2 - 2m_a^2}. \quad (5.6)$$

Rather than presenting limits on  $C_{ah}$  and  $C'_{ah}$  independently, we will focus on limits on the combined effective coupling  $\bar{C}_{ah}$  for the majority of this section. We will specialize to certain values of  $C_{ah}$  and  $C'_{ah}$  in Section 5.2.3.

For  $m_a > m_\ell + m_{\ell'}$ , the process  $a \rightarrow \ell\ell'$  occurs with decay width

$$\Gamma(a \rightarrow \ell\ell') = \frac{C_{\ell\ell'}^2}{8\pi\Lambda^2} \left[ m_{\ell\ell'}^2 (\Theta_{\ell\ell'}) - \frac{(m_\ell^2 - m_{\ell'}^2)^2}{m_a^2} \right] \sqrt{(m_a^2 - (m_\ell - m_{\ell'})^2)(m_a^2 - (m_\ell + m_{\ell'})^2)} \quad (5.7)$$

where  $C_{\ell\ell'} = \sqrt{|A_{\ell\ell'}|^2 + |V_{\ell\ell'}|^2}$ ,  $\Theta_{\ell\ell'} = \tan^{-1} |V_{\ell\ell'}/A_{\ell\ell'}|$ , and  $m_{\ell\ell'}^2(\Theta) = m_\ell^2 + m_{\ell'}^2 + 2m_\ell m_{\ell'} \cos 2\Theta$ .

Due to the lepton mass hierarchy, either  $m_{\ell'} = m_\ell$  or (without loss of generality)  $m_{\ell'} \ll m_\ell$ , so it is useful to express the width in each of these cases:

$$\Gamma(a \rightarrow \ell^\pm \ell'^\mp) = \frac{m_a m_\ell^2}{8\pi \Lambda^2} \begin{cases} C_{\ell\ell'}^2 (1 - m_\ell^2/m_a^2)^2 & \ell' \ll \ell, \\ 4A_{\ell\ell}^2 (1 - 4m_\ell^2/m_a^2)^{1/2} & \ell' = \ell. \end{cases} \quad (5.8)$$

Notably, the decay rate is proportional to the square of the heavier lepton mass, so the ALP will almost always decay via  $a \rightarrow \tau\ell$ . For equivalent couplings and  $m_a \gg m_\ell \gg m_{\ell'}$ , we have  $\Gamma(a \rightarrow \ell\ell) \approx 4\Gamma(a \rightarrow \ell\ell')$ . Hence, one expects the dominant decay mode of the ALP to be  $a \rightarrow \tau\tau$ , followed by  $a \rightarrow \tau\ell$  with  $\ell = e$  or  $\mu$ . Of course, this is subject to change based on the underlying hierarchies between the ALP-lepton couplings.

Even in the absence of a photon coupling, the  $a \rightarrow \gamma\gamma$  decay mode is generated at loop level via a triangle diagram. Specializing Eq. 2.23 to the case of only leptonic couplings, we have

$$\Gamma(a \rightarrow \gamma\gamma) = \frac{4\pi\alpha^2 m_a^3}{\Lambda^2} |C_{\gamma\gamma}^{\text{eff.}}|^2, \quad (5.9)$$

where

$$C_{\gamma\gamma}^{\text{eff.}} = \sum_\ell \frac{A_{\ell\ell}}{8\pi^2} B_1(4m_\ell^2/m_a^2) \quad (5.10)$$

and  $B_1$  is given in Eq. 2.25. In particular,  $B_1(\tau \rightarrow 0) \rightarrow 1$ , so the loop-induced photonic decay rate can grow quite large for heavy ALPs. It is worthwhile to compare the loop-induced photon decay rate to the flavor-violating decay rate  $a \rightarrow \tau\ell$ . Their ratio is given by

$$\frac{\Gamma(a \rightarrow \gamma\gamma)}{\Gamma(a \rightarrow \tau^\pm \ell^\mp)} \sim \frac{9\alpha^2 m_a^2}{2\pi^2 m_\tau^2} \frac{|\overline{A}_{\ell\ell}|^2}{|C_{\tau\ell}|^2} \sim \left( \frac{1}{200} \frac{m_a}{m_\tau} \frac{|\overline{A}_{\ell\ell}|}{|C_{\tau\ell}|} \right)^2 \quad (5.11)$$

where  $\overline{A}_{\ell\ell}$  is the average of the ALP couplings to the lepton axial vector current. Hence, we see that the  $a \rightarrow \gamma\gamma$  rate will become comparable to the  $a \rightarrow \tau\ell$  rate when  $|C_{\tau\ell}| \lesssim \frac{m_a}{200m_\tau} |\overline{A}_{\ell\ell}|$ . Given that we are considering ALPs in the GeV range, it is safe to ignore this decay mode in our discussions. To emphasize this point, we plot the branching-fraction of the ALP assuming a democratic ALP-lepton coupling matrix in Fig. 5.1.

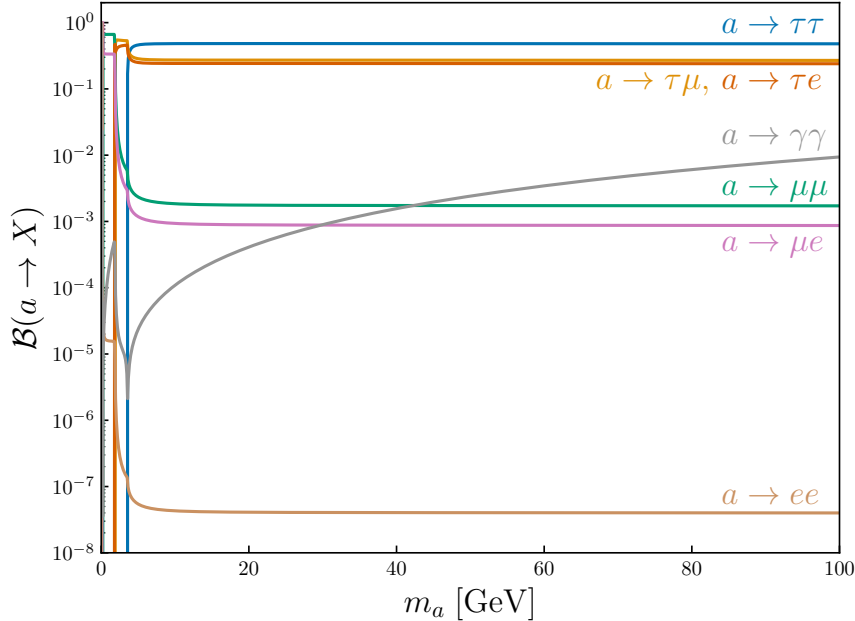


Figure 5.1: ALP branching fraction assuming a democratic lepton coupling matrix (and all other couplings zero). The ALP will decay to at least one  $\tau$  roughly 99.7% of the time.

For the remainder of this section, we will present limits on the model under the assumption of democratic couplings (or at the very least,  $C_{\tau e} \sim C_{\tau \mu} \sim C_{\tau \tau}$ ). However, we should note that our results are more-or-less insensitive to this choice, because  $a \rightarrow \tau\tau$  (which is always dominant) can mimic the  $a \rightarrow \tau\ell$  decay mode via a leptonic decay of one of the final-state  $\tau$ .

### 5.2.1 Prompt ALP Decays at CMS

We will begin by considering the scenario where the ALPs are produced in Higgs decays then themselves decay promptly within the CMS detector at the LHC. We present constraints on the leptonic couplings based on the search in Ref. [156] for proton-proton collisions which result in four charged lepton final states. The Higgs decays that we are most interested in are those of the form  $h \rightarrow (\tau^\pm \ell^\mp)(\tau^\pm \ell^\mp)$  due to the strongly LFV final-state; these primarily contribute to the “OSSF0” signal in Ref. [156], which corresponds to those events for which the number of opposite-sign, same-flavor (OSSF) lepton pairs is zero. The study only includes electrons and muons in the OSSF0 signal, so this requires each  $\tau$  in our final-state to decay leptonically, resulting in decay modes of

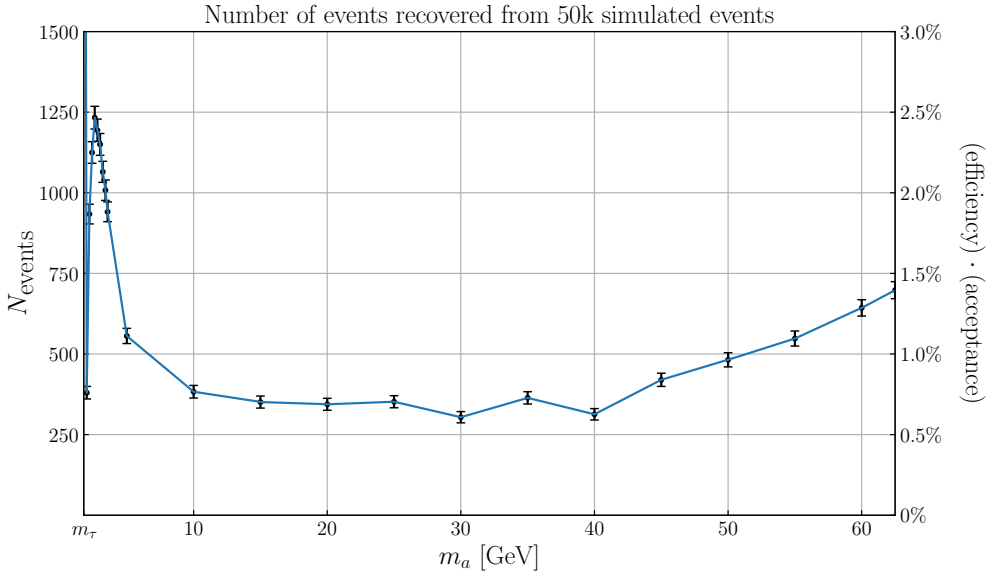


Figure 5.2: The number of OSSF0 events reconstructed from a simulation of 50 000  $h \rightarrow aa$  decay events in **MadGraph** for sample masses between  $m_a = m_\tau$  and  $m_a = m_h/2$ . The signal efficiency is then estimated by taking the fraction of such events.

the form  $h \rightarrow aa \rightarrow \mu^\pm \mu^\pm e^\mp e^\mp (+\text{neutrinos})$ .

To recast this study for our model, we reproduce the LFV ALP EFT in **FeynRules** [157] and simulate parton-level events with **MadGraph5\_aMC@NLO** [158]. We then use **PYTHIA8** for showering and simulate the CMS detector with **DELPHES** [159]. We produce 50 000 events of the form  $gg \rightarrow h, h \rightarrow aa \rightarrow$  OSSF0 for the masses  $m_a = 2\text{-}3.6$  GeV with a step of 0.2 GeV, and  $m_a = 5\text{-}60$  GeV with a step of 5 GeV. We additionally consider  $m_a \approx m_h/2 = 62.5$  GeV for a total of 22 different masses. The number of OSSF0 signal events recorded from the initial 50 000 (along with the corresponding signal efficiency· acceptance), based on the analysis conducted in Ref. [156], is shown in Fig. 5.2. In the study, the number of events with OSSF0 pairs predicted and observed at a luminosity of  $\mathcal{L} = 137 \text{ fb}^{-1}$  was 7. Following the analysis in Ref. [160], the 95% confidence interval on the Poisson mean for the number of signal events when the expected background and observed number of events are both 7 is  $(0, 6.81)$ . A 95% C.L. upper-limit on the branching fraction is then

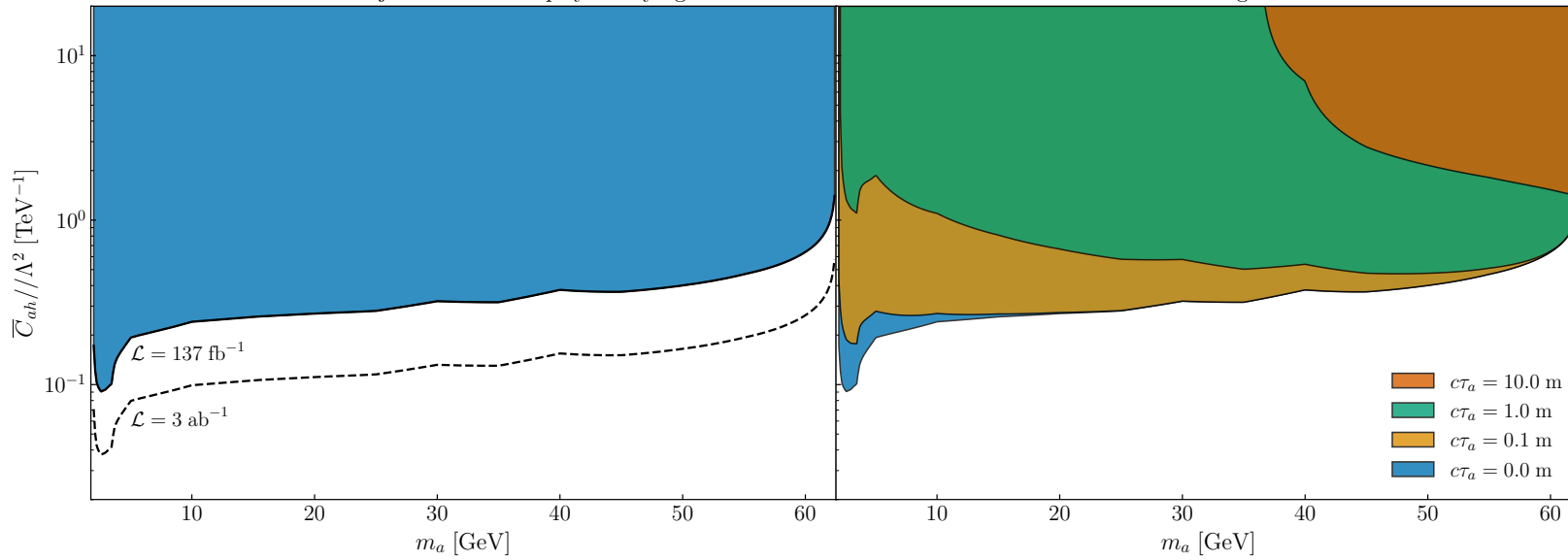


Figure 5.3: (Left) Limits on the Higgs-ALP effective coupling  $\bar{C}_{ah}$  according to the analysis performed in Ref [156], assuming the ALP decays promptly. (Right) the same limits recast assuming the ALP has a non-zero lifetime  $\tau_a$ .

derived via

$$\epsilon\sigma_{gg\text{h}}\mathcal{B}(h \rightarrow aa \rightarrow \text{OSSF0}) \leq 6.81 \quad (5.12)$$

where  $\epsilon$  is the signal efficiency and acceptance. We can recast this constraint to a constraint on  $\bar{C}_{ah}$  using the theoretical branching fraction for  $\mathcal{B}(h \rightarrow aa \rightarrow \text{OSSF0})$  and interpolating  $\epsilon$  from Fig. 5.2 to all values of mass. The results of this constraint for  $\mathcal{L} = 137 \text{ fb}^{-1}$  and a projected value of  $\mathcal{L} = 3 \text{ ab}^{-1}$  are shown in the left panel of Fig. 5.3. For the projection, we take  $\mathcal{L} = 3 \text{ ab}^{-1}$  assume that the number of observed and expected background events scale linearly with  $\mathcal{L}$ , which corresponds to a 95% confidence interval on the Poisson mean of the number of signal events of  $(0, 25.9)$ .

The analysis so far has operated under the assumption that the ALP decays promptly. However, some fraction of ALPs with long lifetimes will also decay within the CMS apparatus. The fraction of pair-produced long-lived ALPs which decay within a cylindrical detector of radius  $L_{\text{det}}$

is [44]

$$f_{aa} = \int_0^{\pi/2} d\theta \sin \theta \left(1 - e^{-L_{\text{det}}/(\gamma_a c \tau_a \sin \theta)}\right)^2 \quad (5.13)$$

where  $\gamma_a$  is the boost of the ALP and  $\tau_a = 1/\Gamma_a$  is the lifetime of the ALP in its rest frame. We take  $\gamma_a \approx m_h/2m_a$ , which is valid under the assumption that the Higgs is not heavily boosted. Taking  $L_{\text{det}} = 1.1$  m for the inner detector of CMS, we can recast the prompt constraints to account for long-lived ALPs by multiplying  $f_{aa}$  to the signal efficiency  $\epsilon$ . These results are shown in the right panel of Fig. 5.3.

### 5.2.2 Displaced ALP Decays at ATLAS and MATHUSLA

In addition to recasting prompt constraints to account for ALPs with long lifetimes, we can also examine constraints from searches for long-lived particles at CERN. One difficulty with such a task is that the main decay mode of the ALP has a very high hadronic background (for example, from  $B$  mesons) for displaced decays in the ATLAS or CMS inner detectors. As a result, we expect displaced decay analyses to become more important and fruitful when the ALP can travel into the muon spectrometer. This corresponds to  $\tau_a \gtrsim 1$  m or  $C_{\tau\ell}/\Lambda \lesssim 10^{-5}$  TeV $^{-1}$  for  $m_a = 10$  GeV. One work that considers such a scenario is Ref. [161], which places constraints on the Higgs decaying into long-lived particles which have displaced jets in the final state by combining data from the ATLAS inner detector with data from the muon spectrometer. In particular, they consider the scenario in which one displaced jet is found in the inner detector and the other is found in the muon spectrometer. Since most of the ALPs in our model decay with at least one  $\tau$  and most  $\tau$ s decay hadronically, this study can be used to constrain our model.

To adopt the work for our purposes, we digitize their results for a 95% C.L. upper limit on the branching fraction for Higgs into two scalars using **DigitizeIt** [162], then use a piecewise polynomial fit to generalize it to a variety of masses and lifetimes. The plots we digitize cover an extensive regions of lifetimes but are presented for only four masses:  $m_a = 10, 25, 40$ , and 55 GeV. Because of the limited data along the mass dimension, we account for the overfitting

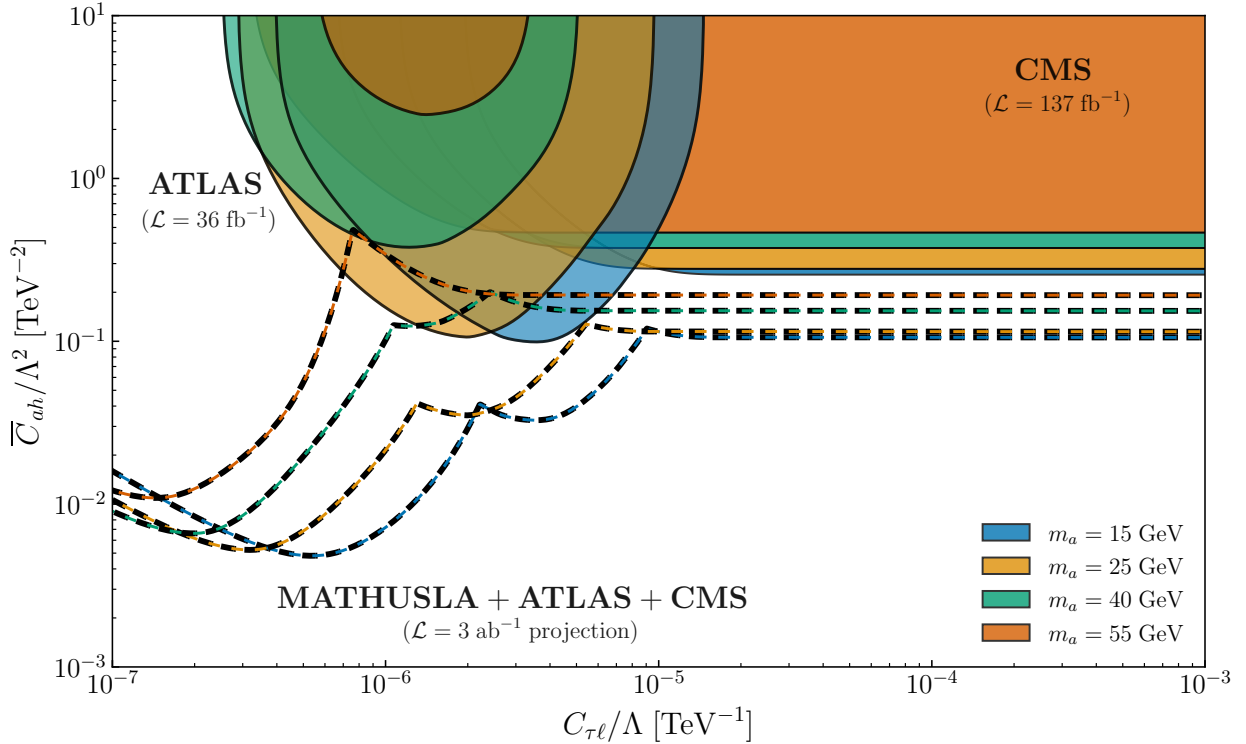


Figure 5.4: Exclusion plots for the Higgs coupling  $C_{ah}$  and LFV coupling  $C_{\tau\ell}$ , for the masses  $m_a = 10, 25, 40$ , and  $55$  GeV. The dashed lines encompass  $3 \text{ ab}^{-1}$  projections from ATLAS and CMS, as well as the proposed MATHUSLA experiment.

by interpolating plots for  $m_a = 15, 32.5$ , and  $47.5$  GeV using the geometric mean of the limits corresponding to the two nearest masses, then use these values along with the original masses to ensure that the fit function has a relatively smooth dependence along the mass dimension. The fit function agrees well with the data in regions of overlap, but we stress the results are likely to be accurate outside of the region  $(10 \text{ GeV}, 55 \text{ GeV})$ . For more accurate data in these mass regimes, the analysis of Ref. [161] would need to be repeated over a wide range of masses. the details of this fitting procedure can be found in the Github repository [163]. While the details of this fit are unimportant for the exclusions presented in this section (which focus on the mass values studied in Ref. [161]), they are necessary to present exclusions in the  $m_a$ - $C_{\tau\ell}$  plane as is done in the next section.

It is also straightforward to generate projections for  $\mathcal{L} = 3 \text{ ab}^{-1}$  by assuming that the limits

on the branching fraction scale inversely with  $\sqrt{\mathcal{L}}$ . However, stronger projections can be achieved by focusing on the community interest in dedicated long-lived particle detectors such as MATHUSLA [53, 164–166], CODEX-b [167], ANUBIS [168], and SHiP [128]. Here we focus on the projected constraints for MATHUSLA in Ref. [165], where the MATHUSLA detector is taken to be located on the surface of the Earth ( $\sim 100$  m above ATLAS and 100 m down the beam pipe, with dimensions  $100 \times 100 \times 20$  m $^3$ ). An estimate is provided in Ref. [164] for the projected constraint on the Higgs cross-section to long-lived particles:

$$(\epsilon \cdot \sigma)^{\text{MATH}} \approx \frac{4}{\mathcal{L} n_{\text{LLP}} P_{\text{decay}}^{\text{MATH}}(c\tau)}, \quad (5.14)$$

with

$$P_{\text{decay}}^{\text{MATH}} = \epsilon_{\text{geom}} \left( e^{-L_2/\gamma c\tau} - e^{-L_1/\gamma c\tau} \right) \quad (5.15)$$

where  $\gamma = m_h/2m_a$ ,  $(L_1, L_2) = (200$  m, 230 m),  $\epsilon_{\text{geom}} = 0.05$ , and  $n_{\text{LLP}}$  is the number of long-lived particles in the Higgs decay channel. We find that this approximation works well for the projected exclusions of  $\mathcal{B}(h \rightarrow aa)$  in Ref. [164] at long lifetimes, provided that we take  $(L_1, L_2) = (180$  m, 200 m) (due to the smaller detector size). At lower lifetimes, the approximation fails due to more complicated dependence on the detector acceptance and efficiency. Hence, for lower lifetimes, we fit the  $\mathcal{B}(h \rightarrow aa)$  projected exclusions in Ref. [164] with a polynomial fit, with the condition that it matches Eq. 5.14 for  $c\tau \gtrsim 10$  m. Details of the fit can once again be found in the Github repository [163]. The combined results of the ATLAS limits and projections, MATHUSLA projections, and CMS limits and projections are presented in Fig. 5.4. Rather than presenting exclusions in the  $\bar{C}_{ah}$ - $c\tau_a$  plane, we present exclusions in the  $\bar{C}_{ah}$ - $C_{\tau\ell}$  plane under the assumption of universal couplings, i.e.  $C_{\tau e} = C_{\tau\mu} = C_{\tau\tau}$ . As long as the Higgs-ALP coupling is substantial, we see that both the ATLAS and CMS constraints can probe the LFV couplings far beyond the limits from LFV leptonic decays in Fig. 3.3.

### 5.2.3 Combined Limits on LFV Couplings

Here we present the combined results from LFV leptonic decays, prompt decays, and displaced decays. To do so, we present exclusion plots on the off-diagonal coupling  $C_{\tau\ell}$  in the event that all couplings (or at the very least, those couplings to the  $\tau$ ) are universal. We note that limits on  $C_{\tau\ell}$  as a function of the ALP mass are dependent on the size and nature of the ALP-Higgs coupling. The terms  $C_{ah}$  and  $C'_{ah}$  are both present for, e.g., the pion in the SM:  $C_{ah}$  arises through a Higgs-gluon effective coupling due to heavy quark loops, whereas  $C'_{ah}$  arises from Yukawa couplings with the lighter quarks. Hence, which of the Higgs couplings is present likely depends on the UV nature of the LFV ALP. Since the  $C'_{ah}$  coupling is multiplied by a factor of  $m_a^2/m_h^2$  in the interaction term (5.3), the most relevant Higgs coupling is  $C_{ah}$  for light ALP masses. However, in scenarios with a heavy composite ALP in a theory with only light quarks which couple to the Higgs, such as the model in Ref. [51],  $C'_{ah}$  is the only significant ALP-Higgs coupling. All limits and projections are presented at the 95% C.L.. The limits are demonstrated in Fig. 5.5.

While one may expect that the leading limits on  $C_{\tau\ell}$  from LFV lepton decays to come from the branching limit on  $\mathcal{B}(\tau \rightarrow \ell\gamma)$ , this is only true if the off-diagonal couplings are small compared to the diagonal couplings. In the universal scenario we are considering, the leading constraint comes from  $\mu \rightarrow e\gamma$  due to the mass-enhancement of the diagram with an internal  $\tau$ . In particular, the leading limit on the branching fraction  $\mathcal{B}(\mu \rightarrow e\gamma)$  comes from the MEG experiment with  $\mathcal{B}(\mu \rightarrow e\gamma) < 4.2 \times 10^{-13}$ , and this can be directly converted into a limit on  $\sqrt{C_{\tau\mu}C_{\tau e}}/\Lambda$ , as is done in the bottom left panel of Fig. 3.3. We reproduce these limits in yellow in Fig. 5.5. The solid and dashed lines correspond to PC and chiral ALPs, respectively.

For significant Higgs-portal interactions, we see that the LHC provides competitive constraints for the  $C_{\tau\ell}$  coupling of the ALP. However, regardless of the value of the Higgs portal coupling, the model is relatively unconstrained for  $C_{\tau\ell}/\Lambda \lesssim 10^{-6} \text{ TeV}^{-1}$  due to the lifetime of the produced ALPs. Hence, there is a lot of unexplored potential for the long-lived ALPs which could potentially be discovered or ruled out by proposed detectors like MATHUSLA.

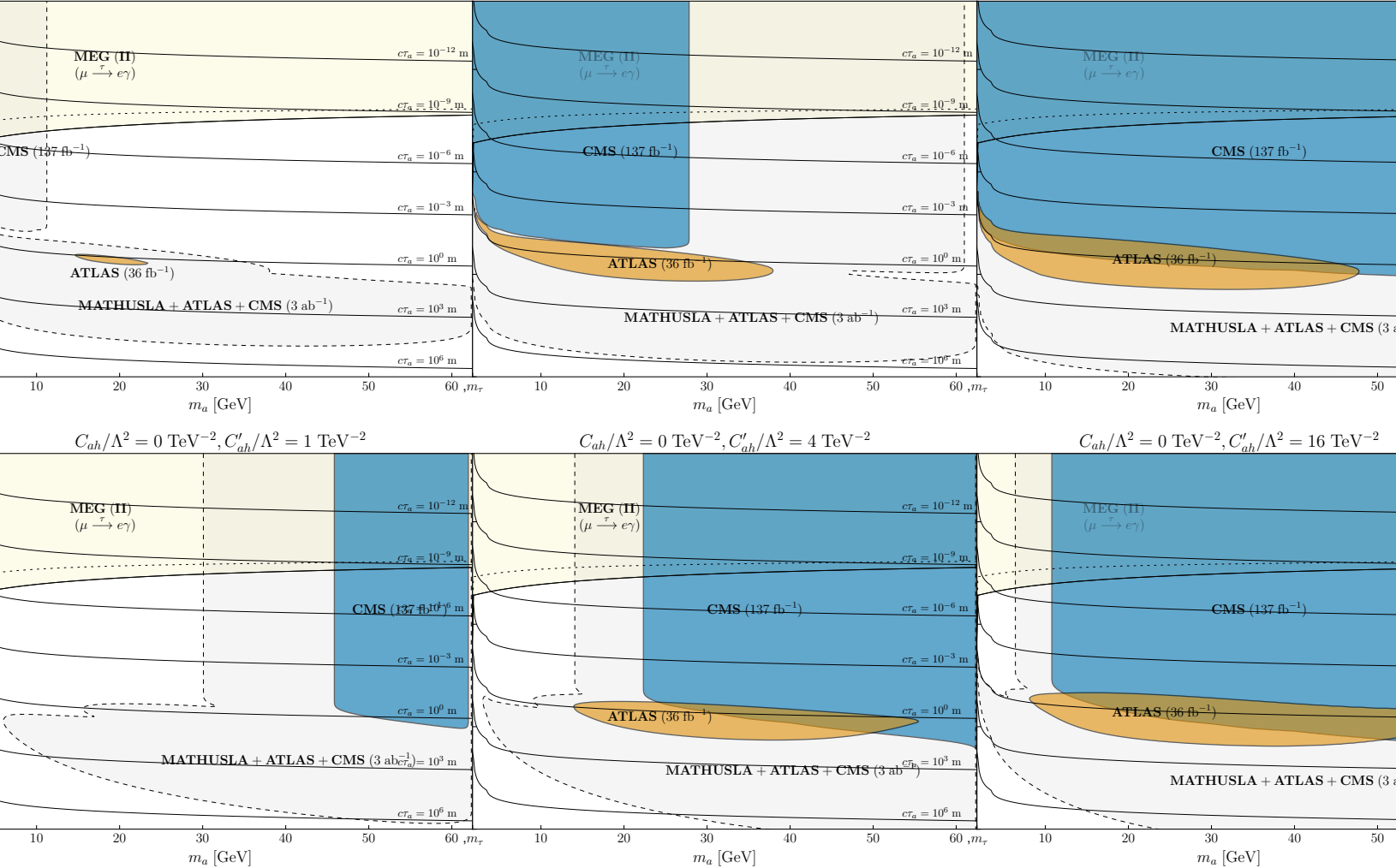
$C_{ah}/\Lambda^2 = 0.1 \text{ TeV}^{-2}, C'_{ah}/\Lambda^2 = 0.0 \text{ TeV}^{-2}$ 
 $C_{ah}/\Lambda^2 = 1.0 \text{ TeV}^{-2}, C'_{ah}/\Lambda^2 = 0.0 \text{ TeV}^{-2}$ 


Figure 5.5: Combined limits on the leptophilic LFV ALP model considered in this section, over a range of different Higgs interaction couplings. Limits from LFV lepton decays are presented in yellow, with the leading limit coming from  $\mu \rightarrow e\gamma$  through an internal  $\tau$ . Limits from Higgs decays at CMS are shown in blue, and at ATLAS are shown in orange. Finally, combined projections from CMS, ATLAS, and MATHUSLA assuming  $\mathcal{L} = 3 \text{ ab}^{-1}$  of integrated luminosity are shown in gray.

Finally, we note that for low enough Higgs coupling, the only significant constraints on the ALP-lepton coupling come from the LFV lepton decays. In this case, the limits presented are on a product of two couplings, so certain models with exotic hierarchies between the couplings (in the extreme case, only  $C_{\tau\ell} \neq 0$ ) will completely evade these constraints as well. We will explore this scenario in the next few sections in the context of ALP production from lepton-nucleus collisions, where a singular ALP coupling can be isolated and constrained, hence providing an absolute limit

on the coupling.

While we have focused on LFV ALPs, our results apply with limited modification to flavor-conserving leptophilic ALPs as well. In particular, each of the analyses we have conducted still have non-zero signals for the decay  $h \rightarrow aa \rightarrow \tau^\pm \tau^\mp$ . For the ATLAS analysis, all that matters is the identification of pairs of displaced jets, which is indeed more likely in the  $h \rightarrow aa \rightarrow \tau^\pm \tau^\mp$  scenario, and for the MATHUSLA scenario, the final-states of the long-lived particle are unimportant as long as they’re identifiable. Hence, the only limit which is noticeably weakened is the prompt CMS limit, because it relies on each  $\tau$  decaying leptonically. This has the effect of multiplying the limits in Fig. 5.5 by a factor of 3. The ALP-Higgs and diagonal ALP- $\tau$  coupling are probed in Fig. 30 of Ref. [44]; we note that while their results rely on a different analysis than ours, the limits we achieve are comparable in magnitude.

### 5.3 LFV ALP Production at The EIC

The EIC is expected to greatly improve our understanding of the strong interactions within heavy nuclei once it begins operation in the 2030s. We have previously considered an alternate possibility for the electron-nucleus collisions at the EIC in Chapter 4: namely, production of GeV-scale particles at the EIC through coherent electron-ion collisions, in which the electromagnetic interaction between the electron and the nucleus is enhanced by the number of protons in the nucleus. Here, we consider the possibility of probing the LFV coupling between an ALP and the flavor-changing  $e$ - $\tau$  current,  $C_{\tau e}/\Lambda$ , directly at the EIC via coherent production of the ALP, according to the process  $e^- A_Z \rightarrow \tau^- A_Z a$ . We will assume that the EIC is in gold mode, with  $E_e = 18$  GeV and  $E_{Au} = 110$  GeV/nuc. In the last section, we considered “democratic” coupling of the ALPs to the leptons. Here, we consider the opposite extreme: an ALP with a singular  $C_{\tau e}$  coupling. The EIC is uniquely poised to probe this region of the parameter space, and it also coincides with LFV ALP explanations to the electron  $g - 2$  anomalies that are not yet ruled out by other experiments.

Given that we are focused on a single coupling, we have the relatively simple interaction

Lagrangian

$$\mathcal{L}_{\text{int.}} = -\frac{\partial_\mu a}{\Lambda} C_{\tau e} \bar{\tau} \gamma^\mu (\sin \Theta + \cos \Theta \gamma^5) e + \text{H.c.} \quad (5.16)$$

We ignore CP-violating phases in this discussion, as any non-zero phase will likely be ruled out by the electron EDM constraints in Fig. 3.4. However, we do allow a PV angle  $\Theta$  in the interaction. The EIC cross-section is only dependent on this PV angle at  $\mathcal{O}(m_e/m_\tau)$ , so the limits obtained on  $C_{\tau e}$  from this section are essentially independent of the PV nature of the interaction. We are agnostic to the UV origins of such an interaction, but we point out that it is perturbatively protected by a  $\mathbb{Z}_4$  symmetry with  $Q(e) = i$ ,  $Q(\tau) = -i$ , and  $Q(a) = -1$ . Hence, one can expect that such a term will survive higher-order corrections from renormalization.

### 5.3.1 Detector Capabilities

For the expected capabilities of the EIC detector apparatus, we refer to the *Detector Requirements* section of the EIC Yellow Report [130]. For our purposes, we will assume that the EIC is operating in gold mode, with  $E_e = 18$  GeV and  $E_{\text{Au}} = 110$  GeV/nuc. In the rest frame of the nucleus, this corresponds to an electron energy of  $E = 4.2$  TeV, so this collision can be likened to a 4.2 TeV beam dump. It is reasonable to expect that a collision of this energy can produce GeV-scale ALPs. We take an integrated luminosity of  $\mathcal{L} = (100/A) \text{ fb}^{-1}$ , corresponding to about one year of operation in ion mode (assuming  $L = 10^{34} \text{ cm}^2/\text{sec}$  luminosity).

Of course, it is not enough to produce such particles, we must also be able to detect them. From the discussion in Section 4.6, we can expect that many of the ALPs which are produced have a high pseudorapidity. The Yellow Report indicates the EIC will have full coverage of  $|\eta| < 3.5$  [130], although the B0 spectrometer on the ion-side of the interaction is expected to have a coverage up to  $|\eta| < 6$  [149]. Given that the ALPs are produced off of the lepton-side of the interaction, they mostly end up on the electron-side of the detector, so we take  $|\eta| < 3.5$  for our study. Examining Fig. 4.7, we see that for scalars produced via  $e\tau$  conversion,  $|\eta| < 3.5$  is sufficient to capture a majority of GeV-scale particles produced in this way at the EIC.

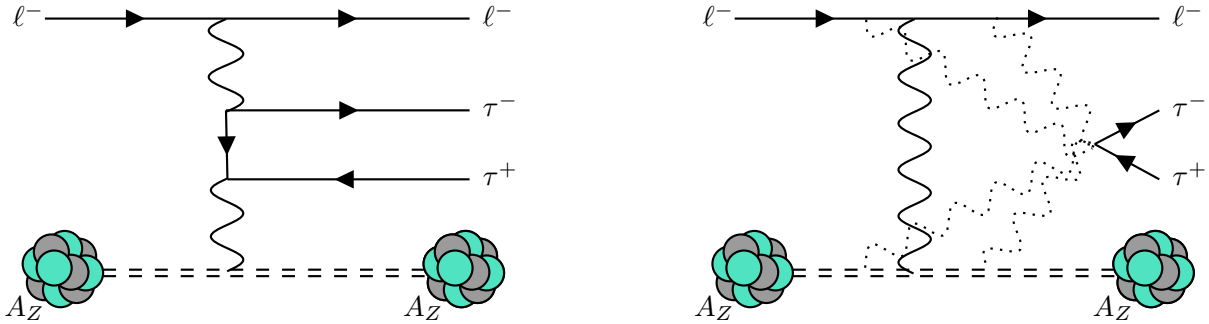


Figure 5.6: Diagrams for ditau production which contribute to the background for the collision  $\ell^- A_Z \rightarrow \tau^- A_Z (a \rightarrow \ell^+ \tau^-)$  at the EIC and MuSIC, particularly when the  $\ell^-$  is lost down the beam-pipe and the  $\tau^+$  decays to  $\ell^+ \bar{\nu} \nu$ . The dashed photon lines in the diagram on the right indicate that the  $\tau$  pair production can occur from a photon off of any one of the legs.

### 5.3.2 Signal and Background

Given the simplicity of the model, the only possible production mode is  $e^- A_Z \rightarrow \tau^- A_Z a$ .<sup>2</sup>

There are then two possible decay modes for the ALP:  $a \rightarrow e^- \tau^+$  and  $a \rightarrow e^+ \tau^-$ . The former is lepton-flavor conserving, so it will be overwhelmed with SM background. Hence, we focus on the decay mode  $a \rightarrow e^+ \tau^-$ . We will leverage the LFV nature of the final state by vetoing on identification of an electron  $e^-$ , and requiring identification of the  $e^+$  and one of the  $\tau^-$ .

The largest source of background is ditau production  $e^- A_Z \rightarrow e^- A_Z \tau^+ \tau^-$ , through one of the diagrams shown in Fig. 5.6. This can mimic  $e^- A_Z \rightarrow \tau^- A_Z (a \rightarrow e^+ \tau^-)$  if the  $\tau^+$  decays leptonically and the final-state electron is lost down the beam pipe. A rough estimate of the cross-section for ditau production at the EIC can be gleaned from Ref. [169], which computes the cross-section for ditau production from cosmic-ray muons incident on rock (which is assumed to be  $^{22}_{11}\text{Na}$ ). Focusing on the energy  $E \approx 4$  TeV (the energy of the electron at the EIC in the frame of the nucleus) in Fig. 3 of the reference and assuming the cross-section is enhanced by  $(Z_{\text{Au}}/Z_{\text{Na}})^2 \approx 50$  at the EIC, we estimate  $\sigma_{\text{b.g.}} \approx 2.6 \times 10^4$  pb. This cross-section is quite large, but as suggested previously, the majority of it can be mitigated by vetoing on the identification of an  $e^-$ . Even so, there is a

<sup>2</sup> Even in the event that other leptonic couplings are present, this is by far the most dominant production mode, since the ALP coupling is proportional to the mass of the leptons in the vertex.

possibility that the incident electron in the SM ditau production process is either lost down the EIC beam-pipe or mis-identified as an  $e^+$ . We take  $10^{-2}$  for the rate of electron loss, in line with the proposed detector requirements for the EIC [130]. We assume the rate of electron misidentification as a positron is  $10^{-3}$ , similar to the rate of a pion faking an electron from simulations in Ref. [130]. Finally, for the  $\tau$  identification rate, we consider two scenarios:  $\epsilon_\tau = 1\%$  in line with the analysis done in Ref. [170], and the more optimistic scenario  $\epsilon_\tau \approx 10\%$ , which corresponds to reconstruction of all three-prong  $\tau$  decays.

### 5.3.3 Combined Limits

Using the analysis above, the background efficiency is  $\epsilon_{\text{b.g.}} \approx 0.0036\epsilon_\tau$ , and the signal efficiency is  $\epsilon_{\text{sig.}} = \epsilon_\tau/2$ , where the factor of 1/2 takes into account the fact that the final-state ALP must decay to  $e^+\tau^-$ . For  $\mathcal{L} = 100/A \text{ fb}^{-1}$ , this corresponds to  $N_{\text{b.g.}} = 47000\epsilon_\tau$  background events. To place 95% C.L. ( $2\sigma$ ) limits on the coupling  $C_{\tau e}/\Lambda$ , we find the value of  $C_{\tau e}/\Lambda$  for which the number of expected signal events is  $N_{\text{sig.}} = 2\sqrt{N_{\text{b.g.}}} \approx 430\sqrt{\epsilon_\tau}$ . Letting  $\hat{\sigma}$  represent the cross-section normalized by  $(C_{\tau e}/\Lambda)^2$ , we have

$$\frac{C_{\tau e}}{\Lambda} \leq \sqrt{\frac{430}{\sqrt{\epsilon_\tau}\hat{\sigma}\mathcal{L}}} \text{ TeV}^{-1}. \quad (5.17)$$

The resulting bounds on  $C_{\tau e}/\Lambda$  are shown in the left panel of Fig. 5.11, with  $\epsilon_\tau = 1\%$  represented as a solid blue line and  $\epsilon_\tau = 10\%$  represented as a dashed blue line. The right panel shows the same limits as in the left panel, but in the context of the LHC Higgs decay limits and projections from the previous section with a representative value of the Higgs-ALP coupling of  $C'_{ah}/\Lambda^2 = 1 \text{ TeV}^{-2}$  and  $C_{ah}/\Lambda^2 = 0 \text{ TeV}^{-2}$ . These limits have been recast for the scenario where  $C_{\tau e}$  is the only non-zero coupling. While the reach at the LHC is much stronger than the reach at the EIC, it is dependent on both the strength and nature (i.e. whether  $C_{ah}$ ,  $C'_{ah}$ , or both are present) of the Higgs-ALP interaction. Hence, there are still scenarios (such as that shown in the second panel of Fig. 5.11) for which the EIC is in a unique position to probe the theory.

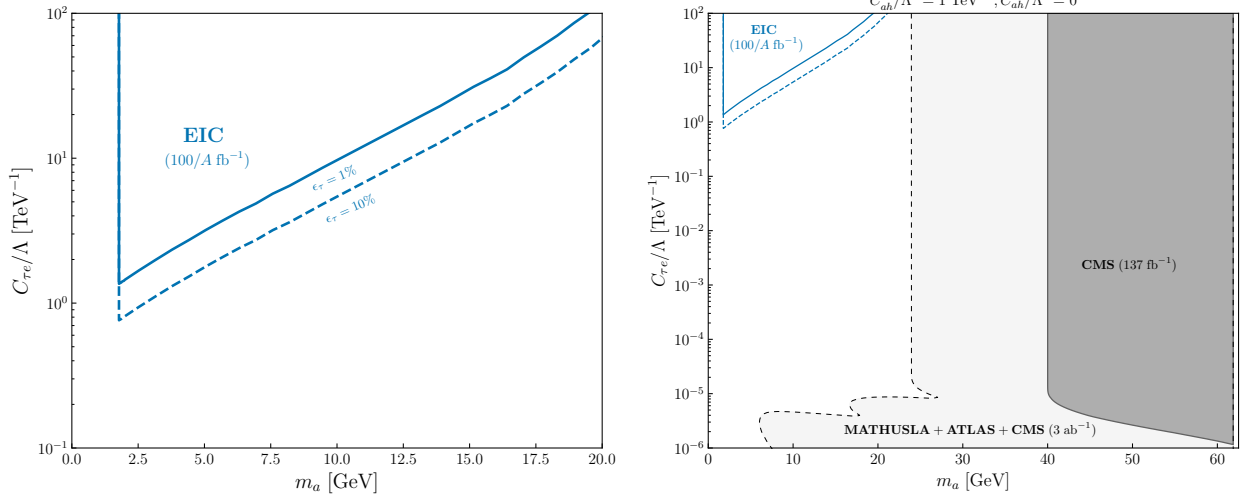


Figure 5.7: (Left) limits on the LFV coupling  $C_{\tau e}/\Lambda$  from the EIC assuming a  $\tau$  efficiency of  $\epsilon_{\tau} = 1\%$  (blue, solid) and  $\epsilon_{\tau} = 10\%$  (blue, dashed). (Right) the same limits in the larger context of the LHC Higgs decay limits from the last section, assuming  $C'_{ah}/\Lambda^2 = 1$  TeV $^{-2}$  and  $C_{ah}/\Lambda^2 = 0$  TeV $^{-2}$ . These limits are recast for the scenario in which  $C_{\tau e}$  is the only non-zero coupling of the ALP.

Although we have focused on the scenario where the ALP only couples to  $e$  and  $\tau$ , our results are mostly insensitive to this choice. In the presence of other LFV couplings, our results are essentially constraints on  $\sqrt{\mathcal{B}(a \rightarrow e\tau)}C_{\tau e}/\Lambda$ , with the caveat that the  $a \rightarrow \tau^+\tau^-$  decay mode could also contribute to the signal if  $\tau^+ \rightarrow e^+\bar{\nu}\nu$ . In this more general scenario, the reach of the EIC is mostly ruled out by the limits from LFV leptonic decays  $\tau \rightarrow 3\ell$  and  $\tau \rightarrow \ell\gamma$ , shown at the bottom of Fig. 3.3. Hence, while the limits placed from the EIC on  $C_{\tau e}$  are weaker, they can be seen as *absolute* limits on the coupling, as any larger value of  $C_{\tau e}$  would be completely ruled out at the EIC, almost entirely irrespective of the other ALP couplings.

Finally, we note that the ditau background can be entirely avoided by requiring positive identification of *both*  $\tau$ s in the final state, along with the  $e^+$ . We have avoided this possibility given the experimental difficulty involved in resolving multiple  $\tau$ s, but if methods improve on this front then this approach may be preferable. One may also be able to leverage other LFV final-states of the ALP decay (e.g., those involving muons) for additional background-free signal events; however, even a complete reduction of background for such processes will not be enough for the

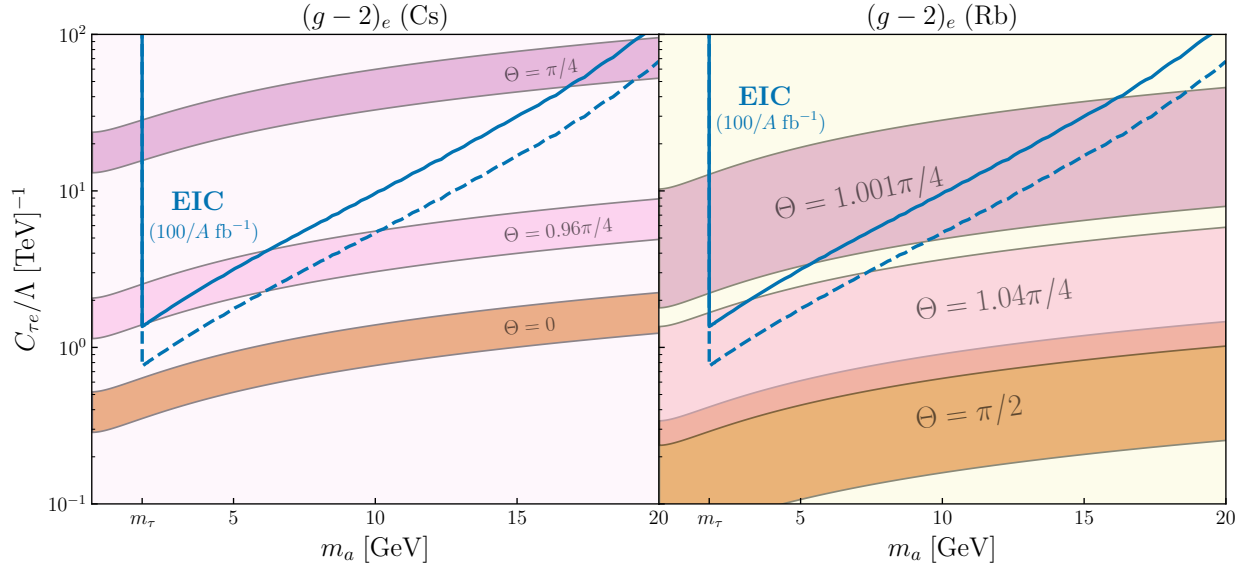


Figure 5.8: Expected limits on  $C_{\tau e}/\Lambda$  from the EIC, alongside explanations for the electron  $g - 2$  anomalies for different PV angles  $\Theta$ . The left panel presents  $2\sigma$  explanations for the anomaly obtained from using  $\alpha(\text{Cs})$ , and the right panel presents explanations for the anomaly obtained from using  $\alpha(\text{Rb})$ .

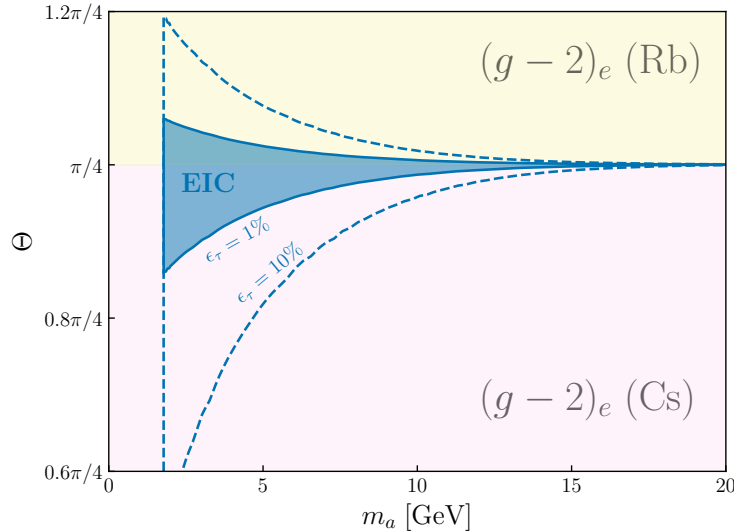


Figure 5.9: The region in the  $m_a$ - $\Theta$  plane for which the EIC probes an LFV ALP explanation to either of the electron  $g - 2$  anomalies.

EIC to compete with the stringent constraints on  $\sqrt{C_{\mu\tau}C_{e\tau}}/\Lambda$  from the MEG limit on the  $\mu \rightarrow e\gamma$  branching fraction.

### 5.3.4 Explanations to $(g - 2)_e$

The reach of the EIC turns out to coincide with the  $C_{\tau e}$  required to explain either of the electron  $g - 2$  anomalies, per the discussion in Section 3.4.7. In particular, the sign of the contribution to  $a_e$  is dependent on the PV angle, so PV angles  $\Theta < \pi/4$  are able to explain the anomaly obtained from using  $\alpha(\text{Cs})$ , whereas PV angles  $\Theta > \pi/4$  are able to explain the anomaly obtained from using  $\alpha(\text{Rb})$ . To illustrate this point, we plot the EIC constraints alongside  $2\sigma$  explanations to each anomaly in Fig. 5.8, for three representative angles. We find that the EIC is equipped to probe near-chiral explanations of the electron  $g - 2$  anomalies, which can occur if the ALP's coupling to right-handed leptons is suppressed relative to its coupling to left-handed leptons, or vice-versa. If one takes the more optimistic  $\tau$  efficiency  $\epsilon_\tau = 10\%$ , the EIC is *just* able to probe the upper end of the  $2\sigma$  band for  $\Delta a_e(\text{Cs})$  with  $\Theta = 0$  (and hence will also have non-zero overlap with the  $2\sigma$  bands for all  $\Theta > 0$ ).

To get a better sense of which anomaly explanations the EIC is sensitive to, we can compute the region in the  $m_a$ - $\Theta$  plane for which the EIC limit intersects the center of the bands shown in Fig. 5.8. The resulting region is presented in Fig. 5.9, with the conservative ( $\epsilon_\tau = 1\%$ ) scenario shaded in blue and the optimistic ( $\epsilon_\tau = 10\%$ ) scenario a dashed blue line. This reinforces the point that the EIC is mostly able to probe near-chiral solutions to the electron  $g - 2$  anomalies, although the angle can deviate farther from  $\pi/4$  for lower masses.

## 5.4 LFV ALP Production at MuBeD and MuSIC

With interest growing in the particle physics community for a multi-TeV muon collider [132–134], it is likely that intermediate experiments involving TeV muon beams are in our future. We have discussed two possibilities for such experiments in Chapter 4, namely a TeV muon beam dump (MuBeD) and a Muon (Synchrotron) Ion Collider (MuSIC). In this section, we will examine the degree to which such experiments would be able to probe the LFV ALP model. We will once again focus on coherent production of an ALP  $a$  via the process  $\mu^- A_Z \rightarrow \tau^- A_Z a$ , which will allow us

to probe the  $C_{\mu\tau}$  coupling. Similar to the previous section, we will assume that this is the only non-zero coupling of the ALP to the leptons, so that the interaction term is

$$\mathcal{L}_{\text{int}} = C_{\tau\mu} \frac{\partial_\mu a}{\Lambda} \bar{\tau} (\sin \Theta + \cos \Theta \gamma^5) \mu + \text{H.c.} \quad (5.18)$$

#### 5.4.1 Detector Capabilities

We are years of research and development away from a functioning TeV muon beam. As such, no serious prototype has yet been put forward for either MuBeD or MuSIC, so here we will speculate about reasonable detector requirements and geometry one might expect for these experiments.

##### 1. Muon Beam Dump (MuBeD)

Here, we consider the possibility of a 1 TeV muon fixed target experiment, similar to the experiments investigated in Refs. [135, 136]. Such an experiment could be constructed as one component of the muon collider facility, or developed even earlier during the muon beam research and development phase. The original proposal considers a TeV-energy muon beam dumped on a thick target ( $\sim 10$  m) along with a detector located  $\sim 100$  m downstream. The muon beam in their proposal is stated to be  $E = 1.5$  TeV, with as many as  $10^{20}$  muons on target (MOT) over the course of operation. Such a setup is well-suited for light, weakly coupled, long-lived particles, such as the gauge bosons discussed in the next chapter. In contrast, the ALPs we consider here are considerably heavier and hence not as long-lived as the particles considered in those references. Hence, we propose a complementary active thin target concept for a 1 TeV muon fixed-target experiment, schematically illustrated in Fig. 5.10. This active thin target run could operate concurrently with the beam-dump mode. In this case, even a small fraction of order  $10^{16}$  MOT is enough for a meaningful search. For reference, this corresponds to only about an hour of operation of the muon beam source to be designed for the muon collider, assuming 5 Hz muon source repetition rate and  $2 \times 10^{12}$  muons per bunch, in line with the Muon Accelerator Program (MAP) parameters [132].

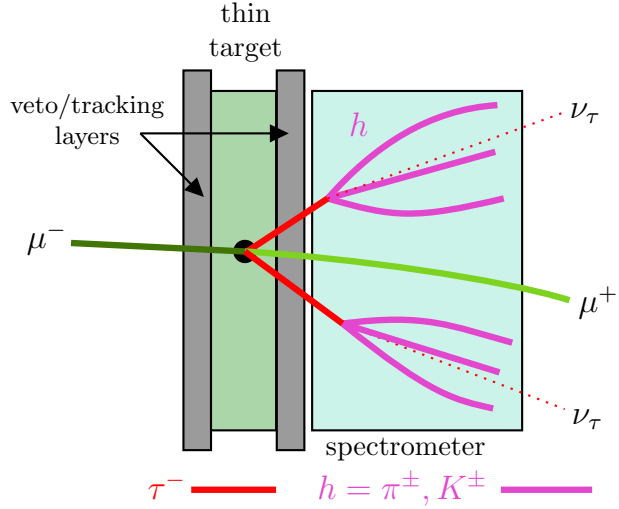


Figure 5.10: A schematic representation of the fixed-target muon beam set up described in the text.

For concreteness, we consider a thin target composed of a 2 cm-thick lead plate, placed in between two veto or tracking layers and directly in front of a spectrometer. Interleaving this target with additional tracking layers could further improve the physics sensitivity, although this may be difficult given the length of the target. In the following, we will assume that a 2 cm track identification resolution is required for identification of the  $\tau$ , essentially requiring it to pass through the external tracking layers and decay in the spectrometer. On top of tracking capabilities and energy measurement, muon identification is essential to study the signal of our interest. We assume that  $\mu^\pm$ s can be disentangled from charged pions with nearly 100% efficiency.

The intensity and energy of the muon beam considered here are unprecedented in current and near-future experiments, which should be considered when designing the experiment. For instance, a highly collimated muon beam could potentially damage the active detector. In this case, defocusing the beam would be advantageous before it hits the target. The experiment could also operate under a reduced beam intensity in a short, dedicated run. Additional effects will be related to interactions of an electron cloud surrounding the muon beam. Being less energetic than muons, these could be partially deflected away or shielded on their way to the detector. These and other detector requirements, e.g., cooling, must be analyzed in detail to assess the feasibility of

such a detector. We leave this for future studies.

## *2. Muon (Synchrotron) Ion Collider (MuSIC)*

For the detector apparatus at MuSIC, we will follow Ref. [137], which proposes that the electron beam at the EIC is eventually upgraded to a 1 TeV muon beam for the purpose of probing deep nuclear structure. If interest for such a detector grows, it is possible that it will be constructed at another facility, but this has limited impact on our discussion. We assume that the gold ion energy remains at 110 GeV/nucleon, which corresponds to a COM energy of 660 GeV/nucleon, and a muon energy of  $E = 20$  TeV in the rest frame of the gold ion. We will additionally assume a five-year integrated luminosity of  $\mathcal{L} = 400/A \text{ fb}^{-1} \approx 2 \text{ fb}^{-1}$  for gold.

While the COM energy of a TeV muon-ion collider such as MuSIC is tantalizing, this comes with a cost: very low deflection angles. The situation is described more fully in Section 4.6.1; almost all particles (at least in the peripheral production process we are concerned with) have pseudorapidity  $|\eta| > 4$ . Hence, if the geometry of the detector is identical to that at the EIC (which has a pseudo-rapidity range  $|\eta| < 3.5$ ), any hope of detecting particles produced in this way will be dashed. However, we anticipate that an experiment such as MuSIC would require a higher pseudo-rapidity range for the simple fact that TeV muons have a much higher inertia than 18 GeV electrons, and thus will have lower deflection angles. In particular, we note that per the specifications of the ePIC collaboration (previously ECCE), the ion side of the EIC will currently be instrumented for tracking up to  $4 < \eta < 6$  with the B0 spectrometer [149] for the purpose of identifying high-energy protons. We assume that a similar instrumentation can be added on the muon-side of interaction point, so that  $|\eta| < 6$  can be achieved. While this will still not capture the majority of the MeV-scale particles MuSIC (see Fig. 4.7) it is sufficient for MuSIC to be sensitive to GeV-scale particles produced in peripheral interactions.

### **5.4.2 Signal and Background**

#### *1. Muon Beam Dump (MuBeD)*

The number of ALPs produced from the collision of a muon beam and a lead target of thickness  $L_{\text{tar}}$  which land inside the detector is given by [136, 171]

$$\frac{dN}{dE_k dz} = \frac{N_\mu \rho_{\text{tar}}}{M_{\text{tar}}} \int_{E_k}^{E_0} \frac{dE'}{E'} \int_0^{L_{\text{tar}}} d\ell I(E'; E, \rho_{\text{tar}} \ell / X_0) \times E_0 \frac{d\sigma}{dE'_k} \frac{dP(z - \ell)}{dz} \quad (5.19)$$

where  $E$  is the incident energy,  $N_\mu$  is the number of muons on target,  $\rho_{\text{tar}}$  and  $M_{\text{tar}}$  are the density and atomic mass of the material,  $L_{\text{tar}}$  is the length of the target,  $X_0$  is the radiation length of the target,  $P(z)$  is the probability the ALP decays a distance  $z$  from where it is produced, and  $I(E'; E, t)$  is a function which parametrizes radiative loss of the muon beam energy as it moves through the material. We specialize to the thin-target scenario, for which we can ignore energy loss of the muon beam as it moves through the material; e.g.  $I(E'; E, \rho \ell / X_0) = \delta(E' - E)$ . For the probability that the ALP decays a distance  $z$  from where it is produced, we have

$$P(z) = \Theta(z) \left( 1 - e^{-\frac{z}{\gamma c \tau_a}} \right) \quad (5.20)$$

where  $\tau_a$  is the lifetime of the ALP and  $\gamma$  its boost. Under the assumption that the ALP decays promptly (which we find is reasonable assumption for the masses and parameters probed), we have

$$\begin{aligned} \frac{dN}{dE_k dz} &= \frac{N_\mu \rho_{\text{tar}}}{M_{\text{tar}}} \int_0^{L_{\text{tar}}} d\ell \frac{d\sigma}{dE'_k} \delta(z - \ell) \\ \implies N &= \frac{N_\mu \rho L_{\text{tar}}}{M} \sigma \end{aligned} \quad (5.21)$$

where we have used  $P'(z) \approx \delta(z - \ell)$  for  $\gamma c \tau_a \ll z$ . This gives an effective integrated luminosity of  $\mathcal{L}_{\text{eff.}} = N_\mu (\rho_{\text{tar}} L_{\text{tar}} / M_{\text{tar}}) \approx (6.6 \times 10^{-17} \text{ fb}^{-1}) N_\mu$ . Even for  $N_\mu = 10^{16}$ , this luminosity allows MuBeD to compete with the results from the EIC in the previous section, as well as the results from MuSIC (which is assumed to have a similar luminosity to the EIC).

Like with the EIC, we will focus on the purely flavor-violating signal from  $a \rightarrow \mu^+ \tau^-$ , which corresponds to half of all decay events. We assume that the  $\mu^+$  can be identified with 100% efficiency, and we veto on identification of a  $\mu^-$  in the final state to ensure a purely LFV final state. We expect the final-state muon can also be vetoed with 100% efficiency, since the detector can be instrumented directly in front of the muon beam (in contrast to the EIC, which has the

possibility of losing the incident electron down the beam pipe). This alone should remove all SM background.<sup>3</sup> We also require identification of both  $\tau^-$  in the final-state. We expect that the efficiency for this process can be relatively high if one combines charged tracks with hadronic final states in the spectrometer. In particular, we assume that all three-prong  $\tau$ s with a track length  $> 2$  cm can be resolved. To enforce the 2 cm track-length requirement, we estimate the energy distributions of both  $\tau^-$  then compute those fraction of  $\tau^-$  for which  $(E_\tau/m_\tau)c\tau_\tau > 2$  cm, where  $\tau_\tau$  is the rest-frame lifetime of the  $\tau$ . Labeling the  $\tau$  converted from the muon  $\tau_1$  and the  $\tau$  which is a decay product of the ALP  $\tau_2$ , we can estimate the fraction of each  $\tau$  that we detect. In particular, if the  $\tau$  has Lorentz boost distribution  $\rho_\gamma(\gamma_\tau)$ , we define the  $\tau$  detection efficiency as

$$\epsilon_\tau = \mathcal{B}(\tau \rightarrow 3\text{-prong}) \int_{(2\text{cm})/c\tau_\tau}^{\infty} d\gamma_\tau \rho_\gamma(\gamma_\tau) \quad (5.22)$$

For  $\tau_1$ , we use the technique described in Section 4.7 to compute its final-state boost distribution under the assumption that the photon transfer momentum is small, finding  $\epsilon_\tau^{(1)} \approx 0.03\% - 3\%$  over the range of masses considered. For  $\tau_2$ , we assume the ALP decays promptly, and the  $\tau_2$  carries half of its energy  $E_k/2$  away ( $\gamma_\tau = E_k/(2m_\tau)$ ), finding  $\epsilon_\tau^{(2)} \approx 5\%$  over the range of masses considered.

## 2. Muon (Synchrotron) Ion Collider (MuSIC)

Given the similarities between MuSIC and the EIC, we will perform the same analysis as in Section 5.3, but assuming we can detect decaying ALPs with  $|\eta| < 6$ . In particular, we will leverage the LFV final-state of the process  $\mu^- A_Z \rightarrow \tau^- A_Z (a \rightarrow \mu^+ \tau^-)$  by identifying the  $\mu^+$  and a  $\tau^-$ . Like before, the leading background will be from ditau production (Fig. 5.6). Referring again to the cross-sections computed for ditau production from muons on rock [169], we estimate the cross-section for this at MuSIC (with  $E = 20$  TeV) is  $\sigma_{\text{b.g.}} \approx 10^5$  pb. We will once again take the muon loss rate to be  $10^{-2}$  and the rate of muon misidentification as an anti-muon to be  $10^{-3}$ . For direct comparison with the EIC, we will assume  $\tau$  efficiencies of  $\epsilon_\tau = 1\%$  and  $\epsilon_\tau = 10\%$ .

---

<sup>3</sup> Given that the muon can also decay to an electron and two neutrinos, it may be necessary to veto on identification of an electron in the final-state as well, but this does not affect our signal.

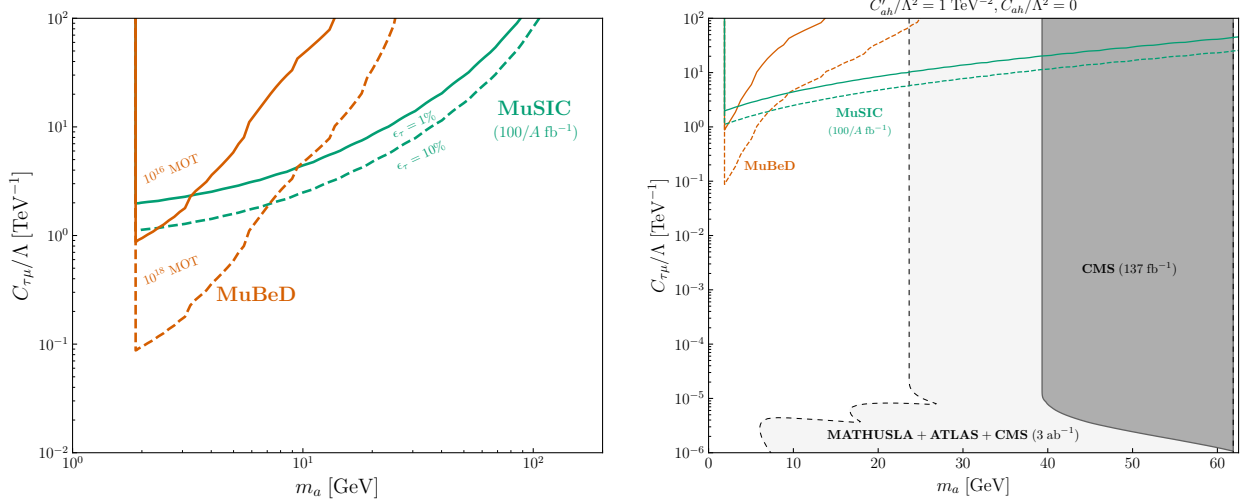


Figure 5.11: (Left) limits on the LFV coupling  $C_{\tau\mu}/\Lambda$  from MuBeD assuming  $N_\mu = 10^{16}$  (orange, solid) and  $N_\mu = 10^{18}$  (orange, dashed), and from MuSIC assuming a  $\tau$  efficiency of  $\epsilon_\tau = 1\%$  (green, solid) and  $\epsilon_\tau = 10\%$  (green, dashed). (Right) the same limits in the larger context of the LHC Higgs decay limits from the last section, assuming  $C'_{ah}/\Lambda^2 = 1 \text{ TeV}^{-2}$  and  $C_{ah}/\Lambda^2 = 0 \text{ TeV}^{-2}$ . These limits are recast to the scenario in which  $C_{\tau\mu}$  is the only non-zero coupling of the ALP.

#### 5.4.3 Combined Limits

We are now equipped to place 95% exclusion limits on the  $C_{\tau\mu}$  couplings from each of these experiments. Beginning with MuBeD, the zero-background signal entails that the coupling  $C_{\mu\tau}$  is excluded at the 95% C.L. by

$$\frac{C_{\tau\mu}}{\Lambda} (\text{MuBeD}) \leq \sqrt{\frac{3.09}{\epsilon_\tau^{(1)} \epsilon_\tau^{(2)} \hat{\sigma} \mathcal{L}_{\text{eff}}}} \text{ TeV}^{-1} \sim \sqrt{\frac{6 \times 10^{15} \text{ pb}}{N_\mu \hat{\sigma}}} \text{ TeV}^{-1} \quad (5.23)$$

where  $\hat{\sigma}$  is the production cross-section normalized by  $(C_{\tau\mu}/\Lambda)^2$ .

For MuSIC, the signal is not zero-background. Rather, the analysis in the previous section indicates there will be approximately  $N_{\text{b.g.}} = 180000 \epsilon_\tau$  background events. To place 95% C.L. ( $2\sigma$ ) limits on the coupling  $C_{\tau e}/\Lambda$ , we find the value of  $C_{\tau e}/\Lambda$  for which the number of expected signal events is  $N_{\text{sig}} = 2\sqrt{N_{\text{b.g.}}} \approx 850\sqrt{\epsilon_\tau}$ . Hence, the MuSIC bounds are given by

$$\frac{C_{\tau\mu}}{\Lambda} (\text{MuSIC}) \leq \sqrt{\frac{850}{\sqrt{\epsilon_\tau \hat{\sigma} \mathcal{L}}}} \text{ TeV}^{-1} \sim \sqrt{\frac{1.7 \text{ pb}}{\sqrt{\epsilon_\tau \hat{\sigma}}}} \text{ TeV}^{-1} \quad (5.24)$$

One downside of MuSIC (and the EIC) for detection through this production process is that there is not much room for improvement. Their luminosity is fundamentally limited by the ability to focus

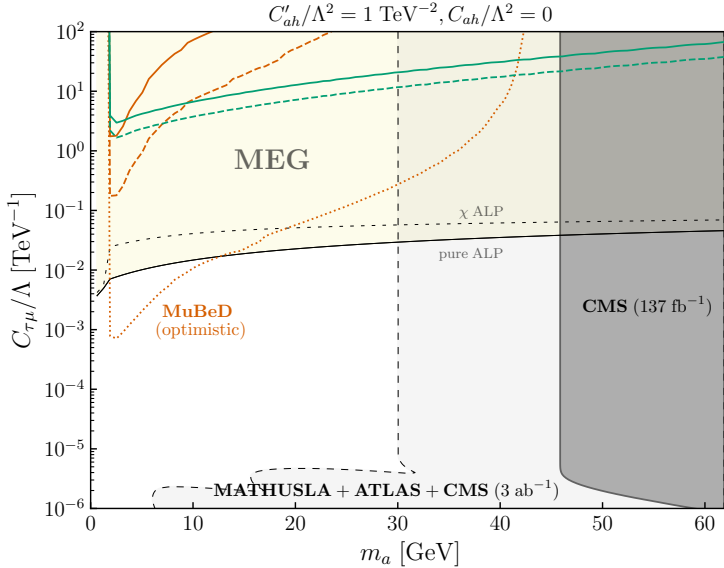


Figure 5.12: Limits on  $C_{\tau\ell}/\Lambda$  for democratic ALP-lepton couplings, assuming the most optimistic scenario for a muon beam dump experiment (described in the text). The leading constraint for the democratic scenario from LFV lepton decays comes from the MEG experiment due to the process  $\mu \xrightarrow{\tau} e\gamma$ , which is enhanced by the  $\tau$  mass at both LFV vertices.

the lepton and ion beams, and the detector geometry is inopportune for capturing particles which are produced with high pseudo-rapidity. For MuBeD, on the other hand, we have made somewhat modest assumptions. While we have assumed an instrumented target of length  $L_{\text{tar}} = 2$  cm, it is not difficult to imagine a much thicker target, such as the proposed 2 m thick FASER $\nu$ 2 detector at the Forward Physics Facility at CERN [172]. This would also allow for finer  $\tau$  track resolution, and hence a better  $\tau$  detection efficiency.

In Fig 5.12, we plot the *most* optimistic case for MuBeD which is still experimentally reasonable:  $N_\mu = 10^{20}$ ,  $L_{\text{tar}} = 2$  m, and a  $\tau$  track resolution of 2 mm. In particular, such a  $\tau$  track resolution could be achieved if the 2 m lead target is interleaved with trackers or emulsion detectors, again like FASER $\nu$ 2. Rather than focusing on a singular off-diagonal coupling, here we focus on the “democratic” coupling scenario, for which all of the ALP-lepton couplings are the same. While the democratic scenario is already excluded beyond the reach of the EIC and MuSIC by LFV lepton decays, we see that the most optimistic scenario for MuBeD is competitive with these constraints.

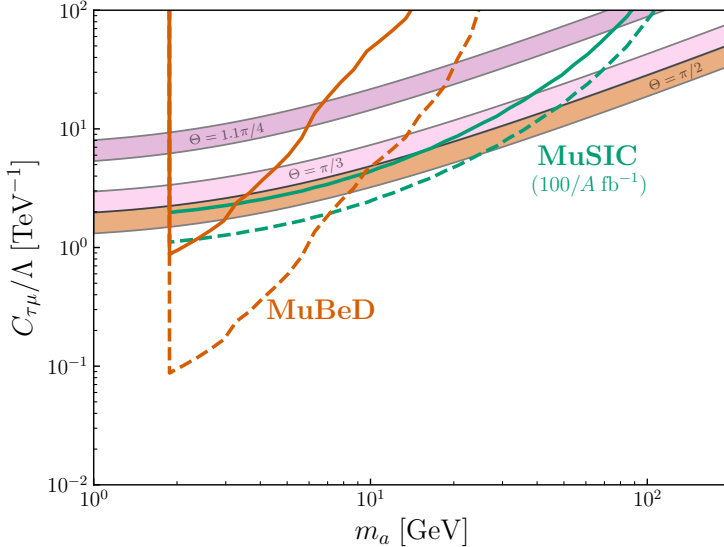


Figure 5.13: Expected limits on  $C_{\tau\mu}/\Lambda$  from MuBeD and MuSIC, alongside explanations for the muon  $g - 2$  anomaly for different PV angles  $\Theta$ .

#### 5.4.4 Explanation to $(g - 2)_\mu$ Anomaly

Here, we perform a similar analysis to the analysis performed in Section 5.3.4 for probing explanations to the electron  $g - 2$  at the EIC. In particular, we will explore the sensitivity of MuSIC and MuBeD to PV ALP explanations to the muon  $g - 2$  anomaly. One notable difference is that there is only *one* muon  $g - 2$  anomaly, and it is a *positive* anomaly. For ALPs, this corresponds to PV angles  $\Theta \gtrsim \pi/4$ . PV ALP explanations to the muon  $g - 2$  anomaly were already explored in Section 3.4.7, and the resulting couplings  $C_{\tau\mu}$  are notably within reach of the limits found for MuBeD and MuSIC in the previous Section. We plot these constraints alongside explanations to the muon  $g - 2$  anomaly for three representative angles in Fig. 5.13. In this case, for all angles that contribute the right sign to the anomaly, there is a range of masses  $m_a$  for which both MuSIC and MuBeD probe solutions to the anomaly. While MuBeD requires less statistics to probe solutions at smaller masses, MuSIC has the advantage at probing larger-mass solutions to the  $g - 2$  anomaly. In Fig. 5.14, we plot the region in the  $\Theta$ - $m_a$  parameter-space for which MuBeD and MuSIC probe solutions to the muon  $g - 2$  anomaly. This reemphasizes the point that while both experiments can probe solutions for any permissible angle  $\Theta$ , MuSIC has a wider mass-reach.

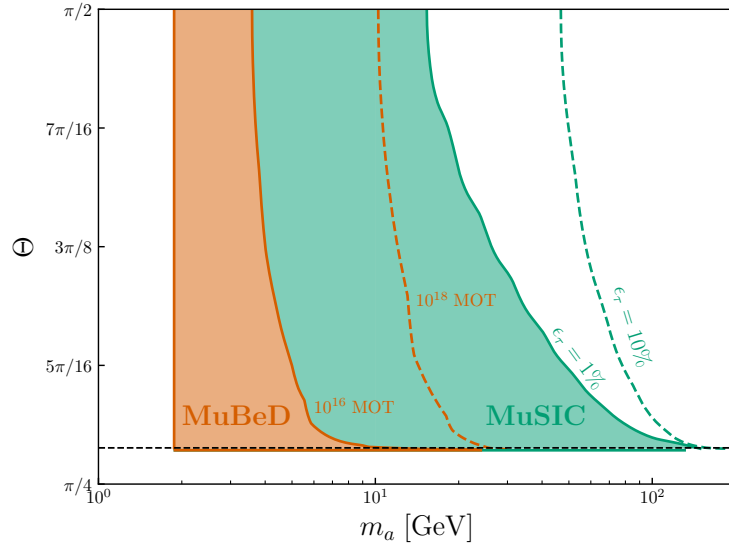


Figure 5.14: The region in the  $m_a$ - $\Theta$  plane for which MuBeD and MuSIC probe an LFV ALP explanation to the muon  $g - 2$  anomaly.

Although we have presented these results for an ALP, the fact that the explanation requires  $\Theta > \pi/4$  is in-line with the understanding that scalars, not pseudoscalars, contribute the correct sign to account for the  $(g - 2)_\mu$  anomaly. Nonetheless, as we have explored in previous chapters, the notions of “scalar” vs. “pseudo-scalar” are less concrete for flavor off-diagonal interactions, so it is reasonable to consider an ALP with  $\Theta > \pi/4$ .

## Chapter 6

### Hidden Gauge Bosons at Lepton-Ion Colliders

*This chapter is based on work done in Refs. [139, 173].*

#### 6.1 Introduction

Most of the results obtained in this dissertation thus far have concerned direct production of particles through an LFV coupling. However, as we have seen in Chapter 2, LFV is a generic feature of many leptophilic new physics models. One class of such models, discussed in Section 2.5, is the anomaly-free  $U(1)_{L_i-L_j}$  lepton family gauge theories. While these models do not have flavor-violation at the outset, any spontaneous breaking of the  $U(1)_{L_i-L_j}$  will lead to LFV processes. Spontaneous symmetry breaking of the abelian symmetry can generically lead to off-diagonal couplings of the gauge boson  $A'$  to both the charged and neutral leptons, and the scalars responsible for the symmetry breaking typically exhibit LFV couplings as well.

It is worthwhile to consider whether the  $A'$  of these theories can be produced via the production mechanism described in Chapter 4. In particular, a prompt decay of such a particle would be rife with SM background, since these gauge bosons mostly decay to  $\bar{f}f$ , where  $f$  is a Standard-Model fermion.<sup>1</sup> However, if the coupling  $g$  of the  $A'$  is small enough and its mass  $m_{A'}$  light enough, the decay of the  $A'$  can be come displaced. Indeed, for displacements  $d \gtrsim 0.1$  mm, we expect there to be no SM background.

---

<sup>1</sup> While  $A' \rightarrow \bar{f}f'$  is also often possible, the branching for this relative to  $A \rightarrow \bar{f}f$  is suppressed.

One potential issue with production of light particles via  $\ell^- A_Z \rightarrow \ell^- A_Z A'$  is that the  $A'$  will have high pseudo-rapidity. Beam-dumps have the advantage in this regard, as detectors can be placed directly beyond the target material, allowing detection of displaced decays with  $\eta \gg 1$ . For colliders such as the EIC or MuSIC discussed in Chapter 4, this is only possible with additional instrumentation far beyond the interaction point. Otherwise, the EIC has  $\eta \lesssim 3.5$  and, in line with our assumptions, MuSIC has  $\eta \lesssim 6$ . While such pseudo-rapidity constraints aren't prohibitive, they do limit the reach of these experiments for detecting displaced particles.

In this chapter, we will explore limits from displaced decays of  $U(1)$  gauge bosons at the EIC, MuSIC, and a 1 TeV muon beam dump (MuBeD). For completion, we will consider gauge bosons not only from the  $U(1)_{L_i-L_j}$  lepton family symmetries, but also a dark photon and the gauge boson of an abelian  $U(1)_{B-L}$  symmetry. In Section 6.2, we will review the branching fractions of the gauge bosons to SM final states. In Section 6.3, we will consider this signal in the context of the geometry of each of the signals, and discuss the requirements necessary to reconstruct the displaced signal. In Sections 6.4 and 6.5 we will provide limits on the gauge boson coupling (or kinetic mixing for the dark photon) at the EIC, MuBeD, and MuSIC. Finally, in Section 6.6, we will discuss the reliability of assumptions we have made when analyzing displaced vertices at lepton-ion colliders.

## 6.2 Vector Boson Decay Rates

The process under consideration is production of a massive vector boson  $A'$ , represented by the process  $\ell^- A_Z \rightarrow \ell^- A_Z A'$ . If the  $A'$  is light enough, it is likely that its decay will be displaced relative to the production vertex, which yields a signal with virtually zero SM background. For simplicity, we will focus on the scenario in which the  $A'$  decays to  $e^+e^-$  at the EIC (taking advantage of the EIC's electron tracking capabilities), and to  $e^+e^-$  or  $\mu^+\mu^-$  at MuSIC and MuBeD. We only consider emission of the  $A'$  from the lepton and not from the ion; emission from the ion will be suppressed by the nuclear form-factor  $F(m_{A'}^2)$  except for fairly light  $A'$  masses, where other experiments already provide stringent limits. The Feynman diagrams representing the process are shown in Fig. 4.1. The total cross-sections and kinematic distributions for scalars produced in this

charge	$U(1)_{\text{EM}}$	$U(1)_{B-L}$	$U(1)_{L_e-L_\mu}$	$U(1)_{L_e-L_\tau}$	$U(1)_{L_\mu-L_\tau}$
$Q_e$	-1	-1	+1	+1	0
$Q_\mu$	-1	-1	-1	0	+1
$Q_\tau$	-1	-1	0	-1	-1
$Q_{\nu_e}$	0	-1	+1	+1	0
$Q_{\nu_\mu}$	0	-1	-1	0	+1
$Q_{\nu_\tau}$	0	-1	0	-1	-1
$Q_{u_i}$	+2/3	+1/3	0	0	0
$Q_{d_i}$	-1/3	+1/3	0	0	0

Table 6.1: The charges of the SM fermions under each of the anomaly-free abelian groups discussed in the text.

way were reviewed in Chapter 4. The vector scenario is very similar.

We will be interested in decays of the hidden vector to SM final states. We assume that these are the only accessible decay modes of the hidden vector. We begin by considering an interaction of the form

$$\mathcal{L}_{\text{int.}} = -A'_\mu \sum_f Q_f \bar{f} \gamma^\mu (g_L P_L + g_R P_R) f \quad (6.1)$$

which yields a decay rate for  $A' \rightarrow \bar{f}f$  (assuming  $m_{A'} > 2m_f$ )

$$\Gamma(A' \rightarrow \bar{f}f) = \frac{Q_f^2 C_f}{24\pi} m_{A'} \sqrt{1 - \frac{4m_f^2}{m_{A'}^2}} \left( (g_L^2 + g_R^2) \left( 1 - \frac{m_f^2}{m_{A'}^2} \right) + 6g_L g_R \frac{m_f^2}{m_{A'}^2} \right) \quad (6.2)$$

where  $Q_f$  is the charge under the gauge group  $U(1)_X$  and  $C_f$  is a color factor (3 for quarks and 1 for leptons). A table representing the charges  $Q_f$  of the SM fermions  $f$  for each of the gauge theories considered is shown in Table 6.1. While we will assume that the  $A'$  couples to the vector current for the quarks and charged leptons, whether this is the case for neutrinos depends on whether the neutrinos are Dirac or Majorana fermions. If they are Dirac, then  $\nu_L$  and  $\nu_R$  carry the same mass, so one can package them into a Dirac spinor and take  $g_L = g_R = g_X$ . Otherwise,  $\nu_L$  and  $\nu_R$  must be treated separately, with  $\nu_R$  generically much heavier than  $\nu_L$ . This scenario corresponds to  $g_L = g_X$  and  $g_R = 0$  or vice versa, as the interaction must contain a left- or right-handed projection operator to treat each field separately.<sup>2</sup> While a Majorana mass term violates the

<sup>2</sup> One could still package them into a Dirac spinor, but this is inconvenient since there is a mass splitting between the left- and right-handed components of the spinor.

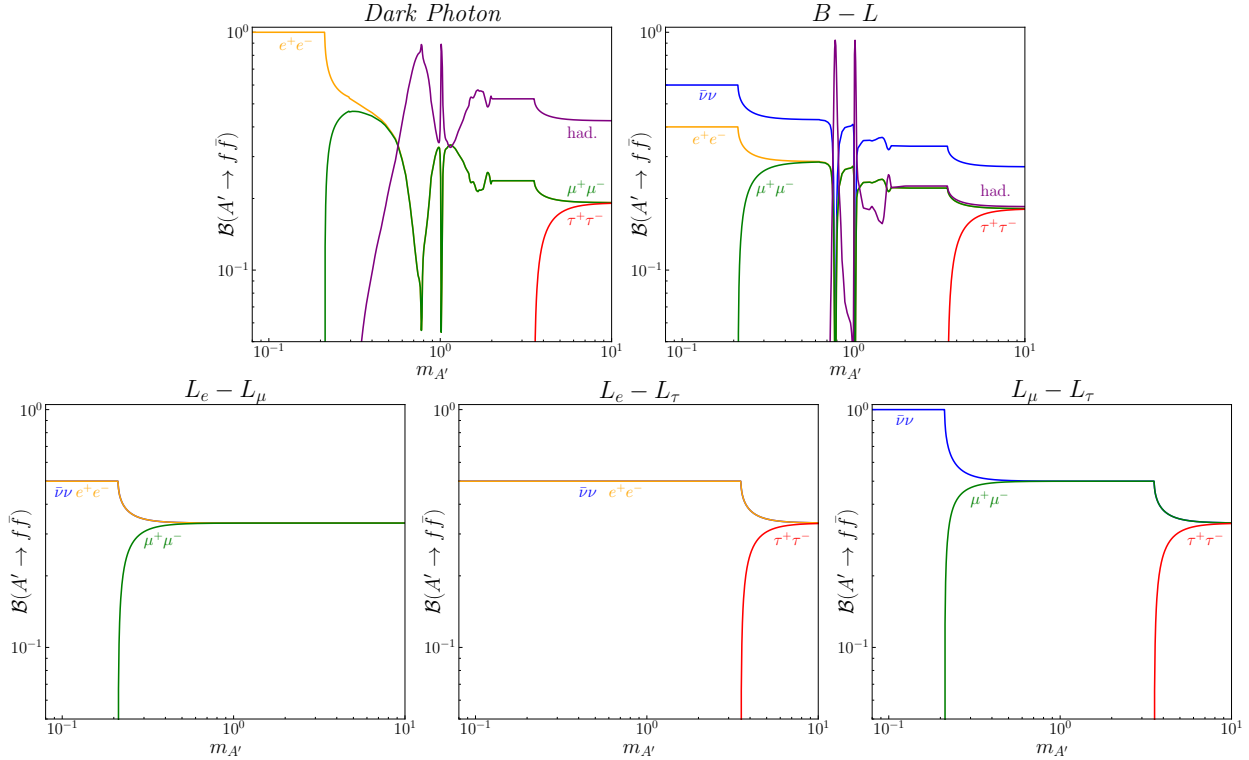


Figure 6.1: Branching fractions of a dark photon and anomaly-free  $U(1)_X$  gauge bosons into SM final states.

$U(1)_{B-L}$  and  $U(1)_{L_i - L_j}$  symmetries, such a term often arises alongside the spontaneous breaking of said symmetries due to interaction with a charge  $\pm 2$  scalar which acquires a VEV [62]. Given the predictive power of a Majorana mass term for the right-handed neutrino in describing the observed neutrino masses, we will assume that this is the case. Then, the decay rate to neutrinos is

$$\Gamma(A' \rightarrow \bar{\nu}_\ell \nu_\ell) \approx \frac{g_X^2 Q_{\nu_\ell}^2}{24\pi} m_{A'} \quad (6.3)$$

whereas the decay rate to charged leptons is

$$\Gamma(A' \rightarrow \bar{\ell} \ell) = \frac{g_X^2 Q_\ell^2}{12\pi} m_{A'} \left(1 + \frac{2m_\ell^2}{m_{A'}^2}\right) \sqrt{1 - \frac{4m_\ell^2}{m_{A'}^2}}. \quad (6.4)$$

The decay rate to quark final states is less straightforward due to the nonperturbative nature of the strong interaction. In this case, Ref. [174] computes the decay rate of the  $A'$  to hadrons using the  $\mathcal{R}$ -ratio for dark photons, and uses a combination of vector meson dominance and a more general

data-driven approach to recast the rate for other gauge bosons. For our purposes, we digitize the rates for the dark photon and  $U(1)_{B-L}$  gauge boson from Fig. 9 of Ref. [174]. The plots of the branching fractions to neutrinos, hadrons, and each charged lepton are shown in Fig. 6.1.

### 6.3 Detector Geometry and Displaced Signal

Here, we review the expected detector requirements and geometry for the EIC, as well as reasonable assumptions for MuSIC and MuBeD. In general, we can parameterize the number of signal events in terms of the differential production cross-section  $d\sigma/d\gamma d\eta$  as follows:

$$N_{\text{sig.}} = \mathcal{L} \int d\gamma \int_{\eta_{\min}}^{\eta_{\max}} d\eta \left\{ \frac{d\sigma}{d\gamma d\eta} P_{\text{disp.}} \sum_X \epsilon_X \mathcal{B}(A' \rightarrow X) \right\} \quad (6.5)$$

where  $\mathcal{L}$  is the luminosity,  $\gamma$  and  $\eta$  represent the boost and pseudo-rapidity of the produced vector boson  $A'$ , and  $\epsilon_X$  is the efficiency of detecting the final-state  $X$ . Here,  $P_{\text{disp.}}$  denotes the probability that the  $A'$  decays in a region of the detector apparatus for which it is possible to discern that its decay products are displaced. For the situations that we consider, we take it to be given by

$$P_{\text{disp.}} = e^{-d_{\min}/\gamma c \tau_{A'}} - e^{-d_{\max}/\gamma c \tau_{A'}} \quad (6.6)$$

where  $d_{\min}$  and  $d_{\max}$  are the minimum and maximum distances for which a displaced decay can be resolved, and  $\tau_{A'}$  is the rest-frame lifetime of the  $A'$ . While  $d_{\min}$  and  $d_{\max}$  are straightforward parameters in a fixed-target experiment, they can depend greatly on the kinematics of the final-state decay products in collider experiments. Rather than focusing directly on the kinematics of the decay products, we operate under the assumption that  $\eta_X \approx \eta_{A'}^3$ <sup>3</sup> and  $E_X \approx E_{A'}/2$ . We note that the detection efficiencies  $\epsilon_X$  in principle depend on the kinematics of the SM final states, but we take them to be constant for simplicity. We will focus on leptonic final-states, so  $X = \ell^+ \ell^-$  for  $\ell = e$  or  $\ell = \mu$ .

#### 1. EIC

---

<sup>3</sup> For leptonic final-states, the opening angle  $\theta_{\ell\ell} \approx 2/\gamma \ll 1$  for most of the parameter space considered, so this is a reasonable assumption.

We will assume that the EIC has excellent electron detection capabilities, but will ignore the possibility of muon reconstruction. Hence, we take  $\epsilon_e = 100\%$  and  $\epsilon_\mu = 0\%$ . Then, the main difficulty in computing 6.5 is determining the minimum and maximum resolvable displacements at the EIC.

To determine  $d_{\min}$ , we refer to the design document for the ECCE detector (now the ePIC Collaboration) at the EIC [149], which provides resolutions for the two-dimensional (2D) distance of closest approach ( $\text{DCA}_{2\text{D}}$ ) of pions. In particular,  $\text{DCA}_{2\text{D}}^{\min} = 100 \mu\text{m}$  for almost all track transverse momenta and pseudorapidities. If we adopt this as the resolution for the  $\text{DCA}_{2\text{D}}$  for the electrons at the EIC, we can relate  $d_{\min}$  to the lifetime  $\tau_{A'}$  of the  $A'$ . In particular, the transverse DCA is defined as the spatial separation between the primary vertex and reconstructed particle paths projected onto the transverse plane (see Fig. 6.2). We take the opening angle of the final-state leptons to be  $\theta_{\ell\ell}$ , and assume that each lepton has angle  $\theta_{\ell\ell}/2$  w.r.t. the direction of the vector boson. In the limit of  $m_{A'} \gg m_e$ , this corresponds to  $\theta_{\ell\ell} \sim 2v/\gamma$ , where  $v$  and  $\gamma$  are the speed and boost of the vector boson in the lab frame. Assuming  $m_e \ll m_{A'}$ , we find  $d_{\min} \approx \gamma(\text{DCA}_{2\text{D}}^{\min})/v \cos \theta$ , where  $\theta$  is the angle the vector boson makes with the beam axis in the laboratory frame. The details are provided in Appendix B.

Determination of  $d_{\max}$  is more straightforward. Referring again to Ref. [149], the tracking region consists of nine silicon trackers roughly evenly spaced in the region  $|z| < 1 \text{ m}$  and  $|\eta| < 3.5$ , with the first trackers at  $|z| = 25 \text{ cm}$ , where  $z$  is the position along the beam-axis from the interaction point (as illustrated in Fig. 6.2). In order to determine that the electron and positron decay products are displaced, it is crucial that their trajectories can be adequately reconstructed, so we require that the  $A'$  decays with  $|\eta| < 3.5$  before it reaches the first silicon tracker. This corresponds to a maximum resolvable displacement of  $d_{\max} = (25 \text{ cm})/\cos \theta$ . It is possible that a determination can be made as to whether the decay products are displaced with fewer trackers involved, but we find negligible difference in our results choosing  $z_{\max} = 25 \text{ cm}$  or  $z_{\max} = 1 \text{ m}$ .

One of the main limiting factors of our production cross-section is the production of dark photons with far-backward pseudorapidities ( $\eta < -3.5$ ) which are beyond the EIC's current tracking

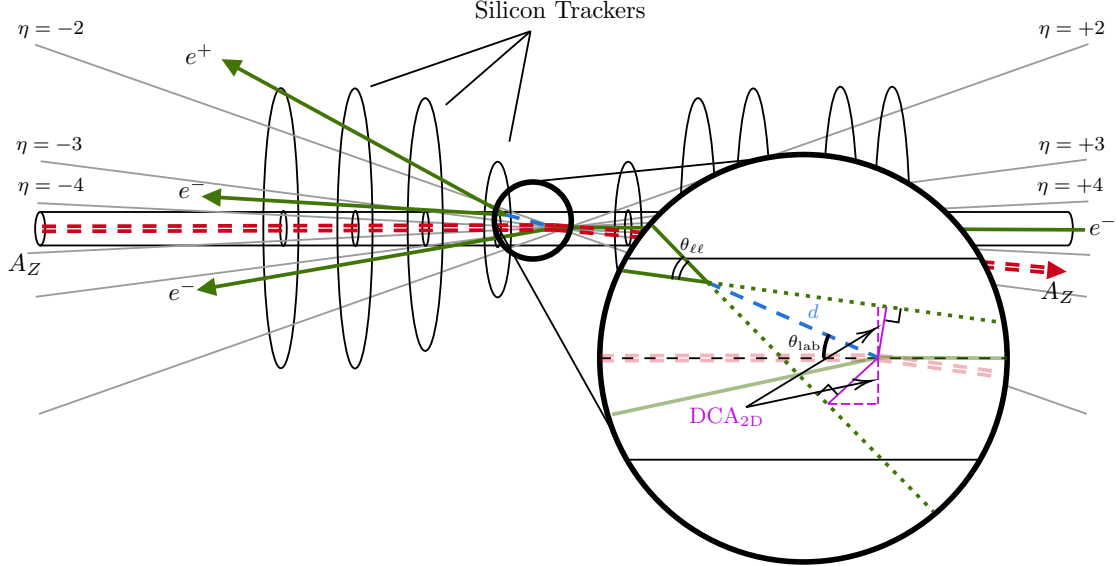


Figure 6.2: A schematic representation of the displaced process under consideration, including a diagram the transverse distance-of-closest-approach ( $DCA_{2D}$ ) for the final-state decay  $e^+e^-$  products of a vector boson with displacement  $d$  at the EIC. The tracks of the electrons and positrons in the final-state are shown as solid green lines, and the reconstructed tracks of the  $e^+e^-$  decay products from the dark boson are shown as dashed green lines. The distance-of-closest-approach for each decay product is depicted as a solid magenta line, and its transverse component (the  $DCA_{2D}$ ) is depicted as a vertical dashed magenta line. The size of the beam-pipe and placement of the silicon tracker is reproduced from Ref. [149]. In order to ensure each track can be reconstructed with the desired precision, we require that the vector boson decays before the first silicon tracker, which is placed 25 cm from the interaction point.

capabilities. Notably, the ECCE/ePIC detector proposal includes a far-forward detector, the B0 spectrometer, with the capability to track particles with  $4 < \eta < 6$ . Thus, we consider a scenario in which a similar detector is installed in the backward region at around  $z = -5$  m,<sup>4</sup> with the ability to track electrons with  $-6 < \eta < -4$ . We assume that this detector has a weaker DCA resolution than the rest of the detector given its distance from the interaction point, taking  $DCA_{2D}^{\min} = 200 \mu\text{m}$ .

For such vector bosons, a concerning background is ordinary photon conversion. However, because our signal is concentrated at large  $|\eta|$  in the direction of the electron beam, the vast majority of signal events will occur in a region of the proposed ECCE/ePIC detector which is very sparse. As a result, cutting away displaced vertices which originate at the silicon disks or on the beam-pipe

<sup>4</sup> The precise location is not crucial, so long as it is far enough away that it can track those decay products of the  $A'$  with large pseudorapidities; we simply make this choice for a direct comparison to the B0 spectrometer.

should be sufficient for avoiding this background while minimally affecting the number of signal events. Reconstruction of the invariant mass of lepton pairs could be another experimental handle to distinguish  $A'$  events from photon conversions in order to satisfy our assumption of negligible SM background.

Another potential source of background is misidentification of charged pions, which will be copiously produced in ion collisions, as  $e^\pm$ . However, in the electron end cap where our signal is concentrated, the fake rate is quite low, approximately  $10^{-4}$ . Since our signal requires both  $e^-$  and  $e^+$  as well as the displaced vertex, this background should be negligible.

Finally, there is also the possibility of signal reduction if electrons and positrons from the  $A'$  decay are lost down the beam pipe. We have used our kinematic distributions with some simplifying assumptions to estimate that, conservatively, this rate is no larger than 20% – 30% even with the signal strongly collimated in the backward direction. Since our estimate is somewhat crude (and would not affect our projections significantly), we do not include it in our projections, but a future study with a full Monte Carlo detector simulation could take this possibility into account for more accurate bounds.

## 2. MuSIC

We repeat the analysis for the EIC but with MuSIC, assuming an integrated luminosity of  $\mathcal{L} = 400/A \approx 2 \text{ fb}^{-1}$  over the course of 10 years. As in earlier chapters, we assume the main detector apparatus at MuSIC has a pseudo-rapidity range of  $|\eta| < 6$ . We additionally consider a far-backward scenario, in which there is tracking instrumentation in the region  $6 < |\eta| < 8$ . This will allow for a considerable increase in reach, given the anticipated pseudorapidity distributions at MuSIC (see Section 4.6). Such a reach in pseudorapidity would require instrumentation many meters away from the interaction point, so we take a maximum displacement of  $z_{\max} \approx 30 \text{ m}$ . Like the EIC, we assume that MuSIC will only be able to resolve displaced vertices for particles whose reconstructed trajectories exceed some minimum transverse DCA,  $\text{DCA}_{2\text{D}}^{\min}$ , from the interaction point. For the region  $|\eta| < 6$ , we assume a transverse DCA resolution of  $\text{DCA}_{2\text{D}}^{\min} = 200 \mu\text{m}$ , in line

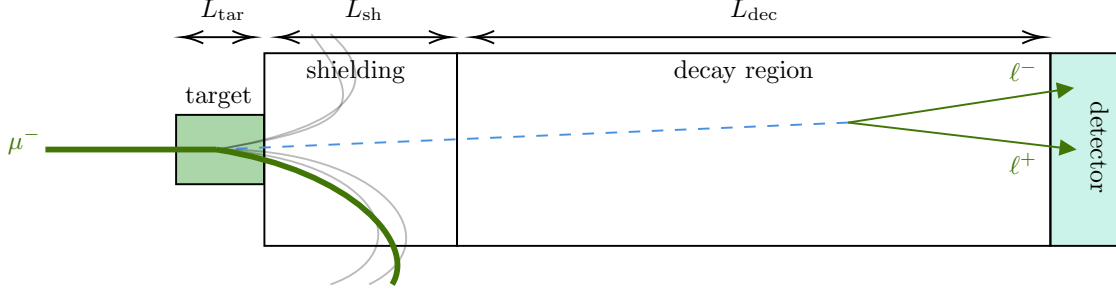


Figure 6.3: A schematic depiction of a muon beam dump experiment. The muon beam collides with the target (length  $L_{\text{tar}}$ ), producing a long-lived vector boson. All charged Standard-Model particles are deflected in the shielding region (length  $L_{\text{sh}}$ ), and the vector decays in the decay region (length  $L_{\text{dec}}$ ). Finally, the SM decay products of the vector are detected in the detector placed beyond the decay region. Recreated from Ref. [136].

with our assumption for the far-backward scenario at the EIC (which has a similar pseudo-rapidity requirement). For the far-backward scenario at MuSIC, we anticipate that the transverse DCA resolution will worsen considerably for  $|\eta| < 8$ , at which point the reconstructed trajectories will be many meters long. Hence, we will take a minimum DCA resolution of  $\text{DCA}_{\text{2D}}^{\min} = 1 \text{ mm}$ .

### 3. MuBeD

For the muon beam dump scenario, we assume a 1 TeV muon beam, then repeat the analysis performed in Refs. [135, 136]. The set-up is shown in Fig. 6.3. Once again, the number of vector boson production events in the thin-target approximation is

$$\begin{aligned} \frac{dN_{\text{prod.}}}{dE_k d\theta_k dz} &= \frac{N_\mu \rho_{\text{tar}}}{M_{\text{tar}}} \int_0^{L_{\text{tar}}} d\ell \frac{d\sigma}{dE_k d\theta_k} \frac{dP(z - \ell)}{dz} \\ &= N_\mu \frac{\rho_{\text{tar}} L_{\text{tar}}}{M_{\text{tar}}} \frac{d\sigma}{dE_k d\theta_k} \frac{P(z) - P(z - L_{\text{tar}})}{L_{\text{tar}}} \end{aligned} \quad (6.7)$$

where we have included a differential w.r.t.  $\theta_k$  so that we can get the number of signal events into the form (6.5). In this case, while we have assumed the target is small relative to the decay length of the material, we can no longer assume that the decay is prompt; i.e.  $\gamma c\tau \ll L_{\text{tar}}$ . The probability that the boson decays between the shielding region ( $z \approx L_{\text{tar}} + L_{\text{sh}}$ ) and the detector

region ( $z \approx L_{\text{tar}} + L_{\text{sh}} + L_{\text{det}}$ ) is

$$\begin{aligned} P_{\text{disp.}} &= \int_{L_{\text{tar}}+L_{\text{sh}}}^{L_{\text{tar}}+L_{\text{sh}}+L_{\text{det}}} \frac{dz}{L_{\text{tar}}} \left[ \left(1 - e^{-z/\gamma c \tau_{A'}}\right) - \left(1 - e^{-(z-L_{\text{tar}})/\gamma c \tau_{A'}}\right) \right] \\ &= \int_{L_{\text{tar}}+L_{\text{sh}}}^{L_{\text{tar}}+L_{\text{sh}}+L_{\text{det}}} \frac{dz}{L_{\text{tar}}} \left[ e^{-(z-L_{\text{tar}})/\gamma c \tau_{A'}} - e^{-z/\gamma c \tau_{A'}} \right] \\ &= \frac{\gamma c \tau_{A'}}{L_{\text{tar}}} \left(1 - e^{-L_{\text{tar}}/\gamma c \tau_{A'}}\right) \left(1 - e^{-L_{\text{det}}/\gamma c \tau_{A'}}\right) e^{-L_{\text{sh}}/\gamma c \tau_{A'}} \end{aligned} \quad (6.8)$$

While this looks considerably more complicated than the probability of a displaced decay in Eq. 6.6, we can make the additional approximation that  $L_{\text{tar}} \ll \gamma c \tau_{A'}$ . Then, we have

$$P_{\text{disp.}} = e^{-(L_{\text{sh}}+L_{\text{det}})/\gamma c \tau_{A'}} - e^{-L_{\text{sh}}/\gamma c \tau_{A'}}. \quad (6.9)$$

In line with the 1.5 TeV scenario in Refs. [135, 136], we take  $L_{\text{tar}} = 5.0$  m,  $L_{\text{sh}} = 10.0$  m,  $L_{\text{dec}} = 100.0$  m, and  $|\eta| \gtrsim 5$ . However, we assume a beam energy of 1 TeV rather than 1.5 TeV for a more direct comparison to MuSIC. Defining the effective integrated luminosity to be  $\mathcal{L}_{\text{eff}} \equiv N_\mu(\rho_{\text{tar}} L_{\text{tar}} / M_{\text{tar}})$ , we recover the form (6.5) for the total number of signal events. In terms of final-states, we assume that the detector apparatus is well-instrumented to detect displaced decays of the gauge boson to  $e^+e^-$  and  $\mu^+\mu^-$  with 100% efficiency.

#### 6.4 Limits at the EIC

We compute 95% C.L. limits on the coupling of the gauge boson  $g_X$  at the EIC by computing those values of  $g_X$  for which  $N_{\text{sig.}}(g_X) > 3.09$  [160]. For a given mass, there are typically two  $g_X$  for which  $N_{\text{sig.}} = 3.09$ , and hence the corresponding limits will be double-sided. If  $g_X$  is too large, the lifetime of the  $A'$  is too large for the decay to be considered displaced; if  $g_X$  is too small, then either the cross-section is too small to produce  $A'$  at a detectable rate, or the majority of produced  $A'$  live too long to decay inside the detector.

In Fig 6.4, we show our projected limits at the 95% C.L. for displaced dark photons, as well as the gauge bosons for  $B - L$ ,  $L_e - L_\tau$  and  $L_\mu - L_\tau$ . We also show for comparison various existing limits (gray shaded region) and projected limits from current experiments (dashed lines) and future proposed experiments (dotted lines). These are mostly digitized from Ref. [55] using

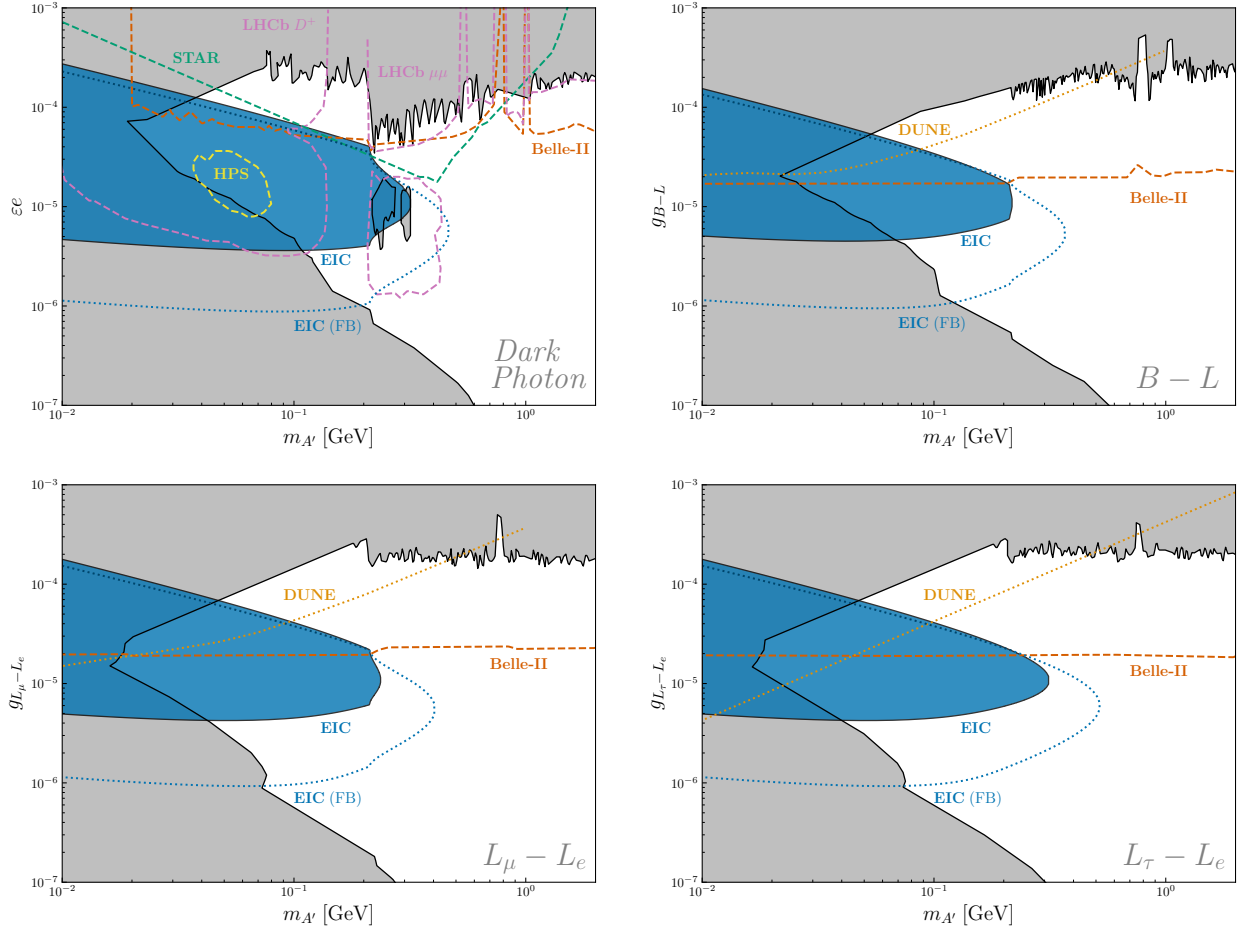


Figure 6.4: Projected constraints (95% C.L.) at the EIC on the kinetic mixing of a dark photon (top left), and gauge coupling for a  $U(1)_{B-L}$  (top right),  $U(1)_{L_\mu - L_e}$  (bottom left), and  $U(1)_{L_\tau - L_e}$  (bottom right) vector boson. The blue filled region corresponds to the sensitivity at the EIC assuming a pseudorapidity resolution of  $|\eta| < 3.5$ , whereas the dotted blue line considers a “far-backward” scenario in which the electron-side of the EIC is instrumented for pseudo-rapidity coverage  $4 < |\eta| < 6$ . Exclusion limits and projections are mostly reproduced from Ref. [55], but updated to reflect the current state of experiments. The exclusion limits (filled gray region) include U70/NuCal [124, 175], Orsay [176], E137 [177], E141 [178], E774 [120], NA48 [179], BaBar [180, 181], KLOE [182–184], LHCb [185], Borexino [186], Texono [187], NA64 [188] and FASER [189]. Projections from current experiments (dashed lines) are shown from STAR [190], Belle II [80], HPS [191], and LHCb [192, 193]. We also show projections from DUNE as a dotted line [194]. For a more comprehensive set of projected bounds for dark photons, we refer to the Snowmass White Paper [126].

DigitizeIt [162], although a few additional constraints and projections are included. The blue filled region shows our baseline projection using the ePIC detector and a luminosity for gold ion collisions of  $\mathcal{L} = 100 \text{ fb}^{-1}/A$ . We see that the EIC can provide significant new constraints on the

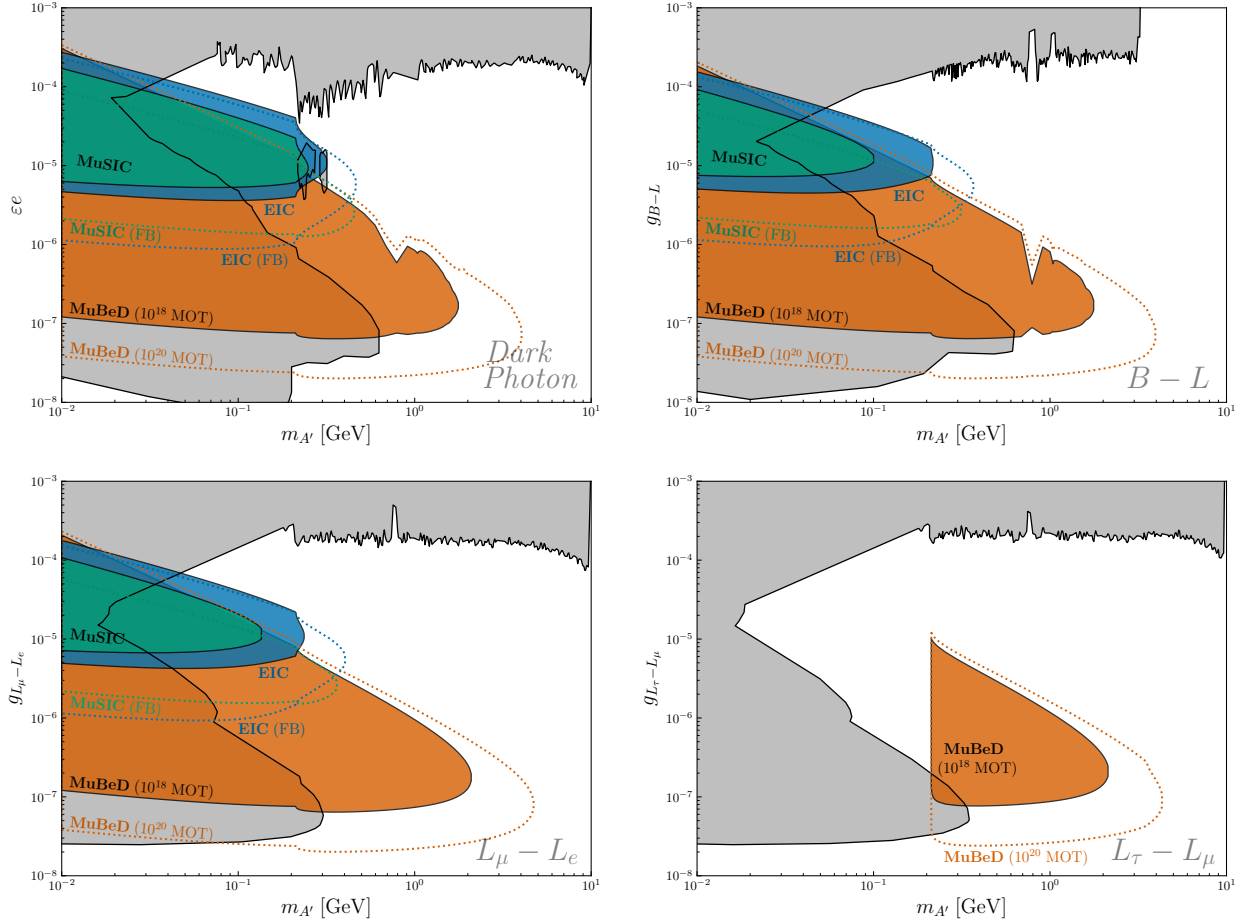


Figure 6.5: Projected constraints at the EIC, MuBeD, and MuSIC on the kinetic mixing of a dark photon (top left) and gauge strength of the anomaly-free abelian theories  $U(1)_{B-L}$  (top right),  $U(1)_{L_\mu - L_e}$  (bottom left) and  $U(1)_{L_\tau - L_\mu}$  (bottom right). To avoid clutter, we only show prior constraints, and no projections from other future experiments. An explanation of the exclusion limits is given in the caption of Fig. 6.4. A comprehensive list of projections can be found in Ref. [55]. Our results for the dark photon and  $L_\tau - L_\mu$  are in agreement with Ref. [135].

parameter space for masses  $m_{A'} \sim 100$  MeV and moderately weak couplings  $g_X \sim 10^{-5}$  for each of the considered bosons. Even comparing to other projected experimental bounds, the EIC provides useful reach in this parameter space. The blue dotted line labeled “EIC (FB)” shows how the projected bounds from the EIC could be improved by the inclusion of a far-backward detector in the direction of the electron beam, as described above. The additional pseudo-rapidity coverage up to  $|\eta| < 6$  expands the mass reach to 400 MeV, for a coupling of  $g_X \sim 10^{-5}$ .

## 6.5 Limits at MuBeD and MuSIC

To place 95% C.L. limits at MuBeD and MuSIC, we once again compute those values of  $g_X$  for which  $N_{\text{sig.}}(g_X) > 3.09$ . The results are shown alongside the EIC projected constraints in Fig. 6.5. The MuSIC results are shown in green, and the MuBeD results are shown in orange. MuBeD and MuSIC are not sensitive to  $L_\tau - L_e$ , but are potentially sensitive to  $L_\tau - L_\mu$ . Hence, we show the results for  $L_\tau - L_\mu$  instead (bottom right), alongside the results for the dark photon (top left),  $B - L$  (top right), and  $L_\mu - L_e$  (bottom left). As with the EIC, results for MuSIC are presented for two scenarios: a pseudo-rapidity coverage of  $-6 < \eta < 6$ , and a wider “far-backward” coverage of  $|\eta| < 8$ .

Surprisingly, MuSIC does not appear to be competitive with the EIC, despite the additional energy of the muon beam. Part of the reason for this is the large pseudo-rapidity of the produced bosons at MuSIC. As a result, only the far-backward coverage of MuSIC is competitive with the EIC, because most particles produced have a pseudo-rapidity  $|\eta| > 6$ . In addition, it is important to note that while the available energy is higher at MuSIC than the EIC (with a muon beam energy of  $E_{\text{MuSIC}} \approx 20$  TeV in the ion frame at the MuSIC as opposed to an electron beam energy of  $E_{\text{EIC}} \approx 4$  TeV in the ion frame at the EIC), a look at Fig. 4.2 reveals that the cross-section for on-diagonal production at MuSIC is smaller than that at the EIC for  $m_{A'} \lesssim m_\mu$ . This can be understood in the WW approximation from the fact that most of the cross-section is sampled near the minimum possible photon transfer  $t_- \sim [m_\varphi(2m_\ell + m_\varphi)/2E]^2$ , and scales as  $\sigma \sim 1/t^2$ . While  $E$  is larger at MuSIC than the EIC, the numerator for  $m_\varphi < m_\mu$  is  $[m_\varphi(2m_\mu + m_\varphi)]^2 \sim 4m_\varphi^2 m_\mu^2$  at MuSIC, but  $[m_\varphi(2m_e + m_\varphi)]^2 \sim m_\varphi^4$  at the EIC. Hence,  $t_-$  is ultimately suppressed at the EIC relative to MuSIC, making the resulting production cross-section larger. While MuSIC is technically sensitive to  $U(1)_{L_\tau - L_\mu}$  gauge bosons, we find that given our assumptions, the sensitivity is too weak to provide meaningful limits.

MuBeD, on the other hand, is competitive over the entire range of couplings, for both  $N_\mu = 10^{18}$  and  $N_\mu = 10^{20}$  muons on target. This result highlights the advantage of beam dump

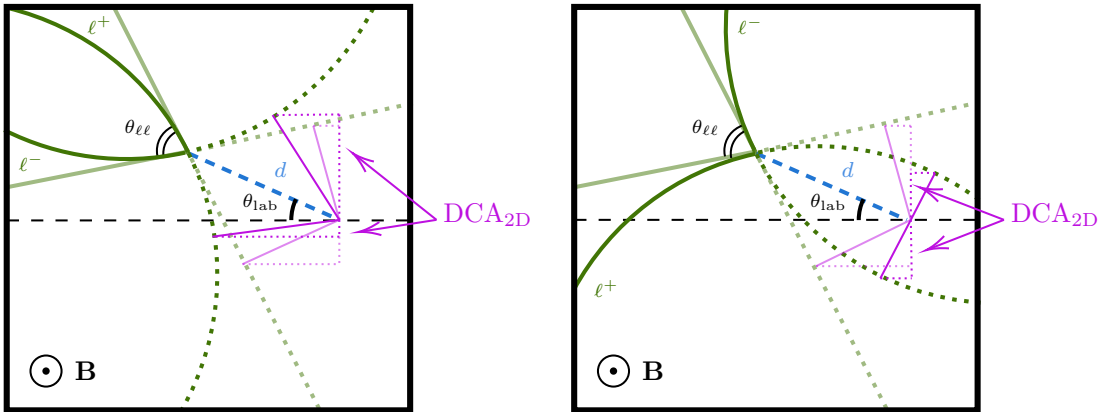


Figure 6.6: A schematic representation of the difference between the transverse DCAs for a straight-line reconstructed trajectory and a circular reconstructed trajectory (consistent with the final-state leptons being immersed in a uniform magnetic field  $\mathbf{B}$ ). The diagrams on the left and right demonstrate the two possible in-plane orientations of the  $\ell^+$  relative to the  $\ell^-$ .

experiments over lepton-ion colliders: a higher luminosity (by virtue of the dense target) and increased pseudorapidity coverage (capturing all particles with  $\eta \gtrsim 5$ ). While lepton-ion colliders can peripherally produce higher-mass particles than their beam-dump counterparts (which is what allows the EIC to compete with past beam-dump experiments), this effect is not enough to give MuSIC or the EIC an edge over a 1 TeV muon beam dump. The rate of production for GeV-scale particles, and their corresponding lab-frame lifetimes, are just too low for either experiment to provide meaningful displaced limits at this mass range.

## 6.6 Displaced Vertex Resolution Considerations

The analysis for the EIC and MuSIC above notably relied on the assumption that the reconstructed tracks of the vector boson final states were straight-line trajectories. Here we will evaluate the sensitivity of this analysis to the details of the reconstructed trajectory. In particular, we will consider two alternative analyses: one will estimate the effect of an external magnetic field of 1 T, and the other will completely discard the transverse DCA analysis in favor of a simpler fiducial  $d_{\min}$ , which is independent of the kinematics of the final-state particle.

To estimate the sensitivity of the analysis to deviations in a straight-line trajectory, we

consider the scenario where the final-state leptons experience a uniform magnetic field  $\mathbf{B}$  with magnitude 1 T (which is the anticipated strength of the magnets at the EIC [149]). For simplicity, we assume that the leptonic decay products of the  $A'$  are always in the plane perpendicular to the magnetic field, so that their reconstructed tracks are circular arcs of radius  $R_B = E_\ell v / eBc$ . This assumption is far from realistic, but represents the *maximal* deviation from a straight-line trajectory one can expect either of the leptonic final states to follow. Hence, this analysis will be a useful metric for evaluating the validity of our initial assumption of a straight-line trajectory. A schematic representation of this set-up is shown in Fig. 6.6. For simplicity, we assume that each final-state lepton has an initial direction at an angle of  $\theta_{\ell\ell}/2 \approx m_{A'}/E_{A'}$  w.r.t. the direction of the boson. We consider both possible orientations of in-plane final states (i.e., whether the  $\ell^+$  is clockwise or counterclockwise from the  $\ell^-$ ) and assume that each of these occurs for 50% of produced events. For each orientation, we compute the average transverse DCA of both final-states  $\overline{\text{DCA}_{2\text{D}}}$ , and only count those events for which  $\overline{\text{DCA}_{2\text{D}}} > \text{DCA}_{2\text{D}}^{\min}$ .

We would also like to assess how much the analysis differs if we choose a fiducial minimum displacement  $d_{\min}$  in Eq. 6.6. For both the EIC and MuSIC, we assume that  $d_{\min} = 1$  cm. This is a relatively large displacement, so it may seem like a reasonable assumption given the sensitivity of modern detectors. However, when the opening angle of the final-state lepton pair is small, it can be difficult to discern exactly where the leptons originated, which is why the transverse DCA is likely a more reliable metric for resolving displacements.

Projected exclusions on the kinetic mixing of a dark photon at the EIC and MuSIC for both of these analyses are shown in Fig. 6.7. The limits from the  $B$ -field analysis shown in the left panel and limits from the fiducial  $d_{\min}$  analysis shown in the right panel. The addition of a large transverse magnetic field has minimal effect on the results found in Section 6.5. The only difference appears for low masses ( $m_{A'} = \mathcal{O}(10 \text{ MeV})$ ) and large couplings ( $g_{A'} \sim 10^{-4}\text{--}10^{-3}$ ), in a region that is already mostly excluded by existing experiments. This aligns with the understanding that lower-mass particles do not carry away as much energy from the interaction, which results in a reduced energy for the final-state decay products. This in turn causes small turning radius in the

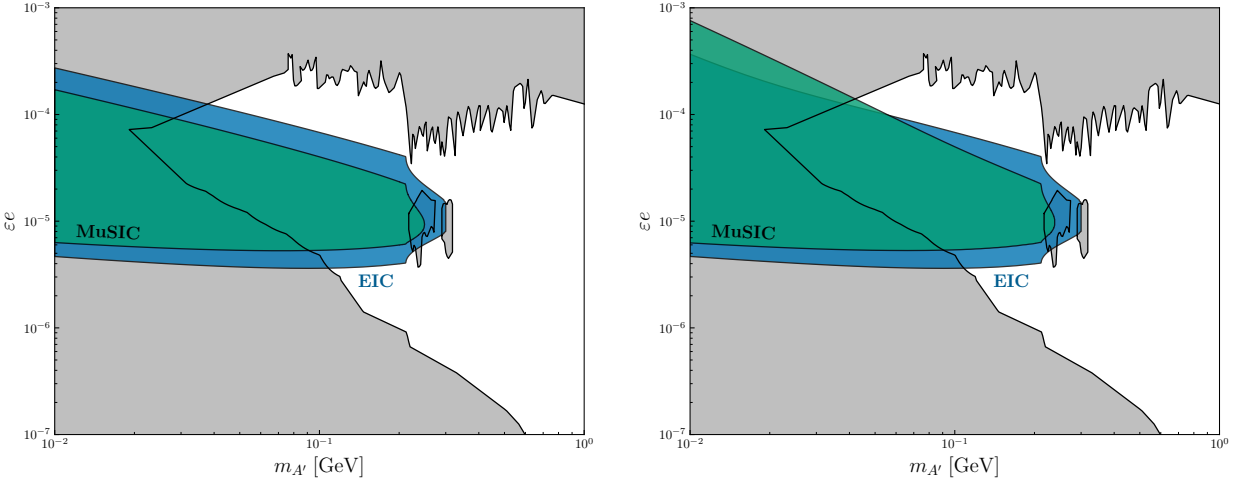


Figure 6.7: Limits on the dark photon kinetic mixing  $\varepsilon e$  assuming each final-state lepton is deflected by a 1 T magnetic field (left) and assuming a fiducial minimum displacement of  $d_{\min} = 1$  cm (right). Limits from the EIC are shown in blue, and limits from MuSIC are shown in green.

magnetic field, which leads to a more drastic deviation from the straight-line trajectory scenario. The effect all but vanishes for larger masses at both experiments. By contrast, we see that use of a fiducial minimum displacement  $d_{\min} = 1$  cm has a profound effect on the projected exclusions, especially for MuSIC. Hence, if other experimental methods can be used to identify displacements, they would have the potential to drastically improve the reach of these experiments. In addition, we note that limits at both the EIC and MuSIC can be improved with a better DCA resolution.

## Chapter 7

### Concluding Remarks

It is difficult to overstate the success that particle physics has enjoyed over the past century. Since 1925, our catalog of fundamental particles has grown from two (the electron and photon) to thirty (including antiparticles).<sup>1</sup> In that time, the framework of quantum field theory was developed to describe the nature of these particles, and the framework of local symmetries (or gauge theories) to describe their interactions. The puzzle of missing energy in nuclear decays led to the discovery of the neutrino and the formulation of the weak interaction. Deep inelastic scattering experiments and the tower of hadrons observed in cosmic rays revealed the existence of quarks and laid the groundwork for the development of the strong interaction. The observation of CP-violation in kaon decays and discovery of the  $\tau$  lepton pointed to the existence of three generations of each fermion type. The need to give mass to the weak interaction's gauge bosons while preserving gauge symmetry led to the development of the Brout-Englert-Higgs mechanism and the prediction of the Higgs boson, which also provided a natural framework for fermion mass generation. This is but a brief account of the milestones that culminated in the development of the Standard Model of particle physics, all in the span of a human lifetime.

Despite this success, we are currently in a drought of new discoveries. The Standard Model

---

<sup>1</sup> There is some ambiguity as to what constitutes a particle. I have counted each *Dirac* fermion field as two particles (a particle and antiparticle), but this is tricky for the neutrino which is a *Weyl* fermion in the current formulation of the Standard Model. I still count each neutrino and anti-neutrino as a separate particle. I have also counted the gluon as *one* particle instead of *eight*, treating it as a single field which is in the adjoint representation of  $SU(3)_C$  and hence has eight colored components. While this is consistent with treating each quark as *one* particle as opposed to *three* (one for each color in the  $SU(3)_C$  triplet), it is somewhat at odds with our treatment of the gauge bosons in  $SU(2)_L$ . However, given that  $SU(2)_L$  is broken by the Higgs VEV and a spectrum of different massive states arise, I believe this number is internally consistent. One can more objectively refer to the number of *particle degrees of freedom* between 1925 and today (four and 128), but this is less narratively compelling.

as we know it today was finalized in the late 1970s with the unification of the electromagnetic and weak interactions into the electroweak theory, and the establishment of quantum chromodynamics as the theory of the strong force. In the years that followed, its predictions were slowly verified: in the early 1980s, with the discovery of the  $W^\pm$  and  $Z$  bosons; in 1995, with the discovery of the top quark; and finally, in 2012, with the discovery of the Higgs boson. In that period and up until today, no new elementary particles or forces have been observed. The Standard Model continues to agree with experimental data across a vast range of energies and processes, and remains to this day our most accurate description of fundamental physics ever constructed.

And yet, we are reasonably certain that the Standard Model is an incomplete description of the particle content of our Universe. Our astrophysical observations indicate that 85% of the matter in the universe is not comprised of Standard Model particles, but is instead *dark matter* that has very weak Standard Model interactions (if any at all).<sup>2</sup> In addition, the observation of neutrino oscillations is a direct hint that particles beyond the Standard Model must exist. Perhaps most strikingly, the Standard Model is completely silent on the force we are most familiar with: gravity. Nearly every attempt to unify gravity with the other three forces inevitably predicts a vast spectrum of particles, none of which have appeared in any of our collider experiments.

Even within the Standard Model, there are both inconsistencies and mysteries. Ignoring neutrinos, the masses of the fermions still span four orders of magnitude, and the Standard Model offers no explanation for this hierarchy. Worse still, the Standard Model predicts that quantum corrections to the Higgs boson mass should push it toward the Planck scale, and yet we observe it to have a mass of only 125 GeV. In addition, the CP-violating gluon-gluon interaction  $\frac{\theta}{4\pi^2} \text{Tr}\{G_{\mu\nu}\tilde{G}^{\mu\nu}\}$  is apparently absent from the Standard Model, despite respecting all of the Standard Model gauge symmetries.

A variety of particle explanations for the phenomena described above were reviewed in Chap-

---

<sup>2</sup> While “Modified Newtonian Dynamics” (MOND) can also solve this problem by changing the form of the gravitational interaction at large scales, observations of gravitational lensing from dark matter in the empty space around colliding galaxies [195] and possibly even galaxies which contain no dark matter at all [196] render a particle solution more likely.

ter 2. They almost all have one feature in common that is completely absent in the Standard Model: charged lepton flavor violation (CLFV). While the degree of this flavor-violation can be made arbitrarily small by tuning the couplings in each model, we have the benefit of knowing from neutrino oscillations that lepton flavor is *not* a good symmetry of the Universe. Then it is not a matter of *if* CLFV processes occurs, but rather *how often*. If the only process which directly contributes to CLFV is neutrino oscillation, we will likely never observe a CLFV event in our lifetimes. However, if any of the models discussed in Chapter 2 is realized in our Universe, CLFV processes could have rates many orders of magnitude higher than neutrino oscillation-mediated processes.

Given the ubiquity of CLFV in extensions to the Standard Model, it is a very promising avenue for discovery. In Chapter 3, we reviewed some of the leading constraints on CLFV couplings: limits on the branching fraction of the LFV lepton decays  $\ell_i \rightarrow \ell_j \ell_k \bar{\ell}_l$  and  $\ell_i \rightarrow \ell_j \gamma$ . While the resulting constraints are strong, they are dependent on products of the CLFV couplings, and hence sensitive to relative hierarchies between said couplings. In addition, the degree of PV in the interaction can lead to a suppression of the limits for certain channels, in particular for purely chiral interactions. Hence, when placing limits on a new CLFV model of physics, one must keep these properties of the model in mind to ensure that the results are accurate.

In order to find exclusions on *singular* couplings as opposed to coupling products, we turned to the lepton electric and magnetic dipole moments. The strongest constraints on singular couplings (which in some instances out-perform the LFV lepton decay constraints above) come from the electron EDM on  $|g_{e\ell}|$ . However, these constraints are only present for CP-violating interactions, so neither purely parity-conserving nor purely chiral interactions are constrained by this measurement. On the other hand, interactions with any degree of PV contribute to the magnetic dipole moments of the leptons. Limits on these couplings assuming their contributions lie within the current experimental uncertainty were obtained in Section 3.4.6; it was found once again that in some cases, there is a vast suppression in the contribution from chiral interactions compared to purely parity conserving interactions, resulting in weaker limits for the chiral scenario. Of course, both of these measurements are currently (at least somewhat) plagued by anomalies, so agreement

must be found between the theoretical and experimental values before the bounds can be taken at face value. In the interim, we have presented flavor-violating solutions to the electron and muon  $g - 2$  anomalies assuming a singular flavor off-diagonal coupling  $g_{\ell\tau}$ , exploring how the result varies with the PV angle  $\theta_{\ell\tau}$ .

The work in Chapter 3 only explored scalars which contribute to flavor-changing neutral currents. It would be interesting to see whether a similar chiral suppression can be obtained for vectors. Results from Ref. [197] indicate that this is indeed the case for LFV dark photon contributions to the electron  $g - 2$ , although more work needs to be done to determine whether this generalizes. In addition, charged scalars and vectors can also contribute to the LFV decays and dipole moments discussed above; it would be interesting to explore the role that PV plays in these contexts.

In Chapter 4, we explored an alternative process that has the potential to probe LFV couplings which is largely insensitive both to model hierarchies and degree of PV in the interaction (at least for heavy particles): production of a new boson in lepton-nucleus collisions via the process  $\ell^- A_Z \rightarrow \ell'^- A_Z \varphi$ . For concreteness, we have compared four experimental set-ups: the E137 beam dump experiment at SLAC, the upcoming EIC at BNL, a hypothetical 1 TeV Muon Beam Dump (dubbed MuBeD), and a hypothetical 1 TeV Muon (Synchrotron)-Ion Collider (dubbed MuSIC). Due to the additional luminosity from a solid target combined with the large pseudo-rapidity reach, we find that beam dump experiments are a superior mode for production and detection of *light* bosons ( $m_\varphi \lesssim 1$  GeV), but lepton-ion colliders become competitive for heavier bosons. Improvements in luminosity or pseudo-rapidity reach for lepton-ion colliders would improve their sensitivity. Of course, there are also other possible production modes that may be more promising at these experiments than their beam-dump counterparts.

The code developed for this chapter allows for a detailed reconstruction not only of the production cross-section of the new boson, but its kinematical distributions over a wide range of masses as well. These methods should be broadly applicable to any  $2 \rightarrow 3$  scattering processes, provided integrability of the amplitude over  $\phi_q$ . Alternatively, in the event that the integral over  $\phi_q$  is in-

tractable, one can still use the identification (4.45) in situations for which the Weizsäcker-Williams approximation applies. In particular, we find that while the *Improved* Weizsäcker-Williams approximation can differ somewhat substantially from the true cross-section at heavy boson masses, the original Weizsäcker-Williams approximation remains reliable across all of the processes considered, and can save on computational costs. To conclude the chapter, we explored limits one can obtain from an LFV scalar at the EIC, MuBeD, and MuSIC, finding that limits on  $g_{\ell\tau}$  are not as competitive as those considered in Chapter 3 *in general*, but have the benefit of being mostly independent of the other model parameters (up to the branching fraction of the final-state boson).

In Chapter 5, we examined collider constraints on a certain class of CLFV particles: GeV-scale leptophilic ALPs. Such particles are realized e.g. in  $\mathbb{Z}_N$  Froggatt-Nielsen models [49] and the composite dark sector scenario in Ref. [51]. We began by exploring the ability to produce and detect these particles at CERN in the event that they have a substantial coupling to the Higgs. We find that for substantial Higgs couplings ( $C_{ah}/\Lambda^2 \sim 1 \text{ TeV}^{-2}$ ,  $C'_{ah}/\Lambda^2 \sim 10 \text{ TeV}^{-2}$ ), the LFV coupling  $C_{\tau\ell}/\Lambda$  has already been probed down to  $10^{-5} \text{ TeV}^{-1}$  at CMS and  $10^{-6} \text{ TeV}^{-1}$  at ATLAS, far exceeding the current limits from LFV lepton decays. In addition, it was found that the proposed MATHUSLA experiment would be able to push the coupling limits even further to  $C_{\tau\ell}/\Lambda \gtrsim 10^{-8} \text{ TeV}^{-1}$  at the high-luminosity LHC.

However, in the event that the Higgs couplings are small ( $C_{ah}/\Lambda^2 \lesssim 1 \text{ TeV}^{-2}$ ,  $C'_{ah}/\Lambda^2 \lesssim 10 \text{ TeV}^{-2}$ ), the limits and projections weaken and eventually disappear. In this event, we apply the results of Chapter 4 to find model-independent limits. As with scalars, it is found that these limits are substantially weaker, probing couplings at around  $C_{\tau\ell}/\Lambda \gtrsim 1 \text{ TeV}^{-1}$ , but represent absolute limits in the absence of other model couplings. For a muon beam dump, however, we find that the most optimistic scenario (for which a 1 TeV muon beam is incident on a 2 m block of lead for  $\mathcal{O}(1 \text{ year})$  of total operation, corresponding to  $10^{20}$  muons on target), the resulting limits are competitive with existing limits from LFV lepton decays, while remaining largely insensitive to the other model parameters.

Finally, in Chapter 6, we explored the possibility of detecting displaced decays of hidden gauge

bosons produced via the process discussed in Chapter 4 at the EIC, MuBeD, and MuSIC. A certain class of these bosons, the  $U(1)_{L_i-L_j}$  gauge bosons, exhibit CLFV couplings after spontaneous breaking of the abelian symmetry, but here we only focus on production via the on-diagonal channel  $\ell A_Z \rightarrow \ell A_Z A'$ . The EIC is able to fill in a currently untouched region of the parameter space near  $(m_{A'}, g_{A'}) \sim (100 \text{ MeV}, 10^{-5})$  for a dark photon,  $U(1)_{B-L}$ ,  $U(1)_{L_e-L_\mu}$ , and  $U(1)_{L_e-L_\tau}$ . MuSIC and MuBeD are sensitive to all of these except  $U(1)_{L_e-L_\tau}$ , but are additionally sensitive to  $U(1)_{L_\mu-L_\tau}$ . Surprisingly, we find that a similar analysis at MuSIC yields slightly worse results than at the EIC, despite the vast increase in available energy at the hypothetical collider. This is mostly due to the increased pseudorapidity of the produced bosons at MuSIC, but is also due to a slight decrease in the production cross-section at MuSIC compared to the EIC in the relevant mass range. Given its higher luminosity and pseudorapidity reach, MuBeD would be able to probe much heavier dark bosons with displaced decays, providing limits or possibly detecting particles near  $(m_{A'}, g_{A'}) \sim (1 \text{ GeV}, 10^{-7})$ , a region which is entirely untouched by modern experiments.

This chapter focused solely on parity-conserving couplings of the dark boson, so it would be interesting to see whether stronger limits can be obtained for axial vectors (whose production cross-section per Fig. 4.2 appears to be substantially larger for some masses). However, the mass range for which the PV nature of the interaction matters is  $m_{A'} < m_e$  at the EIC and  $m_{A'} < m_\mu$  at MuBeD and MuSIC, which are regions that are already heavily covered by existing experiments. However, in the event that such a signal is found, one could potentially use the left-right asymmetry with a polarized beam to determine the PV nature of the interaction. Finally, we note that we have only considered production off of the lepton side off of the interaction, whereas dark photons and  $U(1)_{B-L}$  gauge bosons will also have significant interactions with the nucleus. These diagrams are suppressed by an evaluation of the form-factor at the mass-squared of the boson,  $G(m_{A'}^2)$ . While this may matter for  $m_{A'} \lesssim 10 \text{ MeV}$ , it drops off rapidly for larger masses due to the expression for the form factor (4.7).

## Bibliography

- [1] John N. Bahcall. Solar neutrinos. I: Theoretical. *Phys. Rev. Lett.*, 12:300–302, 1964. doi: 10.1103/PhysRevLett.12.300.
- [2] Raymond Davis, Jr., Don S. Harmer, and Kenneth C. Hoffman. Search for neutrinos from the sun. *Phys. Rev. Lett.*, 20:1205–1209, 1968. doi: 10.1103/PhysRevLett.20.1205.
- [3] Y. Fukuda et al. Evidence for oscillation of atmospheric neutrinos. *Phys. Rev. Lett.*, 81: 1562–1567, 1998. doi: 10.1103/PhysRevLett.81.1562.
- [4] S. M. Oser. Neutrino oscillation results from the Sudbury Neutrino Observatory. In *31st International Conference on High Energy Physics*, pages 8–17, 12 2001.
- [5] Peter Minkowski.  $\mu \rightarrow e\gamma$  at a Rate of One Out of  $10^9$  Muon Decays? *Phys. Lett. B*, 67: 421–428, 1977. doi: 10.1016/0370-2693(77)90435-X.
- [6] M. Magg and C. Wetterich. Neutrino Mass Problem and Gauge Hierarchy. *Phys. Lett. B*, 94:61–64, 1980. doi: 10.1016/0370-2693(80)90825-4.
- [7] Samoil M. Bilenky, S. T. Petcov, and B. Pontecorvo. Lepton Mixing, mu → e + gamma Decay and Neutrino Oscillations. *Phys. Lett. B*, 67:309, 1977. doi: 10.1016/0370-2693(77)90379-3.
- [8] S. Navas et al. Review of particle physics. *Phys. Rev. D*, 110(3):030001, 2024. doi: 10.1103/PhysRevD.110.030001.
- [9] Roman Marcarelli. Thesis. <https://github.com/rmarcarelli/thesis>, 2025.
- [10] Nicola Cabibbo. Unitary Symmetry and Leptonic Decays. *Phys. Rev. Lett.*, 10:531–533, 1963. doi: 10.1103/PhysRevLett.10.531.
- [11] Makoto Kobayashi and Toshihide Maskawa. CP Violation in the Renormalizable Theory of Weak Interaction. *Prog. Theor. Phys.*, 49:652–657, 1973. doi: 10.1143/PTP.49.652.
- [12] B. Pontecorvo. Neutrino Experiments and the Problem of Conservation of Leptonic Charge. *Zh. Eksp. Teor. Fiz.*, 53:1717–1725, 1967.
- [13] Ziro Maki, Masami Nakagawa, and Shoichi Sakata. Remarks on the unified model of elementary particles. *Prog. Theor. Phys.*, 28:870–880, 1962. doi: 10.1143/PTP.28.870.
- [14] Howard E. Haber and Gordon L. Kane. The Search for Supersymmetry: Probing Physics Beyond the Standard Model. *Phys. Rept.*, 117:75–263, 1985. doi: 10.1016/0370-1573(85)90051-1.

- [15] Csaba Csaki. The Minimal supersymmetric standard model (MSSM). *Mod. Phys. Lett. A*, 11:599, 1996. doi: 10.1142/S021773239600062X.
- [16] Ernest Ma. Naturally small seesaw neutrino mass with no new physics beyond the TeV scale. *Phys. Rev. Lett.*, 86:2502–2504, 2001. doi: 10.1103/PhysRevLett.86.2502.
- [17] S. Gabriel and S. Nandi. A New two Higgs doublet model. *Phys. Lett. B*, 655:141–147, 2007. doi: 10.1016/j.physletb.2007.04.062.
- [18] Fei Wang, Wenyu Wang, and Jin Min Yang. Split two-Higgs-doublet model and neutrino condensation. *EPL*, 76:388–394, 2006. doi: 10.1209/epl/i2006-10293-3.
- [19] Ernest Ma. Common origin of neutrino mass, dark matter, and baryogenesis. *Mod. Phys. Lett. A*, 21:1777–1782, 2006. doi: 10.1142/S0217732306021141.
- [20] Ernest Ma. Verifiable radiative seesaw mechanism of neutrino mass and dark matter. *Phys. Rev. D*, 73:077301, 2006. doi: 10.1103/PhysRevD.73.077301.
- [21] Mayumi Aoki, Shinya Kanemura, and Osamu Seto. Neutrino mass, Dark Matter and Baryon Asymmetry via TeV-Scale Physics without Fine-Tuning. *Phys. Rev. Lett.*, 102:051805, 2009. doi: 10.1103/PhysRevLett.102.051805.
- [22] Mayumi Aoki, Shinya Kanemura, Koji Tsumura, and Kei Yagyu. Models of Yukawa interaction in the two Higgs doublet model, and their collider phenomenology. *Phys. Rev. D*, 80: 015017, 2009. doi: 10.1103/PhysRevD.80.015017.
- [23] G. C. Branco, P. M. Ferreira, L. Lavoura, M. N. Rebelo, Marc Sher, and Joao P. Silva. Theory and phenomenology of two-Higgs-doublet models. *Phys. Rept.*, 516:1–102, 2012. doi: 10.1016/j.physrep.2012.02.002.
- [24] Lei Wang, Jin Min Yang, and Yang Zhang. Two-Higgs-doublet models in light of current experiments: a brief review. *Commun. Theor. Phys.*, 74(9):097202, 2022. doi: 10.1088/1572-9494/ac7fe9.
- [25] Sheldon L. Glashow and Steven Weinberg. Natural Conservation Laws for Neutral Currents. *Phys. Rev. D*, 15:1958, 1977. doi: 10.1103/PhysRevD.15.1958.
- [26] E. A. Paschos. Diagonal Neutral Currents. *Phys. Rev. D*, 15:1966, 1977. doi: 10.1103/PhysRevD.15.1966.
- [27] Roni Harnik, Joachim Kopp, and Jure Zupan. Flavor Violating Higgs Decays. *JHEP*, 03:026, 2013. doi: 10.1007/JHEP03(2013)026.
- [28] R. Primulando, J. Julio, and P. Uttayarat. Collider Constraints on Lepton Flavor Violation in the 2HDM. *Phys. Rev. D*, 101(5):055021, 2020. doi: 10.1103/PhysRevD.101.055021.
- [29] C. D. Froggatt and Holger Bech Nielsen. Hierarchy of Quark Masses, Cabibbo Angles and CP Violation. *Nucl. Phys. B*, 147:277–298, 1979. doi: 10.1016/0550-3213(79)90316-X.
- [30] Claudia Cornella, David Curtin, Gordan Krnjaic, and Micah Mellors. Testing the Froggatt-Nielsen Mechanism with Lepton Violation. 12 2024.

- [31] Lorenzo Calibbi, Florian Goertz, Diego Redigolo, Robert Ziegler, and Jure Zupan. Minimal axion model from flavor. *Phys. Rev. D*, 95(9):095009, 2017. doi: 10.1103/PhysRevD.95.095009.
- [32] Yohei Ema, Koichi Hamaguchi, Takeo Moroi, and Kazunori Nakayama. Flaxion: a minimal extension to solve puzzles in the standard model. *JHEP*, 01:096, 2017. doi: 10.1007/JHEP01(2017)096.
- [33] A. Ringwald. Axions and Axion-Like Particles. In *49th Rencontres de Moriond on Electroweak Interactions and Unified Theories*, pages 223–230, 2014.
- [34] Kiwoon Choi, Sang Hui Im, and Chang Sub Shin. Recent Progress in the Physics of Axions and Axion-Like Particles. *Ann. Rev. Nucl. Part. Sci.*, 71:225–252, 2021. doi: 10.1146/annurev-nucl-120720-031147.
- [35] R. D. Peccei and Helen R. Quinn. CP Conservation in the Presence of Instantons. *Phys. Rev. Lett.*, 38:1440–1443, 1977. doi: 10.1103/PhysRevLett.38.1440.
- [36] R. D. Peccei and Helen R. Quinn. Constraints Imposed by CP Conservation in the Presence of Instantons. *Phys. Rev. D*, 16:1791–1797, 1977. doi: 10.1103/PhysRevD.16.1791.
- [37] Michael Dine, Willy Fischler, and Mark Srednicki. A Simple Solution to the Strong CP Problem with a Harmless Axion. *Phys. Lett. B*, 104:199–202, 1981. doi: 10.1016/0370-2693(81)90590-6.
- [38] A. R. Zhitnitsky. On Possible Suppression of the Axion Hadron Interactions. (In Russian). *Sov. J. Nucl. Phys.*, 31:260, 1980.
- [39] Jihn E. Kim. Weak Interaction Singlet and Strong CP Invariance. *Phys. Rev. Lett.*, 43:103, 1979. doi: 10.1103/PhysRevLett.43.103.
- [40] Mikhail A. Shifman, A. I. Vainshtein, and Valentin I. Zakharov. Can Confinement Ensure Natural CP Invariance of Strong Interactions? *Nucl. Phys. B*, 166:493–506, 1980. doi: 10.1016/0550-3213(80)90209-6.
- [41] C. B. Adams et al. Axion Dark Matter. In *Snowmass 2021*, 3 2022.
- [42] Murray Gell-Mann. The Eightfold Way: A Theory of strong interaction symmetry. 3 1961. doi: 10.2172/4008239.
- [43] Howard Georgi, David B. Kaplan, and Lisa Randall. Manifesting the Invisible Axion at Low-energies. *Phys. Lett. B*, 169:73–78, 1986. doi: 10.1016/0370-2693(86)90688-X.
- [44] Martin Bauer, Matthias Neubert, and Andrea Thamm. Collider Probes of Axion-Like Particles. *JHEP*, 12:044, 2017. doi: 10.1007/JHEP12(2017)044.
- [45] Martin Bauer, Matthias Neubert, Sophie Renner, Marvin Schnubel, and Andrea Thamm. The Low-Energy Effective Theory of Axions and ALPs. *JHEP*, 04:063, 2021. doi: 10.1007/JHEP04(2021)063.
- [46] Martin Bauer, Matthias Neubert, Sophie Renner, Marvin Schnubel, and Andrea Thamm. Flavor probes of axion-like particles. *JHEP*, 09:056, 2022. doi: 10.1007/JHEP09(2022)056.

- [47] Manuel A. Buen-Abad, JiJi Fan, Matthew Reece, and Chen Sun. Challenges for an axion explanation of the muon  $g-2$  measurement. *JHEP*, 09:101, 2021. doi: 10.1007/JHEP09(2021)101.
- [48] Matthias Neubert and Marvin Schnubel. Two-loop contributions of axion-like particles to electromagnetic and chromomagnetic form factors. *Eur. Phys. J. C*, 84(6):571, 2024. doi: 10.1140/epjc/s10052-024-12881-9.
- [49] Admir Greljo, Aleks Smolković, and Alessandro Valenti. Froggatt-Nielsen ALP. *JHEP*, 09:174, 2024. doi: 10.1007/JHEP09(2024)174.
- [50] Graham D. Kribs and Ethan T. Neil. Review of strongly-coupled composite dark matter models and lattice simulations. *Int. J. Mod. Phys. A*, 31(22):1643004, 2016. doi: 10.1142/S0217751X16430041.
- [51] Hooman Davoudiasl, Pier Paolo Giardino, Ethan T. Neil, and Enrico Rinaldi. Unified Scenario for Composite Right-Handed Neutrinos and Dark Matter. *Phys. Rev. D*, 96(11):115003, 2017. doi: 10.1103/PhysRevD.96.115003.
- [52] Murray Gell-Mann, R. J. Oakes, and B. Renner. Behavior of current divergences under  $SU(3) \times SU(3)$ . *Phys. Rev.*, 175:2195–2199, 1968. doi: 10.1103/PhysRev.175.2195.
- [53] Branden Aitken et al. MATHUSLA: An External Long-Lived Particle Detector to Maximize the Discovery Potential of the HL-LHC. 4 2025.
- [54] Helge Kragh. Physics and the totalitarian principle, 2019. URL <https://arxiv.org/abs/1907.04623>.
- [55] Martin Bauer, Patrick Foldenauer, and Joerg Jaeckel. Hunting All the Hidden Photons. *JHEP*, 07:094, 2018. doi: 10.1007/JHEP07(2018)094.
- [56] Robert Foot. New Physics From Electric Charge Quantization? *Mod. Phys. Lett. A*, 6:527–530, 1991. doi: 10.1142/S0217732391000543.
- [57] X. G. He, Girish C. Joshi, H. Lew, and R. R. Volkas. NEW Z-prime PHENOMENOLOGY. *Phys. Rev. D*, 43:22–24, 1991. doi: 10.1103/PhysRevD.43.R22.
- [58] Xiao-Gang He, Girish C. Joshi, H. Lew, and R. R. Volkas. Simplest Z-prime model. *Phys. Rev. D*, 44:2118–2132, 1991. doi: 10.1103/PhysRevD.44.2118.
- [59] Ernest Ma, D. P. Roy, and Sourov Roy. Gauged  $L(\mu) - L(\tau)$  with large muon anomalous magnetic moment and the bimaximal mixing of neutrinos. *Phys. Lett. B*, 525:101–106, 2002. doi: 10.1016/S0370-2693(01)01428-9.
- [60] Julian Heeck and Werner Rodejohann. Gauged  $L_\mu - L_\tau$  Symmetry at the Electroweak Scale. *Phys. Rev. D*, 84:075007, 2011. doi: 10.1103/PhysRevD.84.075007.
- [61] Keisuke Harigaya, Takafumi Igari, Mihoko M. Nojiri, Michihisa Takeuchi, and Kazuhiro Tobe. Muon  $g-2$  and LHC phenomenology in the  $L_\mu - L_\tau$  gauge symmetric model. *JHEP*, 03:105, 2014. doi: 10.1007/JHEP03(2014)105.

- [62] Rabindra N. Mohapatra and R. E. Marshak. Local B-L Symmetry of Electroweak Interactions, Majorana Neutrinos and Neutron Oscillations. *Phys. Rev. Lett.*, 44:1316–1319, 1980. doi: 10.1103/PhysRevLett.44.1316. [Erratum: Phys.Rev.Lett. 44, 1643 (1980)].
- [63] W. Buchmuller, C. Greub, and P. Minkowski. Neutrino masses, neutral vector bosons and the scale of B-L breaking. *Phys. Lett. B*, 267:395–399, 1991. doi: 10.1016/0370-2693(91)90952-M.
- [64] Kevin E. Cahill. B L neutrinos. 12 1999.
- [65] Jia-Peng Huo, Xing-Xing Dong, Jiao Ma, Shu-Min Zhao, Cai Guo, Hai-Bin Zhang, Jin-Lei Yang, and Tai-Fu Feng. Lepton flavor violating decays  $Z l \pm l j \mp$  in the B-L Supersymmetric Standard Model. *J. Phys. G*, 52(2):025006, 2025. doi: 10.1088/1361-6471/ada04e.
- [66] Xing-Xing Dong, Shu-Min Zhao, Jia-Peng Huo, Tong-Tong Wang, and Tai-Fu Feng. Charged lepton flavor violation in the B-L symmetric SSM. *Phys. Rev. D*, 109(5):055019, 2024. doi: 10.1103/PhysRevD.109.055019.
- [67] Junjie Cao, Peihua Wan, Lei Wu, and Jin Min Yang. Lepton-Specific Two-Higgs Doublet Model: Experimental Constraints and Implication on Higgs Phenomenology. *Phys. Rev. D*, 80:071701, 2009. doi: 10.1103/PhysRevD.80.071701.
- [68] William J. Marciano, Toshinori Mori, and J. Michael Roney. Charged Lepton Flavor Violation Experiments. *Ann. Rev. Nucl. Part. Sci.*, 58:315–341, 2008. doi: 10.1146/annurev.nucl.58.110707.171126.
- [69] Sacha Davidson, Bertrand Echenard, Robert H. Bernstein, Julian Heeck, and David G. Hitlin. Charged Lepton Flavor Violation. 8 2022.
- [70] Pablo Escribano and Avelino Vicente. Ultralight scalars in leptonic observables. *JHEP*, 03:240, 2021. doi: 10.1007/JHEP03(2021)240.
- [71] Claudia Cornella, Paride Paradisi, and Olcyr Sumensari. Hunting for ALPs with Lepton Flavor Violation. *JHEP*, 01:158, 2020. doi: 10.1007/JHEP01(2020)158.
- [72] Marek Nowakowski, E. A. Paschos, and J. M. Rodriguez. All electromagnetic form-factors. *Eur. J. Phys.*, 26:545–560, 2005. doi: 10.1088/0143-0807/26/4/001.
- [73] Hiren H. Patel. Package-X 2.0: A Mathematica package for the analytic calculation of one-loop integrals. *Comput. Phys. Commun.*, 218:66–70, 2017. doi: 10.1016/j.cpc.2017.04.015.
- [74] G. Passarino and M. J. G. Veltman. One Loop Corrections for  $e^+ e^-$  Annihilation Into  $\mu^+ \mu^-$  in the Weinberg Model. *Nucl. Phys. B*, 160:151–207, 1979. doi: 10.1016/0550-3213(79)90234-7.
- [75] R. Keith Ellis, Zoltan Kunszt, Kirill Melnikov, and Giulia Zanderighi. One-loop calculations in quantum field theory: from Feynman diagrams to unitarity cuts. *Phys. Rept.*, 518:141–250, 2012. doi: 10.1016/j.physrep.2012.01.008.
- [76] Toshinori Mori. Final Results of the MEG Experiment. *Nuovo Cim. C*, 39(4):325, 2017. doi: 10.1393/ncc/i2016-16325-7.

- [77] K. Afanaciev et al. A search for  $\mu^+ \rightarrow e^+\gamma$  with the first dataset of the MEG II experiment. *Eur. Phys. J. C*, 84(3):216, 2024. doi: 10.1140/epjc/s10052-024-12416-2. [Erratum: Eur.Phys.J.C 84, 1042 (2024)].
- [78] A. M. Baldini et al. The design of the MEG II experiment. *Eur. Phys. J. C*, 78(5):380, 2018. doi: 10.1140/epjc/s10052-018-5845-6.
- [79] J. P. Lees et al. Limits on tau Lepton-Flavor Violating Decays in three charged leptons. *Phys. Rev. D*, 81:111101, 2010. doi: 10.1103/PhysRevD.81.111101.
- [80] W. Altmannshofer et al. The Belle II Physics Book. *PTEP*, 2019(12):123C01, 2019. doi: 10.1093/ptep/ptz106. [Erratum: PTEP 2020, 029201 (2020)].
- [81] A. Abdesselam et al. Search for lepton-flavor-violating tau-lepton decays to  $\ell\gamma$  at Belle. *JHEP*, 10:19, 2021. doi: 10.1007/JHEP10(2021)019.
- [82] U. Bellgardt et al. Search for the Decay  $\mu^+ \rightarrow e^+e^+e^-$ . *Nucl. Phys. B*, 299:1–6, 1988. doi: 10.1016/0550-3213(88)90462-2.
- [83] K. Arndt et al. Technical design of the phase I Mu3e experiment. *Nucl. Instrum. Meth. A*, 1014:165679, 2021. doi: 10.1016/j.nima.2021.165679.
- [84] K. Hayasaka et al. Search for Lepton Flavor Violating Tau Decays into Three Leptons with 719 Million Produced Tau+Tau- Pairs. *Phys. Lett. B*, 687:139–143, 2010. doi: 10.1016/j.physletb.2010.03.037.
- [85] Swagato Banerjee. Searches for Lepton Flavor Violation in Tau Decays at Belle II. *Universe*, 8(9):480, 2022. doi: 10.3390/universe8090480.
- [86] A. Abada, Manuel E. Krauss, W. Porod, F. Staub, A. Vicente, and Cedric Weiland. Lepton flavor violation in low-scale seesaw models: SUSY and non-SUSY contributions. *JHEP*, 11:048, 2014. doi: 10.1007/JHEP11(2014)048.
- [87] P. S. Bhupal Dev, Rabindra N. Mohapatra, and Yongchao Zhang. Lepton Flavor Violation Induced by a Neutral Scalar at Future Lepton Colliders. *Phys. Rev. Lett.*, 120(22):221804, 2018. doi: 10.1103/PhysRevLett.120.221804.
- [88] Gino Isidori and David M. Straub. Minimal Flavour Violation and Beyond. *Eur. Phys. J. C*, 72:2103, 2012. doi: 10.1140/epjc/s10052-012-2103-1.
- [89] Andreas Crivellin, Giancarlo D'Ambrosio, and Julian Heeck. Explaining  $h \rightarrow \mu^\pm\tau^\mp$ ,  $B \rightarrow K^*\mu^+\mu^-$  and  $B \rightarrow K\mu^+\mu^-/B \rightarrow Ke^+e^-$  in a two-Higgs-doublet model with gauged  $L_\mu - L_\tau$ . *Phys. Rev. Lett.*, 114:151801, 2015. doi: 10.1103/PhysRevLett.114.151801.
- [90] Tanya S. Roussy et al. An improved bound on the electron's electric dipole moment. *Science*, 381(6653):adg4084, 2023. doi: 10.1126/science.adg4084.
- [91] Yohei Ema, Ting Gao, and Maxim Pospelov. Standard Model Prediction for Paramagnetic Electric Dipole Moments. *Phys. Rev. Lett.*, 129(23):231801, 2022. doi: 10.1103/PhysRevLett.129.231801.

- [92] Yasuhiro Yamaguchi and Nodoka Yamanaka. Large long-distance contributions to the electric dipole moments of charged leptons in the standard model. *Phys. Rev. Lett.*, 125:241802, 2020. doi: 10.1103/PhysRevLett.125.241802.
- [93] Cari Cesarotti, Qianshu Lu, Yuichiro Nakai, Aditya Parikh, and Matthew Reece. Interpreting the Electron EDM Constraint. *JHEP*, 05:059, 2019. doi: 10.1007/JHEP05(2019)059.
- [94] Maxim Pospelov and Adam Ritz. Electric dipole moments as probes of new physics. *Annals Phys.*, 318:119–169, 2005. doi: 10.1016/j.aop.2005.04.002.
- [95] Yohei Ema, Ting Gao, and Maxim Pospelov. Improved Indirect Limits on Muon Electric Dipole Moment. *Phys. Rev. Lett.*, 128(13):131803, 2022. doi: 10.1103/PhysRevLett.128.131803.
- [96] Uma Mahanta. Dipole moments of  $\tau$  as a sensitive probe for beyond standard model physics. *Phys. Rev. D*, 54:3377–3381, 1996. doi: 10.1103/PhysRevD.54.3377.
- [97] Sin-Itiro Tomonaga and J. R. Oppenheimer. On Infinite Field Reactions in Quantum Field Theory. *Phys. Rev.*, 74:224–225, 1948. doi: 10.1103/PhysRev.74.224.
- [98] Julian S. Schwinger. On Quantum electrodynamics and the magnetic moment of the electron. *Phys. Rev.*, 73:416–417, 1948. doi: 10.1103/PhysRev.73.416.
- [99] R. P. Feynman. Space-time approach to nonrelativistic quantum mechanics. *Rev. Mod. Phys.*, 20:367–387, 1948. doi: 10.1103/RevModPhys.20.367.
- [100] Nobel Prize Outreach. The nobel prize in physics 1965. <https://www.nobelprize.org/prizes/physics/1965/summary/>, 2025. Accessed: 2025-05-18.
- [101] Richard H. Parker, Chenghui Yu, Weicheng Zhong, Brian Estey, and Holger Müller. Measurement of the fine-structure constant as a test of the Standard Model. *Science*, 360:191, 2018. doi: 10.1126/science.aap7706.
- [102] Léo Morel, Zhibin Yao, Pierre Cladé, and Saïda Guellati-Khélifa. Determination of the fine-structure constant with an accuracy of 81 parts per trillion. *Nature*, 588(7836):61–65, 2020. doi: 10.1038/s41586-020-2964-7.
- [103] X. Fan, T. G. Myers, B. A. D. Sukra, and G. Gabrielse. Measurement of the Electron Magnetic Moment. *Phys. Rev. Lett.*, 130(7):071801, 2023. doi: 10.1103/PhysRevLett.130.071801.
- [104] H. N. Brown et al. Precise measurement of the positive muon anomalous magnetic moment. *Phys. Rev. Lett.*, 86:2227–2231, 2001. doi: 10.1103/PhysRevLett.86.2227.
- [105] G. W. Bennett et al. Final Report of the Muon E821 Anomalous Magnetic Moment Measurement at BNL. *Phys. Rev. D*, 73:072003, 2006. doi: 10.1103/PhysRevD.73.072003.
- [106] B. Abi et al. Measurement of the Positive Muon Anomalous Magnetic Moment to 0.46 ppm. *Phys. Rev. Lett.*, 126(14):141801, 2021. doi: 10.1103/PhysRevLett.126.141801.
- [107] T. Aoyama et al. The anomalous magnetic moment of the muon in the Standard Model. *Phys. Rept.*, 887:1–166, 2020. doi: 10.1016/j.physrep.2020.07.006.

- [108] Christoph Lehner and Aaron S. Meyer. Consistency of hadronic vacuum polarization between lattice QCD and the R-ratio. *Phys. Rev. D*, 101:074515, 2020. doi: 10.1103/PhysRevD.101.074515.
- [109] Sz. Borsanyi et al. Leading hadronic contribution to the muon magnetic moment from lattice QCD. *Nature*, 593(7857):51–55, 2021. doi: 10.1038/s41586-021-03418-1.
- [110] A. Boccaletti et al. High precision calculation of the hadronic vacuum polarisation contribution to the muon anomaly. 7 2024.
- [111] Alexei Bazavov et al. Hadronic vacuum polarization for the muon  $g - 2$  from lattice QCD: Long-distance and full light-quark connected contribution. 12 2024.
- [112] Graziano Venanzoni. New results from the Muon g-2 Experiment. *PoS*, EPS-HEP2023:037, 2024. doi: 10.22323/1.449.0037.
- [113] E. Rutherford. The scattering of alpha and beta particles by matter and the structure of the atom. *Phil. Mag. Ser. 6*, 21:669–688, 1911. doi: 10.1080/14786440508637080.
- [114] Professor Sir E. Rutherford F. R. S. LIV. Collision of  $\alpha$  particles with light atoms. IV. An anomalous effect in nitrogen. *Phil. Mag. Ser. 6*, 37(222):581–587, 1919. doi: 10.1080/14786440608635919.
- [115] J. Chadwick. The Existence of a Neutron. *Proc. Roy. Soc. Lond. A*, 136(830):692–708, 1932. doi: 10.1098/rspa.1932.0112.
- [116] Elliott D. Bloom et al. High-Energy Inelastic e p Scattering at 6-Degrees and 10-Degrees. *Phys. Rev. Lett.*, 23:930–934, 1969. doi: 10.1103/PhysRevLett.23.930.
- [117] Martin Breidenbach, Jerome I. Friedman, Henry W. Kendall, Elliott D. Bloom, D. H. Coward, H. C. DeStaeler, J. Drees, Luke W. Mo, and Richard E. Taylor. Observed behavior of highly inelastic electron-proton scattering. *Phys. Rev. Lett.*, 23:935–939, 1969. doi: 10.1103/PhysRevLett.23.935.
- [118] J. D. Bjorken, S. Ecklund, W. R. Nelson, A. Abashian, L. Mo, P. Rassmann, C. Church, and T. Nunamaker. Search for Neutral, Penetrating, Metastable Particles Produced in the SLAC Beam Dump. In *4th Moriond Workshop: Massive Neutrinos in Particle Astrophysics*, pages 227–242, 1984.
- [119] E. M. Riordan et al. An Electron Beam Dump Search for Light, Shortlived Particles. In *23rd International Conference on High-Energy Physics*, 7 1986.
- [120] A. Bross, M. Crisler, Stephen H. Pordes, J. Volk, S. Errede, and J. Wrbanek. A Search for Shortlived Particles Produced in an Electron Beam Dump. *Phys. Rev. Lett.*, 67:2942–2945, 1991. doi: 10.1103/PhysRevLett.67.2942.
- [121] S. N. Glinenko and N. V. Krasnikov. Search for light dark vector boson: NA64 experiment. In *Quantum Field Theory at the Limits: from Strong Fields to Heavy Quarks*, pages 167–176, 2017. doi: 10.3204/DESY-PROC-2016-04/Krasnikov.
- [122] F. Bergsma et al. A Search for Decays of Heavy Neutrinos in the Mass Range 0.5-GeV to 2.8-GeV. *Phys. Lett. B*, 166:473–478, 1986. doi: 10.1016/0370-2693(86)91601-1.

- [123] R. Ball et al. The Neutrino Beam Dump Experiment at Fermilab (E613). *eConf*, C801002: 172–174, 1980.
- [124] Johannes Blumlein and Jurgen Brunner. New Exclusion Limits for Dark Gauge Forces from Beam-Dump Data. *Phys. Lett. B*, 701:155–159, 2011. doi: 10.1016/j.physletb.2011.05.046.
- [125] S. V. Gertsenberger. THE NA64 $\mu$  Experiment at the CERN SPS. *Phys. Atom. Nucl.*, 86(6): 1310–1314, 2023. doi: 10.1134/S1063778823060133.
- [126] Brian Batell, Nikita Blinov, Christopher Hearty, and Robert McGehee. Exploring Dark Sector Portals with High Intensity Experiments. In Snowmass 2021, 7 2022.
- [127] M. Anelli et al. A facility to Search for Hidden Particles (SHiP) at the CERN SPS. 4 2015.
- [128] C. Ahdida et al. The SHiP experiment at the proposed CERN SPS Beam Dump Facility. *Eur. Phys. J. C*, 82(5):486, 2022. doi: 10.1140/epjc/s10052-022-10346-5.
- [129] Katarzyna Wichmann. Recent Results from HERA Experiments. In 17th Symposium on Hadron Collider Physics 2006 (HCP 2006), 7 2007.
- [130] R. Abdul Khalek et al. Science Requirements and Detector Concepts for the Electron-Ion Collider: EIC Yellow Report. *Nucl. Phys. A*, 1026:122447, 2022. doi: 10.1016/j.nuclphysa.2022.122447.
- [131] Daniele P. Anderle et al. Electron-ion collider in China. *Front. Phys. (Beijing)*, 16(6):64701, 2021. doi: 10.1007/s11467-021-1062-0.
- [132] J-P. Delahaye et al. Enabling Intensity and Energy Frontier Science with a Muon Accelerator Facility in the U.S.: A White Paper Submitted to the 2013 U.S. Community Summer Study of the Division of Particles and Fields of the American Physical Society. In Snowmass 2013: Snowmass on the Mississippi, 8 2013.
- [133] K. Long, D. Lucchesi, M. Palmer, N. Pastrone, D. Schulte, and V. Shiltsev. Muon colliders to expand frontiers of particle physics. *Nature Phys.*, 17(3):289–292, 2021. doi: 10.1038/s41567-020-01130-x.
- [134] Carlotta Accettura et al. Towards a muon collider. *Eur. Phys. J. C*, 83(9):864, 2023. doi: 10.1140/epjc/s10052-023-11889-x. [Erratum: Eur.Phys.J.C 84, 36 (2024)].
- [135] Cari Cesarotti, Samuel Homiller, Rashmish K. Mishra, and Matthew Reece. Probing New Gauge Forces with a High-Energy Muon Beam Dump. *Phys. Rev. Lett.*, 130(7):071803, 2023. doi: 10.1103/PhysRevLett.130.071803.
- [136] Cari Cesarotti and Rikab Gambhir. The new physics case for beam-dump experiments with accelerated muon beams. *JHEP*, 05:283, 2024. doi: 10.1007/JHEP05(2024)283.
- [137] Darin Acosta and Wei Li. A muon–ion collider at BNL: The future QCD frontier and path to a new energy frontier of  $\mu+\mu-$  colliders. *Nucl. Instrum. Meth. A*, 1027:166334, 2022. doi: 10.1016/j.nima.2022.166334.
- [138] Darin Acosta, Emanuela Barberis, Nicholas Hurley, Wei Li, Osvaldo Miguel Colin, Yijie Wang, Darien Wood, and Xunwu Zuo. The potential of a TeV-scale muon-ion collider. *JINST*, 18(09):P09025, 2023. doi: 10.1088/1748-0221/18/09/P09025.

- [139] Hooman Davoudiasl, Hongkai Liu, Roman Marcarelli, Yotam Soreq, and Sokratis Trifinopoulos. New physics at the Muon (Synchrotron) Ion Collider: MuSIC for several scales. *JHEP*, 03:046, 2025. doi: 10.1007/JHEP03(2025)046.
- [140] Spencer Klein and Joakim Nystrand. Exclusive vector meson production in relativistic heavy ion collisions. *Phys. Rev. C*, 60:014903, 1999. doi: 10.1103/PhysRevC.60.014903.
- [141] Kwang Je Kim and Yung-Su Tsai. IMPROVED WEIZSACKER-WILLIAMS METHOD AND ITS APPLICATION TO LEPTON AND W BOSON PAIR PRODUCTION. *Phys. Rev. D*, 8:3109, 1973. doi: 10.1103/PhysRevD.8.3109.
- [142] Yung-Su Tsai. Pair Production and Bremsstrahlung of Charged Leptons. *Rev. Mod. Phys.*, 46:815, 1974. doi: 10.1103/RevModPhys.46.815. [Erratum: *Rev.Mod.Phys.* 49, 421–423 (1977)].
- [143] I. A. Qattan et al. High precision measurements of the proton elastic electromagnetic form factors and their ratio at  $Q^2 = 0.50, 2.64, 3.20$ , and  $4.10 \text{ GeV}^2$ . 11 2024.
- [144] Yu-Sheng Liu, David McKeen, and Gerald A. Miller. Validity of the Weizsäcker-Williams approximation and the analysis of beam dump experiments: Production of a new scalar boson. *Phys. Rev. D*, 95(3):036010, 2017. doi: 10.1103/PhysRevD.95.036010.
- [145] Yu-Sheng Liu and Gerald A. Miller. Validity of the Weizsäcker-Williams approximation and the analysis of beam dump experiments: Production of an axion, a dark photon, or a new axial-vector boson. *Phys. Rev. D*, 96(1):016004, 2017. doi: 10.1103/PhysRevD.96.016004.
- [146] C. F. von Weizsäcker. Radiation emitted in collisions of very fast electrons. *Z. Phys.*, 88: 612–625, 1934. doi: 10.1007/BF01333110.
- [147] E. J. Williams. Correlation of certain collision problems with radiation theory. *Kong. Dan. Vid. Sel. Mat. Fys. Medd.*, 13N4(4):1–50, 1935.
- [148] Chien-Yi Chen, Maxim Pospelov, and Yi-Ming Zhong. Muon Beam Experiments to Probe the Dark Sector. *Phys. Rev. D*, 95(11):115005, 2017. doi: 10.1103/PhysRevD.95.115005.
- [149] J. K. Adkins et al. Design of the ECCE detector for the Electron Ion Collider. *Nucl. Instrum. Meth. A*, 1073:170240, 2025. doi: 10.1016/j.nima.2025.170240.
- [150] Hooman Davoudiasl, Roman Marcarelli, and Ethan T. Neil. Lepton-flavor-violating ALPs at the Electron-Ion Collider: a golden opportunity. *JHEP*, 02:071, 2023. doi: 10.1007/JHEP02(2023)071.
- [151] Brian Batell, Hooman Davoudiasl, Roman Marcarelli, Ethan T. Neil, and Sebastian Trojanowski. Lepton-flavor-violating ALP signals with TeV-scale muon beams. *Phys. Rev. D*, 110(7):075039, 2024. doi: 10.1103/PhysRevD.110.075039.
- [152] Hooman Davoudiasl, Roman Marcarelli, Nicholas Miesch, and Ethan T. Neil. Searching for flavor-violating ALPs in Higgs boson decays. *Phys. Rev. D*, 104(5):055022, 2021. doi: 10.1103/PhysRevD.104.055022.
- [153] Hooman Davoudiasl, Roman Marcarelli, and Ethan T. Neil. Flavor-violating ALPs, electron g-2, and the Electron-Ion Collider. *Phys. Rev. D*, 109(11):115013, 2024. doi: 10.1103/PhysRevD.109.115013.

- [154] R. N. Mohapatra. Neutrino mass and grand unification. *Phys. Scripta T*, 121:185–191, 2005. doi: 10.1088/0031-8949/2005/T121/029.
- [155] Jared A. Evans, Philip Tanedo, and Mohammadreza Zakeri. Exotic Lepton-Flavor Violating Higgs Decays. *JHEP*, 01:028, 2020. doi: 10.1007/JHEP01(2020)028.
- [156] Albert M Sirunyan et al. Search for physics beyond the standard model in multilepton final states in proton-proton collisions at  $\sqrt{s} = 13$  TeV. *JHEP*, 03:051, 2020. doi: 10.1007/JHEP03(2020)051.
- [157] Adam Alloul, Neil D. Christensen, Céline Degrande, Claude Duhr, and Benjamin Fuks. FeynRules 2.0 - A complete toolbox for tree-level phenomenology. *Comput. Phys. Commun.*, 185: 2250–2300, 2014. doi: 10.1016/j.cpc.2014.04.012.
- [158] Johan Alwall, Michel Herquet, Fabio Maltoni, Olivier Mattelaer, and Tim Stelzer. MadGraph 5 : Going Beyond. *JHEP*, 06:128, 2011. doi: 10.1007/JHEP06(2011)128.
- [159] J. de Favereau, C. Delaere, P. Demin, A. Giammanco, V. Lemaître, A. Mertens, and M. Selvaggi. DELPHES 3, A modular framework for fast simulation of a generic collider experiment. *JHEP*, 02:057, 2014. doi: 10.1007/JHEP02(2014)057.
- [160] Gary J. Feldman and Robert D. Cousins. A Unified approach to the classical statistical analysis of small signals. *Phys. Rev. D*, 57:3873–3889, 1998. doi: 10.1103/PhysRevD.57.3873.
- [161] Georges Aad et al. Search for neutral long-lived particles in  $pp$  collisions at  $\sqrt{s} = 13$  TeV that decay into displaced hadronic jets in the ATLAS calorimeter. *JHEP*, 06:005, 2022. doi: 10.1007/JHEP06(2022)005.
- [162] Ingo Bormann. DigitizeIt - digitizing software for graphs, plots and maps, 2025. URL <https://www.digitizeit.xyz>.
- [163] Roman Marcarelli. Exclusion Plot Fits. <https://github.com/rmarcarelli/Exclusion-Plot-Fits>, 2021.
- [164] David Curtin et al. Long-Lived Particles at the Energy Frontier: The MATHUSLA Physics Case. *Rept. Prog. Phys.*, 82(11):116201, 2019. doi: 10.1088/1361-6633/ab28d6.
- [165] Henry Lubatti et al. Explore the lifetime frontier with MATHUSLA. *JINST*, 15(06):C06026, 2020. doi: 10.1088/1748-0221/15/06/C06026.
- [166] Cristiano Alpigiani et al. An Update to the Letter of Intent for MATHUSLA: Search for Long-Lived Particles at the HL-LHC. 9 2020.
- [167] Giulio Aielli et al. Expression of interest for the CODEX-b detector. *Eur. Phys. J. C*, 80(12): 1177, 2020. doi: 10.1140/epjc/s10052-020-08711-3.
- [168] Aashaq Shah. Searches for long-lived particles with the ANUBIS experiment. *PoS*, EPS-HEP2023:051, 2024. doi: 10.22323/1.449.0051.
- [169] A. Bulmahn and M. H. Reno. Cross sections and energy loss for lepton pair production in muon transport. *Phys. Rev. D*, 79:053008, 2009. doi: 10.1103/PhysRevD.79.053008.

- [170] J. L. Zhang et al. Search for  $e \rightarrow \tau$  charged lepton flavor violation at the EIC with the ECCE detector. *Nucl. Instrum. Meth. A*, 1053:168276, 2023. doi: 10.1016/j.nima.2023.168276.
- [171] James D. Bjorken, Rouven Essig, Philip Schuster, and Natalia Toro. New Fixed-Target Experiments to Search for Dark Gauge Forces. *Phys. Rev. D*, 80:075018, 2009. doi: 10.1103/PhysRevD.80.075018.
- [172] Luis A. Anchordoqui et al. The Forward Physics Facility at the Large Hadron Collider. 3 2025.
- [173] Hooman Davoudiasl, Roman Marcarelli, and Ethan T. Neil. Displaced signals of hidden vectors at the Electron-Ion Collider. *Phys. Rev. D*, 108(7):075017, 2023. doi: 10.1103/PhysRevD.108.075017.
- [174] Philip Ilten, Yotam Soreq, Mike Williams, and Wei Xue. Serendipity in dark photon searches. *JHEP*, 06:004, 2018. doi: 10.1007/JHEP06(2018)004.
- [175] Johannes Blümlein and Jürgen Brunner. New Exclusion Limits on Dark Gauge Forces from Proton Bremsstrahlung in Beam-Dump Data. *Phys. Lett. B*, 731:320–326, 2014. doi: 10.1016/j.physletb.2014.02.029.
- [176] M. Davier and H. Nguyen Ngoc. An Unambiguous Search for a Light Higgs Boson. *Phys. Lett. B*, 229:150–155, 1989. doi: 10.1016/0370-2693(89)90174-3.
- [177] J. D. Bjorken, S. Ecklund, W. R. Nelson, A. Abashian, C. Church, B. Lu, L. W. Mo, T. A. Nunamaker, and P. Rassmann. Search for Neutral Metastable Penetrating Particles Produced in the SLAC Beam Dump. *Phys. Rev. D*, 38:3375, 1988. doi: 10.1103/PhysRevD.38.3375.
- [178] E. M. Riordan et al. A Search for Short Lived Axions in an Electron Beam Dump Experiment. *Phys. Rev. Lett.*, 59:755, 1987. doi: 10.1103/PhysRevLett.59.755.
- [179] J. R. Batley et al. Search for the dark photon in  $\pi^0$  decays. *Phys. Lett. B*, 746:178–185, 2015. doi: 10.1016/j.physletb.2015.04.068.
- [180] Bernard Aubert et al. Search for Dimuon Decays of a Light Scalar Boson in Radiative Transitions  $\Upsilon \rightarrow \gamma A_0$ . *Phys. Rev. Lett.*, 103:081803, 2009. doi: 10.1103/PhysRevLett.103.081803.
- [181] J. P. Lees et al. Search for a Dark Photon in  $e^+e^-$  Collisions at BaBar. *Phys. Rev. Lett.*, 113(20):201801, 2014. doi: 10.1103/PhysRevLett.113.201801.
- [182] F. Archilli et al. Search for a vector gauge boson in  $\phi$  meson decays with the KLOE detector. *Phys. Lett. B*, 706:251–255, 2012. doi: 10.1016/j.physletb.2011.11.033.
- [183] D. Babusci et al. Limit on the production of a light vector gauge boson in phi meson decays with the KLOE detector. *Phys. Lett. B*, 720:111–115, 2013. doi: 10.1016/j.physletb.2013.01.067.
- [184] A. Anastasi et al. Limit on the production of a new vector boson in  $e^+e^- \rightarrow U\gamma$ ,  $U \rightarrow \pi^+\pi^-$  with the KLOE experiment. *Phys. Lett. B*, 757:356–361, 2016. doi: 10.1016/j.physletb.2016.04.019.

- [185] Roel Aaij et al. Search for Dark Photons Produced in 13 TeV  $pp$  Collisions. *Phys. Rev. Lett.*, 120(6):061801, 2018. doi: 10.1103/PhysRevLett.120.061801.
- [186] Roni Harnik, Joachim Kopp, and Pedro A. N. Machado. Exploring nu Signals in Dark Matter Detectors. *JCAP*, 07:026, 2012. doi: 10.1088/1475-7516/2012/07/026.
- [187] Manfred Lindner, Farinaldo S. Queiroz, Werner Rodejohann, and Xun-Jie Xu. Neutrino-electron scattering: general constraints on  $Z'$  and dark photon models. *JHEP*, 05:098, 2018. doi: 10.1007/JHEP05(2018)098.
- [188] D. Banerjee et al. Dark matter search in missing energy events with NA64. *Phys. Rev. Lett.*, 123(12):121801, 2019. doi: 10.1103/PhysRevLett.123.121801.
- [189] Akitaka Ariga et al. FASER's physics reach for long-lived particles. *Phys. Rev. D*, 99(9):095011, 2019. doi: 10.1103/PhysRevD.99.095011.
- [190] Isabel Xu, Nicole Lewis, Xiaofeng Wang, James Daniel Brandenburg, and Lijuan Ruan. Search for Dark Photons in  $\gamma\gamma \rightarrow e^+e^-$  at RHIC. 11 2022.
- [191] Nathan Baltzell et al. The Heavy Photon Search Experiment. 3 2022.
- [192] Philip Ilten, Jesse Thaler, Mike Williams, and Wei Xue. Dark photons from charm mesons at LHCb. *Phys. Rev. D*, 92(11):115017, 2015. doi: 10.1103/PhysRevD.92.115017.
- [193] Philip Ilten, Yotam Soreq, Jesse Thaler, Mike Williams, and Wei Xue. Proposed Inclusive Dark Photon Search at LHCb. *Phys. Rev. Lett.*, 116(25):251803, 2016. doi: 10.1103/PhysRevLett.116.251803.
- [194] Mark B. Wise and Yue Zhang. Lepton Flavorful Fifth Force and Depth-dependent Neutrino Matter Interactions. *JHEP*, 06:053, 2018. doi: 10.1007/JHEP06(2018)053.
- [195] Douglas Clowe, Marusa Bradac, Anthony H. Gonzalez, Maxim Markevitch, Scott W. Randall, Christine Jones, and Dennis Zaritsky. A direct empirical proof of the existence of dark matter. *Astrophys. J. Lett.*, 648:L109–L113, 2006. doi: 10.1086/508162.
- [196] Pieter van Dokkum, Shany Danieli, Yotam Cohen, Allison Merritt, Aaron J. Romanowsky, Roberto Abraham, Jean Brodie, Charlie Conroy, Deborah Lokhorst, Lamiya Mowla, Ewan O'Sullivan, and Jielai Zhang. A galaxy lacking dark matter. *Nature*, 555(7698):629–632, March 2018. ISSN 1476-4687. doi: 10.1038/nature25767. URL <http://dx.doi.org/10.1038/nature25767>.
- [197] Alexey S. Zhevlakov, Dmitry V. Kirpichnikov, and Valery E. Lyubovitskij. Lepton flavor violating dark photon. *Phys. Rev. D*, 109(1):015015, 2024. doi: 10.1103/PhysRevD.109.015015.
- [198] Stefan Scherer and Matthias R. Schindler. A Chiral perturbation theory primer. 5 2005.

## Appendix A

### Composite ALP Matching

#### A.1 UV Lagrangian

As a case study, we consider a particular BSM model which gives rise to an effective axion model with flavor off-diagonal lepton couplings: the composite dark matter and composite neutrino model of Ref. [51]. Ref. [51] provides a UV realization of their model by introducing two vector-like fermions with charge  $F$  and  $F'$  and  $(3, 2, -1/2, +)$  and  $(3, 2, -1/2, -)$  under  $SU(3)_D \times SU(2)_L \times U(1)_Y \times \mathbb{Z}_2$ , along with a generational triplet of scalars  $S_a$  with  $a = e, \mu, \tau$  and quantum numbers  $(3, 1, 0, +)$ . The resulting UV Lagrangian is<sup>1</sup>

$$\begin{aligned} \mathcal{L}_{\text{UV}} = & \lambda_1 \tilde{H}^* \bar{F} \psi_1 + \lambda_2 \tilde{H}^* \bar{F} \psi_2 + \lambda_3 \tilde{H}^* \bar{F}' \psi_3 \\ & + \lambda'_a S_a \bar{F} L_a + \sum_{i,j=1}^3 S_a \bar{\psi}_i^c \left[ g_{aS}^{ij} + i g_{aPS}^{ij} \gamma^5 \right] \psi_j \Big|_{\mathbb{Z}_2=+} \\ & + \mu_S S_e S_\mu S_\tau + \text{H.c.} \end{aligned} \quad (\text{A.1})$$

The scalar  $S$  and vector-like fermions  $F$  are heavy states, which when integrated out leave an effective Lagrangian containing the “dark quark” fields  $\psi_i$  and the Standard Model Higgs field  $H$  and left-handed lepton doublets  $L_a$ . The dark quark fields carry a  $\mathbb{Z}_2$  discrete symmetry under which only  $\psi_3$  is odd; the other fields carry appropriate  $\mathbb{Z}_2$  charges so that the Lagrangian is invariant.

---

<sup>1</sup> The  $S$ - $\psi_i$ - $\psi_j$  interaction requires that the  $S$  doesn’t couple to the usual current  $\bar{\psi}_i \psi_j$ , but instead to  $\bar{\psi}_i^c \psi_j$ . This is because the decomposition  $3 \times \bar{3} \times 3 = 3 \oplus 3 \oplus 6 \oplus 15$  does not contain a singlet, whereas  $3 \times 3 \times 3 = 1 \oplus 8 \oplus 8 \oplus 10$  does. The color contractions for the  $S$  and  $\psi_i$  are suppressed; explicitly,  $S_a \bar{\psi}_i^c \psi_j \sim \epsilon_{\alpha\beta\gamma} (S_a)_\alpha (\bar{\psi}_i^c)_\beta (\psi_j)_\gamma$ .

The dark quarks are charged under a confining  $SU(3)_D$  gauge interaction, so that below the dark confinement scale  $\Lambda_D$  the appropriate degrees of freedom are meson-like and baryon-like states formed from the  $\psi_i$ . The low-lying spectrum of composite states in this theory include  $N \sim (\psi_i^3)$  “dark neutrons”, which play a role in neutrino mass generation, and  $\kappa \sim (\bar{\psi}_i \psi_3)$  “dark kaons,” the lightest of which is stable and provides a dark matter candidate. The four remaining light meson states, a “dark pion” triplet  $\Pi \sim (\bar{\psi}_1 \psi_2)$  and an equivalent of the  $\eta$  meson, are unstable and can be identified as axion-like particles at low energies.

To match on to a low-energy effective Lagrangian, the unstable dark meson states should be identified as four different ALP states. In practice, following the parameters of the UV completion, we will assume that these states are degenerate and match on to the simplified Lagrangian Eqs. 2.41–2.43 by introducing counting factors to treat them as a single  $a$  state. Exploration of the dynamics of composite ALP states where mass splittings are important would be interesting to consider in future work.

## A.2 Higgs couplings

We begin by consideration of the Higgs-dark pion couplings to determine  $C_{ah}$  and  $C'_{ah}$  in the ALP Lagrangian. For pions in the Standard Model, both couplings arise; however, the derivative  $C_{ah}$  coupling arises due to matching from the coupling of the Higgs to the gluonic  $G\tilde{G}$  operator, which in turn is induced by integrating the heavy quarks  $c, b, t$  out of the theory. In the present model, there are no such heavy dark fermions, so that the Higgs coupling to axions is entirely due to matching on to the same operator  $h\bar{\psi}_i \psi_i$  which is responsible for generation of dark fermion mass. This leads to generation of only the  $C'_{ah}$  operator when matching at leading order. We have

$$\mathcal{L}_{\Pi h} = \sum_{\Pi} \frac{1}{2v} M_{\Pi}^2 \Pi^2 h = \sum_{\Pi} \frac{C'_{\Pi h}}{\Lambda^2} v M_{\Pi}^2 \Pi^2 h \quad (\text{A.2})$$

where the sum is over the four light meson states, and we are defining the effective coupling

$$\frac{C'_{\Pi h}}{\Lambda^2} \equiv \frac{1}{2v^2}. \quad (\text{A.3})$$

This is not quite the same as  $C'_{ah}$ , due to the fact that there are multiple  $\Pi$  states but only a single  $a$  in the ALP EFT Lagrangian (2.21). This leads to an enhancement of  $\Gamma(h \rightarrow \Pi\Pi)$  by a factor of 4 relative to the magnitude of  $\Gamma(h \rightarrow aa)$  for equivalent values of the coupling. As a result, bounds on  $C'_{\Pi h}$  will be stronger by a factor of 2. To compare with the bounds we have derived, the equivalent value of  $C'_{ah}$  is thus

$$\frac{C'_{ah}}{\Lambda^2} = \frac{1}{v^2} \approx 16 \text{ TeV}^{-2}. \quad (\text{A.4})$$

It is interesting to note that the result Eq. (A.4) is completely independent of the parameters of the UV model.<sup>2</sup> This indicates that the same result would hold in any composite axion model satisfying the conditions that all fermion mass is generated by Higgs Yukawa couplings, and that there are no additional heavy fermions in the composite sector that would give rise to a  $C_{ah}$  coupling.

### A.3 Lepton couplings

The other coupling we would like to match onto the low-energy ALP Lagrangian is the lepton-ALP coupling  $C_{\ell\ell'}$ . This requires a detailed matching calculation of dark pion decay into lepton pairs in the UV-complete model,  $\Pi \rightarrow \ell_a^- \ell_b^+$ . In general, because confinement is a strong-coupling process, we would need a non-perturbative approach such as lattice calculation to predict the properties of the infrared theory. However, since the  $\Pi$  is a pGNB associated with chiral symmetry breaking, we can match on to chiral perturbation theory in the infrared.

Ordinarily, effective matching proceeds by calculation of the same amplitude in the UV and effective theories. However, matching over a confinement transition is not amenable to this approach, because the state  $\Pi$  does not exist in the UV theory. We instead follow the standard method for chiral perturbation theory of identifying symmetry currents shared between the UV and IR theories, in particular we use the  $SU(3)_L \times SU(3)_R$  chiral symmetry group. The full set of eight pNBGs are represented by the matrix field  $\Pi \equiv \Pi_x \lambda^x$ , where  $x = 1, \dots, 8$  is the adjoint label and  $\lambda^x$  are the Gell-Mann matrices, the generators of  $SU(3)$ .

---

<sup>2</sup> up to the number of degenerate ALP states  $N_\Pi$ : to recast in general, we would constrain the combination  $C'_{ah}/\Lambda^2 = 1/(\sqrt{N_\Pi} v^2)$ .

In chiral perturbation theory, keeping terms only up to first order in the  $\Pi$  fields since we are interested only in pion decays, only the axial-vector current

$$j_A^{\mu,x} = -F_{\Pi_x} \partial^\mu \Pi_x. \quad (\text{A.5})$$

is non-zero [198]. In the ultraviolet theory, the matching axial-vector symmetry current is

$$j_A^{\mu,x} = \bar{\psi} \lambda^x \gamma^\mu \gamma^5 \psi. \quad (\text{A.6})$$

For the “dark pion” fields  $\Pi$  in particular, we do not have to consider the full set of  $SU(3)$  generators; they are formed from linear combinations of  $\psi_1$  and  $\psi_2$  only, with the Pauli matrices as the corresponding generators. Using Eqs. (A.5,A.6) and the conventions of Ref. [198] for the  $SU(3)$  flavor symmetry generators, and identifying the effective cutoff  $\Lambda \sim M_S^2/F_\Pi$ , we find for the matched “dark pion” version of this interaction

$$\mathcal{L}_{\Pi\ell\ell} = \sum_x \partial_\mu \Pi_x \sum_{a,b} \frac{C_{ab}^x}{\Lambda} \bar{\ell}_a \gamma^\mu P_L \ell_b. \quad (\text{A.7})$$

We will compute  $C_{ab}^x/\Lambda$  below.

### A.3.1 Amplitude calculation

To proceed, we will calculate the amplitude for the process  $\psi_i \bar{\psi}_j \rightarrow \ell_a^- \ell_b^+$  in the UV theory, the diagram for which is shown in Fig. A.1. We will then identify the components of this amplitude that overlap with the axial-vector quark current. Integrating out the heavy  $S$  and  $F$  states will lead us to a four-fermion interaction between the leptons and the axial-vector dark quark current, which we can then replace with a dark pion interaction through current matching. Using the Feynman rules for the Lagrangian (A.1), the amplitude can be expressed in the form

$$i\mathcal{M} = \lambda'_a \lambda'^*_b N_c \bar{v}(p_j) \gamma^5 \left[ G_{ab}^{ij-} \gamma_\nu \mathcal{I}_1^{\mu\nu} + G_{ab}^{ij+} \mathcal{I}_2^\mu \right] u(p_i) \bar{u}(k_a) \gamma_\mu P_L v(k_b) \quad (\text{A.8})$$

where  $N_c$  is a dark color factor,  $p_i$  and  $p_j$  are the momenta of the dark quarks  $\psi_i$  and  $\psi_j$ ,  $k_a$  and  $k_b$  are the momenta of the leptons  $\ell_a$  and  $\ell_b$ ,  $G_{ab}^{ij\pm} = g_{aS}^{ij} g_{bPS}^{ij*} \pm g_{aPS}^{ij} g_{bS}^{ij*}$ , and  $\mathcal{I}_1$  and  $\mathcal{I}_2$  are integral

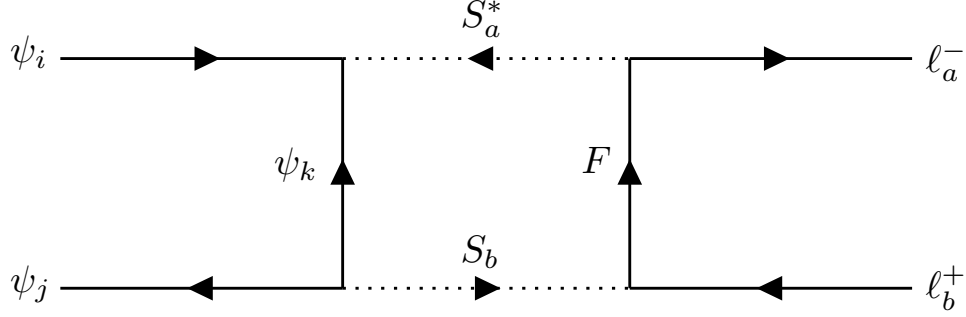


Figure A.1: A diagram in the UV theory which can be matched onto  $\Pi \rightarrow \ell_a^- \ell_b^+$  in the low-energy EFT. Note that the arrow on the internal  $\psi_k$  line is reversed, due to the presence of a charge conjugation operator in the  $S$  interaction in A.1.

expressions given by

$$\mathcal{I}_1^{\mu\nu} = \int \frac{d^4 q}{(2\pi)^4} \frac{q^\nu}{q^2 - m^2} \frac{1}{(p_i + q)^2 - M_S^2} \frac{1}{(p_j - q)^2 - M_S^2} \frac{p_i^\mu + q^\mu - k_a^\mu}{(p_i + q - k_a)^2 - M_F^2}, \quad (\text{A.9})$$

$$\mathcal{I}_2^\mu = \int \frac{d^4 q}{(2\pi)^4} \frac{m_k}{q^2 - m^2} \frac{1}{(p_i + q)^2 - M_S^2} \frac{1}{(p_j - q)^2 - M_S^2} \frac{p_i^\mu + q^\mu - k_a^\mu}{(p_i + q - k_a)^2 - M_F^2}. \quad (\text{A.10})$$

These integrals have solutions (to lowest order in  $m/M_F, m/M_S$ ),

$$I_1^{\mu\nu} = \frac{ig^{\mu\nu}}{16\pi^2 M_S^2} g_1(M_F^2/M_S^2), \quad I_2^\mu = \frac{i}{16\pi^2 M_S^2} \frac{m(p_i^\mu - k_a^\mu)}{M_S^2} g_2(M_F^2/M_S^2), \quad (\text{A.11})$$

where

$$g_1(x) = \frac{1 - x + x \log x}{(1 - x)^2}, \quad g_2(x) = \frac{1 - x + \log x}{(1 - x)^2}. \quad (\text{A.12})$$

Taking  $M_F \approx M_S$ , we note that  $\lim_{x \rightarrow 1} g_1(x) = -\lim_{x \rightarrow 1} g_2(x) = 1/2$ . In addition,  $I_2 \ll I_1$  due to a suppression of  $m_k/M_S$  (and a potential additional suppression by  $(p_i^\mu - k_a^\mu)/M_S$  as well depending on the energy scale of the interaction). Finally, we note that the color factor is  $N_C = \epsilon_{\alpha\beta\gamma}\delta_\delta^\gamma\epsilon^{\rho\sigma\tau}\delta_\tau^\beta = \epsilon_{\alpha\beta\gamma}\epsilon^{\gamma\sigma\beta} = 2\delta_\alpha^\sigma$ . Hence, the amplitude at low energy scales ( $\ll M_S$ ) can be written

$$i\mathcal{M} \approx \frac{\lambda'_a \lambda'^*_b C_{ab}^{ij-}}{16\pi^2 M_S^2} [\bar{v}(p_j)\gamma^5\gamma^\mu u(p_i)][\bar{u}(k_a)\gamma_\mu P_L v(k_b)], \quad (\text{A.13})$$

corresponding to an effective interaction

$$\mathcal{L}_{\psi\psi\ell\ell} = \sum_{a,b} \frac{\lambda'_a \lambda'^*_b}{16\pi^2 M_S^2} \sum_{i,j} \left[ i G_{ab}^{ij-} \bar{\psi}_j \gamma^\mu \gamma^5 \psi_i \right]_{\mathbb{Z}_2=+} \bar{\ell}_a \gamma_\mu P_L \ell_b. \quad (\text{A.14})$$

where we have placed the factor of  $i$  adjacent to  $G_{ab}^{x-}$  to emphasize that  $G_{ab}^{x-}$  is *anti-Hermitian* in the lepton indices  $a, b$ .

### A.3.2 Dark Pion Matching

Treating the dark quarks  $\psi_i$  as a global  $SU(3)$  triplet, the interaction Lagrangian (A.14) can be written in the form

$$\mathcal{L}_{\psi\psi\ell\ell} = \sum_{a,b} \frac{\lambda'_a \lambda'^*_b}{16\pi^2 M_S^2} \sum_{i,j} i \bar{\psi} \mathbf{G}_{ab}^- \gamma^\mu \gamma^5 \psi \bar{\ell}_a \gamma_\mu P_L \ell_b. \quad (\text{A.15})$$

where

$$\psi \equiv \begin{pmatrix} \psi_1 \\ \psi_2 \\ \psi_3 \end{pmatrix} \quad \text{and} \quad \mathbf{G}_{ab}^- \equiv \begin{pmatrix} G_{ab}^{11-} & G_{ab}^{12-} & 0 \\ G_{ab}^{21-} & G_{ab}^{22-} & 0 \\ 0 & 0 & G_{ab}^{33-} \end{pmatrix} \quad (\text{A.16})$$

and  $G_{ab}^{i3-} = G_{ab}^{3i-} = 0$  for  $i = 1, 2$  to enforce the  $\mathbb{Z}_2$  symmetry. We wish to match onto the  $\mathbb{Z}_2$ -even dark pions  $\Pi_x \in \{\pi_D, \pi'_D, \bar{\pi}'_D, \eta_D\}$ . To do so, we note that the overlap between the axial current operator and the pion wavefunction is given by

$$\langle 0 | \bar{\psi}_i \gamma^\mu \gamma^5 \lambda_{ij}^x \psi_j | \Pi_y(p) \rangle = i p^\mu F_{\Pi_y} \delta_y^x. \quad (\text{A.17})$$

Hence, in order to find the contribution of the dark quark effective interaction Lagrangian to the pion interactions, we must decompose the interaction matrix  $\mathbf{G}_{ab}^-$  into the identity and Gell-Mann matrices  $\mathbf{G}_{ab}^- = G_{ab}^{0-} \mathbf{1} + \sum_z G_{ab}^{x-} \lambda^x$ , which is always possible for a  $3 \times 3$  complex Hermitian matrix. We can invert this equation using the property  $\sum_{i,j} \lambda_{ij}^x \lambda_{ij}^y = 2\delta^{xy}$ , so  $G_{ab}^{x-} = \frac{1}{2} \sum_{i,j} \lambda_{ij}^x G_{ab}^{ij,-}$ . Explicitly,

$$G_{ab}^{\pi-} = \frac{1}{2} (G_{ab}^{11-} - G_{ab}^{22-}) \quad (\text{A.18})$$

$$G_{ab}^{\bar{\pi}'-} = \frac{1}{\sqrt{2}} G_{ab}^{12-}, \quad (\text{A.19})$$

$$G_{ab}^{\pi'-} = \frac{1}{\sqrt{2}} G_{ab}^{21-}, \quad (\text{A.20})$$

$$G_{ab}^{\eta-} = \frac{1}{2\sqrt{3}} (G_{ab}^{11-} + G_{ab}^{22-} - 2G_{ab}^{33-}). \quad (\text{A.21})$$

Then, the effective lepton-pion interaction strength is given by

$$\frac{C_{ab}^x}{\Lambda} = \frac{\lambda'_a \lambda'^*_b}{16\pi^2 M_S} \frac{F_{\Pi_x}}{M_S} \frac{iG_{ab}^{x-}}{M_S} \quad (\text{A.22})$$

In terms of the original parameters of the UV Lagrangian

$$\frac{C_{ab}^x}{\Lambda} = \frac{\lambda'_a \lambda'^*_b}{32\pi^2 M_S} \sum_{i,j} i \left[ g_{aS}^{ij} g_{bPS}^{ij*} - g_{aPS}^{ij} g_{bS}^{ij*} \right] \frac{F_{\Pi_x}}{M_S} \lambda_{ij}^x. \quad (\text{A.23})$$

In the event that the dark pions  $\Pi^-$  are nearly degenerate, we can approximately match this onto the ALP EFT (2.21) parameter  $C_{\ell\ell'}$ . Roughly,

$$\frac{C_{\ell\ell'}}{\Lambda} \sim \frac{\lambda'^2 g^2}{32\pi^2 M_S} \frac{F_{\Pi}}{M_S}. \quad (\text{A.24})$$

Adopting the numerical values for the benchmark UV model in [51] of  $\lambda' \approx 0.1$ ,  $g \approx 0.3$ ,  $F_{\Pi} \sim 80$  GeV, and  $M_S \sim 1$  TeV we find the numerical value

$$\frac{|C_{\ell\ell'}|}{\Lambda} \approx 2 \times 10^{-7} \text{ TeV}^{-1}. \quad (\text{A.25})$$

So while the Higgs coupling  $C'_{ah}/\Lambda^2$  from this model is quite large, the lepton coupling  $C_{\ell\ell'}/\Lambda$  is substantially smaller, too weak to be probed at current experiments. However, given the flavor-violating nature of the interaction, such a coupling may be probed at experiments in the near future, as discussed in the text.

## Appendix B

### Distance of Closest Approach

In Chapter 6, we presented exclusion limits on the gauge coupling of dark bosons at the EIC and MuSIC. These exclusion limits required an estimate of the minimum resolvable displacement of the dark boson, which is related to the transverse distance-of-closest approach (DCA) of the reconstructed trajectories of its final-state decay products. We initially assumed the final states followed straight-line trajectories to estimate the DCA and derive the limits in Section 6.5, then considered the potential effect of a strong magnetic field in Section 6.6. Here, we present derivations of the expressions for the DCA used in those analyses.

For simplicity, we will focus on the analysis which assumes the final-state leptons experience a transverse magnetic field  $\mathbf{B}$ . The analysis for a straight-line trajectory corresponds to the limit  $|\mathbf{B}| \rightarrow 0$ . Given that we assume that all particle trajectories lie in the plane, it is easiest to work in the complex plane.<sup>1</sup> We assume that the interaction point lies at the origin, and parametrize the trajectory of the dark boson by

$$\tilde{\mathbf{d}} = de^{i\theta}. \quad (\text{B.1})$$

If the final-state leptonic decay products of the dark boson open at an angle  $\theta_{\ell\ell}$  subject to a magnetic field of magnitude  $B = 1 \text{ T}$ , they will follow circular trajectories with radius  $R = E_\ell/ecB$ . We assume that each lepton carries away half the energy of the dark boson, so  $E_\ell = E_{A'}/2$ ; as such, their angles w.r.t. the direction of the dark boson will each be  $\theta_{\ell\ell}/2$ . Without loss of

---

<sup>1</sup> I have recently begun learning about geometric algebras, and my feeling is that this derivation would be even cleaner using the conformal geometric algebra. This is left as an exercise for the reader.

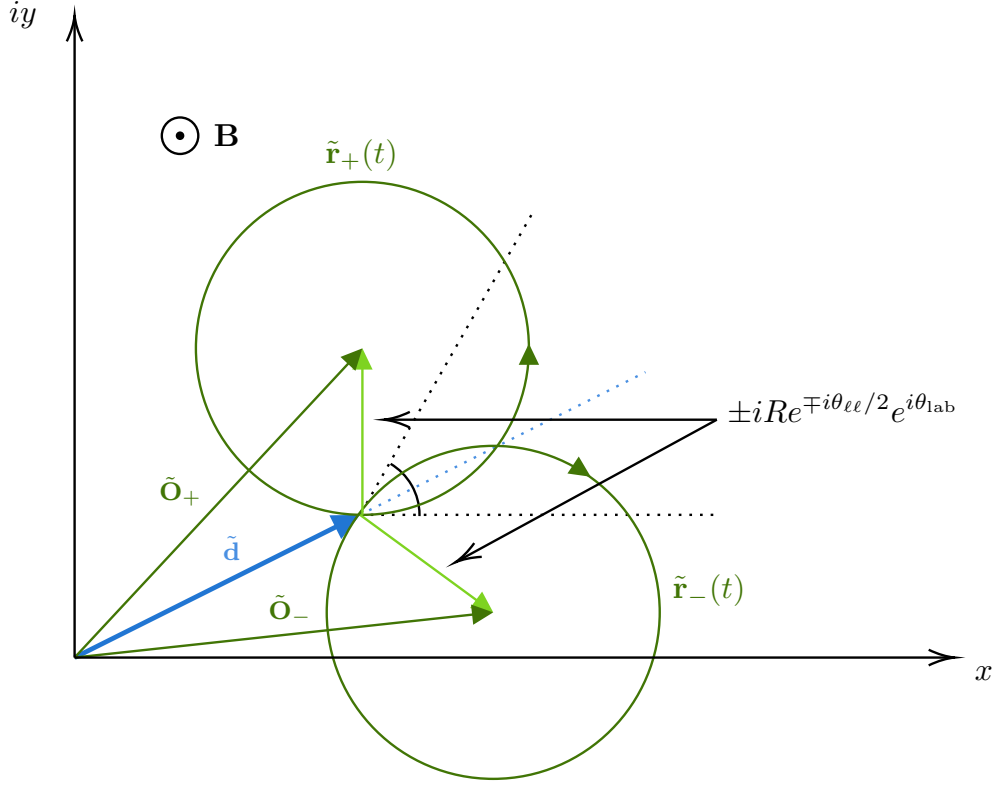


Figure B.1: A schematic representation of the complex geometry used to compute the DCA of the final-state leptons assuming they follow circular arcs.

generality, we can assume that the magnetic field points out of the page, and that the  $\ell^-$  is emitted *councclockwise* relative to the  $\ell^+$ . A schematic of our set-up is shown in Fig. B.1. The alternate orientation (the  $\ell^-$  emitted clockwise relative to the  $\ell^+$ ) is encapsulated by taking  $R \rightarrow -R$ . With these assumptions, the location of the center of the trajectories of the  $\ell^\pm$  is given by

$$\begin{aligned}\tilde{\mathbf{O}}_\pm &= (d \pm iRe^{\mp i\theta_{\ell\ell}/2})e^{i\theta} \\ &= \tilde{\mathbf{d}} \pm iRe^{i\theta \mp i\theta_{\ell\ell}/2}\end{aligned}\tag{B.2}$$

and their trajectories are parametrized by

$$\begin{aligned}\tilde{\mathbf{r}}_\pm(t) &= \tilde{\mathbf{O}}_\pm \mp iRe^{i\theta \mp i\theta_{\ell\ell}/2}e^{\pm it} \\ &= \tilde{\mathbf{d}} \pm iR(1 - e^{\pm it})e^{i\theta \mp i\theta_{\ell\ell}/2} \\ &= \tilde{\mathbf{d}} + 2R \sin(t/2)e^{i\theta \mp i\theta_{\ell\ell}/2 \pm it/2}\end{aligned}\tag{B.3}$$

where we have chosen  $t$  such that  $t > 0$  corresponds to the trajectories *after* decay of the dark boson, and  $t < 0$  corresponds to the reconstructed trajectories.<sup>2</sup> The DCA of each trajectory to the interaction point is given by

$$\text{DCA}_\pm = \min_t |\tilde{\mathbf{r}}_\pm(t)|. \quad (\text{B.4})$$

The distance from either trajectory to the interaction point can be written

$$\begin{aligned} |\tilde{\mathbf{r}}_\pm(t)|^2 &= |\tilde{\mathbf{d}}|^2 + 4R^2 \sin^2(t/2) + 4\text{Re} \left\{ \tilde{\mathbf{d}}^* R \sin(t/2) e^{i\theta \mp i\theta_{\ell\ell}/2 \pm it/2} \right\} \\ &= d^2 + 4R^2 \sin^2(t/2) + 4dR \sin(t/2) \cos((t - \theta_{\ell\ell})/2) \\ &= d^2 + 2R^2(1 - \cos t) + 2dR [\sin(t - \theta_{\ell\ell}/2) + \sin(\theta_{\ell\ell}/2)]. \end{aligned} \quad (\text{B.5})$$

Notably, dependence on  $\ell^\pm$  has dropped out. In particular, the circular trajectories in Fig. B.1 are equidistant from the origin (interaction point), and we have chosen a parametrization such that this is manifest in Eq. B.5. Those values of  $t$  which extremize the distance are then given by

$$2R^2 \sin t + 2dR \cos(t - \theta_{\ell\ell}/2) = 0 \quad (\text{B.6})$$

which has solutions

$$t = \pm \arccos \left( \pm \frac{R + d \sin(\theta_{\ell\ell}/2)}{\sqrt{d^2 + R^2 + 2dR \sin(\theta_{\ell\ell}/2)}} \right) \quad (\text{B.7})$$

where the signs no longer correspond to  $\ell^\pm$  labels, and any combination of the signs is a valid solution. Through explicit evaluation, we find that the value of  $t$  depends on whether  $R > 0$  or  $R < 0$  (which corresponds to swapping the  $\ell^+$  and  $\ell^-$  in the final-state). We have

$$t_> = -\arccos \left( \frac{R + d \sin(\theta_{\ell\ell}/2)}{\sqrt{d^2 + R^2}} \right) \quad (\text{B.8})$$

$$t_< = \arccos \left( \frac{|R| - d \sin(\theta_{\ell\ell}/2)}{\sqrt{d^2 + |R|^2}} \right) \quad (\text{B.9})$$

which, when substituted into our expression for  $|\tilde{\mathbf{r}}_\pm(t)|^2$ , yield

$$(\text{DCA}_>)^2 = \left| \sqrt{R^2 + d^2 + 2dR \sin(\theta_{\ell\ell}/2)} - R \right|^2 \quad (\text{B.10})$$

---

<sup>2</sup> For  $R < 0$ , one must replace  $t$  with  $-t$  to retain this property.

and

$$(\text{DCA}_<)^2 = \left| \sqrt{|R|^2 + d^2 - 2d|R| \sin(\theta_{\ell\ell}/2)} - |R| \right|^2. \quad (\text{B.11})$$

For each of these scenarios, we define the *average transverse DCA*,  $\overline{\text{DCA}_{2\text{D}}}$ , as the average of the transverse components of the DCA for each lepton. Notably, the DCA is the same for both of them, but the transverse components are given by

$$\text{DCA}_{2\text{D}}^\pm = \text{DCA} \cos(\theta \pm \theta_{\ell\ell}/2) \quad (\text{B.12})$$

yielding an average

$$\begin{aligned} \overline{\text{DCA}_{2\text{D}}} &= \frac{1}{2} (\text{DCA}_{2\text{D}}^+ + \text{DCA}_{2\text{D}}^-) \\ &= \text{DCA} \cos \theta \cos(\theta_{\ell\ell}/2). \end{aligned} \quad (\text{B.13})$$

Hence, given a minimum DCA resolution  $\text{DCA}_{2\text{D}}^{\min}$  (and defining  $\text{DCA}^{\min} \equiv \text{DCA}_{2\text{D}}^{\min}/(\cos \theta \cos(\theta_{\ell\ell}/2))$  for convenience), the minimum resolvable displacement  $d^{\min}$  can be found by solving the equation

$$\left| \sqrt{|R|^2 + d^2 + 2d|R| \sin(\theta_{\ell\ell}/2)} - R \right| > \text{DCA}^{\min} \quad (\text{B.14})$$

for  $R > 0$  and

$$\left| \sqrt{|R|^2 + d^2 - 2d|R| \sin(\theta_{\ell\ell}/2)} - |R| \right| > \text{DCA}^{\min} \quad (\text{B.15})$$

for  $R < 0$ . The first equation is slightly easier to solve, because the term inside of the absolute value is always positive. In contrast, the sign of the absolute value in the second equation is conditional on the relative size of  $|R| \sin(\theta_{\ell\ell}/2)$  and  $d$ . After evaluation of all possible solutions, we find

$$d_>^{\min} = -R \sin(\theta_{\ell\ell}/2) + \begin{cases} \sqrt{(\text{DCA}^{\min})^2 - 2R(\text{DCA}^{\min}) + R^2 \sin^2(\theta_{\ell\ell}/2)} \\ \sqrt{(\text{DCA}^{\min})^2 + 2R(\text{DCA}^{\min}) + R^2 \sin^2(\theta_{\ell\ell}/2)} \end{cases} \quad (\text{B.16})$$

and

$$d_<^{\min} = |R| \sin(\theta_{\ell\ell}/2) + \begin{cases} -\sqrt{(\text{DCA}^{\min})^2 - 2|R|(\text{DCA}^{\min}) + |R|^2 \sin^2(\theta_{\ell\ell}/2)} \\ \sqrt{(\text{DCA}^{\min})^2 + 2|R|(\text{DCA}^{\min}) + |R|^2 \sin^2(\theta_{\ell\ell}/2)} \end{cases} \quad (\text{B.17})$$

where the upper cases are chosen unless the resulting expression is negative or complex. To complete our analysis, we assume that half of the dark bosons decay with the  $\ell^-$  counterclockwise relative to the  $\ell^+$  (the ‘<’ orientation) and half of the dark bosons decay with the  $\ell^-$  clockwise relative to the  $\ell^+$  (the ‘>’ orientation).

In the limit of infinite  $R$ , we can recover the straight-line trajectories. We find

$$d_{\min} \equiv \lim_{R \rightarrow \infty} d_{>}^{\min} = \lim_{|R| \rightarrow \infty} d_{<}^{\min} = \frac{\text{DCA}_{2\text{D}}^{\min}}{\sin(\theta_{\ell\ell}/2)}. \quad (\text{B.18})$$

Finally, we must provide an estimate for the opening angle  $\theta_{\ell\ell}$ . We can approximate  $\theta_{\ell\ell}$  using four-momentum conservation:

$$\gamma m_{A'} = 2\gamma_\ell m_\ell \quad (\text{B.19})$$

$$\gamma v m_{A'} = 2\gamma_\ell v_\ell m_\ell \cos(\theta_{\ell\ell}/2) \quad (\text{B.20})$$

which gives

$$\sin \theta_{\ell\ell} = \frac{2\gamma v m_{A'}}{\gamma^2 m_{A'}^2 - 4m_\ell^2} \sqrt{m_{A'}^2 - 4m_\ell^2} \quad (\text{B.21})$$

$$\approx \frac{2v}{\gamma}. \quad (\text{B.22})$$

Hence, we take  $\theta_{\ell\ell} \approx 2v/\gamma$  for our analyses. Use of the exact formula (B.21) will yield a better estimate of the limits near mass threshold ( $m_{A'} \gtrsim 2m_\ell$ ), but should otherwise have a negligible effect on the results.